



THE HONG KONG
POLYTECHNIC UNIVERSITY

香港理工大學

Pao Yue-kong Library

包玉剛圖書館

Copyright Undertaking

This thesis is protected by copyright, with all rights reserved.

By reading and using the thesis, the reader understands and agrees to the following terms:

1. The reader will abide by the rules and legal ordinances governing copyright regarding the use of the thesis.
2. The reader will use the thesis for the purpose of research or private study only and not for distribution or further reproduction or any other purpose.
3. The reader agrees to indemnify and hold the University harmless from and against any loss, damage, cost, liability or expenses arising from copyright infringement or unauthorized usage.

IMPORTANT

If you have reasons to believe that any materials in this thesis are deemed not suitable to be distributed in this form, or a copyright owner having difficulty with the material being included in our database, please contact lbsys@polyu.edu.hk providing details. The Library will look into your claim and consider taking remedial action upon receipt of the written requests.

**ADVANCED OXIDATION OF
PHARMACEUTICALS WITH
PEROXYMONOSULFATE (PMS)
ACTIVATED BY NOVEL SPINEL-
TYPE OXIDES SUPPORTED ON
POROUS CLAY MINERALS**

XUE YANG

PhD

The Hong Kong Polytechnic University

2023

The Hong Kong Polytechnic University

**Department of Civil and Environmental
Engineering**

**Advanced oxidation of pharmaceuticals
with peroxymonosulfate (PMS)
activated by novel spinel-type oxides
supported on porous clay minerals**

Xue YANG

A thesis submitted in partial fulfillment of the requirements for
the degree of Doctor of Philosophy

October 2022

CERTIFICATE OF ORIGINALITY

I hereby declare that this thesis is my own work and that, to the best of my knowledge and belief, it reproduces no material previously published or written, nor material that has been accepted for the award of any other degree or diploma, except where due acknowledgement has been made in the text.

_____ (Signed)

Xue YANG _____ (Name of Student)

Abstract

The presence of pharmaceuticals and their metabolites in waterbodies has been recognized as an emerging environmental issue globally partly due to their easy entry, continuous release, bioaccumulation, considerable toxicity, and possible carcinogenic effects on organisms. However, since conventional wastewater treatment plants (WWTPs) are never designed for the removal of pharmaceuticals, it has in turn become a point source of pollution. Therefore, advanced oxidation processes (AOPs) with the generation of oxidative reactive oxygen species, have experienced remarkably development in the elimination of emerging contaminants including pharmaceuticals due to factors such as simplicity, higher efficiency, cost-effectiveness, and mineralization potential.

In this study, novel composite catalysts tailored by CoMn_2O_4 (CMO) and porous natural clay minerals, *e.g.* halloysite (Hal) and kaolinite (Kln), were developed to activate peroxymonosulfate (PMS) for efficient degradation of pharmaceuticals in aqueous environment.

The results showed that among the series of halloysite (Hal)-based composite catalysts with different CMO loading percentage, 40-CMO/Hal with a moderate CMO content displayed homogeneous dispersion, restricted grain size, and superior catalytic ability with better stability and durability than bare CMO.

Therefore, 40-CMO/Hal (*Abbrev.* CMO/Hal) with the optimal overall performances was chosen to further investigate the effects caused by different clay mineral substrates through comparisons with CMO anchored on kaolinite (Kln), a natural lamellar clay mineral, at the same percentage, 40%. Hal and Kln helped to control the crystallinity of CMO simultaneously with inducing more oxygen vacancies (OVs), which significantly enhanced the working efficiency. The presence of Hal and/or Kln contributed to the composite catalysts with better stability and durability than CMO. In addition, CMO/Hal contained more OVs, while CMO/Kln showed higher structural stability with lower metal leaching.

This work shed light on the understanding of unearth surface reaction mechanism during PMS activation, which also provides a new reference in enhancing the catalytic performance of transition metal oxides by immobilizing them on natural clay mineral substrates. What's more, since Kln and Hal are both abundant in China and many other countries, the application of them in wastewater treatment and chemical industries also offers another chance in enhancing regional fundamental researches related to natural resources applications.

Since inorganic anions and natural organic matter (NOM) are unavoidable in nature water bodies and wastewaters, their effects towards AOP using activated PMS should be considered, which, however, still remains unknown. Therefore, the degradation efficiency of tetracycline (TC) using PMS activated by LaCoO_3 with the presence of

some common inorganic anions and NOM (e.g., humic acid (HA)) were investigated. The results showed that the presence of inorganic anions (i.e., H_2PO_4^- , Cl^- and SO_4^{2-}) and low-concentration of HA promoted the degradation. Among them, H_2PO_4^- and lower concentration of HA showed the most obvious outcome, while the SO_4^{2-} can regulate the radical formation, minimize the peak radical level, and therefore promote the overall performance of the process. Generally, the $\text{LaCoO}_3/\text{PMS}$ system was proved as a rapid, economical and stable approach for TC degradation, which provided a novel strategy for pharmaceutical removal during water purification.

Keywords: Spinel Oxide, natural clay minerals, Peroxymonosulfate activation, Pharmaceutical degradation, Oxygen vacancies, Perovskite.

List of publications

Journal papers:

1. **Yang X**, Wei G, Wu P, Liu P, Liang X, Chu W. Controlling oxygen vacancies of CoMn_2O_4 by loading on planar and tubular clay minerals and its application for boosted PMS activation. *Journal of Hazardous Materials* 2022; 436: 129060.
2. **Yang X**, Wei G, Wu P, Liu P, Liang X, Chu W. Novel halloysite nanotube-based ultrafine CoMn_2O_4 catalyst for efficient degradation of pharmaceuticals through peroxymonosulfate activation. *Applied Surface Science* 2022; 588: 152899.
3. **Yang X**, Wu P, Chu W, Wei G. Peroxymonosulfate/ LaCoO_3 system for tetracycline degradation: Performance and effects of co-existing inorganic anions and natural organic matter. *Journal of Water Process Engineering* 2021; 43: 102231.

Acknowledgements

First things first, I would like to dedicate my deep gratitude and respect to my chief supervisor, also the principal investigator (PI) of the sponsored project for this work, Prof. W. Chu, who is always amiable, patient, caring, and professional. At the same time, I would like to extend my heart-felt gratitude and respect to the CoI of this project, Prof. X. L. Liang from Guangzhou Institute of Geochemistry, Chinese Academy of Sciences (GIG-CAS). Thank them for their valuable guidance and inspiration, and more important, their continuous support, encouragement, and never-give-up even when I myself have completely lost confidence in me and my work during the darkest days. Without their help, caring, and supervision, it would be impossible for me to continue my research work and reach this stage.

I would like to express my sincere thanks to the technicians in the Water and Wastewater Laboratory, especially Mr. W. S. Lam, Mr. Y. H. Chan Jonathan, Ms. Y. Che Celine, and Ms. Carmen Yip, for their enthusiastic and professional assistance at all the times. I would also extend my appreciation to the technical officers, Dr. Melody Wong and Dr. Sirius Tse, from the University Research Facility in Chemical and Environmental Analysis (UCEA), for their professional technical support. In addition, special appreciation goes to Dr. G. L. Wei from Guangdong Key Laboratory of Integrated Agroenvironmental Pollution Control and Management, for her cheerful personality, rigorous academic attitude, caring, and professional assistance with solid foundations. My sincere thanks also goes to the lab-in-charge, technicians, and colleagues in the

CAS Key Laboratory of Mineralogy and Metallogeny/Guangdong Provincial Key Laboratory of Mineral Physics and Materials.

I would like to acknowledge my companion, Ms. Y. L. Zhang, who we have been with each other since our first day in this group, for her delicious cooking, caring, understanding, and all the joys and sorrows we have experienced together. I wish to deliver my heart-felt appreciation to all the past and current members of our research group, for their guidance and advice, especially Ms. H. L. So Christy, Dr. H. Gong, Dr. X. X. Zhang, Dr. L. B. Jiang, Dr. M. T. Yan, Dr. Z. L. Zhao, Prof. Z. H. Diao, Prof. S. Y. Pu, and Prof. F. Qi. I would also like to extend sincere thanks to my labmates and office colleagues, especially Dr. D. L. Zhong, Mr. Q. M. Wang, Mr. X. H. Zhang, Ms. Y. M. Cai, Ms. L. H. Gan, Mr. Z. H. Yan, and Mr. Y. Jiang in PolyU; Dr. Y. Lv, Dr. P. Liu, Dr. X. J. Lin, Dr. H. L. Chen, Dr. M. J. Yang, and Mr. P. Q. Wu in GIG-CAS, for their help, caring, and support.

I would like to express my faithful appreciation to the teachers of CEE, especially Dr. S. Y. Leu Ben, Dr. Y. Jiang, Dr. P. Wang, Dr. Z. Leng, and Prof. Y. H. Wang, for their great help during my PhD study. Special acknowledgement to the panel members, Prof. Kaimin Shih from The University of Hong Kong, Prof. Dionysios (Dion) D. Dionysiou from University of Cincinnati, and Prof. Tao Wang from PolyU, for their precious advices and inspirations. Many thanks to everyone who offered me love, caring, and support in my research and life during these years.

My sincere thank also goes to my parents, for their selfless love, forever respect, and unreserved support. They are always the ones who care more about whether I am happy and healthy instead of how much I can achieve. They are always my strong backing. Words cannot describe how much I love and miss them.

Lastly, the financial support from the Hong Kong Polytechnic University and General Research Fund of University Grants Committee are highly appreciated.

Table of contents

Abstract.....	I
List of publications.....	IV
Acknowledgements	V
Table of contents.....	VIII
List of abbreviations	XIII
List of figures.....	XV
List of tables.....	XXII
Chapter 1 Introduction.....	1
1.1 Background.....	1
1.2 Pharmaceutical industry: then and now.....	3
1.3 The shrouded haze: environmental factors	4
1.3.1 Presence of pharmaceuticals.....	4
1.3.2 Risk and toxic effects of pharmaceuticals in waterbodies.....	6
1.4 Aims and objectives	9
1.5 Structure of the thesis	11
Chapter 2 Literature review	14
2.1 Remediation technologies towards pharmaceutical pollution in water environment	14
2.1.1 Removal of pharmaceuticals through physical processes ...	15
2.1.2 Removal of pharmaceuticals through biological treatments	17

2.1.3 Removal of pharmaceuticals through chemical treatments	18
2.1.4 Hybrid reaction system	27
2.2 Sulfate-based AOPs (SR-AOPs)	28
2.2.1 Characteristics of the SR-AOPs	28
2.2.2. Homogeneous PMS activation with transition metal ions	29
2.2.3 Heterogeneous PMS activation with transition metals	31
2.2.4 Heterogeneous activation of PMS with metal-nonmetal catalysts	38
2.2.5 Metal-nonmetals catalysts with clay and clay minerals	40
Chapter 3 Materials and methods	48
3.1 Materials	48
3.1.1 Chemical reagents	48
3.1.2 Natural clay minerals	50
3.2 Methods	51
3.2.1 Preparation of the catalysts	51
3.2.2 Characterization methods of the catalysts	52
3.2.3 Analytical methods	54
3.3 Experimental procedures	58
Chapter 4 Characterization of the catalysts	60
4.1 Introduction	60
4.2 Results and discussion: CMO catalysts	61
4.2.1 XRD results of the catalysts	61

4.2.2 Morphology of the catalysts	63
4.2.3 Surface chemical properties of the catalysts.....	67
4.2.4 Texture and pore structure of the catalysts	70
4.2.5. Defects and oxygen vacancies	72
4.2.6. Point of zero charge (pHpzc) of the catalysts.....	73
4.3 Results and discussion: LCO catalyst.....	74
4.3.1 Characterisation of LCO catalyst	74
4.4 Summary	76
Chapter 5 Removal of carbamazepine using PMS activated by <i>x</i>-CMO/Hal.....	78
5.1 Introduction.....	78
5.2 Results and discussion	79
5.2.1 Catalytic performance of the <i>x</i> -CMO/Hal series	79
5.2.2 Effects of working parameters towards CBZ degradation ..	85
5.2.3 Change of pH and residue PMS concentration during CBZ degradation.....	88
5.3 Reactive oxygen species and activation mechanism of PMS.....	89
5.4 Recyclability and stability	95
5.5 Degradation performances towards some other pharmaceuticals	98
5.6 Conclusion	99
Chapter 6 Effect of clay mineral substrates towards the catalysts' PMS activation ability	102

6.1 Introduction.....	102
6.2 Results and discussion	104
6.2.1 Catalytic performances of CMO, CMO/KIn and CMO/Hal	104
6.2.2 Effects of working parameters.....	109
6.2.3 Working mechanism	111
6.3. Conclusion	121
Chapter 7 Removal of pharmaceuticals using PMS activated by LaCoO₃	123
7.1 Introduction.....	123
7.2 Results and discussion	124
7.2.1 Influence of experimental parameters	124
7.2.2 Effect of co-existing inorganic anions on degradation efficiency.....	129
7.2.3 Effect of co-existing organic matters on degradation efficiency.....	133
7.2.4 Free radical species and degradation pathways.....	135
7.3 Conclusions.....	141
Chapter 8 Conclusion and recommendation.....	143
8.1 Conclusions.....	143
8.1.1 Characteristics of the CMO-based catalysts.....	145

8.1.2 Effects of CMO content and mineral substrates in pharmaceutical degradation	146
8.1.3 Effects of working parameters on the degradation.....	147
8.1.4 Reaction mechanisms of the degradation process	147
8.1.5 Reusability and stability of the catalysts	148
8.1.6 Universal application of the catalysts	149
8.2 Limitations of this study and recommendations for future work	149
References	152

List of abbreviations

1,4-BZQ	1,4-Benzoquinone
ACN	Acetonitrile
AOP	Advanced oxidation process
BET	Brunauer-Emmett-Teller (theory)
CBZ	Carbamazepine
EDS	Energy dispersive spectrometry
EPR	Electron paramagnetic resonance
ESI	Electrospray ionization
EtOH	Ethanol
FESEM	Field emission scanning electron microscopy
HA	Humic acid
Hal	Halloysite
HPLC	High performance liquid chromatography
HRTEM	High Resolution Transmission Electron Microscope
ICP-OES	Inductively coupled plasma optical emission spectroscopy
Kln	Kaolinite
LC-MS	Liquid chromatography mass spectrometry
MeOH	Methanol
NOM	Natural organic matter
OFX	Ofloxacin
PMS	Peroxymonosulfate
PPCP	Pharmaceutical and personal care products

PZC	Point of zero charge
ROS	Reactive oxygen species
SAED	Selected area (electron) diffraction
SMZ	Sulfamethoxazole
TBA	<i>tert</i> -Butyl alcohol
TC	Tetracycline
WWTP	Wastewater Treatment Plant
XPS	X-ray photoelectron spectroscopy
XRD	X-ray powder diffraction

List of figures

Fig. 2-1 An ideal cubic perovskite structure of ABO_3 . (a) Unit cell (the smaller B site is chosen as the origin of the unit cell, and (b) the coordination of B-site ion.

Fig. 2-2 (a) Schematic illustration of the AB_2O_4 spinel structure composed of AO_4 tetrahedra and BO_6 octahedra, and (b) Crystal structure of the $CoMn_2O_4$ phase.

Fig. 2-3 Structure of the three major clay mineral groups: (a) kaolin, (b) smectite, and (c) mica. Figures show the stacking of Si tetrahedra and Al octahedra and characteristic basic spacing.

Fig. 3-1 Schematic representation of the synthesis process of bare CMO, x -CMO/Hal, and x -CMO/Kln catalysts.

Fig. 3-2 Calibration curve for PMS concentration using KSCN method

Fig. 3-3 Calibration curve for OH^\cdot measurement using p-HBA concentration

Fig. 4-1 XRD patterns of (a) bare $CoMn_2O_4$ and x -CMO/Hal ($x= 20, 40$ and 60) catalysts, and (b) bare CMO, Hal, Kln, CMO/Hal and CMO/Kln.

Fig. 4-2 FESEM images of bare CMO (a), Hal (b), Kln (c), 20-CMO/Hal (d), 60-CMO/Hal (d), 40-CMO/Hal (f), and 40-CMO/Kln (e).

Fig. 4-3 HRTEM images of bare CMO (a), Hal (b), 20-CMO/Hal (d), 40-CMO/Hal (c, e), and 60-CMO/Hal (f).

Fig. 4-4 HRTEM images of CMO/Hal (a–b) with raw Hal inserted in (a), CMO/Kln (d–e) with raw Kln inserted in (d), and SAED patterns of CMO/Hal (c) and CMO/Kln (f).

Fig. 4-5 EDS mapping of 40-CMO/Hal (a-d) and 40-CMO/Kln (e-h).

Fig. 4-6 XPS spectra of survey (a), Co 2p (b), Mn 2p (c), and O 1s (d) for bare CMO,

CMO/Hal and CMO/Kln; Si 2p (e) and Al 2p (f) for CMO/Hal and raw Hal; and Si 2p (g) and Al 2p (h) for CMO/Kln and raw Kln.

Fig. 4-7 N₂ adsorption and desorption isotherms, and BJH pore size distribution plots of (a) bare CMO, Hal, and *x*-CMO/Hal series, and (b) bare CMO, CMO/Hal, CMO/Kln and raw clay minerals.

Fig. 4-8 EPR spectra of bare CMO, CMO/Hal and CMO/Kln.

Fig. 4-9 Zeta potential of CMO/Kln and CMO/Hal

Fig. 4-10 (a) XRD patterns of the fresh and reacted LaCoO₃; (b–c) HRTEM images of LaCoO₃ particles; (d–g) the EDS mapping of LaCoO₃ (d), La (e), Co (f) and O (g).

Fig. 4-11 XPS spectra of LCO (a) a full range scan of the samples; (b) Co 2p core level; (c) O 1s core level

Fig. 5-1 Adsorption kinetics of CBZ by bare CMO, Hal and *x*-CMO/Hal series

General working conditions: [CBZ]= 21.16 μM, [PMS]= 0.1 mM, [catalyst]= 200mg L⁻¹, pH=5.8.

Fig. 5-2 CBZ degradation performances with: (a-b) CMO, Hal, *x*-CMO/Hal series and their corresponding pseudo first order kinetic curves, (c) combination of CMO and Hal, and (d) CMO equivalent conditions. ([20-CMO/Hal] = 400 mg L⁻¹, [40-CMO/Hal] = 200 mg L⁻¹, [60-CMO/Hal] = 133 mg L⁻¹, [CMO] = 80 mg L⁻¹).

General working conditions: [CBZ] = 21.16 μM, [PMS] = 0.1 mM, [catalyst] = 200 mg L⁻¹, pH = 5.8.

Fig. 5-3 Intermediates and potential degradation pathway of CBZ in PMS oxidation process activated by 40-CMO/Hal

Fig. 5-4 Removal of total organic carbon (TOC) using PMS activated by 40-CMO/Hal and bare CMO

Fig. 5-5 Effects of (a) PMS concentration, and (b) CBZ concentration on the degradation of CBZ using PMS activated by 40-CMO/Hal.

General working conditions: [CBZ]= 21.16 μM , [PMS]= 0.1 mM, [catalyst]= 200 mg L^{-1} , pH=5.8.

Fig. 5-6 Effect of initial working pH on CBZ degradation using PMS activated by 40-CMO/Hal

Fig. 5-7 Change of solution pH during CBZ degradation (a), residue PMS with different catalysts analyzed by spectrophotometric method (b), and OH^\cdot accumulation during CBZ degradation using different catalysts.

Fig. 5-8 Effect of different scavengers on the degradation of CBZ by 40-CMO/Hal (a). EPR spectra of: $\text{SO}_4^{\cdot-}$ and OH^\cdot (b), $^1\text{O}_2$ (c), and $\text{O}_2^{\cdot-}$ (d) in the activation of PMS with 40-CMO/Hal.

General working conditions: [CBZ] = 21.16 μM , [PMS] = 0.1 mM, [catalyst] = 200 mg L^{-1} , pH = 5.8.

Fig. 5-9 Comparison of Co, Mn, and O between fresh and recycled 40-CMO/Hal examined by XPS spectra

Fig. 5-10 Degradation of CBZ and effect of NaN_3 under N_2 -bubbling in PMS oxidation process activated by bare CMO and 40-CMO/Hal.

General working conditions: [CBZ]= 21.16 μM , [PMS]= 0.1 mM, [catalyst]= 200mg L^{-1} , pH=5.8.

Fig. 5-11 EPR spectra of $^1\text{O}_2$ under N_2 plugging (a), and normal working conditions in the activation of PMS using 40-CMO/Hal (b).

Fig. 5-12 Sustainability and recyclability of the catalysts after three rounds of CBZ degradation.

General working conditions: [CBZ] = 21.16 μM , [PMS] = 0.1 mM, [catalyst] = 200 mg

L^{-1} , pH = 5.8.

Fig. 5-13 XRD patterns of the fresh and recycled 40-CMO/Hal

Fig. 5-14 Catalytic degradation of CBZ with homogeneous Co^{2+} and Mn^{2+} (at similar concentrations with the dissolved ions in sustainability tests)

General working conditions: [CBZ] = 21.16 μM , [PMS]= 0.1 mM, pH=5.8.

Fig. 5-15 Degradation performance of 40-CMO/Hal towards other pharmaceuticals

General working conditions: [pharmaceuticals] =21.16 μM , [PMS]= 0.1 mM, [catalyst]= 200 mg L^{-1} , pH=5.8.

Fig. 6-1 Adsorption of OFX by CMO, Kln, Hal, CMO/Hal and CMO/Kln

General working conditions: [OFX] = 20 μM , [catalyst]= 400 mg L^{-1} , pH=6.5

Fig. 6-2 Degradation of OFX in different reaction systems ([CMO + Kln or Hal]: 160 mg L^{-1} CMO + 240 mg L^{-1} Kln or Hal) (a), and corresponding pseudo-first-order kinetic models (b).

General working conditions: [OFX] = 20 μM , [PMS] = 0.1 mM, [catalyst] = 400 mg L^{-1} , pH = 6.5.

Fig. 6-3 Proposed transformation pathways of OFX using PMS activated by CMO/Hal (a) and CMO/Kln (b).

Fig. 6-4 TOC reduction during OFX degradation using PMS activated by CMO/Hal and CMO/Kln.

Fig. 6-5 Effects of OFX concentration (a), working pH (b), and PMS concentration (c) on the degradation performances of CMO/Hal and CMO/Kln

General working conditions: [OFX] = 20 μM , [PMS] = 0.1 mM, [catalyst] =400 mg L^{-1} , pH=6.5.

Fig. 6-6 EPR spectra of CMO/Hal and CMO/Kln: (a) OH^{\cdot} and $SO_4^{\cdot-}$, (b) 1O_2 , and (c)

O₂^{•-}. Effects of scavengers on OFX degradation (d). Effects of N₂ purging on OFX degradation (e).

General working conditions: [OFX] = 20 μM, [PMS] = 0.1 mM, [catalyst] = 400 mg L⁻¹, [scavengers] = 10 mM, [spin-trapping reagents] = 0.1 M, pH = 6.5.

Fig. 6-7 Comparison of Co, Mn, and O between fresh and recycled CMO/Hal and CMO/KIn catalysts.

Fig. 6-8 OFX degradation with CMO/Hal and CMO/KIn after three recycle rounds (a), and ICP-OES results of CMO/Hal and CMO/KIn in recycle experiments (b).

General working conditions: [OFX] = 20 μM, [PMS] = 0.1 mM, [catalyst] = 400 mg L⁻¹, pH = 6.5.

Fig. 6-9 XRD patterns of recycled CMO/Hal and CMO/KIn comparing to fresh CMO

Fig. 6-10 Homogeneous degradation of OFX using Co²⁺ and Mn²⁺ (a), and *k_{obs}* of Co²⁺ calculated from pseudo-first order model (b).

Fig. 6-11 Effect of water matrix on the degradation of OFX using PMS activated by CMO/Hal (a) and CMO/KIn (b).

General working conditions: [OFX] = 20 μM, [PMS] = 0.1 mM, [anions] = 0.5 or 0.1 mM, [humic acid] = 5 or 10 mg L⁻¹, [catalyst] = 400 mg L⁻¹, pH = 6.5.

Fig. 7-1 Effect of TC concentration on degradation efficiency.

General working conditions: [PMS] = 50 mg L⁻¹, [LaCoO₃] = 200 mg L⁻¹, pH = 3.3 (unadjusted).

Fig. 7-2 Effect of PMS concentration on degradation efficiency.

General working conditions: [TC] = 20 mg L⁻¹, [LaCoO₃] = 200 mg L⁻¹, pH = 3.3 (unadjusted).

Fig. 7-3 (a) Effect of initial solution pH on degradation efficiency and (b) the variation of pH during the reaction.

General working conditions: [TC] = 20 mg L⁻¹, [PMS] = 50 mg L⁻¹, [LaCoO₃] = 200 mg L⁻¹.

Fig. 7-4 Effect of inorganic anions on the degradation of TC in LaCoO₃/PMS system.

General working conditions: [TC] = 20 mg L⁻¹, [PMS] = 50 mg L⁻¹, [LaCoO₃] = 200 mg L⁻¹, initial concentration of Cl⁻, NO₃⁻, H₂PO₄⁻ and SO₄²⁻: 10 mmol L⁻¹, and pH = 7.0.

Fig. 7-5 Effect of common anions on the degradation of TC in LaCoO₃/PMS system.

General working conditions: [TC] = 20 mg L⁻¹, [PMS] = 50 mg L⁻¹, [LaCoO₃] = 200 mg L⁻¹, pH = 7.0

Fig. 7-6 Effect of humic acid on the degradation of TC in LaCoO₃/PMS system.

General working conditions: [TC] = 20 mg L⁻¹, [PMS] = 50 mg L⁻¹, [LaCoO₃] = 200 mg L⁻¹, pH = 7.0

Fig. 7-7 Effect of scavengers on the degradation of TC in LaCoO₃/PMS system.

General working conditions: [TC] = 20 mg L⁻¹, [PMS] = 50 mg L⁻¹, [LaCoO₃] = 200 mg L⁻¹, pH = 7.0, [EtOH] = [TBA] = 1 mol L⁻¹, [NaN₃] = [BZQ] = 0.8 mol L⁻¹, and pH = 7.0

Fig. 7-8 EPR spectra of PMS activation in LaCoO₃/PMS system during the degradation of TC: (a-b) DMPO and (c) TEMP spin trapping.

General working conditions: [TC] = 20 mg L⁻¹, [PMS] = 50 mg L⁻¹, [LaCoO₃] = 200 mg L⁻¹, [DMPO] = 10 mmol L⁻¹, [TEMP] = 10 mmol L⁻¹.

Fig. 7-9 Degradation pathways of TC in LaCoO₃/PMS system.

General working conditions: [TC] = 20 mg L⁻¹, [PMS] = 50 mg L⁻¹, [LaCoO₃] = 200 mg L⁻¹, pH = 7.0

Fig. 7-10 TOC removal rate on the degradation of TC.

General working conditions: $[TC] = 20 \text{ mg L}^{-1}$, $[PMS] = 50 \text{ mg L}^{-1}$, $[LaCoO_3] = 200 \text{ mg L}^{-1}$, $pH = 7.0$

Scheme 1 The schematic illustration of radical generation mechanism through PMS activated by 40-CMO/Hal.

Scheme 2 The schematic illustration of radical generation mechanism through PMS activated by CMO/Hal and CMO/KIn.

List of tables

Table 2-1 One electron redox potential of ROS, relative to standard hydrogen electrode (SHE)

Table 2-2 Comparison between OH^\cdot and $\text{SO}_4^{\cdot-}$

Table 2-3 Performances of some bimetallic catalysts in PMS activation and the dominant ROSs generated

Table 2-4 Metal-nonmetals catalysts with clay and clay minerals for AOPs

Table 3-1 Chemical composition of halloysite (Hal) and kaolinite (Kln) tested by XRF

Table 3-2 Working parameters of HPLC for OFX CBZ, SMZ and TC

Table 3-3 Working parameters of LC-MS for OFX CBZ, SMZ and TC

Table 4-1 Specific surface area and pore volume of the catalysts and raw materials

Table 5-1 Summary of the scavengers and their target ROSs

Table 5-2 ICP-OES results: the leaching concentration of Co^{2+} and Mn^{2+} from CMO and 40-CMO/Hal during the sustainability tests

Table 6-1 A brief summary about the target ROS and their scavengers

Chapter 1 Introduction

1.1 Background

It has been widely recognized that liquid water is of core essential and basic necessity for various fields concerning: 1) life, or more precisely, carbon-based life within biosphere; 2) natural processes including hydrological cycle; 3) the on-coming generations. There are also aspects like economic, society, and communities of a country. Although more than 97% of the earth is covered with water in the form of oceans, only fresh water is suitable for the living of human beings and most of the carbon-based lives. It seems that fresh water still counts for 3% on the earth, but it should be noted that more than 85% of the fresh water is hardly available since they exist in the form of glaciers.

However, with the rapid development and booming of human population, deforestation, urbanization, industrialization, etc. since the 20th century, the shrinkage and conservation of water have gradually become a major concern globally. Although water can be purified continuously through evaporation and precipitation, water pollution has emerged as global concern in aspects of water supply as well as water quality.

Water pollution can be classified as point source and nonpoint source based on the origin of pollutants. As for water pollutants, they can be roughly categorized into oxygen-demanding materials, sediments and suspended solids (SS), nutrients, heat, **synthetic chemicals including pesticides, herbicides, fertilizers, pharmaceutical substances**, pathogenic microorganisms, oil pollution, and acids and bases (Abu Shmeis, 2018).

Since the 2000s, the potential adverse effects caused by the production, use, and disposal of the synthetic chemicals which offered developments in industry, agriculture, medical treatment, and even common household conveniences have become an increasing concern. Previous researches have revealed that these compounds which entered into waterbodies through wide transportation pathways such as industrial discharges, animal and agricultural wastes, and even wastewater treatment processes including plants and domestic septic systems, showed further harms in environmental waters including dispersion and persistence. From 1999 to 2000, the U. S. Geological Survey carried out a study by measuring the concentrations of 95 organic wastewater contaminants (OWCs) including but not limited to pharmaceuticals and hormones in water samples from a network of 139 streams across 30 states to provide the first nationwide reconnaissance of the occurrence, transport, and fate of these pollutants in water resources. The results was shocking, since more than 80% of the 139 streams were detected with at least one kind of OWCs. Besides, 82 out of the 95 OWCs were found at least once during this study, and only eight antibiotics and five other prescription drugs were not detected in the samples (Kolpin et al., 2002). A few years later, in 2010, a pan-European reconnaissance of the occurrence of polar organic persistent pollutants in European ground water reported that none of the studied 164 individual samples from 23 European countries was free of the 59 listed organic chemical compounds. Furthermore, the maximum number of compounds detected at any site was 29, and the median number of detections per site was 12 (Loos et al., 2010).

One of the key organic chemical pollutants that the two studies above have spontaneously focused on is pharmaceutical substances, which was originally

developed to treat human and animal diseases. However, these inventions, along with some personal care products which aimed at improving living qualities, have already been recognized with another name, emerging pollutants, due to their frequent and unintentional presence in aquatic environments.

1.2 Pharmaceutical industry: then and now

Pharmaceutical industry is a special and critical component within the chemical industry, while pharmaceuticals is a large conception with diverse groups. Generally, pharmaceuticals refer to both human and veterinary medical compounds, and nutraceuticals including bioactive food supplements, which are often small drug molecules produced through organic synthesis (Khetan and Collins, 2007).

The manufacture of synthetic dyestuffs in the 20th century brought an important derivative, the modern pharmaceutical industry. It can be dated back to 1935, when a German chemist and pathologist, Gerhard Domagk, discovered that prontosil, a synthesized red azo dye with low toxicity, could effectively combat streptococcal diseases in both animal and human. Thus, prontosil, the prototype of a range of sulfa drugs, had become the first synthetic drug for the treatment of general bacterial infections, which then opened a new era for the pharmaceutical industry (Greenwood, 2010; Lee, 2007). A few years later, the observation of penicillin, followed by the isolation and identification of its active constituent, marked the beginning of antibiotic era which still continues today (Bentley, 2009).

The explosion of modern pharmaceutical industry came lately in the 1940s. The war

crash programmes in the mentioned sulfa and penicillin provided the pharmaceutical manufacturers (particularly in the US and in the UK) with rich financial, technical and organizational capabilities and innovation opportunities, which was initially in antibiotics and then spread into other therapeutic areas. Although many researchers carried with the negative view towards the future development of pharmaceutical industry due to reasons like lower productivity and fewer innovative researches, the revenue of the global pharmaceutical market still boosted from 390 billion in 2001 to about 1.25 trillion US dollars in 2019 so far (González Peña et al., 2021). Except for the tight patent protection in the US and UK which made the pharmaceutical industry become a very profitable business, the emerging demand for drugs driven by factors including population growth, the trend of aging population globally, rising living standards, and the vastness of unmet medical needs (Taylor, 2016).

1.3 The shrouded haze: environmental factors

1.3.1 Presence of pharmaceuticals

The occurrence and fate of pharmaceuticals and their derivative in the aqueous environment have received growing attention from the public from the 20th century, including their possible adverse effects towards the ecosystem and human health. However, it was not until the 2000s that the pharmaceutical residues in water were identified as a contributor towards the poor water quality and relevant environment standards needed to be set specifically for it. For example, in the US, the Contaminant Candidate List released in 2008 by EPA identified 287 pharmaceuticals along with personal care products which might occur in drinking water provided by public utilities (Eckstein, 2015). Similar documents were also released by the EU from 2000 with

several times of update, which identified pharmaceuticals such as carbamazepine, bisphenol A, and ibuprofen as future emerging priority candidates under the EU Water Framework Directive (WFD) (Ebele et al., 2017).

Pharmaceuticals can enter into the aquatic environment not just from the manufacturing plants, but also livestock feeding industry, runoff from animal-feeding operations, drugs taken by people internally but not metabolized, and traditional wastewater treatment plants (WWTPs) receiving effluents from those mentioned. Since traditional WWTPs which are not originally designed for these contaminants can hardly remove most of the pharmaceuticals from water, the residue concentrations of these substances in the receiving waterbodies still ranges from ng L^{-1} to $\mu\text{g L}^{-1}$, according to the actual situation (Ebele et al., 2017). A severe example was found in India in 2007, as an extremely high concentration of ciprofloxacin, up to 31 ppm, was detected in an effluent from a WWTP impacted by pharmaceutical manufacturer (Larsson et al., 2007). However, ciprofloxacin was not the only drug found at this site, five more pharmaceuticals, including a veterinary drug, enrofloxacin, were detected at concentrations higher than 0.77 ppm (Larsson et al., 2007). A German study carried out in 2017 reported that among the 43 locations in the Baltic Sea and Skagerrak, more than 40% of the 93 sample pharmaceuticals belonging to different classes were detected in at least one sample, while the highest levels were measured close to the discharge points of the local WWTPs (Björlenius et al., 2018). Another study performed in Korea which investigated the effluent from livestock wastewater treatment plants (LWTPs) revealed that high concentrations of antibiotics including chlortetracycline, oxytetracycline and acetylsalicylic acid were all detectable in the 11 studied sample LWTPs (Chung et al., 2016). As only part of the pharmaceuticals took by human beings or animals can be

digested during the metabolite process, and the residues of these substances intake might still be extracted into the environment via urine and feces in their parent form (Jones et al., 2015).

Except for the consumed ones mentioned above which is discharged from the WWTPs, the unused pharmaceuticals disposed without special treatments at domestic waste landfills might also distribute in the groundwater through the leachates (Jones et al., 2015; Yu, X. et al., 2020). Furthermore, the metabolites of the livestock can reach soil directly, and these extracted organics may still reach the groundwater, no matter whether they are bound to soil constituents. Furthermore, some of them may even be transported to surface water by runoff in the case of heavy rain events (Kümmerer, 2010).

Thus, it is clear that both surface water and groundwater are threatened by the invasion of pharmaceutical pollutants, which would finally interfere the quality of our drinking water. A report provided by the World Health Organization (WHO) in 2012 warned that up to date, several kinds of pharmaceuticals were detected in tap water within various European countries including Germany, the Netherlands and Italy, at concentrations ranging from ng L^{-1} to mg L^{-1} , and about 15 to 25 pharmaceuticals had been detected in the treated drinking water globally even though at very low levels (World Health Organization (2012).

1.3.2 Risk and toxic effects of pharmaceuticals in waterbodies

It has been widely stated that the pharmaceuticals frequently detected in environment

are highly persistent, which is biased in some ways. Generally, the concept of persistence is quantified based on the half-life of the target material, which indicates the time interval required for the half decay of its initial value. However, the half-life of the pharmaceuticals in water environment is not only related to their physicochemical properties, but also the nature of where they are found. This lead to the varied and even contradictory results concerning the persistence of the pharmaceuticals (Bu et al., 2016). For example, the half-life of carbamazepine reported based on laboratory and in-field research varied from 3.5 to over 230 days and from 63 to 1200 days, respectively (Björlenius et al., 2018; Tixier et al., 2003; Yamamoto et al., 2009). Thus, the persistence here for the pharmaceuticals can be better described by their continuous discharge into aquatic environment and lower removal efficiency by traditional WWTPs, which lead to the gradual accumulation of them in live forms with biologically activation (Bu et al., 2016).

Toxic effects from various pharmaceuticals towards microorganisms and some higher animals have been frequently reported, *i.e.*, carbamazepine restricted the growth of zebrafish embryos by retarding their hatching, sometimes even with pericardial edema and delayed heartbeat; the complex effluent containing 17 β -oestradiol (E2) 17A-ethinyloestradiol (EE2) from the sewage treatment works (STWs) can cause the feminization of male fish in the downstream; and diclofenac, a prevalent anti-inflammatory drug, can cause chronic and deadly effects on fishes by damaging their renal and gastrointestinal tissue (Örn et al., 2003; van den Brandhof and Montforts, 2010; Varsha et al., 2022). In addition, the unwanted antibiotic resistance and other negative impacts possibly caused by residue antibiotics, *i.e.*, gene expression alterations, abnormal protein and enzyme activities, have been found in bacteria and microbial

communities, or reflected by the growth malformations in rats, fish, and frogs (Larsson, 2014).

Except for toxicity, a certain part of pharmaceuticals are considered as potentially bioaccumulative as they are relatively hydrophobic, especially when the resident biota are chronically exposed to them. Solla et al. reported in 2016 that 5 among the overall 43 pharmaceuticals investigated in effluent from one WWTP in the Grand River water were detected in the tissue of unionid mussel *Lasmigona costata* (de Solla et al., 2016). Grabicová et al. reported in 2020 that during a 6 months study in a wastewater stabilization pond, 14 pharmaceuticals and their metabolites were detected in at least one fish tissue collected, including muscle, kidney, brain, and liver (Grabicová et al., 2020). Furthermore, since the pharmaceuticals occurred in water environment are usually like cocktails, the toxic effects of these mixture are still unclear.

Since WWTPs are never designed and thus cannot remove pharmaceuticals completely, they have become one of the major resources of the pharmaceuticals in aqueous environment. Unfortunately, this situation go even worse for those pharmaceuticals with aromatic rings attached and/or functional groups including chloro-, nitro-, and fluoro- (Patel et al., 2019). The lower removal efficiency and the continuous discharge both contribute to the environmental persistence of pharmaceuticals today (Eggen and Vogelsang, 2015). All these facts urge the development of efficient, low-cost and ecofriendly strategies to remove pharmaceuticals from aqueous environment. Thus, tremendous efforts have been put into the development of advanced water treatment processes for the remediation of persistent pharmaceuticals from angles including physical, chemical and biological during the past three decades.

Herein, in response to the growing contamination worldwide caused by residue pharmaceuticals from various sources in waterbodies, a systematic study including: i) designation, synthesis, and characterization of efficient and environmental-friendly catalysts for advanced oxidation processes (AOP); 2) evaluation of the obtained catalysts' working performances in the decomposition of several typical pharmaceuticals; and 3) determination of the reaction mechanism, has been carried out.

1.4 Aims and objectives

The aim of this study is to provide a novel, effective, and environmental friendly advanced oxidation process (AOP) for efficient and effective degradation of residue pharmaceuticals in waterbodies with the designation and fabrication of some transition metal oxide based catalysts. The objectives are listed separately based on the working stages as below.

1) The design and synthesis of the transitional metal based catalyst

A spinel oxide catalyst tailored by two active transition metals, CoMn_2O_4 (CMO), is synthesized for efficient peroxymonosulfate (PMS) activation in the removal of pharmaceuticals in water. Besides, another perovskite-structured catalyst, LaCoO_3 (LCO), is also fabricated for the same aim. The physicochemical properties of obtained CMO and LCO including phase identification, crystal structure, relationships between microstructure of transition metals (*e.g.*, species, valence and occupancy), surface properties etc., are characterized separately.

2) The catalytic activity of CMO

The PMS activation ability of CMO is tested and confirmed by the efficient removal of several typical pharmaceuticals with different chemical structures from water.

3) The design and synthesis of CoMn_2O_4 loaded on porous clay minerals

The CMO obtained with satisfied PMS activation ability confirmed before is loaded on two kinds of porous clay minerals with the same chemical composition but different morphology, kaolinite (Kln) and halloysite (Hal), at various weight percentages (x , w/w, %).

4) The working activity of CoMn_2O_4 loaded on Hal and Kln

After the characterization tests, systematic studies about the effects of CMO loading percentages on Hal towards the physicochemical properties of the x -CMO/Hal composite catalysts are performed. The reaction parameters such as working pH, PMS dosages, and the influence of co-existing anions during the degradation reaction are analyzed and optimized. The PMS activation mechanisms, the possible decomposition pathways of the target compounds, and the stability of the typical x -CMO/Hal and bare CMO are verified separately.

After that, based on the preliminary results obtained from the above stage, the x -CMO/Hal with the best working performances is chosen for further comparison studies with the corresponding CMO/Kln with the same CMO loading percentage, *e.g.*, x . The advantages of composite catalysts using Kln and/or Hal as substrates is summarized in comparison with bare CMO. Besides, the differences between Kln and Hal substrate are also compared to further determine the most suitable working conditions for them individually.

5) The effects of water matrix, *e.g.*, co-existing inorganic anions and natural organic matter (NOM), towards PMS activated by LCO

In wastewater and natural waterbodies, residue pharmaceuticals usually coexist with inorganic anions and NOM, which poses various effects on the removal processes. It is not rare reported that the same anion could pose reversal impacts, promoter or inhibitor, on similar AOPs except for the catalysts they adopted. Due to the widespread distribution of inorganic anions and NOM, as well as their intriguing performance in the AOP reaction, their effects should be considered in the test of the activity of catalysts in activating PMS. Herein, the degradation of TC using PMS activated by LCO are investigated thoroughly and emphasized on the effects of NOM and several common inorganic anions.

1.5 Structure of the thesis

Based on the aims and objective of this work, the whole thesis is divided into 8 chapters in a clear and logical way as below.

Chapter 1 (*e.g.*, the current one): Some background information, the aims and objectives, and the research strategy of this thesis.

Chapter 2: Literature review of the following parts: 1) fundamental information of AOP, including its brief history and several typical techniques; 2) the development of transition metal catalysts and their application in heterogeneous PMS activation; and 3) the current research frontier about the composite transition metal catalysts with

different substrates and their practical applications.

Chapter 3: Information about the materials and methods adopted in this thesis. The materials include the introduction of chemical reagents and clay minerals used in this work. The methods can be divided into four parts: the fabrication, characterization, experimental procedures for the degradations, and the testing methods (including the concentration of target pharmaceuticals, its transformation products during the degradation, the mineralization performance, the working ROS, and metal leakage of the catalysts, etc.).

Chapter 4: The characterization results of the catalysts. These results are presented in XRD spectra, XPS spectra, FESEM and HETEM images, EPR spectra, and BET adsorption-desorption results, etc.

Chapter 5: The degradation of pharmaceuticals using PMS activated by bare CMO vs. *x*-CMO/Hal. In this chapter, the PMS activation ability of CMO and CMO loaded on Hal at different weight percentages (20%, 40%, and 60%) are compared systematically. For the composite 20, 40 and 60-CMO/Hal, the one with the best working performance is chosen for further investigation concerning mineralization, recyclability and stability. Besides, the reaction mechanisms, the reactive oxygen species (ROS), and the degradation intermediates, are analyzed and/or identified systematically.

Chapter 6: The effects caused by substrates, Kln and Hal, towards the composite CMO catalysts. This chapter mainly focuses on the comparison between CMO/Hal and CMO/Kln concerning their morphology, crystal structure, defects, working and

structural stability, and PMS activation ability. One of the main purposes is to provide a reference for the choice of the minerals during the synthesis of the catalysts.

Chapter 7: The degradation of pharmaceuticals using PMS activated by perovskite-structured LCO. In this chapter, the PMS activation ability of LCO, and the effects caused by water matrix including some common inorganic anions and natural organic matter (NOM) on the degradation reaction are analyzed systematically. In addition, the working mechanisms, reactive working species, and the degradation intermediates, are identified separately.

Chapter 8: The last chapter is the conclusion and meaning of this study, which also provides some recommendations and potential ideas for the future work.

Chapter 2 Literature review

2.1 Remediation technologies towards pharmaceutical pollution in water environment

Since traditional WWTPs are never designed and thus cannot remove pharmaceuticals completely, they have in turn become one of the major resources of the pharmaceuticals in aqueous environment (Kay et al., 2017). Generally, WWTPs employ three parts of sewage treatments including primary sedimentation, secondary treatment, and final sedimentation (Wu et al., 2022). This set of process is feasible to remove classical contaminants like suspended solids, nutrients and some organic pollutants. These organic methods can be transformed into primary and secondary sludge through hydrolysis, biotransformation and sorption, etc. (Carneiro et al., 2020; Le-Minh et al., 2010). However, the working efficiency of this conventional process is largely depended on various factors, *i.e.*, the physicochemical properties of the compounds (*e.g.*, the affinity of the compounds to retain in the treated effluent, or to be adsorbed to sludge), the local climate conditions, the operation parameters of the treatment process (working temperature, redox conditions, solids and/or hydraulic retention time), and the age of the activated sludge used in the plant (Gracia-Lor et al., 2012). Unfortunately, most of the pharmaceuticals are of environmental persistence due to their continuous discharge and lower removal efficiency through conventional treatments. Furthermore, a large number of them are significantly recalcitrant, and sometimes even resistant to the common treatments provided by traditional WWTPs such as anaerobic/anoxic/oxic systems, oxidation ditches and filters, which allows the continuous release of residue pharmaceuticals and their metabolites into the aquatic environment (Frascaroli et al.,

2021). Thus, tremendous efforts have been put into the development of advanced water treatment processes for the remediation of these persistent pharmaceuticals using methods including physical, chemical, biological, and hybrid ones in the past three decades (Wang and Chu, 2016).

2.1.1 Removal of pharmaceuticals through physical processes

Physical treatment refers to the removal of pharmaceuticals from water without using chemical or biologicals agents, which maintains the contaminants' biochemical properties (Ahmed et al., 2021). Common physical treatment strategies include screening, sedimentation, skimming, adsorption, and membrane-based technology, etc., while screening, sedimentation, and skimming have widely been used as pre-treatment mechanisms in common WWTPs (Sun et al., 2019). Among them, screening enables the removal of some large and floating solids which might cause blockage in the following treatment processes, while sedimentation helps to settle the sludge and isolate the remained heavy suspends after screening to make sure that these precipitations would not clog the later systems. As another common pre-treatment process, skimming refers to the removal of oil, grease, and fat or oil-like substances that are lighter than water, which is also an alternative of flotation (Sathya et al., 2022; Sun et al., 2019).

In addition to preliminary treatments like screening, sedimentation, and skimming mentioned above, some other physical processes including adsorption and membrane-based technology are often categorized as advanced treatment process, which can also be used as the primary or pretreatment processes for the secondary treatment to accelerate the removal efficiency of contaminants (Gadipelly et al., 2014).

Adsorption refers to the removal of soluble contaminants, including organic, inorganic and even metal ions, through their attachment to solid substrates which usually come with a higher specific surface area (SSA) and well-developed pore structure. Generally, carbon-based materials such as carbon nanotubes, graphene, graphene oxide, and activated carbon, are considered as promising adsorbent for organic compounds not limited to pharmaceuticals in water treatment (Cheng et al., 2021; Shan et al., 2018). It is also feasible to incorporate adsorption into other water treatment modules to ensure the effective removal of the emerging contaminants. However, the large scale application of carbon-based adsorbents is faced by critical issues including high cost of production, rapid saturation, and the regeneration and/or disposal of the saturated ones (Cheng et al., 2021). Thus, in order to ensure environmental sustainability of adsorption, the development of other adsorbents such as clays, polymeric adsorbents, zeolites, chitosan, and some low-cost materials like biochars produced from torrefied loblolly pine chips after thermal treatment, have received increasing attention (Kyzas et al., 2015; Morin-Crini et al., 2022).

Membrane technology refers to the filtration of contaminants under hydrostatic pressure through membranes. It can be classified into several types based on the size of the pores on the membrane, e.g., microfiltration (MF, 0.001-0.1 μm), ultrafiltration (UF, less than 0.001 μm), and nanofiltration (NF, 1–10 nm) (Ahmed et al., 2021). A special case within the membrane technology is reverse osmosis (RO), as the selective semipermeable membrane under gradient pressure allows the removal of particles less than 1 nm, which has been proved with a high rejection of pharmaceuticals including carbamazepine, clofibrac acid, caffeine, naproxen, and propylphenazone (>95%),

however, dissatisfied working performances are also found concerning ketoprofen (64.3%) and diclofenac (55.2-60%) (Ahmed et al., 2021; Patel et al., 2019). However, since the retention of contaminants is largely depended on the pore size of the membranes, it is clear that factors including the physicochemical properties of the membrane, the composition of source water, and even operating conditions would pose important impact on the working capability of membrane technology, which leads to its limited practical applications due to the possible clogging of membrane pores (Dolar and Košutić, 2013). Besides, just like carbon-based adsorbents mentioned above, the crux of membrane regeneration and retentate/concentrate disposal remains the same. Therefore, in order to lower the fouling propensity of the membranes, spontaneously with reducing costs and increasing their lifetime, the development of some appropriate pretreatment methods is inevitable (Anis et al., 2019; Yoon et al., 2007).

2.1.2 Removal of pharmaceuticals through biological treatments

Biological treatment has been considered as one of the most important means in the removal of organic pollutants including pharmaceuticals due to its special advantages such as mild operating conditions, easy working process, and cost-effectiveness (Simon et al., 2021). The degradation mechanism of organic contaminants mainly relies on the normal cellular process of the microorganisms such as the metabolic functions during their growth, which leads to the decomposition, transformation and decay of organic contaminants into biomass (Sathya et al., 2022; Simon et al., 2021). Besides, it has been reported that some specific microorganisms are even able to utilize certain pharmaceuticals without the need of additional substrates which provide necessary

carbon and energy for their normal metabolic functions (Scaria et al., 2020). Generally, biological treatment can be divided into aerobic and anaerobic treatment systems, and each of them can be further subdivided based on different operating modes. Aerobic treatment is commonly applied in the forms of activated sludge process (ASP), membrane batch reactors (MBRs), and sequence batch reactors (SBRs), etc., while anaerobic treatment mainly includes anaerobic digestion, anaerobic film reactors (AFRs), anaerobic filters (AFs), and anaerobic sludge reactors (ASRs) (Gadipelly et al., 2014; Simon et al., 2021). The working efficiency of biological treatment in the removal of pharmaceuticals depends heavily on seasonal variations, and other factors like target compounds, wastewater types, and operating conditions such as retention time also affect its degradation performance. For example, the removal efficiency of polar pharmaceuticals and beta blockers vary significantly in different biological processes, and lower water temperature in winter limits the elimination of pharmaceuticals possibly due to the retarded biodegradation and enhanced consumption of medicaments against illness and flu, therefore leading to the higher concentration of pharmaceuticals detected in the effluents (Ahmed et al., 2017; Kot-Wasik et al., 2016; Manna et al., 2021). Besides, secondary contamination with sludge is usually produced during the biological treatment processes (Xu, Y. et al., 2017).

2.1.3 Removal of pharmaceuticals through chemical treatments

Chemical treatment, as the name suggests, refers to the elimination of contaminants in water by adding specific chemicals. Common chemical treatment techniques include chemical oxidation, ion exchange, disinfection (*e.g.*, chlorination, ultraviolet (UV) light,

and ozone), and precipitation, etc. (Ahmed et al., 2021). Among them, chemical oxidation has received emerging attention these days, as various organic pollutants including emerging contaminants (*e.g.*, pharmaceuticals, pesticides, and dyes) can be reduced significantly and sometimes even converted into harmless and controllable by-products like water and carbon dioxide during the process (Kao et al., 2020). Typically, the aqueous-phase oxidation methods based on the generation of free radicals and highly reactive species which can attack and destruct the organic contaminants at a high reaction rate constant can be broadly defined as advanced oxidation processes (AOPs) (Klavarioti et al., 2009). AOPs are usually described as environmentally compatible, highly efficient, easy to implement, and capable of oxidizing a wide range of contaminants.

AOPs have experienced a rapid development during the past 30 years with great potential in surface water and wastewater treatment owing to their broad applicability and weak persistence, accompanied by high efficiency in the elimination of hazardous organic pollutants (Li, H. et al., 2020). Numerous studies have demonstrated that pharmaceuticals, along with a wide range of emerging contaminants, can be efficiently degraded by AOPs using chemical oxidants including but not limited to H_2O_2 , KMnO_4 , O_3 , and persulfate salts (Hassani et al., 2018). The activation of these oxidants through initiators including ultraviolet (UV), catalysts, the Fenton's reagent, ozonation, ultrasound, electrolysis, and some less conventional processes such as microwaves, ferrate reagent, ionizing radiation, and pulsed plasma, leads to the *in-situ* generation of free radical species. These often refer to atoms or molecules containing at least one unpaired electron, such as hydroxyl radical (OH^\cdot), sulfate radicle ($\text{SO}_4^{\cdot-}$), superoxide anion radical ($\text{O}_2^{\cdot-}$), hydroperoxyl radical ($\text{HO}_2^{\cdot-}$), or even alkoxy radical (RO^\cdot),

which are of high reactivity, strong oxidation ability, and non-selective nature (Kanakaraju et al., 2018; Rivera-Utrilla et al., 2013).

Table 2-1 One electron redox potential of ROS, relative to standard hydrogen electrode (SHE)

ROS	Standard redox potential, E ⁰ /V	Ref.
OH [•]	1.8-2.7	(Cai et al., 2019; Giannakis et al., 2021)
SO ₄ ^{•-}	2.5-3.1	(Giannakis et al., 2021)
O ₂ ^{•-}	0.94	(Krumova and Cosa, 2016; Rao and Hayon, 1973)
HO ₂ ^{•-}	1.06	(Krumova and Cosa, 2016)
RO [•]	1.60	(Krumova and Cosa, 2016)

Due to the high efficiency and great versatility, a lot of effort has been devoted to the application of AOPs, and with successful elimination of emerging contaminants, e.g., pesticides, pharmaceutical and personal care products (PPCPs), dyes, plasticizers, and microcystin from water. Relevant studies show that specific AOPs towards pharmaceutical degradations commonly include photochemical processes, non-photochemical processes and hybrid /combined processes, while the representative ones are namely ozonation, photolysis, Fenton oxidation, electrochemical oxidation, ultrasonic oxidation, and radiolysis, etc.

2.1.3.1 Ozonation

Ozone (O_3) is a strong oxidant which has been widely studied in the efficient removal of pharmaceuticals from water. The main working mechanism of ozonation in pharmaceutical degradation relies on the OH^\cdot with strong and non-selective oxidizing activity which can be generated from the reaction between ozone and hydroxide anions in water (Andreozzi et al., 1999). Since the concentration of OH^\cdot is directly related to the working efficiency of ozonation, H_2O_2 are usually added into the working solution to increase the content of OH^\cdot and promote the decomposition of O_3 . In addition to H_2O_2 , it is also reported that the performance of ozonation can be enhanced significantly under the combination of light irradiation and transition metals, metal oxides, carbon materials, clay materials, etc., which serve as catalysts (Rivera-Utrilla et al., 2013). Wang et al. reported that carbon materials contribute to the generation of surface radicals by adsorbing O_3 on its surface and promoting its decomposition, thus yield OH^\cdot generation (Wang and Wang, 2019). An et al. reported that the combination of O_3 and $MgO/g-C_3N_4$ under photocatalysis using visible light showed complete degradation of phenol in just 2 min, which was significantly faster than that of single catalytic ozonation or single photocatalysis (An et al., 2020). Gómez-Pacheco et al. reported that the presence of activated carbon during ozonation not only enhanced the generation of OH^\cdot , but also lower the medium toxicity and residue dissolved organic carbon during the degradation of tetracycline, which was attributed to the adsorption ability of activated carbon and its capacity in transforming dissolved O_3 into OH^\cdot (Gómez-Pacheco et al., 2011).

2.1.3.2 Photolysis

Photolysis enables the removal of various pharmaceuticals from waterbodies based on the fact that individual compounds will undergo decomposition on varying degrees depending on their chemical structure with the presence of artificial or natural light. Although most of the pharmaceuticals are designed with thermal stability, many of them are of light sensitive, indicating that they will go photodecomposition (Tonnesen, 2004). For example, pharmaceuticals with aromatic rings and conjugated π systems can be at least partly degraded with direct solar photolysis, since such chemical structure facilitates a strong adsorption within the wavelength of UVC ($\lambda=200-280$ nm), a tailing absorption within the UVB ($\lambda=280-315$ nm), and sometimes even within the UVA ($\lambda=315-400$ nm), which partially overlaps with sunlight ($\lambda > 290$ nm) (Challis et al., 2014; Dasgupta and Klein, 2014). Besides, pharmaceuticals can also react feasibly with some photosensitive substances originated from indirect photolysis, *i.e.*, carbonate, nitrate, natural organic matter (NOM), and iron present in the waterbodies, etc. (Baalbaki et al., 2017; Challis et al., 2014). Both direct and indirect photolysis have been confirmed effective in the breakdown of many emerging contaminants including pharmaceuticals. In direct photolysis, the contaminant is decomposed due to the adsorption of photons coming from light radiation, while indirect photolysis involves the participation of reactive species, *i.e.*, hydroxyl radicals (OH^\cdot), singlet oxygen ($^1\text{O}_2$), and triplet excited dissolved organic matter (^3DOM), which can be generated by photosensitizers at an excited state after absorbing radiation (Fatta-Kassinos et al., 2011). Up to now, considerable researches have been focused on the elimination of pharmaceuticals from water through photolysis and most of them revealed that the efficiency of photolysis depends on various factors including but not limited to the chemical properties of the pharmaceutical, the operating conditions such as the UV lamp type and the concentration of H_2O_2 employed, and even the possible competition

raised by some other substances from water matrix, etc. (Wols et al., 2014).

2.1.3.3 Fenton oxidation

The Fenton and related chemical reactions encompasses the generation of highly reactive oxygen species with strong oxidizing capacity from the activation of peroxides (usually H_2O_2) with iron ions. The history of Fenton chemistry can be traced back to 1894, while Henry J. Fenton first reported that the spontaneous presence of H_2O_2 and Fe (II) salts enabled the oxidation of tartaric acid (Wardman and Candeias, 1996). After that, in 1934, Haber and Weiss firstly proposed that the active oxidant generated from the Fenton reaction was hydroxyl radical (OH^\cdot), one of the most powerful oxidants known, and its production is recognized as a critical step by later researchers (Liochev and Fridovich, 2013). From then on, the Fenton oxidation has developed with enhanced working efficiency with the assistance of photochemical reactions using illumination sources such as UV and visible light, electrochemical reactions, iron complexes which serve as Fenton catalysts, and designed heterogeneous catalysts using iron ions immobilized on solid supports (Pignatello et al., 2006). Generally, the Fenton oxidation is viewed as a convenient and economical way for the degradation and treatment of chemical wastes in both waterbodies and soil, since H_2O_2 is a cheap, safe, and environmental friendly oxidant with almost no long-lasting environmental effect. Although there still exists some drawbacks of Fenton oxidation including a relatively tight control of working pH (commonly mild acidic conditions), the unavoidable waste of H_2O_2 in the conversion of O_2 instead of OH^\cdot , and the unstable working solution with mixed reagents, the capability of Fenton oxidation in the treatment of hospital and pharmaceutical manufacturing effluents with serious pollution has been confirmed, as the substances formed after Fenton oxidation can be less toxic or with increased

biodegradability, making the biological post-treatment after mineralization more readily (Ahmed et al., 2021; Chaturvedi and Katoch, 2019; Germán et al., 2019; Hosny et al., 2019; Klavarioti et al., 2009; Kumar et al., 2019).

2.1.3.4 Electrochemical oxidation, ultrasonic oxidation, and radiolysis

Electrochemical oxidation can also be referred as anodic oxidation (AO) when the wastewater to be treated is chlorine-free. AOPs based on electrochemical reactions mainly involves two mechanisms in the oxidation of pollutants, the direct oxidation happens at the anode through electron transfer between the compound and anode, and the indirect oxidation occurs in bulk solution where the radicals and active species with higher reduction potential can be formed through electrochemical activation of oxidants such as hydrogen peroxide, hydroxyl radicals, ozone, chlorine, and hypochlorite (Rivera-Utrilla et al., 2013). The anode activity has a strong influence on the efficiency and selectivity of electrochemical oxidation. In addition to conventional anodes such as Pt, IrO₂, PbO₂ and RuO₂, the boron-doped diamond (BDD) anodes have been confirmed effectively in the degradation of pharmaceuticals and hospital wastewater due to its high stability, high oxygen-over potential which can boost the generation of OH[·], and inert surfaces (Kanakaraju et al., 2018; Loos et al., 2018; Siedlecka et al., 2018; Sopaj et al., 2015).

Ultrasonic oxidation is also known as sonolysis, among which the generation of OH[·] radicals relies on the pyrolysis of water molecules under high-frequency ultrasound waves. The acoustic cavitation caused by the ultrasonic waves helps to enhance the mass transfer in aqueous solution through turbulence and exert positive and negative pressures on a liquid through cycles of compression and expansion (Alfonso-

Muniozguren et al., 2021; Salimi et al., 2017). The efficiency of ultrasonic oxidation is highly depended on the frequency, ultrasonic power, and the reactor applied which are closely related to the production of symmetrical or asymmetric cavitation bubbles. Besides, the addition of external oxidants and/or coupling with other AOPs such as ozonation, photolysis, and electrochemical treatment enhance the convenience and feasibility of ultrasonic oxidation in the degradation of various emerging contaminants (Reggiane de Carvalho Costa et al., 2021). Although a number of studies have demonstrated the effectiveness and efficiency of ultrasonic oxidation in the degradation of pharmaceuticals including painkillers, psychiatric products, antihypertensives, and antibiotics, the mineralization and toxicity removal are sometimes hard to achieve, not to mention its higher energy consumption, longer reaction time and lower economic viability (Rayaroth et al., 2016; Xiao et al., 2014).

Radiolysis, also known as ionizing radiation or chemical radiation, was first studied in water sector in the 1950s. Although positive results were obtained at that time, its wide sectorial application was restricted by the clumsy and difficult-to-operate technology (Capodaglio, 2017). The theoretical basis of ionizing radiation in the degradation of water contaminants mainly lies in the products of water radiolysis, e.g., radical cation (OH^\cdot , H^\cdot , and H_3O^+) and electrons (e^-), instead of direct radiolysis of the dissolved compounds. The primary radicals generated from water radiolysis include both oxidant (e.g., OH^\cdot) and reductant (e.g., hydrated electron, e_{aq}^- , $E = -2.9\text{V}$ vs. NHE), indicating that radiolysis in water treatment enables both oxidative and reductive processes depending on contaminant (Wojnárovits, 2011). Although ionization radiation involves irradiators such as beam of photons (X , γ), high energy electrons (electron accelerator beam, β^-), heavy, charged particles and neutrons, concerning economic, safety, and

technological issues, the first two types, also known as electromagnetic radiation and electronic beam (EB) radiation, are more appropriate for water treatment industry. Besides, it has been reported that the application of radiation including X-ray, γ and EB, contribute to the removal of bacterial pathogens, coliforms and salmonellae from waters and wastewaters of various origins. Also, although radiolysis basically does not require additional reagents, the working efficiency of it can still be enhanced by employing additional chemical reagents such as O_3 , persulfate anions, and H_2O_2 to increase the yield of active radicals. Radiolysis is considered as a clean technology, since it does not pose risk when inducing radioactivity in irradiated media for waste treatment, while no organic sludge or air emission is produced (Alkhuraji, 2019; Trojanowicz et al., 2018).

2.1.3.5 Sulfate-based AOPs

From the 2000s, the sulfate-based advanced oxidation processes (SR-AOPs) have emerged and drawn increasing interests by both academic and industrial communities due to their non-selective behavior and eco-friendly nature in water and wastewater purification. Due to the special advantages such as longer half-life, higher standard redox potential, and wider working pH, SR-AOPs have been applied and investigated in various research aspects with notable efficacy and performances concerning environmental remediation including disinfection, tertiary treatment for organic and emerging contaminants, and sludge and soil remediation (Scaria and Nidheesh, 2022). Since SR-AOP is adopted in this work, its introduction, features and applications will be discussed in detail later in 2.2.

2.1.4 Hybrid reaction system

Hybrid reaction system here refers to the combination of at least two conventional and/or advanced treatment technologies to maximize the degradation of contaminants from water. Although AOPs (not limited to the mentioned ones above) are widely known with special advantages such as high versatility and environmental compatibility in the degradation of emerging contaminants including pharmaceuticals and personal care products, pesticides, dyes, and surfactants, it still remains challenging for the full-scale application of AOPs due to the higher energy requirements and costs (Mukimin et al., 2020). Furthermore, reports about the generation of more toxic or harmful intermediates than the original contaminants after AOPs are not uncommon (García-Espinoza et al., 2018; Han, C.-H. et al., 2020; Tang et al., 2021; Wu, J.-l. et al., 2019). These suggest the necessity of approaches which combine the advantages of AOPs with other treatment techniques spontaneously with elimination of their drawbacks. Thus, the integration of AOPs with biological treatments, membrane technologies, hydrodynamic cavitation, adsorption, and electro-coagulation, etc., have been conducted. For example, the combination of hydrodynamic cavitation with ozonation enhanced the degradation, mineralization, and biodegradability of naproxen; the combination of $\text{TiO}_2/\text{Fe}^{2+}$ /sonolysis showed synergistic effects in the elimination and mineralization of ibuprofen, and a more efficient consumption of H_2O_2 ; and the hybrid system of UVC/ H_2O_2 and UF ceramic membrane presented the best results regarding the permeate flux and oxytetracycline degradation (Espíndola et al., 2019; Jaafarzadeh et al., 2016; Méndez-Arriaga et al., 2009; Taoufik et al., 2021; Thanekar et al., 2019).

2.2 Sulfate-based AOPs (SR-AOPs)

2.2.1 Characteristics of the SR-AOPs

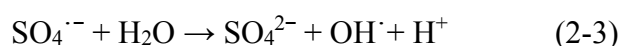
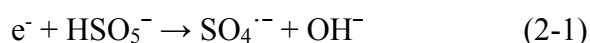
Among the various AOPs studied and mentioned above, the sulfate-based advanced oxidation processes (SR-AOPs) consist a special group. Sulfate radicals ($\text{SO}_4^{\cdot-}$) with higher oxidation potential can be promoted mainly from peroxymonosulfate (PMS) and peroxydisulfate (PDS), which can be generated alone or spontaneously with OH^{\cdot} and other radicals like $^1\text{O}_2$ and $\text{O}_2^{\cdot-}$.

Table 2-2 Comparison between OH^{\cdot} and $\text{SO}_4^{\cdot-}$

	Oxidation potential vs. SHE /V	Working pH range	Shelf-life period/ μs
OH^{\cdot}	1.8-2.7	2-4	<1
$\text{SO}_4^{\cdot-}$	2.5-3.1	2-8	30-40

As indicated in Table 2-2, $\text{SO}_4^{\cdot-}$ shows stronger oxidation ability, a wider working pH ranges, and a significantly longer half-life than OH^{\cdot} . Furthermore, since $\text{SO}_4^{\cdot-}$ mainly interacts with contaminants containing unsaturated bonds or aromatic π electrons through electron transfer due to its lack of the hydrogen abstraction or electrophilic addition, it shows higher working efficiency than OH^{\cdot} . This has been witnessed in tackling some tricky emerging contaminants and thus has gradually become an alternative for H_2O_2 and experienced a rapid progress in recent years (Ghanbari and Moradi, 2017). Comparing to the traditional hydroxyl radical (OH^{\cdot})-based AOPs induced using H_2O_2 , SR-AOPs generally show higher selectivity in the degradation of electron-rich organic contaminants, and lower requirements for external reaction such as water matrixes (Ding et al., 2021).

Although both PDS and PMS are precursors of $\text{SO}_4^{\cdot-}$, there are some differences between them. Briefly, the O-O bond distance within the unsymmetrical PMS molecule is shorter than that of symmetric PDS molecule (1.453 Å vs 1.497 Å), while PDS possesses a higher standard redox potential (2.01-2.12 V) than PMS (1.75-1.82 V) (Wang and Wang, 2018; Wang et al., 2021). The generation of $\text{SO}_4^{\cdot-}$ is induced by the breaking of the O-O bond within either PMS or PDS, while OH^{\cdot} can be formed via the reactions between $\text{SO}_4^{\cdot-}$ and H_2O , as implied in Eqs. (2-1) - (2-3).



Due to the symmetric structure, PDS is commonly considered harder to be activated than PMS, thus, PMS is adopted in this work (Peng, Y. et al., 2021).

2.2.2. Homogeneous PMS activation with transition metal ions

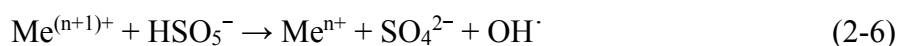
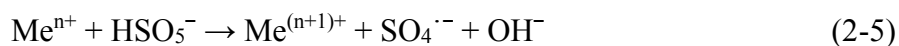
The generation of active species such as OH^{\cdot} and $\text{SO}_4^{\cdot-}$ radicals mainly relies on the activation and cleavage of the O-O bond within PMS via energy-transfer or reductive electron-transfer. Although PMS can be activated effectively via ways like UV, heat, alkaline, ultrasound, and microwave, heterogeneous catalytic activation still occupies an important position due to the possible longer life span (recyclability and reusability) and easier solid-liquid separation of the catalysts, lower energy requirements, and the feasibility to work under diverse operational conditions (Giannakis et al., 2021;

Kohantorabi et al., 2021; Xia et al., 2020).

The adoption of transitional metals as the activators for strong oxidants can be traced back to the classical Fenton process using H_2O_2 as stated in Eq. (2-4) due to the existence of $\text{Fe}^{2+}/\text{Fe}^{3+}$ redox cycle, which is proved sufficient and effective in the degradation of various pharmaceutical pollutants.



In SR-AOPs using PMS as oxidant, transition metals (Me) with lower valance can facilitate the fracture of the O-O bonds within HSO_5^- , followed by the production of $\text{SO}_4^{\cdot-}$ and OH^\cdot as indicated in Eqs. (2-5)-(2-6) (Ding et al., 2021).



Then, from 2003 to 2004, Anipsitakis and Dionysiou reported a highly efficient method based on the Fenton reaction by using Co^{2+} to generate $\text{SO}_4^{\cdot-}$ from PMS in degrading 2,4-DCP, a precursor to the herbicide 2,4-dichlorophenoxyacetic acid. Furthermore, these two researchers also found that among the nine transitional metals tested, their PMS activation ability increased in the sequence of $\text{Ni}^{2+} < \text{Fe}^{3+} < \text{Mn}^{2+} < \text{V}^{3+} < \text{Ce}^{3+} < \text{Fe}^{2+} < \text{Ru}^{3+} < \text{Co}^{2+}$ (Anipsitakis and Dionysiou, 2003, 2004).

From then on, investigations into homogeneous PMS activation using transition metal ions have gained increasing attention, and the effects from working parameters such as

pH, NOM, inorganic anions have also been considered.

2.2.3 Heterogeneous PMS activation with transition metals

However, although homogeneous PMS activation using metal ions has advantages such as the little interfered mass transfer process with higher working efficiency, unavoidable limitations still exist in this route. Despite the less economical effect and hard recovery of metal ions after the reactions, the residual metal ions in the effluents could induce secondary pollution with potential environmental impacts, which might even pose health hazards towards human being (Wang and Wang, 2018). For example, Co^{2+} , one of the most effective PMS activator, tends to accumulate in the liver and kidneys of fish, followed by flesh and skin. These accumulation might result in the changes concerning vital physiological functions such as respiration, osmotic and ionic regulations, nitrogenous waste excretion and absorption, storage and secretion of various enzymes, which ultimately affect the survival and growth of the studied fish (Kubrak et al., 2011). Besides, higher amount of Co^{2+} can accumulate in the terrestrial and aerial animals through the successive links of the food chain. Furthermore, the excessive exposure of Co^{2+} for human beings is potentially to cause heart and thyroid damage, allergic contact dermatitis, asthma, and even hard-metal lung disease, a rare interstitial lung disease (Banza et al., 2009). Furthermore, the species of transition metals are highly influenced by the pH and composition of the water, since metal ions may precipitate or become hydrated under basic or acidic conditions, which would interfere their working activity (Wang and Wang, 2018).

Thus, tremendous efforts have been put into the investigation of heterogeneous

transition metal based catalysts which can overcome the mentioned drawbacks with easier solid-liquid separation and less environmental hazards. The transitional metal-based catalysts with various structures and/or substrates have been developed for heterogeneous PMS activation in the removal of emerging contaminants from water for more than two decades. Similar to the homogeneous process mentioned before, the flexible decomposition of PMS using transition metal-based catalysts still lies mainly on the redox cycle reactions between HSO_5^- and $\text{Me}^{n+}/\text{Me}^{(n+1)+}$. Furthermore, depending on the characterizations of the catalysts, other ROSs such as superoxide ($\text{O}_2^{\cdot-}$), singlet oxygen ($^1\text{O}_2$) and even electron (e^-) can also be generated during PMS activation.

Comparing to traditional transition metal-based catalysts with single metal component, bimetallic oxides and their derivatives with more metal composites present additional physiochemical characteristics (e.g. magnetically separable and photoactive) and synergetic electron transfer during PMS activation, which can not only help to optimize their selectivity, stability, life-span, and working efficiency, but also alleviate the possible biological effects and second pollution caused by the metal leakage (Durán-Álvarez et al., 2016). Table 2-3 below summarizes some representative bimetallic catalysts reported for PMS activation, along with the main ROSs they generated during the oxidation of organic compound in water.

Table 2-3 Performances of some bimetallic catalysts in PMS activation and the dominant ROSs generated

Catalyst	Contaminant and its dosage		PMS dosage	Catalyst dosage /ppm	Dominant ROS	Reaction time/min	Removal /%	Ref.
CoAlMn	Bisphenol A	10 ppm	150ppm	20	SO ₄ ^{•-}	100	>99	(Li et al., 2015)
CuFeO ₂	Sulfadiazine	8 μm	33μm	100	SO ₄ ^{•-}	12	>80	(Feng et al., 2016)
CuFe ₂ O ₄	Atrazine	2μm	1 mM	100	SO ₄ ^{•-} , OH [•]	15	>98	(Guan et al., 2013)
BiFeO ₃	Diclofenac	0.025 mM	0.5 mM	300	SO ₄ ^{•-} , OH [•]	60	47	(Han, F. et al., 2020)
Co ₂ Mn ₁ O ₄	Triclosan	10 ppm	50 ppm	20	¹ O ₂ , SO ₄ ^{•-}	30	96.4	(Chen, Z. et al., 2020)
Mn _x Co _{3-x} O ₄	Carbazepine	21.16 μm	0.5 mM	50	SO ₄ ^{•-} , OH [•]	30	100	(Deng et

LaCoO ₃	PBSA	5 ppm	5 mM	50	SO ₄ ²⁻	30	100	al., 2017) (Pang et al., 2016)
LaFeO ₃ / Al ₂ O ₃	Acid Orange 7	20 ppm	0.5 mM	100	SO ₄ ²⁻ , OH ⁻	120	< 90	(Wu, S. et al., 2019)
CeVO ₄	Phenol	100 ppm	2000 ppm	1000	¹ O ₂	75	100	(Othman et al., 2020)
Copper substituted zinc ferrite (ZCFO)	Ciprofloxacin	10 ppm	2.5 mM	100	¹ O ₂ , SO ₄ ²⁻ , OH ⁻ and O ₂ ⁻	15	96	(Yu, R. et al., 2020)

Table 2-3 revealed that bimetallic and even multimetallic catalysts have been extensively studied and applied as PMS activator in the degradation of emerging contaminants such as pharmaceuticals, pesticides and dyes with satisfied performances.

Perovskite is a specific class of metallic materials referring to the mineral calcium titanate (CaTiO_3) in the narrow sense, while can be broadly referred to the compounds with typical structural formula of A_2BO_4 and ABO_3 (Fig. 2-1). Among the perovskite structure, the A site is mainly rare earth, alkali metal or alkaline earth metal ion, the radius of which are usually large; and the B site is usually transition metal ion with relatively small radius (Dai et al., 2018; Wang, Yuxian et al., 2020). Metal oxides with perovskite structures exhibit high stability under aggressive conditions. In addition, oxygen mobility within perovskites, like controllable oxygen vacancy, might help produce more ROS. The oxidation state of the B-site cation might affect the electron-transfer capability during redox reactions, and even increase its ability to accommodate various metal ions without destroying the matrices' structure (Chen, L. et al., 2020; Guo et al., 2020; Su et al., 2016; Wang et al., 2019). Besides, the variability of the transition metal valence state leads to the diversity of perovskite properties. These characteristics make perovskites promising catalysts for chemical oxidation, including PMS activation for the degradation of organics. For example, lanthanum-based perovskites (LaMO_3), a common type of perovskite, have been reported to activate H_2O_2 and PMS to degrade common water contaminants including phenol, Rhodamine B, 2-phenyl-5-sulfobenzimidazole and several herbicides, with high reactivity and stability (Hammouda et al., 2017; Lin et al., 2017; Pang et al., 2016; Solís et al., 2017; Taran et al., 2016). Besides, cobalt has been identified as one of the most reactive sites for PMS activation, where cobalt in the B site of perovskite plays a critical role for PMS

activation (Duan et al., 2018).

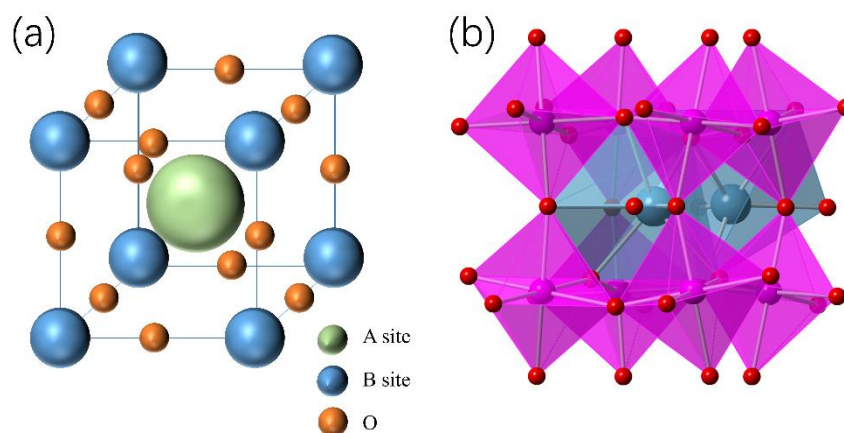


Fig. 2-1 An ideal cubic perovskite structure of ABO₃. (a) Unit cell (the smaller B site is chosen as the origin of the unit cell, and (b) the coordination of B-site ion.

The spinel oxides, with a typical formula of AB₂O₄, is reported with significantly improved stability, activity, higher electrical conductivity and polyfunctionality in AOPs (Yan et al., 2020; Zhou, X. et al., 2020). In this cubic close-packed structure, there are 8 A-sites in which the metal cations are tetrahedrally coordinated with oxygen, and 16 B-sites which possessed octahedral coordination (Mathew and Juang, 2007). According to previous researches, common spinel oxides includes spinel ferrites (AFe₂O₄) with different A site metals (Cu, Co, Zn and Cd) and spinel manganese (AMn₂O₄), which all presented excellent PMS activation ability in the removal of organic contaminants (Dojcinovic et al., 2021; Li, C.-X. et al., 2018; Li, J. et al., 2019; Yang et al., 2018). Recently, the Co_xMn_{3-x}O₄ (x=1, 2) catalyst has received much attention due to its heterogeneous activation of PMS and pollutants degradation (Lim et al., 2019; Yao et al., 2015). As for Mn, in addition to its advantages like earth abundant and environmental benign, a special redox loop with a mid-valence state, Mn²⁺/Mn³⁺/Mn⁴⁺, could be formed during the preparation process, which might provide

more electron transfer pathways (Chen, Z. et al., 2020; Shi et al., 2014). Besides, the partial substitution of Co by Mn in Co_3O_4 can also reduce the amount of toxic from Co element (Yao et al., 2015). Therefore, the spinel structured catalysts with Co and Mn has become a hot spot in the AOPs field, and CoMn_2O_4 is one of those (Zhao et al., 2020).

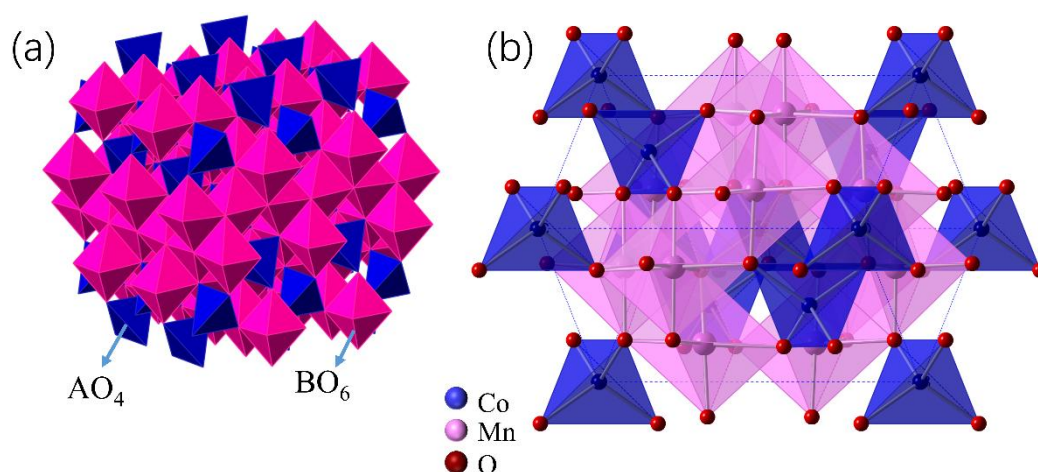


Fig. 2-2 (a) Schematic illustration of the AB_2O_4 spinel structure composed of AO_4 tetrahedra and BO_6 octahedra, and (b) Crystal structure of the CoMn_2O_4 phase.

2.2.4 Heterogeneous activation of PMS with metal-nonmetal catalysts

A number of previous studies implied that the addition of non-metal substrates for the bi-metallic oxide catalysts can further facilitate the catalytic activity via a synergistic mechanism. Generally, the working efficiency of heterogeneous metal-based catalysts follows the descending sequence of metal-nonmetals materials > multi-metals > bi-metals > single metals (Oyekunle et al., 2022). Thus, tremendous efforts have been made in investigating proper non-metal substrates to further enhance the working performance of these catalysts, e.g., silica materials, carbon materials, MXene, layered

double hydroxides (LDHs), resin, and polymeric (Cai et al., 2015; Karim et al., 2022; Li, J. et al., 2017; Wang et al., 2017; Wu, Y. et al., 2019). Ding et al. reported in 2019 that the remarkable synergistic effect within the active sites of the three transition metals (Fe, Co, and Ti) on the surface of $\text{Fe}_2\text{CoTi}_3\text{O}_{10}$ -MXene catalyst contributed to the superior performance of PMS towards the removal of 2, 4-dichlorophenoxyacetic acid (Ding et al., 2019). Wi et al. reported that the loading of ZIF at resin preserved the characteristics porous structures and metal coordination of ZIF-67 spontaneously with the convenient features of resins, which contributed to its superior heterogeneous catalytic activity in PMS activation towards the decolorization and decomposition of RhB (Wu et al., 2018). Gong et al. reported that the loading of MnO_x on polymeric substrate could efficiently activate PMS for the removal of phenolic contaminants mainly through non-radical pathways dominated by the interfacial reactive manganese intermediates (Gong et al., 2022). Zhu et al. reported that Co-Fe catalysts loaded on SiO_2 showed strong PMS activation ability in the degradation of CIP with excellent stability and reusability caused by the strong Co/Fe-O and Co/Fe-Si interaction (Zhu, S. et al., 2020). Tian et al. also reported in 2020 that the loading of FeOOH on Al_2O_3 performed excellent PMS decomposition ability due to surface weak acid-base pair, which also presented a strong tendency in generating abundant $^1\text{O}_2$ caused by its dual-reaction-site (Tian et al., 2020).

Although these materials shared the advantages like extremely large specific area and high stability, most of them suffered from several flaws including costly, time-consuming, and complicated preparation (Sun, Z. et al., 2021). Therefore, it is imperative to find some alternative substrate materials for the modification of nanosized catalysts with higher efficiency, lower cost, and more ecofriendly.

2.2.5 Metal-nonmetals catalysts with clay and clay minerals

In recent years, natural clay minerals have gradually received increasing attention in environmental remediation such as air and water purifications owing to their abundant distribution, satisfied thermo and chemical stability, large surface area, and biocompatible with low cytotoxicity (Dong et al., 2019; Li, C. et al., 2018). Clay minerals are the main mineral components of clay rock and soil with hydrous aluminosilicate minerals, which are described by two-dimensional sheets, tetrahedral (SiO_4) and octahedral (Al_2O_3). Regularly, they can be categorized according to the way that tetrahedral and octahedral sheets are packaged into layers, as a 1:1 layer structure consists of the repetition of one tetrahedral and one octahedral sheet, whereas in the 2:1 layer structure, one octahedral sheet is sandwiched between two tetrahedral sheets (Brigatti et al., 2013).

2.2.5.1 The 1:1 subgroup

The kaolin subgroup consists of dioctahedral 1:1 layer structures with the general composition of $\text{Al}_2\text{Si}_2\text{O}_5 \cdot (\text{OH})_4$, and the most representative one is the kaolinite. Kaolinite (Kln) has plentiful adsorption sites, in which the layer is essentially neutral and the two contiguous layers are linked through -Al-O-H...O-Si- hydrogen bonding, possessing abundant aluminum hydroxyl groups and to help effectively prevent self-agglomeration of the carried nanoparticles (Zhang, X. et al., 2020).

Another important member of this group is halloysite nanotube (Hal), which shares the same chemical composition with kaolinite but with a tubular structure. Generally, Hal

varies in length from submicrons to several microns, and ranges in external diameter from approximately 30 to 190 nm while internal diameter from approximately 10 to 100 nm (Yuan et al., 2015).

It is reported that functionalized Hal constituted a superior support for metal nanoparticles, as its peculiar tubular shape favors the dispersion and surface availability of the supported nanoparticles and thus promote their catalytic applications with tunable properties (Massaro et al., 2017). These Hal-based catalysts have been widely adopted in catalytic fields including water and air remediation, chemical synthetic routes like polymerization and cross coupling reactions, and industries like oil refining and petrochemistry (Glotov et al., 2021b; Massaro et al., 2017). Comparing to other lamellar clay minerals like kaolinite, montmorillonite and bentonite, Hal do not stack in multilayers and might be easier to be exfoliated through stirring (Glotov et al., 2021b). Besides, Hal has Si–O groups at the outer surface with negative charges and Al–OH groups at the inner side with positive charges, which allowed the selective designing of catalysts with tuned wettability for processes in aqueous media or under two-phase conditions (*i.e.*, oil–water) (Glotov et al., 2019). For example, the modification of the outer surface of Hal using alkali helped to increase its stability and reactivity in aqueous solutions due to the increased density of surface hydroxyl groups (Tharmavaram et al., 2018). However, opposite measures were taken on Hal-based catalysts aimed at aromatics hydrogenation in petroleum chemistry, as the outer surface of Hal was modified by alkyltriethoxysilanes to obtain super hydrophobicity and enable the loading of Ru nanoparticles within the lumen, which protected the active sites from deactivation caused by admixed water and metal leaching spontaneously with enhanced working efficiency (Glotov et al., 2021a).

Besides, Hal resembles carbon nanotube (CNT), a commercial nanomaterial with the tubular porous structure with abundant surface hydroxyl groups (Ghanbari et al., 2015). But comparing to CNT that is toxic and hard to synthesis (high production environment requirements and low yields), the natural occurring Hal is much cheaper and easily meets the mass-scale applications in industry (Glotov et al., 2021b; Gusain et al., 2020; Ma, W. et al., 2018). Thus, it seems feasible for Hal to act as an alternative for CNT. But so far, few studies have reported the application of Hal as matrices for heterogeneous catalysts towards AOP processes (Huang, Z. et al., 2020; Kadir et al., 2020). In addition to the mentioned two minerals belonging to the kaolin subgroup, another group of trioctahedral 1:1 clay minerals called the serpentine group is seldom adopted in the researches concerning AOPs. The serpentine group is chemically simple but structurally complex, which can be classified into planar structure, modulated layer structure, tetrahedral sheet strips, and tetrahedral sheet islands. The representative ones are Mg-rich 1:1 trioctahedral layer minerals such as lizardite, antigorite, and chrysotile with an ideal composition of $Mg_3Si_2O_5 \cdot (OH)_4$.

2.2.5.2 The 2:1 subgroup

The 2:1 clay minerals consist of an octahedral sheet sandwiched between two opposing tetrahedral sheets. The layer within pyrophyllite (dioctahedral) and talc (trioctahedral) is electrically neutral, while it is usually negatively charged in other 2:1 phyllosilicates such as smectite, mica, vermiculite, and chlorite (Sethurajaperumal et al., 2021). Among them, smectite such as montmorillonite, chlorite, bentonite, and illite are more frequently used in the synthesis of metal-nonmetal catalysts for AOPs, including Fenton and Fenton-like processes, ozonation, and photocatalysis for efficient removal of

pharmaceuticals, pesticides and dyes (Fatimah et al., 2022). For example, Co_3O_4 /illite and CuFe_2O_4 /sepiolite composites with reduced grain size and crystallinity displayed much stronger activity in the activation of PMS and O_3 towards atrazine and quinolone degradation, respectively, in the comparison with bare Co_3O_4 and CuFe_2O_4 (Dong et al., 2020a; Liu, D. et al., 2019).

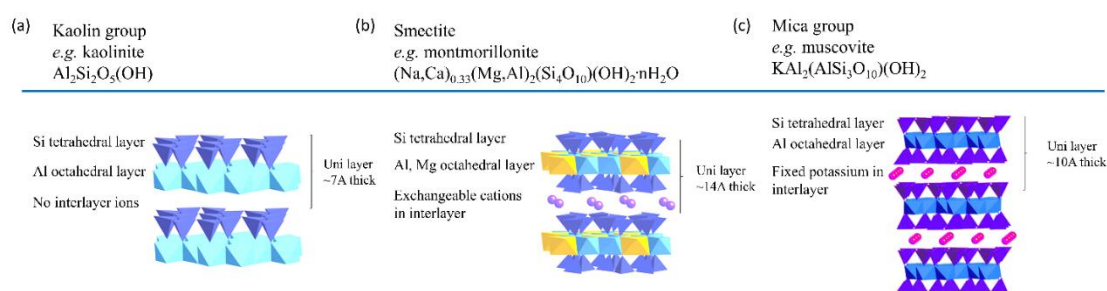


Fig. 2-3 Structure of the three major clay mineral groups: (a) kaolin, (b) smectite, and (c) mica. Figures show the stacking of Si tetrahedra and Al octahedra and characteristic basic spacing.

So far, transitional metal based catalysts loading on natural clay minerals have been reported applicable in various AOPs including Fenton and Fenton-like processes, ozonation, and photolysis for efficient removal of emerging contaminants like pharmaceuticals, pesticides and dyes. However, little of them have focused on the application of Hal in the fabrication of heterogeneous catalysts for the reduction of pharmaceuticals in aqueous environment, even if Hal seems to be a suitable carrier in every aspect. Therefore, it is necessary to investigate the possible effects of Hal towards the structure and morphology of the loaded catalysts, and the catalytic activity of them in pharmaceutical degradation through PMS activation.

Furthermore, the working efficiency and performances of these composite catalysts with natural clay minerals has seldom been linked to the morphology and structural

differences between the substrates, for example, Hal and Kln. Additionally, since the OV_s are also originated from hydroxyl groups, it's possible that Kln and Hal can boost OV_s into catalytic composite during the synthesis, but this information is also still limited (Wu et al., 2017; Zhan et al., 2020).

Table 2-4 Metal-nonmetals catalysts with clay and clay minerals for AOPs

Loaded catalyst	Clay mineral Substrate and its structure	Contaminant and its dosage	Oxidant and its dosage	Reaction time and removal	ROS	Ref.
Cobalt oxide	Halloysite, 1:1	Sulfamethoxazole	PMS	30 min, ~100%	SO ₄ ^{·-} , OH [·] , ¹ O ₂	(He et al., 2022)
Cu-Co	Halloysite, 1:1	Reactive yellow 145 (RY-145), Basic red 46 (BR-46)	H ₂ O ₂	7h, 93% for RY-145; 54% for BR-46	OH [·] and HO ₂ [·]	(Torres-Luna et al., 2019)
TiO ₂	Kaolinite, 1:1	Ciprofloxacin	Under UV or visible light	40 min, >90% for UV; 360 min, ~60% for visible light	OH [·] , O ₂ ^{·-} and e ⁻	(Li, C. et al., 2018)
CuCo ₂ O ₄	Kaolin, 1:1	Phenacetin	PMS	15 min, ~100%	SO ₄ ^{·-} , OH [·] , ¹ O ₂	(Liu et al., 2020)
CuFe ₂ O ₄	Kaolinite, 1:1	Bisphenol A	PMS	60 min, ~100%	SO ₄ ^{·-} , OH [·]	(Dong et al., 2019)
MoS ₂ /FeOOH	Halloysite, 1:1	Aniline aerofloat	H ₂ O ₂ with	60 min, >99%	OH [·] ,	(Liu et al.,

			photo-Fenton			OOH [·] , O ₂ ^{·-}	2023)
FeCo ₂ O ₄	Rectorite, 1:1	Atrazine	PMS	20 min, ~90%		SO ₄ ^{·-} , OH [·]	(Sun, Z. et al., 2021)
Fe ₃ O ₄	Rectorite, 1:1	P-chlorophenol	H ₂ O ₂	60 min, 100%		OH [·]	(Bao et al., 2019)
Fe ₂ O ₃ @CeO ₂ /ZrO ₂	Palygorskite, 2:1	Congo Red dye	H ₂ O ₂	105 min, 95%		OH [·]	(Ouyang et al., 2019)
CoFe ₂ O ₄	Palygorskite, 2:1	Bisphenol S	PMS	30 min, ~100%		SO ₄ ^{·-} , OH [·] , ¹ O ₂	(Li, Y. et al., 2021)
nano zero-valent iron	Bentonite, (main component: Montmorillonite), 2:1	Bisphenol A	H ₂ O ₂	24 h, ~100%		OH [·]	(Bao et al., 2020)
Co _{1.3} Mn _{1.7} O ₄	Bentonite, (main component: Montmorillonite), 2:1	Bisphenol A	PMS	21 min, ~100%		SO ₄ ^{·-} , OH [·] , ¹ O ₂ , O ₂ ^{·-}	(Liu et al., 2022)
Co ₃ O ₄	Illite, 2:1	Atrazine	PMS	30 min, >90%		SO ₄ ^{·-} , OH [·] , ¹ O ₂	(Dong et al., 2020a)
Fe-bearing smectite	Smectite, 2:1	Diethyl phthalate	PMS	300 s, >80%		SO ₄ ^{·-} , OH [·]	(Chen, N. et

clays

al., 2020)

CoFe₂O₄

Montmorillonite, 2:1

Tetracycline

PMS

30 min, ~100%

SO₄²⁻, OH⁻

(Li et al.,
2022)

Chapter 3 Materials and methods

3.1 Materials

3.1.1 Chemical reagents

Synthetic raw materials for bare CoMn_2O_4 catalyst include cobalt (II) nitrate ($\text{Co}(\text{NO}_3)_2 \cdot 6\text{H}_2\text{O}$, CAS No. 10026-22-9), manganese (II) nitrate ($\text{Mn}(\text{NO}_3)_2 \cdot 6\text{H}_2\text{O}$, CAS No. 17141-63-8), and sodium hydroxide (NaOH , CAS No. 1310-73-2). All of them were purchased from Macklin Biochemical Co., Ltd.

Synthetic raw materials for LaCoO_3 catalyst include cobalt (II) nitrate ($\text{Co}(\text{NO}_3)_2 \cdot 6\text{H}_2\text{O}$, CAS No. 10026-22-9), lanthanum(III) nitrate ($\text{La}(\text{NO}_3)_3 \cdot 6\text{H}_2\text{O}$, CAS No. 10277-43-7), and citric acid (CA, CAS No. 77-92-9). All of them were purchased from Macklin Biochemical Co., Ltd.

Quenchers for the traditional trapping experiments include *tert*-butyl alcohol (TBA, provided by Sigma-Aldrich, CAS No. 75-65-0), 1,4-benzoquinone (1,4-BZQ, provided by Sinopharm Chemical Reagent Co., Ltd, CAS No. 106-51-4), sodium azide (NaN_3 , provided by Sigma-Aldrich, CAS No. 26628-22-8) and methanol (MeOH , provided by Sigma-Aldrich, CAS No. 67-56-1).

The mobile phases for High-Performance Liquid Chromatograph (HPLC) analysis include Milli Q water (resistivity $18.2 \text{ M}\Omega \cdot \text{cm}$ at $25 \text{ }^\circ\text{C}$), acetonitrile (ACN, provided by DUKSAN Reagents, CAS No. 75-05-8), MeOH , and oxalic acid (provided by Sigma-Aldrich, CAS No. 144-62-7). In addition, all the solvents adopted here were of

HPLC grade without further purification before using.

The spin trapping agents for EPR analysis include 5, 5-dimethyl-1-pyrrolidine N-oxide (DMPO, CAS No. 3317-61-1) and 2, 2, 6, 6-tetramethylpiperidine (TEMP, CAS No. 768-66-1), both were provided by Sigma-Aldrich.

Target compounds adopted in the degradation experiments later include carbamazepine (CBZ, CAS No. 298-46-4), ofloxacin (OFX, CAS No. 82419-36-1), sulfamethoxazole (SMZ, CAS No. 723-46-6) and tetracycline (TC, CAS No. 60-54-8), which were all purchased from Sigma-Aldrich. The peroxymonosulfate (PMS, $\text{KHSO}_5 \cdot 0.5\text{KHSO}_4 \cdot 0.5\text{K}_2\text{SO}_4$, CAS No. 37222-66-5) used for the degradation was purchased from Acros Organics. The working pH of the experiments were adjusted using NaOH and sulfuric acid (H_2SO_4 , CAS No. 7664-93-9, provided by RCI Labscan Limited).

Other chemical reagents adopted in this work include sodium benzoate (BA, 99.5%, CAS No. 532-32-1) and p-hydroxybenzoic acid (p-HBA, 99%, CAS No. 99-96-7), which were purchased from Macklin Biochemical Co., Ltd. The iron (II) sulfate ($\text{FeSO}_4 \cdot 7\text{H}_2\text{O}$, >99%, CAS No. 7782-63-0) was purchased from Acros Organics. The potassium thiocyanate (KSCN, CAS No. 333-20-0) was purchased from Sigma-Aldrich.

All the chemicals above, except the mobile phases for HPLC analysis, are of analytical purity (AR) or ACS grade without further purification before using. Water from Millipore Waters Milli-Q water purification system (resistivity 18.2 $\text{M}\Omega \cdot \text{cm}$ at 25 °C) was used throughout the whole experiments.

3.1.2 Natural clay minerals

Kaolinite (Kln) used in this work was collected from Maoming City, Guangdong Province, and halloysite (Hal) were from Linfen city, Shanxi Province, China. Their chemical composition were determined by XRF as below (Table 3-1).

Table 3-1 Chemical composition of halloysite (Hal) and kaolinite (Kln) tested by XRF

No.	Halloysite (Hal)		Kaolinite (Kln)	
	Component	Unit mass %	Component	Unit mass %
1	Al ₂ O ₃	40.4	MgO	0.285
2	SiO ₂	56.3	Al ₂ O ₃	42.5
3	P ₂ O ₅	0.0807	SiO ₂	52.7
4	SO ₃	0.0537	P ₂ O ₅	0.69
5	Cl	0.0288	K ₂ O	2.09
6	K ₂ O	2.0	CaO	0.13
7	CaO	0.0913	TiO ₂	0.467
8	TiO ₂	0.175	MnO	0.0121
9	MnO	0.0253	Fe ₂ O ₃	0.565
10	Fe ₂ O ₃	0.796	CuO	0.0321
11	ZnO	0.0084	SrO	0.0158
12	Rb ₂ O	0.0259	PbO	0.511
13	Nb ₂ O ₅	0.0047		

3.2 Methods

3.2.1 Preparation of the catalysts

The catalysts, including bare CoMn_2O_4 (CMO), x -CMO/Hal, and x -CMO/Kln, were synthesized through co-precipitation, as briefly stated in Fig. 3-1. The x in x -CMO/Hal and x -CMO/Kln stands for the loading percentage of CMO on Hal and Kln (w/w, $x=20\%$, 40% , and 60%).

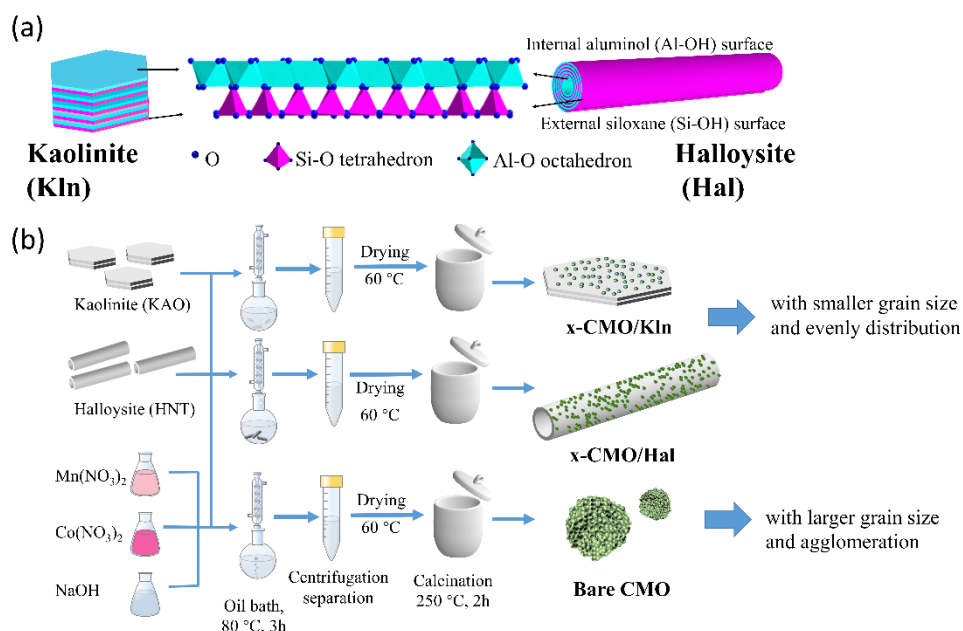


Fig. 3-1 Schematic representation of the synthesis process of bare CMO, x -CMO/Hal, and x -CMO/Kln catalysts.

Typically, 2g halloysite or kaolinite was dispersed in MilliQ water and kept stirring for 6h. Then, based on the predetermined weight ratio, certain amount of cobalt (II) nitrate ($\text{Co}(\text{NO}_3)_2 \cdot 6\text{H}_2\text{O}$) and manganese (II) nitrate ($\text{Mn}(\text{NO}_3)_2 \cdot 6\text{H}_2\text{O}$) were resolved in the natural mineral suspension spontaneously for another 2h to make them evenly distributed, followed by the slow addition of 4M NaOH. Then the whole fabrication system was heated with oil bath at 90 °C for 2 h under continuous stirring. During this

process, the particles would generate gradually. Two hours later, after the whole system was cooled to room temperature, the precipitate was separated by centrifugation and dried at 70 °C for 6 h until it was completely dry. After that, the dried powder was moved into muffle furnace and calcinated at 250 °C for 2h. Then the obtained powder was grounded and named as *x*-CMO/Hal or *x*-CMO/KIn (*x*=20%, 40%, and 60%) according to the weight ratio of CMO. The bare CMO was prepared through the same process without the addition of halloysite or kaolinite. Besides, the raw halloysite and kaolinite without further treatments were also calcinated at 250°C for 2 h, preparing for further analyzation.

The LaCoO₃ (LCO) perovskite was prepared using the sol-gel method (Lu et al., 2018; Zhang et al., 2019). Lanthanum(III) nitrate (La(NO₃)₃·6H₂O) and cobalt trinitrate (Co(NO₃)₃·6H₂O) were taken as precursors, while citric acid (CA) acted as the complexing agent, in the molar ratio of La³⁺ : Co³⁺ : CA at 1:1:2. These reagents were dissolved in an ethanol-water solution (V_{H2O} : V_{Ethanol} = 2:1), followed by a 30 min stirring and another 10 min sonication at room temperature (25 °C) to obtain a uniform mixed solution (sol). The solution (sol) was then placed in a vacuum drying oven and dried in vacuum at 90 °C to obtain a xerogel. After grinding, the xerogel obtained was calcined at 600 °C at a heating rate of 5 °C min⁻¹ for 5 h. The final product was labelled as LCO.

3.2.2 Characterization methods of the catalysts

The crystal structures of the catalysts were determined by D8 ADVANCE X-ray diffractometer (XRD, Bruker, Germany) using Cu K α as the radiation source (λ =

0.15418 nm). The XRD spectra was generated at voltage 40 kV and current 40 mA, with continuous scanning from $2\theta = 3$ to 80° at a step size of 0.01° at a rate of 3° min^{-1} .

The surface composition and chemical valences of the catalysts were analyzed by X-ray photoelectron spectroscopy (XPS, ESCALAB 250, Thermo Fisher Scientific, USA), using Al $K\alpha$ ($h\nu=1486.8 \text{ eV}$) as the excitation light source, and C $1s = 284.4 \text{ eV}$ as the calibration to obtain the binding energy of each element species in the high resolution spectra.

The surface morphology of the catalysts was examined by field emission scanning electron microscope (FESEM, Zeiss, USA). The samples were also analyzed by a High-angle annular dark-field scanning transmission electron microscopy (HAADF-STEM, FEI Talos F200S, Thermo Fisher Scientific, USA) equipped with an energy-dispersive X-ray spectroscopy (EDS) at an acceleration voltage of 200 kV.

The defect centers within the catalysts were characterized using electron paramagnetic resonance (EPR, JES-FA-300, JOEL, Japan).

The Brunauer-Emmett-Teller (BET) analysis (including N_2 adsorption-desorption isotherms) was performed by Accelerated Surface Area and Porosity System (Micromeritics) using liquid nitrogen at -196°C to obtain the specific surface areas (SSA) and pore size distributions of the catalysts. The samples were vacuum degassed for 12h at 120°C before testing. The total pore volume was estimated using nitrogen adsorption at a relative pressure of 0.99.

The zeta potential of the catalysts was measured by a Zetasizer (Malvern, UK) using aqueous suspension.

3.2.3 Analytical methods

The residue concentrations of CBZ, OFX, SMZ and TC were measured by a Waters 2696 high-performance liquid chromatography (HPLC) system equipped with C18 column and 2487 UV detector. Other working parameters were provided below in Table 3-2.

Table 3-2 Working parameters of HPLC for OFX, CBZ, SMZ and TC

Organic compound	Mobile phase A	Mobile phase B	Mobile phase C	Wavelength/nm
OFX	75% water with 0.1% formic acid	25% acetonitrile	0	294
CBZ	40% water	60% acetonitrile	0	286
SMZ	40% water	60% acetonitrile	0	265
TC	72% oxalic acid (0.1M)	20% acetonitrile	8% methanol	357

The degradation intermediates of CBZ, OFX, SMZ and TC were determined by Thermo Scientific Orbitrap MS coupled with LC. The detected mass range was 50-2,000 (m/z). The mass accuracy was less than 3 ppm RMS using external calibration. The resolution was 500,000 FWHM at m/z of 200. Herein, 0.1% formic acid was used as mobile phase A, and pure ACN as phase B. The other working parameters were provided as below in Table 3-3.

Table 3-3 Working parameters of LC-MS for OFX, CBZ, SMZ and TC

Compound	Time/min	Mobile phase		ESI mode	Flow rate/ (ml/min)	Injection volume/ μ L	Column temperature/ $^{\circ}$ C
		A/%	B/%				
CBZ	0-12	95	5	+	0.25	10	30
	12-13	5	95				
	13-15	5	95				
	15-20	95	5				
OFX	0-2	95	5	+	0.4	10	30
	2-4	60	40				
	4-6	20	80				
	6-10	95	5				
TC	0-10	90	10	+	0.45	10	30
	10-14	10	90				
	14-15	10	90				
	15-16	90	10				
SMZ	0-2	90	10	+	0.4	10	30
	2-15	30	70				
	15-18	30	70				
	18-20	90	10				

The EPR spectroscopy (EPR, JES-FA-300, JOEL, Japan) were used to determine the ROS generated during the catalytic degradation processes using 5, 5-dimethyl-1-pyrroline-N-oxide (DMPO) and 2, 2, 6, 6-tetramethyl-4-piperidone (TEMP) as spin reagents.

The concentration of leached metal ions from the catalysts during the degradation was analyzed by inductively coupled plasma-optical emission spectroscopy (ICP-OES, SpectroBlue, Germany) after a total digestion using 68% (w/w) HNO_3 .

The total organic carbon (TOC) reduction was tested by a Shimadzu TOC-5000A analyzer equipped with an ASI-5000A autosampler (Shimadzu, Japan) to determine the mineralization efficiency.

The changes in PMS concentration during the catalytic degradation processes was determined using a colorimetric method (Wang et al., 2014). Briefly, 1 ml of the working suspension was withdrawn by a syringe and filtered using a 0.22 μm PSE membrane plate before being placed into a cuvette (4 ml). Then, 1 mL of the 10 mM acidified iron (II) sulfate solution ($\text{FeSO}_4 \cdot 7\text{H}_2\text{O}$, >99%, acidified using 1 M H_2SO_4) was added. The cuvette above was then stood by for 5 min, and its absorbance was read using a UV spectrophotometer at $\lambda=450$ nm immediately after the injection of 0.2 mL of the 0.3M KSCN solution (Wang et al., 2014). The calibration curve was made using PMS standard solutions ranging between 0 and 200 μM as showed in Fig. 3-2 with a high linear correlation coefficient ($R^2=0.995$).

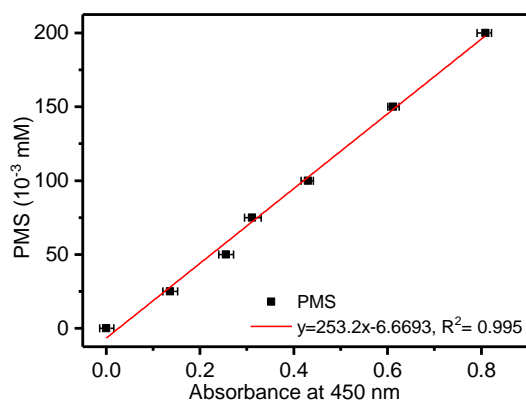
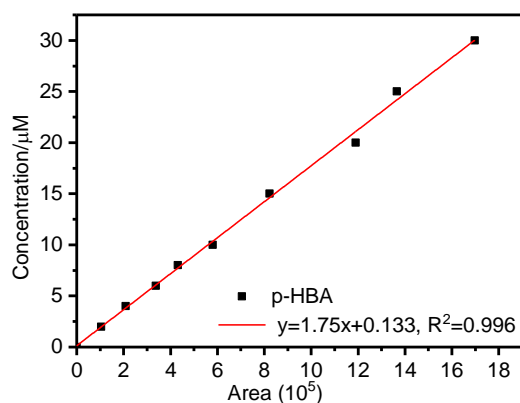


Fig. 3-2 Calibration curve for PMS concentration using KSCN method

The concentration of OH^\cdot generated during the catalytic pharmaceutical degradation was measured using benzoic acid (BA), since BA would be hydroxylated into p-hydroxybenzoic acid (p-HBA) by OH^\cdot produced, and the cumulative OH^\cdot could be approximately estimated by p-HBA from hydrolysis with a conversion factor of 5.87 (Xie et al., 2021). At this time, 10 mM BA was added into the reaction system without the addition of target pharmaceutical. For the measurement of p-HBA, 0.5 mL of BA working suspension was withdrawn and filtered immediately before being quenched by 0.5 mL MeOH, which terminated the generation of OH^\cdot . The generated p-HBA was analyzed by HPLC using 35% acetonitrile and 65% ultrapure water with 0.1% CF_3COOH as mobile phases at a wavelength of 255 nm. The calibration curve was made using p-HBA standard solutions ranging between 0 and 30 μM as showed in Fig. 3-3 with a high linear correlation coefficient ($R^2=0.996$).

**Fig. 3-3** Calibration curve for OH^\cdot measurement using p-HBA concentration

3.3 Experimental procedures

In order to keep the freshness and effectiveness of the reagents, the stocking solution of the pharmaceuticals were prepared on-site right before the experiments with MilliQ Water at room temperature, 25 °C. Special arrangement was made for TC, as its fresh stock solution was prepared 12 h before the experiment by dissolving 0.02 g of TC into 1 L of Milli-Q Water and stirring overnight at 25 °C in darkness, due to its solubility and possible light sensitivity. All the degradation experiments were carried out in 250 ml beakers with continuous magnetic stirring, and the volume of reaction solution was 100 ml. The initial concentrations of the target pharmaceutical, PMS, and catalyst dosage varied case by case, which was stated in detail in the later chapters.

In a typical degradation experiment, after the target pharmaceutical with determined initial concentration was set and prepared, the catalyst was added into the solution and the whole system was kept under magnetic stirring for another 15 min to obtain the adsorption-desorption equilibrium. Then the pre-determined amount of PMS was added into the suspension to initiate the reaction. In order to figure out the optimal working conditions, the dosages of target pharmaceutical and PMS, and the initial working pH of the solution were changed under certain circumstances. The initial pH was adjusted by H₂SO₄ (1M and/or 0.1M) and NaOH (1M and/or 0.1M) before the addition of PMS.

At given time intervals, 1 ml of the suspension was withdrawn by a syringe and filtered using a 0.22 μm PSE membrane plate, then quickly mixed with excessive Na₂S₂O₃ or MeOH to eliminate the reactive oxygen species (ROSs) and thus terminate the reaction. Then the samples were sent for further analyzation like residue concentration evaluation and TOC test. All the degradation experiments were conducted for 3 times, and the

average final value was adopted at last.

Chapter 4 Characterization of the catalysts

4.1 Introduction

Based on the previous chapters, three series of CMO based catalysts were synthesized in this work, namely bare CMO, CMO based on halloysite (x -CMO/Hal), and CMO based on kaolinite (x -CMO/Kln). The x in x -CMO/Hal and x -CMO/Kln referred to the loading percentage of CMO on Hal or Kln, $x=20\%$, 40% , and 60% .

In order to evaluate the effects of CMO content towards the reaction, the x -CMO/Hal series were utilized for detailed characterizations and the results of XRD, FESEM, HRTEM, EDS mapping, XPS, and BET were provided in this chapter.

On the other hand, in order to further investigate the impacts from Hal and Kln substrates towards the working activity of the composite catalysts, the one with the best working performance in the x -CMO/Hal series, 40-CMO/Hal, was chosen, while the corresponding 40-CMO/Kln and bare CMO were being compared. The working data of the chosen x -CMO/Hal was provided in detail in later chapters. For convenience expression, 40-CMO/Hal and 40-CMO/Kln were abbreviated as CMO/Hal and CMO/Kln.

In addition, characterizations of the LCO catalyst including its crystal structure, morphology, surface composition, and chemical valence, etc., were also determined and analysed independently here in this chapter, part 4.3.

4.2 Results and discussion: CMO catalysts

4.2.1 XRD results of the catalysts

The XRD pattern of bare CMO (Fig. 4-1) indicates the successful synthesis of pure spinel CoMn_2O_4 with the diffractions 2θ at 18.2° (101), 29.4° (112), 33.4° (103), 36.1° (211) and 39.6° (004) (JCPDS No. 77-0471). The rest XRD patterns with diffraction 2θ at 12.4° (001), 19.9° (020) and 24.8° (002) well match to halloysite (JCPDS No. 29-1487), while those 2θ at 12.3° (001), 20.3° (1,-1,0), 24.9° (002), 37.7° (003), 39.0° (-113) and 61.2° (3,-1,1) are readily indexed to kaolinite (JCPDS No. 14-0164). After the loading of CMO on Hal, the XRD patterns of these composite all displayed a two-phase diffraction spectra constituting both CMO and clay minerals with little impurities, indicating the successful immobilization of CMO on either Hal or Kln. Besides, with the increasing of CMO loading (e.g., x), the intensities of x -CMO/Hal strengthened gradually, spontaneously with a growing full width at half maximum (FWHM). However, comparing to bare CMO, the XRD signals of CMO loaded on either Hal or Kln were much weaker but with a wider FWHM, indicating a better dispersion and lower crystallinity of CMO on the clay matrices. The average crystalline size of CMO within the x -CMO/Hal was calculated based on the Debye Scherrer equation after deconvolution by the Rietveld peak-shape function, through which the contribution of clay mineral substrate and CMO domain was determined based on peak broadening (Ghanbari et al., 2021). The average crystalline size of bare CMO, 20, 40, and 60-CMO/Hal were determined as ~ 44.5 nm, ~ 8.9 nm, ~ 12.1 nm, and ~ 22.7 nm.

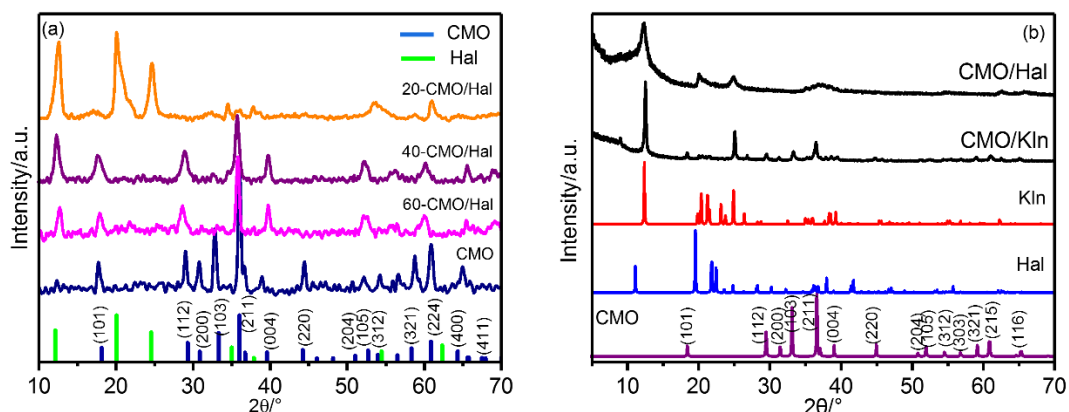


Fig. 4-1 XRD patterns of (a) bare CoMn_2O_4 and x -CMO/Hal ($x= 20, 40$ and 60) catalysts, and (b) bare CMO, Hal, KIn, CMO/Hal and CMO/KIn.

Furthermore, for the chosen CMO/Hal, its insignificant diffractions of CMO comparing to either bare CMO or CMO/KIn designated for comparison all suggested the forming of amorphous phase or nanocrystals on it (Fig. 4-1b). The XRD patterns of both CMO/Hal and CMO/KIn showed slight shift to higher angle, indicating the lattice changes of Hal or KIn during the integration of CMO (Li, X. et al., 2018). Comparing to bare Hal, the diffraction intensity of Hal within CMO/Hal showed significant reduction in the (110) plane near $2\theta = 20^\circ$, while the disappearance of two diffraction peaks in the range of $2\theta = 21^\circ$ - 25° . This is probably ascribed to the decrease in crystallinity of Hal during the preparation (Zheng et al., 2020). As calculated by Scherrer formula on most intense diffraction of CMO ($2\theta= 36.1^\circ$), the average grain size of pure CMO, and CMO on KIn and Hal are 44.5, 22.5 and 12.1 nm, respectively. Thus, the loading on both Hal and KIn both significantly decreased the crystallinity and average particle size of CMO, while this effect was far more obvious on Hal than KIn (Tung et al., 2009).

4.2.2 Morphology of the catalysts

4.2.2.1 FESEM

For the morphology of bare CMO (Fig. 4-2a), the ~ 60 nm particles showed regular cube shape with obvious agglomeration. This can be explained by the fact that CMO particles tended to form bulk crystals during the homogeneous precipitation process, which also account for the sharp reflections with high intensity of its XRD patterns. Pristine Hal presented a one-dimensional tubular shape with smooth surface, while Kln showed a lamellar morphology (Fig. 4-2b and c). After the attachment of CMO on Kln and Hal surface, dispersion of CMO particles is promoted significantly with obvious decrease in grain size and aggregation, while the morphology of clay matrices keeps stable (Figs. 4-2f and g). This is consistent with the XRD results.

The Hal in 20-CMO/Hal and 40-CMO/Hal retains the tubular morphology but the surface of Hal is clearly rough because of uniform distribution of CMO particles (Fig. 4-2d and f). However, the grain size of CMO loaded on Hal is much smaller than bare CMO. Thus, Hal carrier successfully hindered the long-range ordering in unidirectional crystallization of CMO nanoparticles. However, with the increasing content of CMO on Hal, obvious assemblage of CMO was observed, especially on 60-CMO/Hal. This thick wrap on Hal suggests that high loading content greatly suppresses the uniform distribution of CMO nanoparticles (Fig. 4-2e). On the contrary, the particles tend to attach on the lamellar surface of Kln rather than crystal edges, with more severe agglomeration than those on Hal (Fig. 4-2g). These revealed the successful immobilization of CMO on the surface of Hal and Kln.

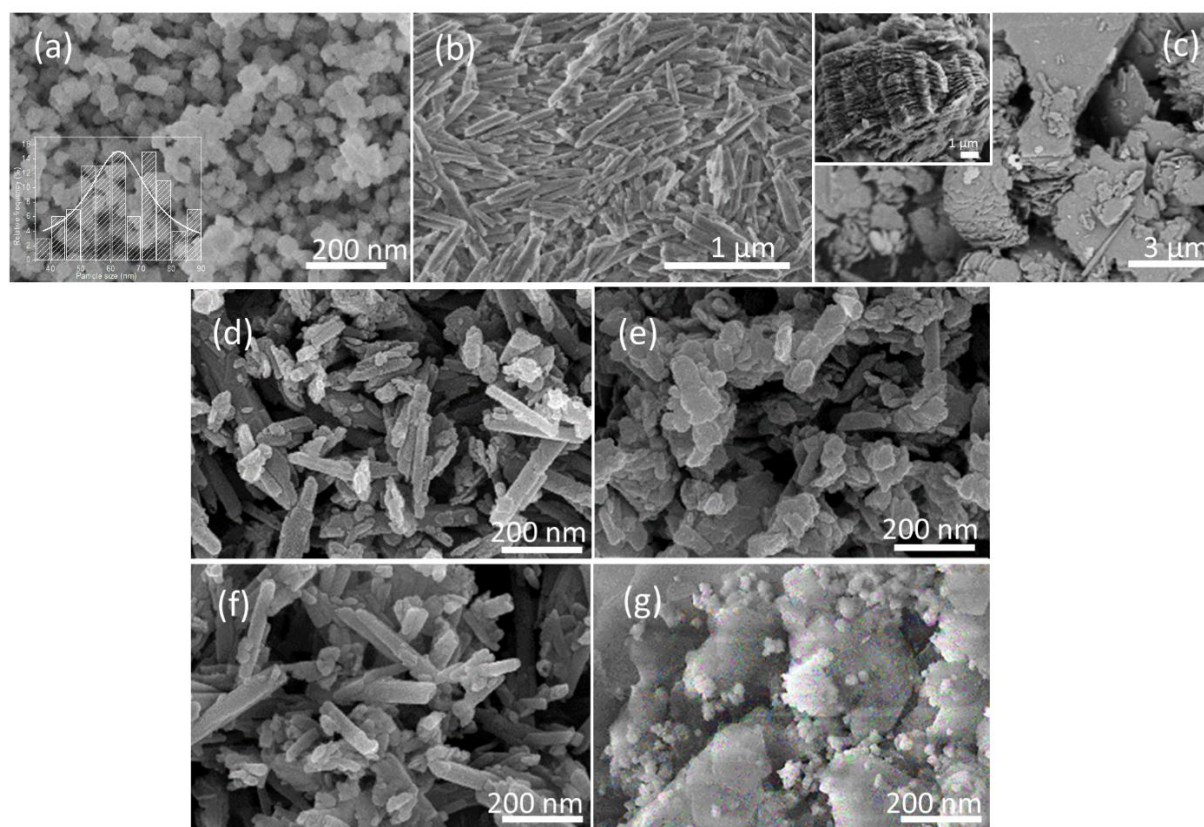


Fig. 4-2 FESEM images of bare CMO (a), Hal (b), KIn (c), 20-CMO/Hal (d), 60-CMO/Hal (e), (40-) CMO/Hal (f), and (40-) CMO/KIn (g).

4.2.2.2. HRTEM, SAED, and EDS

HRTEM and SAED were conducted to further investigate the morphology, crystallinity and distribution of CMO particles on KIn and Hal. The image of bare Hal exhibits one-dimensional tubular morphology with smooth surface, open ends and hollow cavity (Fig. 4-3b), while bare KIn appears as stacking sheets with smooth and well-defined edges (inset in Fig. 4-4d). After the loading of CMO, the surface of Hal nanotubes looks rough with several agglomerated particles, and the open ends of the nanotubes are even occasionally blocked (Fig. 4-3). Additionally, a few CMO particles are found in the lumen of Hal in 20-CMO/Hal (Fig. 4-3c). But with the increment of loading content, CMO particles gradually agglomerate on the external surface of Hal. Especially for 60-CMO/Hal, some large agglomerates even mix with Hal (Fig. 4-3f). Although the

excessive loading of CMO leads to serious agglomeration, their grain size is still smaller than bare CMO, which is in accord with the SEM observation (Fig. 4-2).

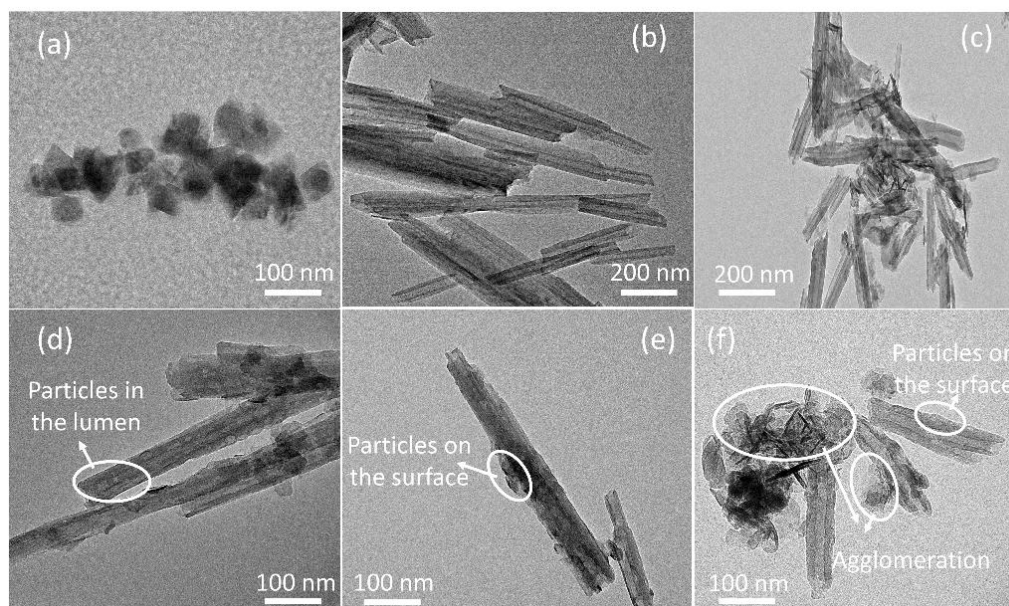


Fig. 4-3 HRTEM images of bare CMO (a), Hal (b), 20-CMO/Hal (d), 40-CMO/Hal (c, e), and 60-CMO/Hal (f).

On the contrary, the particles tend to attach on the lamellar surface of KIn rather than crystal edges, with more severe agglomeration than those on Hal (Fig. 4-4d). These again revealed the successful immobilization of CMO on the surface of Hal and KIn. The lattice fringes of CMO on both Hal and KIn show various orientations with abundant boundaries (Figs. 4-4b and e), and the inter-planar space well corresponds with the planes of spinel structure. The dihedral angles between the exposed facets agree with the theoretical values, i.e., 19.8° for (312) and (213) planes, 53.4° for (202) and (220) planes, and 89.9° for (200) and (004) planes. Interestingly, distorted fringes and several point defects are presented at the lattice boundaries, which is probably attributed to the presence of oxygen vacancies (Sadighi et al., 2017). Compared to CMO/KIn, the point defects are more frequently found in CMO/Hal, probably due to

the smaller crystal size. Moreover, the higher crystallinity of CMO/KIn is also reflected by lattice fringes, as the patterns are far more defined and clearly visible with distinct boundaries (Tian et al., 2021). This is also verified by the selected area electron diffraction patterns (SAED, Figs. 4-4c and f), as CMO/KIn and CMO/Hal both display continuous rings characteristics of polycrystalline phase (Archana et al., 2009). However, CMO/KIn with the enhanced crystallinity shows clear diffraction pattern with bright and random dots (Ramakrishna et al., 2010), while CMO/Hal presents thick rings with weak reflection halo and almost no diffraction spots. The EDS mappings further confirmed the homogeneous dispersion of Co and Mn on the surface of Hal and KIn (Fig. 4-5).

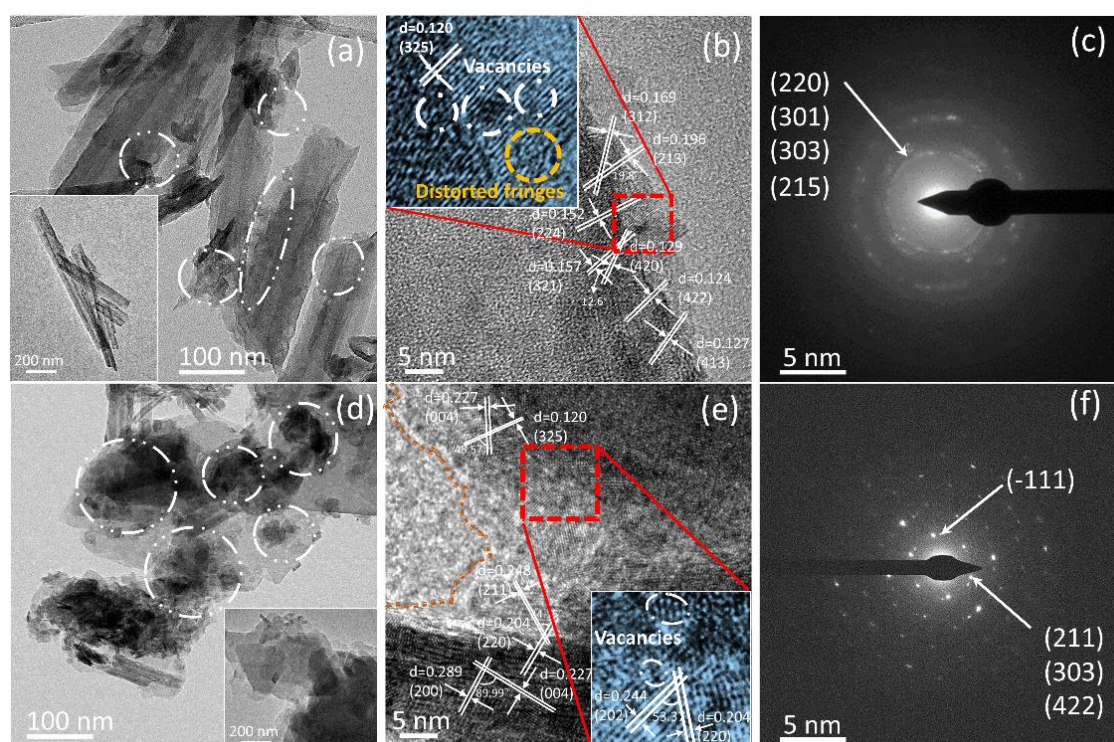


Fig. 4-4 HRTEM images of CMO/Hal (a–b) with raw Hal inserted in (a), CMO/KIn (d–e) with raw KIn inserted in (d), and SAED patterns of CMO/Hal (c) and CMO/KIn (f).

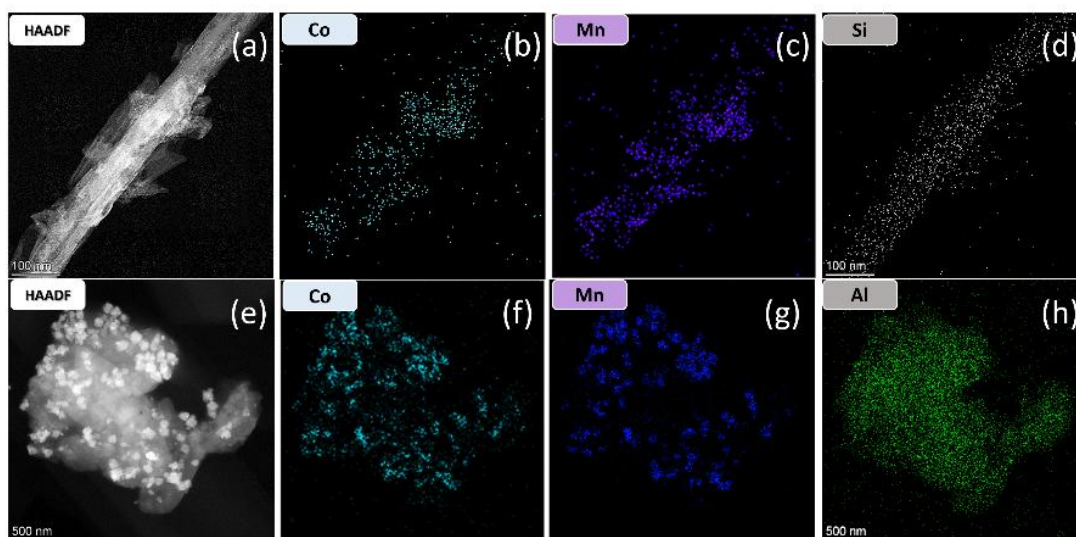


Fig. 4-5 EDS mapping of CMO/Hal (a-d) and CMO/KIn (e-h).

4.2.3 Surface chemical properties of the catalysts

The surface properties including element composition and chemical states were analyzed by XPS (Fig. 4-6). The peaks indexed to Co, Mn and O are clearly distinguished (Fig. 4-6a), while Si and Al are additionally found in those with clay matrices. The surface molar ratio of Co/Mn in bare CMO, CMO/Hal and CMO/KIn were 0.53, 0.52 and 0.48, respectively, close to the feed ratio (0.5). This also confirms the successful synthesis of CMO on Hal and KIn (Liu, L. et al., 2019).

The Co 2p spectra are similar among the catalysts, but slight shifts were observed in those with clays (Fig. 4-6b). The spectra could be divided into two major peaks with binding energies at around 779.5 and 781.6 eV, corresponding to Co^{2+} and Co^{3+} , respectively. The satellite peaks derived from Co 2p 1/2 at 796.9 and 794.8 eV are assigned to tetrahedral Co^{3+} and Co^{2+} , respectively (Wang, Yiping et al., 2020). Thus, Co presents a mixed valence of +2 and +3, where Co^{2+} takes the dominance. The relative ratio of $\text{Co}^{2+}/\text{Co}^{3+}$ in CMO/Hal (0.63:0.37) and CMO/KIn (0.59:0.41) are

higher than that in CMO (0.57:0.43).

The Mn 2p spectra could be fitted into three peaks at ca. 640.1, 641.1, and 643.5 eV, indicating the coexistence of octahedral Mn²⁺, Mn³⁺ and Mn⁴⁺ (Fig. 4-6c) (Yang et al., 2018; Zhao et al., 2020). The surface molecular ratio of (Mn²⁺+Mn³⁺)/Mn⁴⁺ decreases in the order of CMO/Hal > CMO/Kln > bare CMO.

The fitting results reveal that more Co and Mn with low oxidation state, i.e., Co²⁺ and Mn²⁺, are produced when CMO particles is loaded on clay mineral substrates. These finding may result from three aspects: 1) the existence of Hal and/or Kln physically prevent the oxidation of Co and Mn by O₂ in calcination through steric hindrance, 2) the charge redistribution between Co and Mn with surrounding SiO₄ or AlO₄ in mineral substrates, and 3) the nitrate precursors in low crystallinity tends to the formation of low-valent cations (Kaddouri and Mazzocchia, 2004; Kapteijn et al., 1994).

In the O 1s spectra (Fig. 4-6d), the fitted peaks at ca. 532.6, 531.1 and 529.9 eV are assigned to physically adsorbed oxygen (O_{ads}), surface hydroxyls (O_{OH}) and lattice oxygen (O_L), respectively (Peng et al., 2018). Comparing to bare CMO with abundant O_L, the percentage of O_{ads} apparently increase in CMO/Kln and CMO/Hal, indicating their abundant hydroxyl groups. For CMO loaded on either Kln or Hal, however, the peak of O_{ads} (532.5 eV) was broadened and shifted to lower binding energy. On one hand, the coexistence of Co, Mn, Si and Al is ascribed to the loading of CMO particles on clay mineral substrates (Zhang et al., 2014). On the other hand, the broadening and shift of O 1s spectra for CMO/Hal and CMO/Kln are due to the strong interaction between CMO and clay mineral substrates (Sun, Q. et al., 2021; Zhang et al., 2021).

In terms of the Al 2p and Si 2p spectra, the FWHM slightly reduces after CMO loading on Hal and Kln (Fig. 4-6e and h), probably ascribed to the interaction between CMO and Hal/Kln (Kendelewicz et al., 2013; Reddy et al., 2001). Compared to Hal, an obvious shift towards lower binding energy is found in Si 2p spectrum of CMO/Hal, while that of Al 2p shows almost no changes. Thus, the higher electron density near Si-O bond rather than Al-O one, implies that CMO tended to attach on the outer surface of Hal exposed by Si-O group instead of entering into its lumen with the exposure of Al-O group. By contrast, moderate shifts are found in both Si and Al 2p spectra in CMO/Kln relative to those of Kln. But the shift towards the higher binding energy side, as well as an small shoulder peak appear in the Al 2p spectra of CMO/Kln, imply the additional chemical interactions between CMO and Al-O groups other than Si-O ones (Fig. 4-6h) (Zhang et al., 2021).

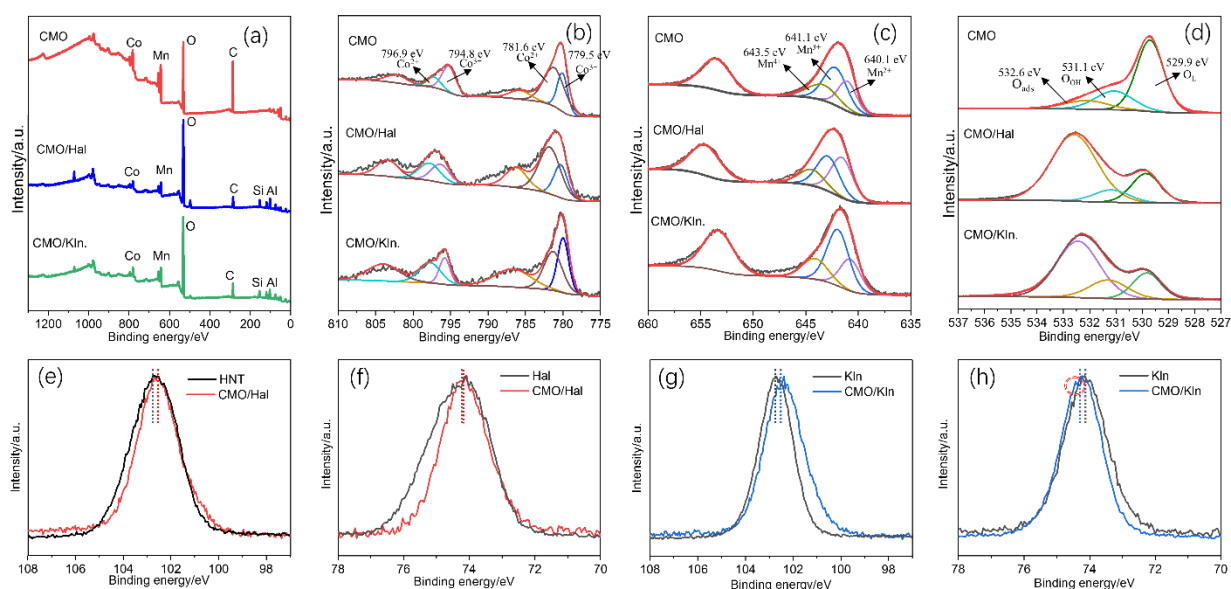


Fig. 4-6 XPS spectra of survey (a), Co 2p (b), Mn 2p (c), and O 1s (d) for bare CMO, CMO/Hal and CMO/Kln; Si 2p (e) and Al 2p (f) for CMO/Hal and raw Hal; and Si 2p (g) and Al 2p (h) for CMO/Kln and raw Kln.

4.2.4 Texture and pore structure of the catalysts

The N₂ adsorption-desorption isotherms and pore size distribution of all the samples are characteristic of IV type with typical H₃ hysteresis loop (Fig. 4-7). This indicates the dominance of mesoporous structure in these catalysts, which is beneficial for the uniform dispersion of CMO particles.

As for the *x*-CMO/Hal series, 40-CMO/Hal possesses the largest specific surface area (SSA) and the maximum pore volume, revealing the uniform distribution of CMO particles on Hal. This helps to enlarge the contact area of the catalyst and provides more reaction sites. But significant decrease of SSA appears at 60-CMO/Hal, probably related to the severe accumulation of the CMO nanoparticles on Hal, as illustrated by FESEM and HRTEM (Figs. 4-2 and 4-3). Yuan et.al reported that Hal revealed two primary populations in the pore size distribution, corresponding to the peaks at 3.4 and 11.2 nm, which are the spaces between particles in bundles or lumen with partially closed openings, and the lumen of Hal, respectively (Yuan et al., 2012). For *x*-CMO/Hal, with the increase of CMO content, the pore volume centered at 3.4 nm decreases, suggesting the gradual fulfillment of CMO in the spaces among Hal. But the volume of pores at 11.2 nm increases with the rising of *x*. This might be ascribed to the partial blockage by CMO particles entering the cavity, as HRTEM observation (Fig. 4-3).

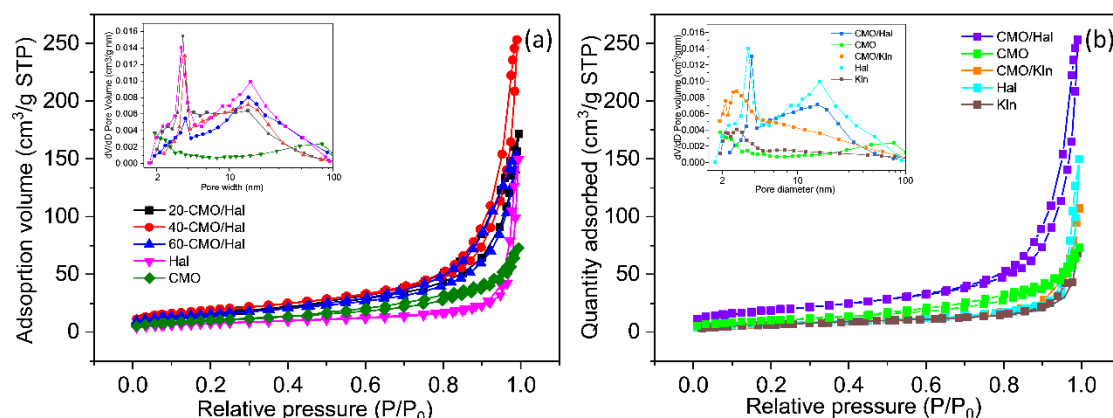


Fig. 4-7 N₂ adsorption and desorption isotherms, and BJH pore size distribution plots of (a) bare CMO, Hal, and *x*-CMO/Hal series, and (b) bare CMO, CMO/Hal, CMO/Kln and raw clay minerals.

The shape of CMO/Hal and CMO/Kln in Fig. 4-7 (b) showed little differences from bare Hal and Kln; thus the impact of CMO loading on porosity is almost neglectable (Iatalese et al., 2019). But the SSA of CMO/Kln and CMO/Hal were higher than bare CMO and their corresponding matrices (Table 4-1), with a slightly reduced pore volume. This would possibly be advantageous for the adsorption and enrichment of contaminants in the degradation.

Table 4-1 Specific surface area and pore volume of the catalysts and raw materials

	CMO	20- CMO/Hal	(40-) CMO/Hal	60- CMO/Hal	(40-) CMO/Kln	Hal	Kln
^a SSA/m ² g ⁻¹	26	60	66	53	28	58	27
^b Pore volume (cm ³ g ⁻¹)	0.18	0.35	0.38	0.24	0.11	0.32	0.15

^a Specific surface area obtained by BET method at P/P₀ 0.05–0.25.

^bTotal pore volume calculated from P/P_0 at 0.99.

4.2.5. Defects and oxygen vacancies

EPR was performed to analyze the formation of OV_s in the structures of bare CMO, CMO/KIn and CMO/Hal (Fig. 4-8). The obtained spectra exhibited single characteristic signal, indicating the existence of individual defect. The calculated g-factors were close to 2.008, well corresponding to the electrons trapped in OV_s (Kang et al., 2021). Based on the intensities and integral areas of EPR signals, CMO/Hal has higher content of OV_s, followed by CMO/KIn and CMO. This is consistent with their variation of $(\text{Mn}^{2+}+\text{Mn}^{3+})/\text{Mn}^{4+}$, in light of the fact that higher percentage of Mn cations with lower valence facilitates the formation of more OV (Kim and Shim, 2010). Thus, the presence of clay substrates create more OV_s.

The abundant hydroxyl groups on the surface of Hal and KIn played important roles in the induction and modification of OV_s within the composite catalysts, as they showed Lewis acidity/basicity with high activity (Zhu, Chengzhang et al., 2020). During the co-precipitation and calcination fabrication processes, hydrated CMO clusters could be strongly bonded to the hydroxyl surface of the minerals through surface hydrogen bonding, charge transfer and proton diffusion between neighboring hydroxyls. Then, partial dehydration between CMO and mineral substrates occurred during the calcination, leading to the generation of OV_s (Li, X. et al., 2020).

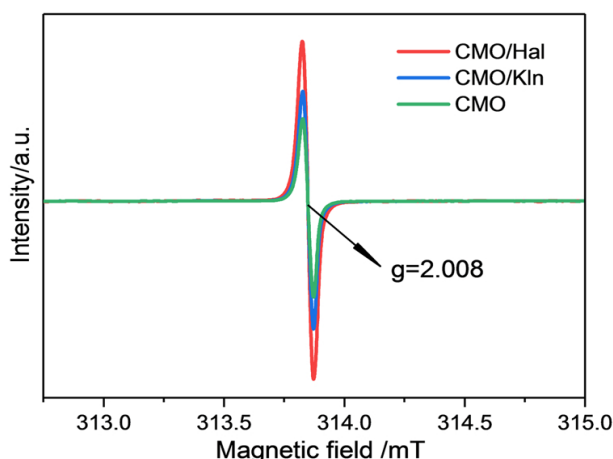


Fig. 4-8 EPR spectra of bare CMO, CMO/Hal and CMO/KIn.

Similar phenomena were also reported by other studies. For example, the content of OV_s in Co₃O₄/KIn composite was significantly higher than bare Co₃O₄, from DFT calculation, the formation energy of OV_s was much higher within bare Co₃O₄ than those on KIn (Zhao, Q. et al., 2019). Moreover, OV_s showed lower formation energy at O sites surrounded by Si atoms than those with Al atoms (Chokawa et al., 2020). This accounts for the higher content of OV_s of CMO/Hal than CMO/KIn, since Hal only had Si-O bond exposed, while KIn exposed Si-O and Al-O half each, turning the formation of OV_s more difficult. Furthermore, the significantly higher crystallinity of CMO/KIn than CMO/Hal also resulted in its insufficient OV_s content, as increasing crystallinity would retard the formation of OV_s (Guan et al., 2019). Therefore, the introducing of Hal and KIn matrices was applicable in providing a new alternative to enhance the generation of OV_s on CMO catalysts, and Hal with more Si-O exposure showed superior improvement than KIn.

4.2.6. Point of zero charge (pHpzc) of the catalysts

The pzc of the catalysts were determined through the measurement of zeta-potential

within the pH range of 3-10 using a zetasizer (Malvern) based on the Smoluchowski equation. The pH of the solution which contained a reasonable amount of catalysts was adjusted by NaOH and H₂SO₄. The pH_{pzc} value of CMO/Hal and CMO/KIn were determined as around 6.2 and 5.5, separately according to Fig. 4-9.

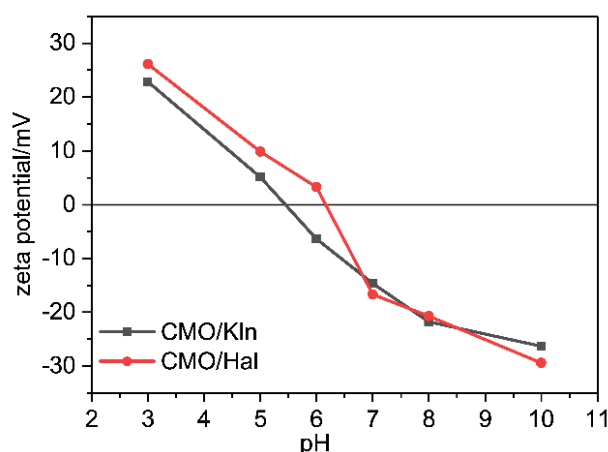


Fig. 4-9 Zeta potential of CMO/KIn and CMO/Hal

4.3 Results and discussion: LCO catalyst

4.3.1 Characterisation of LCO catalyst

Fig. 4-10a shows the XRD pattern of the prepared LCO catalyst. All the characteristic peaks correspond to the cubic LCO perovskite. For example, the characteristic diffraction peaks at $2\theta = 23.2^\circ$, 32.9° , 33.3° , and 47.5° correspond to the hexagonal LCO (JCPDS25-1060). It is clear that except for the lanthanum cobaltate perovskite phase, common oxide impurities, such as Co₃O₄ and La₂O₃, are not formed. The sharp diffraction peak and large peak intensity can be interpreted as good crystallinity of LCO. The mean crystallite size, calculated by the Scherrer equation, is 21 nm.

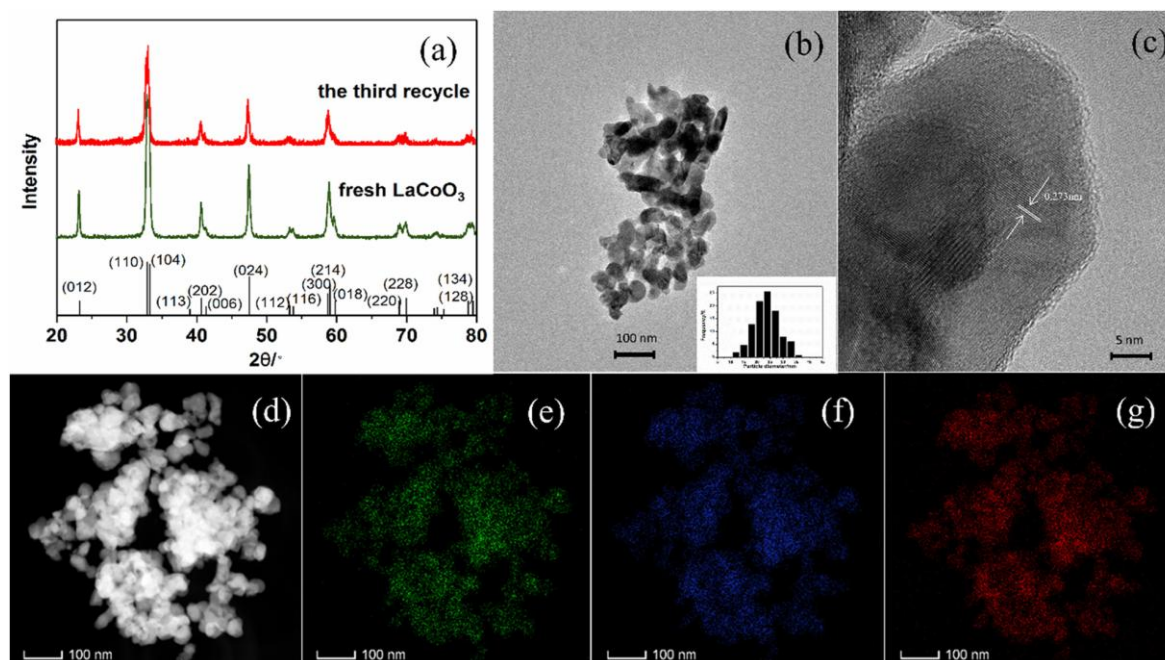


Fig.4-10 (a) XRD patterns of the fresh and reacted LaCoO_3 ; (b–c) HRTEM images of LaCoO_3 particles; (d–g) the EDS mapping of LaCoO_3 (d), La (e), Co (f) and O (g).

The morphology of the synthesised LCO was characterised by HRTEM (Fig. 4-10, b–c). The particle size (27 nm) observed in the TEM image was larger than the crystal size (21 nm), which indicates possible agglomeration. The HRTEM image shows the single-crystal nature of the LaCoO_3 perovskite. The interplanar spacing is approximately 2.73 Å, corresponding to the hexagonal LaCoO_3 (110) crystal plane.

From the EDS analysis (Fig. 4-10, d–g), it is clear that the principal components consist only of La, Co, and O, which are dispersed evenly. In addition, the molar ratio of La to Co was 1. All the above analyses indicate that the valence of cobalt ions in LCO is +3.

The chemical states of LCO as well as the surface element composition were verified by XPS (Fig. 4-11). In case of Co, the binding energies of LCO are 779.8 and 795.0 eV, corresponding to the $2p_{3/2}$ and $2p_{1/2}$ orbits of Co^{3+} , respectively (Zhu, C. et al., 2020). The difference in the orbital binding energy between $2p_{3/2}$ and $2p_{1/2}$ of Co^{3+} is 15.2

eV. In addition, the satellite peak that appears at 790 eV confirms that the cobalt ion in the LCO exists in the form of +3 valence (Zhu, C. et al., 2020). In addition, since the oxygen species on the catalyst surface has an important effect on the catalytic oxidation performance, it is necessary to analyse the O 1s spectrum. The binding energies at 528.6, 531.1 and 533.1 eV correspond to lattice oxygen, surface adsorbed oxygen (O_{ads} , O^- , or O^{2-}), and molecular water adsorbed on the catalyst surface, respectively (Lu et al., 2018; Merino et al., 2006). Both O^- and O^{2-} species are strongly electrophilic species, which can attack the target compound, especially at locations with high electron density in the molecule. They can destroy the carbon skeleton, and subsequently, the compound or its fragments can be further oxidized via heterogeneous oxidation at the catalyst surface, to generate carbon dioxide and water.

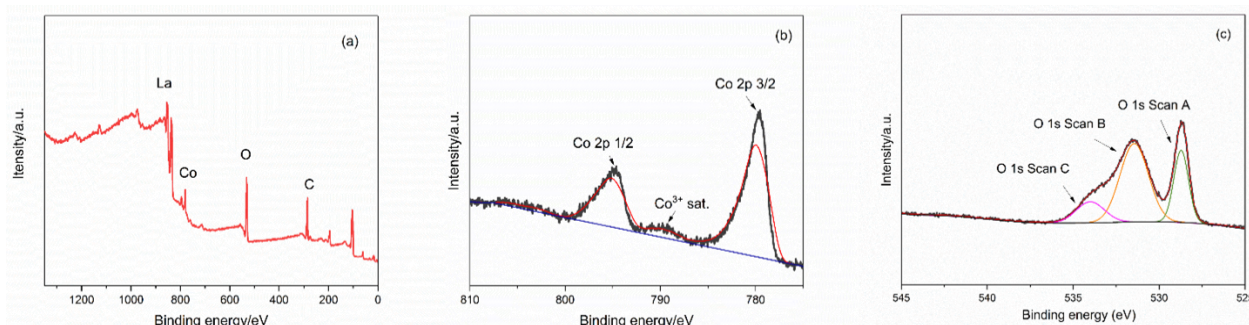


Fig. 4-11 XPS spectra of LCO (a) a full range scan of the samples; (b) Co 2p core level; (c) O 1s core level

4.4 Summary

In this chapter, the characterizations of the obtained CMO based catalysts, *i.e.*, morphology, crystal structure, surface chemical properties and structural defects, were revealed in detail separately. The morphology results provided mainly by SEM and HRTEM images implied that the loading of CMO nanoparticles posed negligible effects

on the structure and shape of either Hal or KIn. The presence of Hal and KIn substrates was beneficial in: 1) regulating the grain size and crystallinity of CMO particles, and 2) promoting the specific surface area by the evenly distribution of CMO particles. This was probably caused by the suppressed long-range ordering in unidirectional crystallization of CMO nanoparticles. The smaller particle size with reduced crystallinity also helped to provide more reactive sites by forming into several indistinct lattice boundaries. Furthermore, the presence of Hal and KIn also helped to induce more oxygen vacancies (OVs) within the composite catalysts, which might promote their catalytic activity by providing more active sites or accelerating electron transfer.

Chapter 5 Removal of carbamazepine using PMS activated by α -CMO/Hal

5.1 Introduction

Carbamazepine (CBZ) is an antiepileptic drug which is widely used for the treatment of psychomotor and grand mal seizures induced by epilepsy and bipolar disorders due to its efficacy and acceptable safety profile (Harkin and Hopkinson, 2010; Zhou et al., 2010). Due to its high use all over the world and an extremely half-life (82 ± 11 days) in the environment, CBZ has been frequently detected in various water matrixes including surface water, wastewater, and seawater in countries located in Asia, America, and Europe (Brandão et al., 2013; Wang and Zhou, 2016). What makes the situation worse is that CBZ of high persistence and can hardly be removed by traditional wastewater treatment plants, and a higher CBZ concentration was even detected in the effluent of a sewage treatment plant (STP) than that in its influent (Zhou et al., 2010). Furthermore, CBZ in aqueous environment can be accumulated through food chain by ingestion, which can in turn lead to some unexpected ecological and evolutionary modifications towards organism behavior, or even interfere the aquatic community compositions (Brodin et al., 2013; Shenker et al., 2011). It was reported that the exposure of zebrafish embryos to environmentally relevant concentrations ($1-5 \text{ } \mu\text{g L}^{-1}$) of CBZ could accelerate its embryonic development, cause impaired expression of important neuron developmental genes, and further disturb the behaviors of the larvae (Qiang et al., 2016).

The removal and decomposition of CBZ from aqueous environment has received great

concern and a large number of different attempts have been performed to alleviate its impact. In this chapter, the *x*-CMO/Hal catalysts with different CMO content obtained before was adopted as PMS activator for the removal of CBZ from water, and the one with the best degradation performance was chosen for detailed studies later. The effects of working parameters including the concentration of CBZ and PMS, and the initial working pH towards the degradation of CBZ were investigated thoroughly. The possible intermediates generated during the decomposition of CBZ were provided based on the LC-MS results and the mineralization of CBZ was determined using TOC tests. The potential PMS activation mechanism was proposed based on the results of traditional trapping experiments and EPR results. Finally, the reusability and stability of the chosen catalyst was investigated through recycle experiments, ICP tests and XRD results.

5.2 Results and discussion

5.2.1 Catalytic performance of the *x*-CMO/Hal series

Before the degradation, the adsorption ability of bare CMO, Hal, and *x*-CMO/Hal catalysts was tested towards CBZ for 30 min at pH 5.8 (Fig. 5-1). Among them, 20-CMO/Hal and 40-CMO/Hal exhibited the highest adsorption ability at 6.2% and 6.7%, respectively; followed by Hal, 60-CMO/Hal and CMO. Such different adsorption performances should be ascribe to the difference in specific surface area. This also indicates that the contribution of adsorption on the removal of CBZ is quite low.

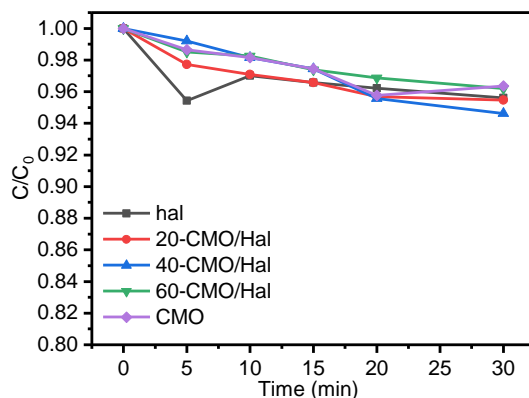


Fig. 5-1 Adsorption kinetics of CBZ by bare CMO, HNT and x -CMO/HNT series

General working conditions: [CBZ]= 21.16 μ M, [PMS]= 0.1 mM, [catalyst]= 200mg L⁻¹, pH=5.8.

After the addition of PMS into Hal suspension, the removal of CBZ did not change obviously (Fig. 5-2a). But the mixture of PMS with x -CMO/Hal resulted in a fast degradation of more than 80% of CBZ within 20 min. This reveals that CMO acted as the main active ingredient of x -CMO/Hal possessing effective PMS activation ability. All the degradation well followed the pseudo first-order kinetics (Fig. 5-2b, $R^2 > 0.97$).

$$-\ln(C/C_0) = k_{\text{obs}}t \quad (5-1)$$

where C_0 and C are the concentration of CBZ at the initial time and instant t , μ M, and k_{obs} is the kinetic rate of constant, min⁻¹.

The reaction rate constant (k_{obs} , min⁻¹) could be determined from Eq. (5-1). It's not surprise that the fastest decay was observed with bare CMO ($k_{\text{obs}}=0.174$ min⁻¹) without using supporting carrier. Among the synthetic catalysts, 40-CMO/Hal ($k_{\text{obs}}=0.168$ min⁻¹) exhibits the next highest catalytic performance than the others, and is almost

comparable to the bare CMO. 60-CMO/Hal with the high CMO loading exhibited a relatively poor catalytic activity ($k_{\text{obs}}=0.097 \text{ min}^{-1}$). Based on the FESEM and HRTEM (Figs. 4-2 and 4-3), this is probably ascribed to serious clustered morphology by the over loading of CMO, which decreases the active sites.

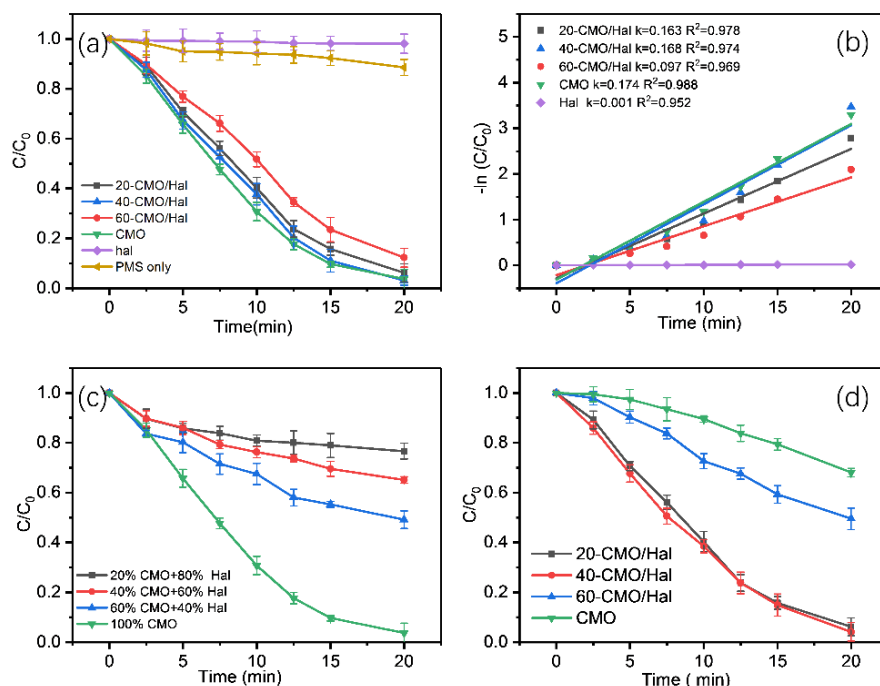


Fig. 5-2 CBZ degradation performances with: (a-b) CMO, Hal, x -CMO/Hal series and their corresponding pseudo first order kinetic curves, (c) combination of CMO and Hal, and (d) CMO equivalent conditions. ($[20\text{-CMO}/\text{Hal}] = 400 \text{ mg L}^{-1}$, $[40\text{-CMO}/\text{Hal}] = 200 \text{ mg L}^{-1}$, $[60\text{-CMO}/\text{Hal}] = 133 \text{ mg L}^{-1}$, $[\text{CMO}] = 80 \text{ mg L}^{-1}$).

General working conditions: $[\text{CBZ}] = 21.16 \text{ }\mu\text{M}$, $[\text{PMS}] = 0.1 \text{ mM}$, $[\text{catalyst}] = 200 \text{ mg L}^{-1}$, $\text{pH} = 5.8$.

Since x -CMO/Hal was a composite, it will be interesting to distinguish the contribution of Hal and CMO on CBZ removal. Comparing with the x -CMO/Hal (Fig. 5-2a), significant decrease in the removal efficiency was observed with the physically mixed (i.e. no chemical bonding) of same dosage of CMO and Hal, though the removal was

gradually enhanced with the increase of CMO dosage (Fig. 5-2c). This infers that strong catalytic activity of x -CMO/Hal is originated from the interaction between CMO and Hal.

When the activity of catalysts was compared in Fig. 5-2a, the dosage of bare CMO and x -CMO/Hal was the same. Thus, the superior performance of bare CMO is largely attributed to its high purity, i.e., the 100% of active ingredient without any carrier. Thus, another series of experiments was carried out with the addition of equivalent CMO. At this time, the dosage of bare CMO and x -CMO/Hal was determined separately by the equivalent weight of CMO ingredient (Fig. 5-2d). Under these circumstances, the obvious gap in the degradation performances can be seen among different catalysts. The removal of CBZ using bare CMO decreased significantly comparing to those of the rest catalysts, with only about 30% of CBZ removed by bare CMO. However, the performance of 40-CMO/Hal and 20-CMO/Hal was comparable, with the capability to completely remove CBZ. This is probably related to their larger volume (and/or surface) of 20-CMO/Hal and 40-CMO/Hal, which significantly improved the contacts among the catalyst, PMS, and CBZ.

The retarded reaction efficiency of 60-CMO/Hal was observed again, which could be attributed to the aggregates with larger grain size, and seriously clustered CMO particles piled on Hal. Therefore, the active sites on the catalysts would be blocked. The above results further illustrated that the activity of CMO for PMS activation could be enhanced significantly through their anchoring on Hal carriers. The Hal is able to control the grain size, suppress the unidirectional crystallization, and promote the evenly dispersion of CMO with an enlarged specific surface area and pore volume,

which helps to enhance the exposure of more reactive sites.

The intermediates and transformation products during the degradation of CBZ was monitored by LC-MS analysis as indicated by Fig. 5-3. Based on the m/z of the results, three different degradation pathways of CBZ were proposed with about ten intermediates detected. The main processes included were oxidation, hydrolysis and the cleavage of rings. At first, the oxidation of CBZ led to the formation of the two intermediates, among which P1 might result from the attack of $O_2^{\cdot-}$ and P2 was more likely to be associated with OH^{\cdot} . The further hydrolysis and ring cleavage on the heterocyclic ring of CBZ led to the formation of P4 and P5 separately. Then P7 could be formed from both P4 and P5 by ring contraction reaction, turning the heptagonal ring into the hexagonal one, then further generated other fragments with losses of groups like amino and carbonyl, resulting in the gradual decrease of molecular mass. The formation of P3 was due to the direct cleavage of the heterocyclic ring of P1, leading to the further formation of P6 through intermolecular reaction by the recombination of amino and carbonyl. The above intermediates would still undergo the processes mainly ring cleavage with the attack of ROSs, generating some short chain organics like propionic and fumaric acid. Based on the TOC test illustrated in Fig. 5-4, the mineralization of CBZ could achieve to about 60% under the PMS/catalyst system activated by either CMO or 40-CMO/Hal, which meant, most of the organics within the degradation process was able to turn into inorganics like CO_2 and H_2O . Therefore, it was feasible to infer that the majority of the short chain organics generated at the later stage of CBZ degradation could be mineralized completely.

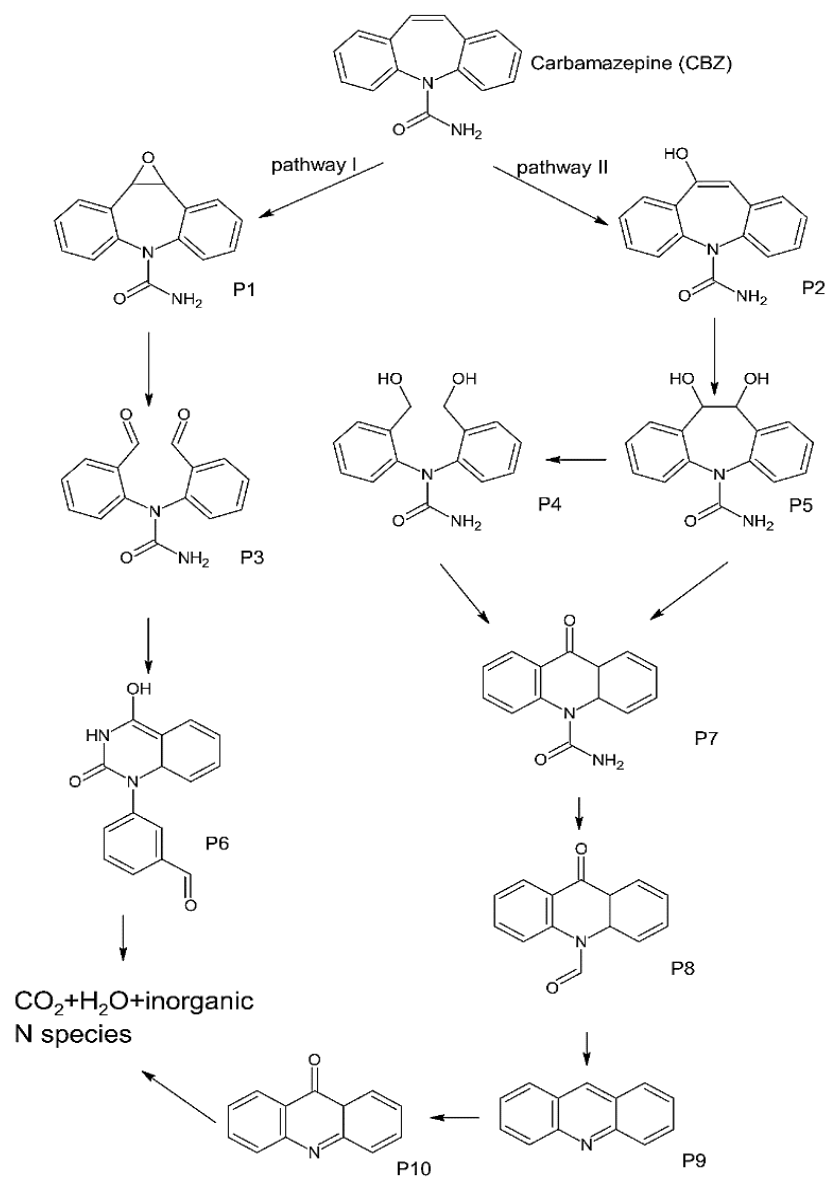


Fig. 5-3 Intermediates and potential degradation pathway of CBZ in PMS oxidation process activated by 40-CMO/Hal

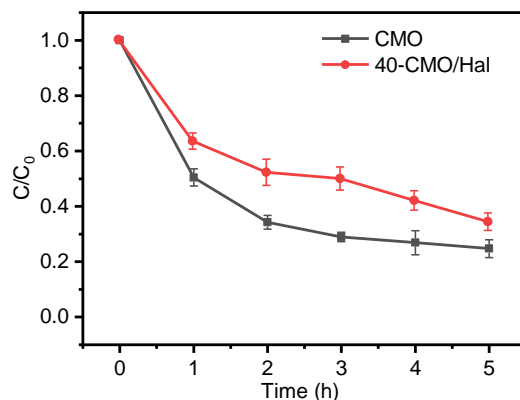


Fig. 5-4 Removal of total organic carbon (TOC) using PMS activated by 40-CMO/Hal and bare CMO

5.2.2 Effects of working parameters towards CBZ degradation

5.2.2.1 Effect of PMS dosage

It was obvious that the removal efficiency of organic compounds within the catalytic degradation was largely depended on the concentrations of PMS and the compound itself. The catalytic performances of 40-CMO/Hal improved gradually with the increasing of PMS concentration within the range of 0.05 to 1.0 mM, as indicated by Fig. 5-5a, as the removal of CBZ rose from about 60% to almost 100%. However, when the dosage of PMS was raised to more than 1.5 mM, the removal of CBZ was slightly retarded than using 1.0 mM PMS, and the situation went even worse when PMS dosage rose again to 2.5 mM, as only 90% of CBZ could be degraded. This phenomenon could be explained by the scavenging effect from HSO_5^- to the generated $\text{SO}_4^{\cdot-}$, as overdosed HSO_5^- would compete with CBZ for $\text{SO}_4^{\cdot-}$. Since more than 70% of CBZ initiated at 63.48 μM could still be removed by 0.1 mM PMS activated by 40-CMO/Hal, the PMS dosage was finally determined as 0.1mM, under which CBZ could be removed

sufficiently with the maximized utilization of PMS. The retarded catalytic performance with the increasing of CBZ, as illustrated by Fig. 5-5b, could be explained easily by the restricted amount of ROSs generated from PMS and the limited active sites on the catalysts.

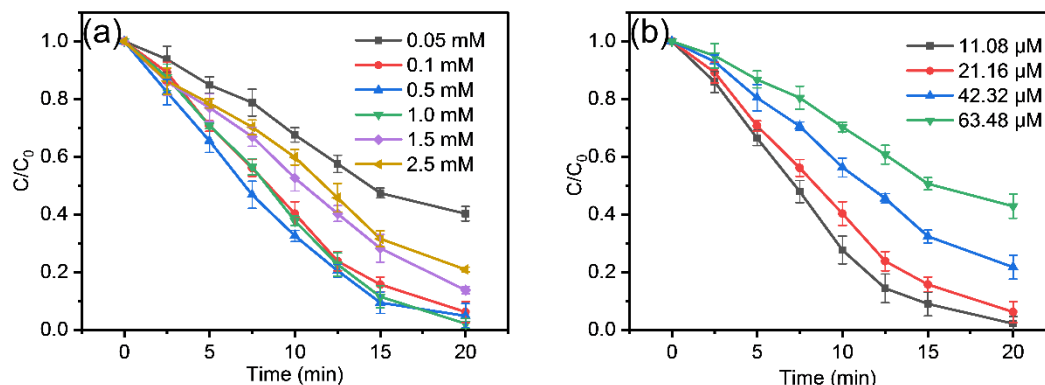


Fig. 5-5 Effects of (a) PMS concentration, and (b) CBZ concentration on the degradation of CBZ using PMS activated by 40-CMO/Hal.

General working conditions: [CBZ]= 21.16 μM , [PMS]= 0.1 mM, [catalyst]= 200 mg L⁻¹, pH=5.8.

5.2.2.2 Effect of pH on the catalytic degradation

The working pH played an important role in the heterogeneous catalytic performance of the catalyst/PMS system since it might interfere PMS decomposition and the transformation of organic compounds (Ren et al., 2021). The pH of the working solution was adjusted by H₂SO₄ and NaOH. Fig. 5-6 revealed that the highest degradation efficiency of CBZ using 40-CMO/Hal appeared at pH=5.8, a weakly acidic environment. Inhibitions were found when the working pH was strongly acidic or basic, while the removal of CBZ was still effective at a near neutral pH (pH=7.5).

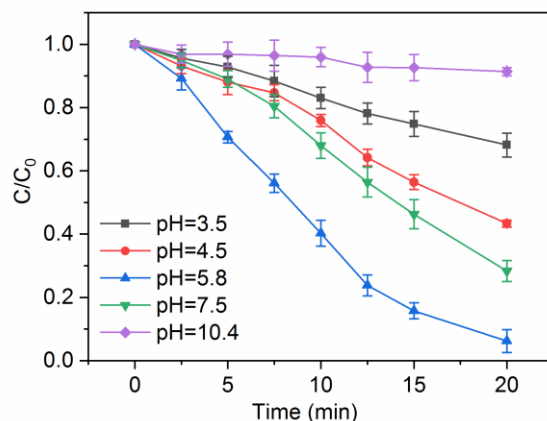
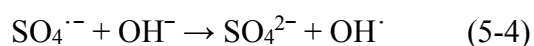
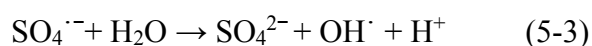
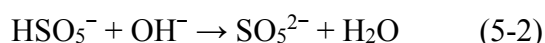


Fig. 5-6 Effect of initial working pH on CBZ degradation using PMS activated by 40-CMO/Hal

The degradation performance of AOPs was closely related to the generation of ROSs like OH^\cdot and $\text{SO}_4^{\cdot-}$, which was seriously affected by working pH. The $\text{pK}_{\text{a}1}$ and $\text{pK}_{\text{a}2}$ of PMS were <0 and 9.4, separately, indicating that HSO_5^- was the dominant existing form within the pH range of 0 and 9.4, and SO_5^{2-} with less catalytic activity at pH over 9.4 (Dong et al., 2019; Zhu, M.-P. et al., 2020). Under strong acidic pH circumstance like pH=3.5, $\text{SO}_4^{\cdot-}$ might be scavenged by H^+ , leading to the retardation of CBZ degradation. When the working pH was over 10, the main existing form of PMS was expected to transform from HSO_5^- to SO_5^{2-} (Eq. (5-2)) (Dong et al., 2019). At the same time, massive OH^\cdot would be generated from $\text{SO}_4^{\cdot-}$ and played the dominant role instead of $\text{SO}_4^{\cdot-}$ in the removal of CBZ, as indicated by Eqs. (5-3)-(5-4). However, the oxidation capacity of OH^\cdot was much weaker than $\text{SO}_4^{\cdot-}$, which also interfered the degradation efficiency (Li, J. et al., 2018).



Except for the two pK_a s of PMS, the point of zero charge (pHpzc) of the catalysts and the existing form of CBZ also had an impact on the degradation efficiency. The pHpzc of 40-CMO/Hal was at around 6.5, as indicated in Fig. 4-9. The pK_a of CBZ (13.1) and PMS ($pK_{a1} < 0$, $pK_{a2} = 9.4$) implied that CBZ and PMS both carried negative charge within the pH range 3-10. When the working pH was 5.8, the positive surface charge of the catalyst accelerated its contact efficiency with HSO_5^- , therefore promoting the decomposition of PMS and generating ROS sufficiently. When working pH rose to 7.5, a little over than the pHpzc of the catalyst, although both the catalyst and HSO_5^- carried negative charge, the mutual repulsion between them was much lower comparing to other higher working pHs. Thus, 80% of CBZ could still be degraded under this situation.

In general, the optimum pH for the degradation of CBZ under the combination of PMS and 40-CMO/Hal catalysts was from weak acidic to neutral, which was close to the pHpzc of the catalyst and could help to keep the stability of HSO_5^- .

5.2.3 Change of pH and residue PMS concentration during CBZ degradation

Furthermore, the change of solution pH during the removal of CBZ was also measured (Fig. 5-7a). Except for pH=10.4, the initial pH of the rest ones dropped slightly at different extent in the first 5 min, which might be caused by the hydrolysis of PMS and the generation of low molecular organic acids as the intermediates/end products (Yin et al., 2021). This was further confirmed by monitoring the residue PMS through the

whole reaction, as its concentration dropped dramatically in the first 10 minutes and then followed by a tailing to the end (Fig. 5-7b). The generation process of OH^\cdot by 40-CMO/Hal, bare CMO and bare CMO with equivalent weight of 40-CMO/Hal was provided in Fig. 5-7c. It was clear that the OH^\cdot generated in the reaction by the two catalysts at same dosage (200 mg L^{-1}) showed unobvious differences at the end of the degradation but with a gradually slowed-down trend. However, when the dosage of bare CMO was equivalent with that in 40-CMO/Hal (40% for 200 mg L^{-1} , which was 80 mg L^{-1}), OH^\cdot generation efficiency was significantly lowered, which partly accounted for its insufficient working performance. The above results revealed that 40-CMO/Hal maintained comparative OH^\cdot generation ability with bare CMO but it only needed 40% of metal during synthesis than its rival.

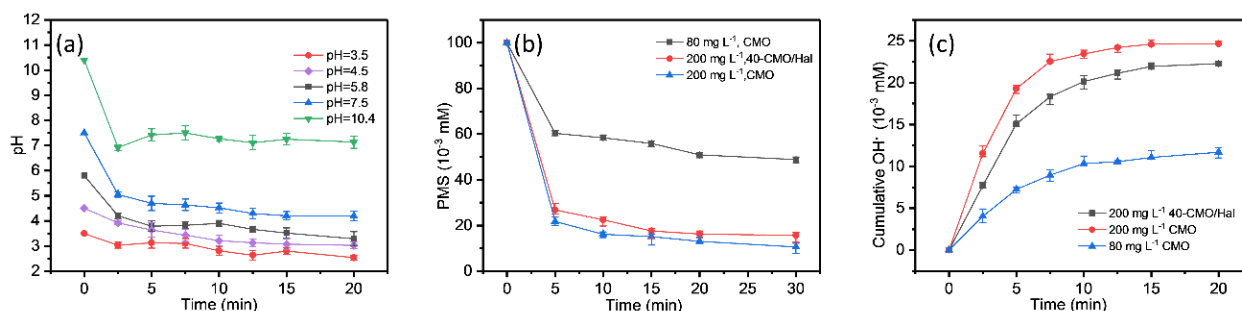


Fig. 5-7 Change of solution pH during CBZ degradation (a), residue PMS with different catalysts analyzed by spectrophotometric method (b), and OH^\cdot accumulation during CBZ degradation using different catalysts.

5.3 Reactive oxygen species and activation mechanism of PMS

The contributions of reactive oxygen species (ROS) were determined by traditional

trapping experiments with MeOH, TBA, NaN₃ and BZQ as scavengers. The reaction rate constants of them towards the specific ROS were provided in Table 5-1.

Table 5-1 Summary of the scavengers and their target ROSs

Scavenger	Target ROSs	Reaction rate / k _{obs}	References
Tert-butyl alcohol (TBA)	OH [·]	k _{OH[·]} = (3.8–7.6) × 10 ⁸ M ⁻¹ · s ⁻¹	(Dong et al., 2021)
Methanol (MeOH)	OH [·] , SO ₄ ^{·-}	k _{OH[·]} = (1.2–2.8) × 10 ⁹ M ⁻¹ · s ⁻¹ k _{SO₄^{·-}} = (1.6–7.7) × 10 ⁷ M ⁻¹ · s ⁻¹	(Dong et al., 2021)
Sodium azide (NaN ₃)	¹ O ₂	k = 2.2 × 10 ⁹ M ⁻¹ · s ⁻¹	(Basu-Modak and Tyrrell, 1993)
1,4-Benzoquinone (BZQ)	O ₂ ^{·-}	k = 2.9 × 10 ⁹ M ⁻¹ · s ⁻¹	(Duan et al., 2020)

The addition of MeOH and BZQ inhibited the degradation process almost completely, but those from TBA and NaN₃ was somehow alleviated (Fig. 5-8a). This confirmed the formation and participation of SO₄^{·-} and OH[·], and the negligible contribution of ¹O₂ and O₂^{·-} in the removal of CBZ using PMS activated by 40-CMO/Hal.

EPR tests were also performed using DMPO and TEMP as the probe compound to confirm the presence SO₄^{·-}, OH[·], O₂^{·-} and ¹O₂ through the formation of spin adducts including DMPO-SO₄, DMPO-OH, DMPO-OOH and TEMPO. The signal of DMPO-SO₄ or DMPO-OH, four consecutive peaks with relative intensities of 1:2:2:1, could only be captured with the spontaneous existence of 40-CMO/Hal and PMS (Fig. 5-8b)

(Zhang, F. et al., 2020). The situation of $O_2^{\cdot-}$ was similar to $SO_4^{\cdot-}$ and OH^{\cdot} , as the DMPO-OOH signals appeared a few minutes later after the addition of the PMS (Fig. 5-8d). This confirmed the successful activation of PMS by 40-CMO/Hal and revealed the important role of PMS in generating the above three ROSs.

However, contrary to the mentioned three radicals above, the EPR signal of 1O_2 in Fig. 5-8d, a series of three consecutive 1:1:1 peaks, appeared right at the time when PMS was added without any delay ($t=0$ min). This was possibly due to the already existence of 1O_2 's precursor in solution before adding PMS (Lin et al., 2019; Liu et al., 2018). The four EPR signals were still strong after 20 min, indicating that 40-CMO/Hal played a vital role in the continuous and stable production of the ROSs.

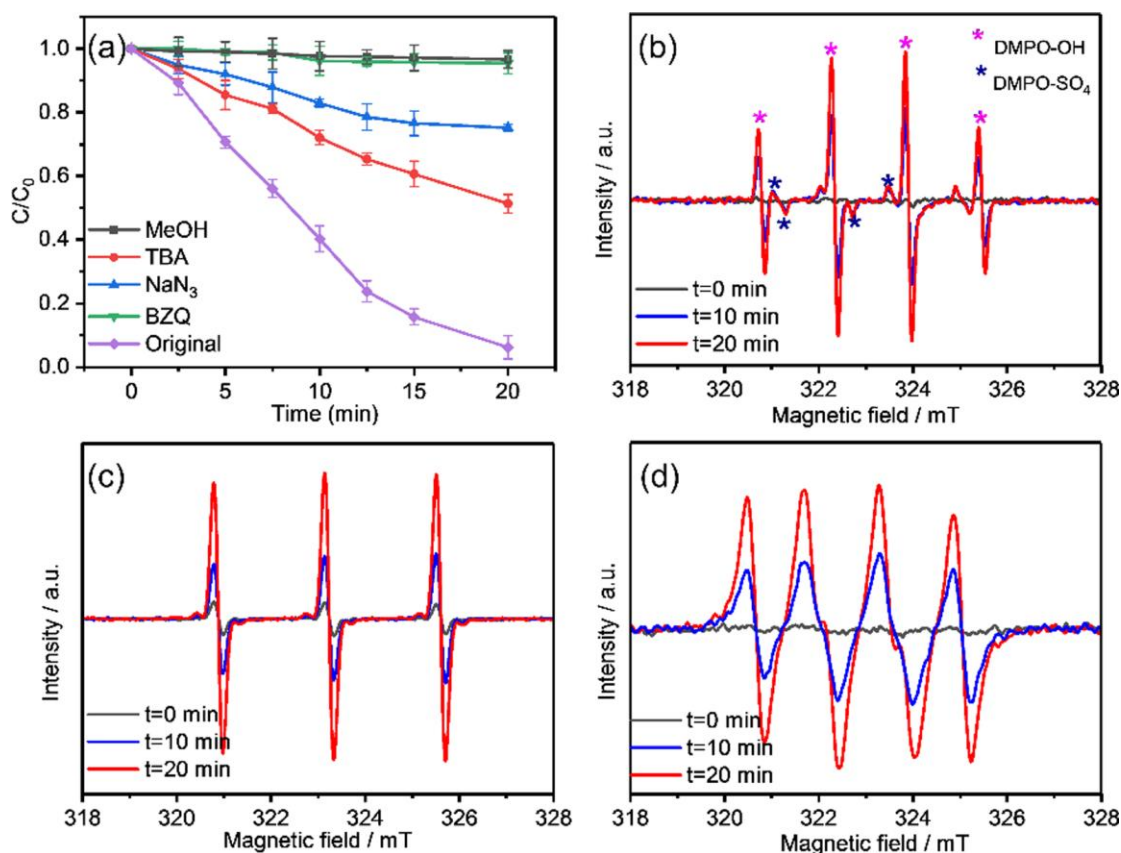


Fig. 5-8 Effect of different scavengers on the degradation of CBZ by 40-CMO/Hal (a). EPR

spectra of: $\text{SO}_4^{\cdot-}$ and OH^\cdot (b), $^1\text{O}_2$ (c), and $\text{O}_2^{\cdot-}$ (d) in the activation of PMS with 40-CMO/Hal. General working conditions: $[\text{CBZ}] = 21.16 \mu\text{M}$, $[\text{PMS}] = 0.1 \text{ mM}$, $[\text{catalyst}] = 200 \text{ mg L}^{-1}$, $\text{pH} = 5.8$.

In order to examine the activation mechanism of PMS, XPS analysis was performed again on the recycled 40-CMO/Hal to explore the chemical changes on its surface. The shift in valence ratios of Co, Mn and O comparing to the fresh ones were briefly illustrated in Fig. 5-9.

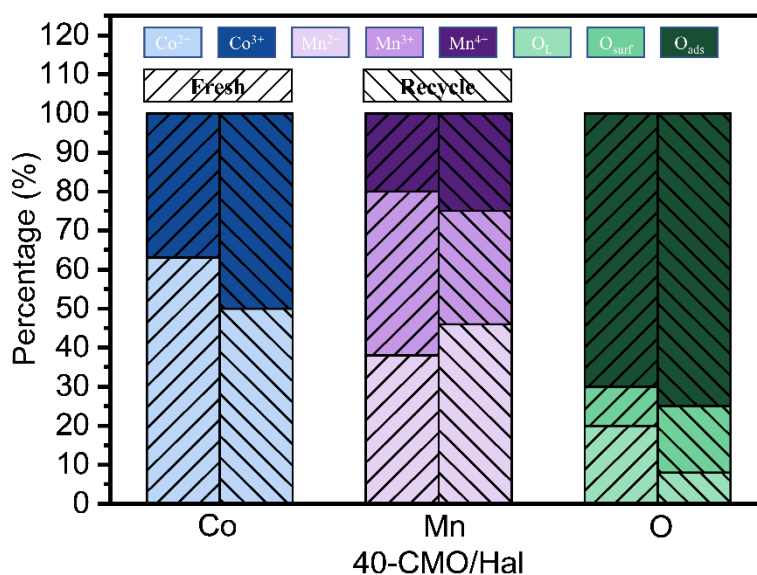


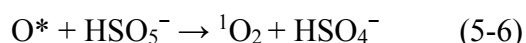
Fig. 5-9 Comparison of Co, Mn, and O between fresh and recycled 40-CMO/Hal examined by XPS spectra

The slight increment of Co^{3+} on the recycled catalysts implied the reduction of HSO_5^- from PMS into $\text{SO}_4^{\cdot-}$ by receiving an electron from Co^{2+} (Yao et al., 2015). Similar alteration was also found in the Mn 2p spectra, especially the obvious reduction of Mn^{3+} , which proved the redox of Mn species during the catalytic degradation. Since the standard reduction potential of $\text{Co}^{2+}/\text{Co}^{3+}$ (1.81V) was higher than $\text{Mn}^{3+}/\text{Mn}^{2+}$ (1.51V)

and $\text{Mn}^{3+}/\text{Mn}^{4+}$ (0.15V), it was thermodynamically favorable for the reduction of Co^{3+} into Co^{2+} by Mn^{2+} and Mn^{3+} (Yao et al., 2015). The continuous redox and regeneration of Mn and Co maintained the steady generation of ROSs and kept charge balance on the surface of the catalyst until PMS was consumed completely (Ren et al., 2015).

The significant reduction of O_L in O 1s spectra also indicated its high catalytic activity and participation in the degradation processes. This might help to explain the early occurrence of $^1\text{O}_2$, since several researches implied the contribution of O_L during the formation of $^1\text{O}_2$ (Li, Chenxu et al., 2019; Liu et al., 2018).

To achieve the equilibrium of the reaction, 40-CMO/Hal were added into CBZ solution 15 minutes before the addition of PMS, during which the releasing and transferring of O_L into active oxygen species (O^*) on its surface could happen (Eq. (5-5)). When PMS was added into the solution, the O^* would convert into $^1\text{O}_2$ with little delay (Eq. (5-6)) (Wang, J. et al., 2020). This explains the earlier appearance of its EPR signal than other ROSs as discussed earlier.



Except for PMS and O_L , $^1\text{O}_2$ could also come from: 1) dissolved oxygen (DO) in solution, 2) the reaction between $\text{OH}^\cdot/\text{H}_2\text{O}$ and $\text{O}_2^{\cdot-}$ (Hu et al., 2018; Zhu, C. et al., 2020). The hypothesis of DO could be verified directly by purging O_2 from solution with N_2 gas (Fig. 5-10). The performance of CMO was retarded slightly, but serious inhibition was found in 40-CMO/Hal, as less than 40% of CBZ could be removed in 20 min. The reversed phenomenon of CMO and 40-CMO/Hal seemed closely related to

the content of CMO. Afterwards, the seriously retarded catalytic performance with the addition of NaN_3 , and the characteristic 1:1:1 EPR signal of $^1\text{O}_2$ detected under N_2 purging, further revealed the participation and generation of $^1\text{O}_2$ under anaerobic environment (Fig. 5-11). Thus, it is reasonable to infer that the generation of $^1\text{O}_2$ via DO pathway is minor.

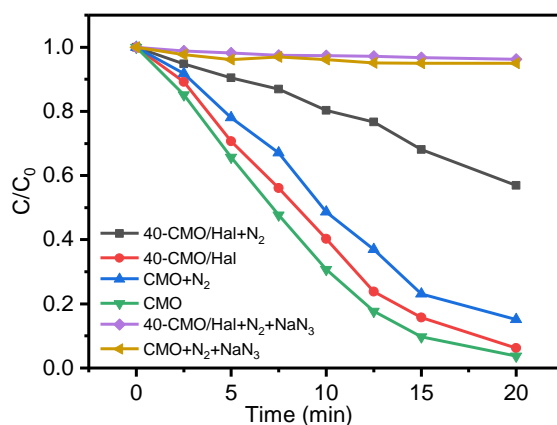


Fig. 5-10 Degradation of CBZ and effect of NaN_3 under N_2 -bubbling in PMS oxidation process activated by bare CMO and 40-CMO/Hal.

General working conditions: $[\text{CBZ}] = 21.16 \mu\text{M}$, $[\text{PMS}] = 0.1 \text{ mM}$, $[\text{catalyst}] = 200 \text{ mg L}^{-1}$, $\text{pH} = 5.8$.

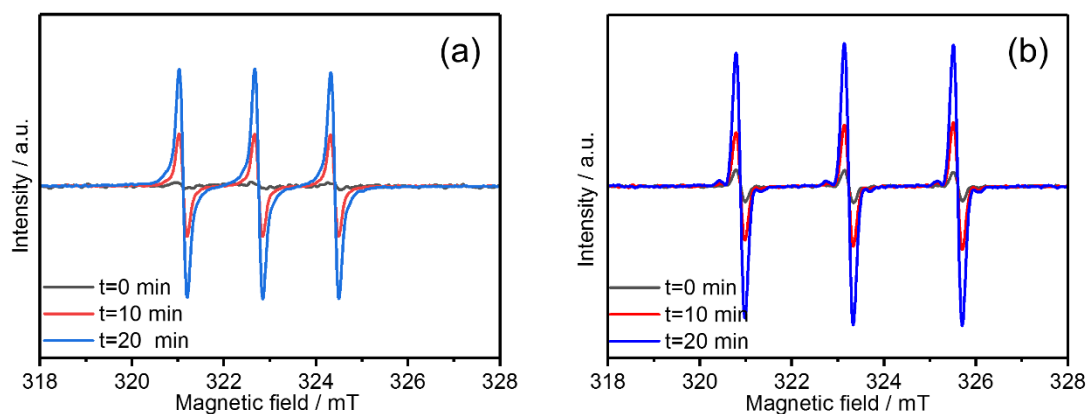


Fig. 5-11 EPR spectra of $^1\text{O}_2$ under N_2 plugging (a), and normal working conditions in the

activation of PMS using 40-CMO/Hal (b).

Except for O_L , the generation of 1O_2 might come from the recombination of $O_2^{\cdot-}$ with OH^{\cdot} as expressed by Eq.(5-7) (Chen, L. et al., 2020).



5.4 Recyclability and stability

The stability of CMO and 40-CMO/Hal catalysts were evaluated in continuous batch usages (Fig. 5-12). A satisfied recyclability of 40-CMO/Hal and CMO was found with 100% to 90% of CBZ removal in three succeeding cycles at 45 min each. The small drops of CBZ removal after each cycle is likely due to the accumulation of yet mineralized intermediates on the active sites (Zhang, S. et al., 2020).

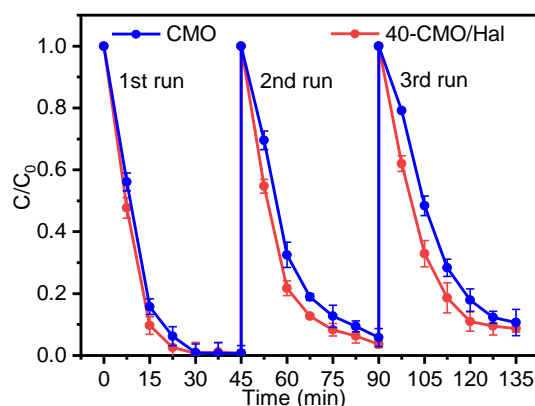


Fig. 5-12 Sustainability and recyclability of the catalysts after three rounds of CBZ degradation.

Working conditions: $[CBZ] = 21.16 \mu M$, $[PMS] = 0.1 \text{ mM}$, $[catalyst] = 200 \text{ mg L}^{-1}$, $pH = 5.8$.

Another important criterion to judge the stability of metal-related catalysts was the leaching extent of metal ions. The leakage of Co and Mn was quantified by ICP-OES

(Table 5-2). Both CMO and 40-CMO/Hal experienced a certain extent of metal leaching, but the latter with Hal carrier showed much lower leaching. It should be noted that same dosage of CMO and 40-CMO/Hal were used in the recycle tests, the latter contains only 40% of CMO to that of the former. However, the metal loss of 40-CMO/Hal is still lower than 40% of bare CMO's leakage (Table 5-2). The results indicated the Hal carrier is capable of reducing metal leaching, minimizing the second contamination from metal leaching, and maintaining the degradation efficiency. Furthermore, the XRD results of the recycled 40-CMO/Hal in Fig. 5-13 showed only slight changes concerning the intensity of CMO part, which might be caused by the unavoidable metal loss during the continuous workings. These revealed that the crystalline structure of 40-CMO/Hal remained generally stable with little deterioration after several times of reusing (Kerber et al., 1998).

Table 5-2 ICP-OES results: the leaching concentration of Co^{2+} and Mn^{2+} from CMO and 40-CMO/Hal during the sustainability tests

Round	CMO		40-CMO/Hal		40% × CMO	
	Co/ppm	Mn/ppm	Co/ppm	Mn/ppm	Co/ppm	Mn/ppm
1	0.237	0.197	0.083	0.072	0.095	0.079
2	0.291	0.260	0.091	0.084	0.116	0.104
3	0.315	0.273	0.102	0.093	0.126	0.109

General working conditions: $[\text{CBZ}] = 21.16 \mu\text{M}$, $[\text{PMS}] = 0.1 \text{ mM}$, $[\text{catalyst}] = 200 \text{ mg L}^{-1}$, $\text{pH} = 5.8$.

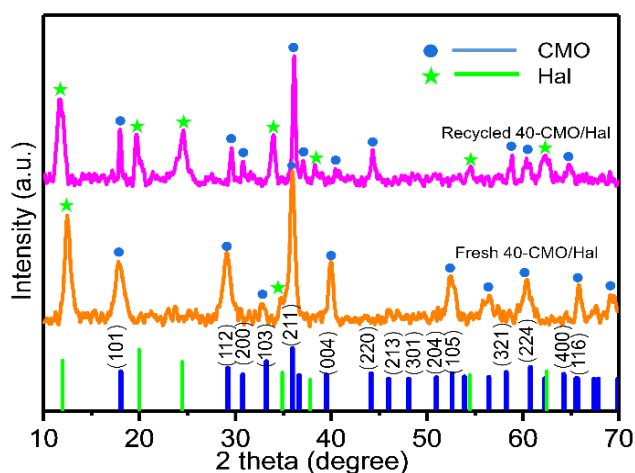


Fig. 5-13 XRD patterns of the fresh and recycled 40-CMO/Hal

The concentration of leached Co and Mn from 40-CMO/Hal after three recycles was still within the limits specified in the Chinese Environmental Quality Standards for Surface Water; *i.e.* less than 1.0 mg L^{-1} and 0.1 mg L^{-1} , separately (China, 2002). This made it advantageous and favorable in practical uses.

Due the dissolution of Co and Mn from CMO and *x*-CMO/Hal, it is interesting to further investigate whether these leached ions would activate PMS in homogeneous mode and help to promote the degradation. These experiments were carried out with Co^{2+} and Mn^{2+} as homogeneous catalysts separately, and the concentrations of them were adopted at the same leakage level from the 3rd round of reuse (*i.e.* 0.1 mg L^{-1} for both). Although the valence of Mn within the catalysts was mainly Mn^{3+} , as indicated by XPS spectra previously, Mn^{3+} was unstable in aqueous environment with pH lower than 9 due to disproportionation reaction (Galán-Mascarós, 2015), and the dissolved Mn from manganese oxides or hydroxides is dominant by Mn^{2+} in solution (Klewicki and Morgan, 1998). Therefore, Mn^{2+} was used for simulation purpose. Fig. 5-14 revealed that Co^{2+} /PMS could remove about 40% of CBZ in 30 min, while Mn^{2+} /PMS posed

little impact on the degradation. This implies that although the leached Co^{2+} from the catalysts was capable of contributing to the catalytic degradation at certain extent (to about 12 %, calculated from the k_{obs} ratio using Co^{2+} and 40-CMO/Hal in Fig. 5-12b), the catalytic ability of homogeneous mode was far less effective than the heterogeneous one. Therefore, heterogeneous 40-CMO/Hal still dominated PMS decomposition.

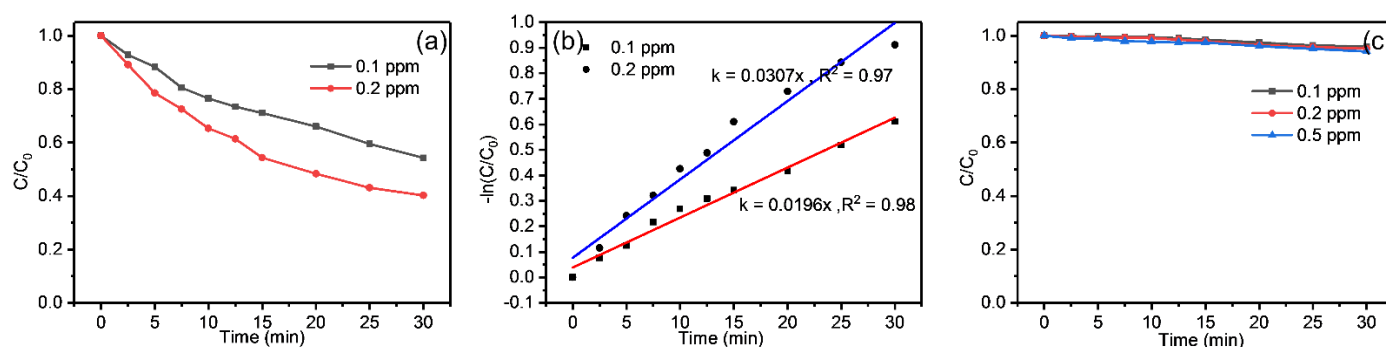


Fig. 5-14 Catalytic degradation of CBZ with homogeneous Co^{2+} and Mn^{2+} (at similar concentrations with the dissolved ions in sustainability tests)

General working conditions: $[\text{CBZ}] = 21.16 \mu\text{M}$, $[\text{PMS}] = 0.1 \text{ mM}$, $\text{pH} = 5.8$.

5.5 Degradation performances towards some other pharmaceuticals

In order to examine the extensive and universal usage of 40-CMO/Hal, the degradation performance of other types of antibiotics were investigated under the same working condition as CBZ. The target antibiotics under different categories, namely tetracycline (TC), sulfamethoxazole (SMZ) and ofloxacin (OFX), were selected; because they are widely used in human and livestock with frequent detection in Asian waters (Ebele et al., 2017; Zhang et al., 2015). The working parameters of the degradation, including molar concentrations of the antibiotics and PMS, and the dosages of 40-CMO/Hal, were

the same as CBZ described before. The experiments were carried out at normal pH (without special adjustment) at 30 min reaction time. The process was found effective in the removal of the mentioned antibiotics, as shown in Fig. 5-15, and the lowest degradation rate was OFX at 65% removal, and the others were all over 90%. This indicates that the ROS generated from PMS activated by 40-CMO/Hal was promising to attack and remove these organics; however, for different target compounds, the process needs to be adjusted by optimizing the reaction parameters.

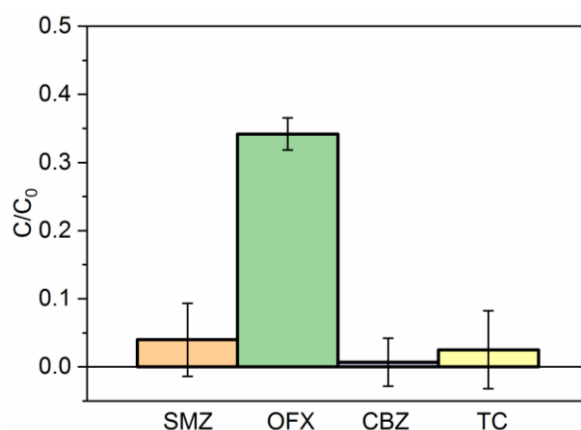


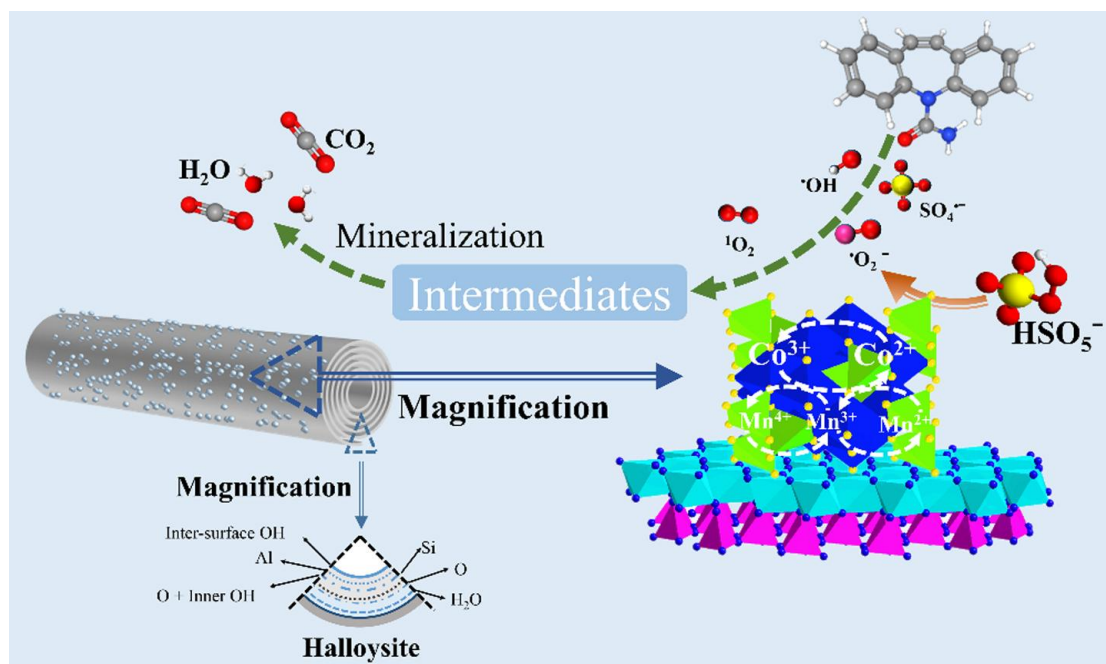
Fig. 5-15 Degradation performance of 40-CMO/Hal towards other pharmaceuticals

General working conditions: [pharmaceuticals]=21.16 μ M, [PMS]= 0.1 mM, [catalyst]= 200mg L⁻¹, pH=5.8.

5.6 Conclusion

In this chapter, a series of *x*-CMO/Hal were fabricated with different CMO content by co-precipitation method to degrade CBZ in water under different working conditions. The characterization results derived from XRD, FESEM, HRTEM and BET demonstrated that the presence of Hal carrier was beneficial in: 1) regulating the grain size and crystallinity of CMO particles, and 2) promoting the specific surface area by

the evenly distribution of CMO particles. The smaller particle size with reduced crystallinity also helped to provide more reactive sites by forming into several indistinct lattice boundaries. Comparing to bare CMO, 40-CMO/Hal was still active in removing more than 90% of CBZ after three reuses with low leakage of metal ions. The main working ROSs determined by traditional trapping experiments and EPR tests were $\text{SO}_4^{\cdot-}$, OH^{\cdot} , $\text{O}_2^{\cdot-}$ and $^1\text{O}_2$. The activation mechanism of PMS by 40-CMO/Hal was revealed by XPS analysis and the generation of $^1\text{O}_2$ was closely related to the lattice oxygen on the catalyst instead of DO. Except for CBZ, 40-CMO/Hal was capable remove the other three frequent detected antibiotics efficiently, justifying the practical value of the proposed process. The modified 40-CMO/Hal catalyst not only overcame the disadvantages of bare CMO (i.e. higher metal leaching and production costs), but also promoted the PMS activation efficiency for the degradation of pharmaceuticals. Therefore, Hal, an abundant natural mineral with a special nanotube structure, was feasible to act as an effective substrate for metal based catalysts in the activation of PMS. This work provides a novel reference to the application of natural minerals in the fabrication of heterogeneous PMS activator with enhanced catalytic ability and lower environmental impact in the field of wastewater treatment and chemical industries.



Scheme 1. The schematic illustration of radical generation mechanism through PMS activated by 40-CMO/Hal

Chapter 6 Effect of clay mineral substrates towards the catalysts' PMS activation ability

6.1 Introduction

As stated in the chapters before, two kinds of natural clay minerals with the same chemical composition but totally different morphology, Hal and Kln, were adopted as substrates for CMO catalysts at different loading percentage.

In recent years, the generation of OVs in metal oxides has gained increasing popularity for boosting the performances of semiconductors, electrocatalysis, photocatalysis, energy storage devices and gas sensing (Hu et al., 2020; Li, H. et al., 2017). It is well-known that OVs with abundant localized electrons occupying the O 2p orbital can make the oxygen-deficient surface much more activated as an electron-rich center, resulting in the acceleration of activation and dissociation of small molecules such as H₂O and O₂ through enhanced electron transfer and conductivity. OVs are commonly induced into crystals during synthesis through vacuum annealing, microwave plasma etching, and solution reduction using supplementary chemicals like NaBH₄, etc., while it is also feasible to increase OVs into composite catalysts by providing a proper substrate (Büchele et al., 2020; Guo et al., 2019; Xiong et al., 2020; Yuan et al., 2009).

Although transition metal oxides loading on clay minerals (e.g., bentonite, montmorillonite, kaolinite and illite) have been used in AOPs, including Fenton and Fenton-like processes, ozonation, and photocatalysis for efficient removal of pharmaceuticals, pesticides and dyes (Fatimah et al., 2022), the catalytic performance

of the obtained catalyst composition has seldom been linked to the structural differences between Hal and Kln. Besides, in addition to facilitating the assemblage of transition metal oxides by improving their dispersion and regulating crystallization, the clay mineral substrates might also boost oxygen vacancies (OVs) into catalytic composite during the synthesis, since the OVs are also originated from hydroxyl groups (Wu et al., 2017; Zhan et al., 2020).

Based on chapter 5, 40-CMO/Hal showed the best performance in the degradation of CBZ through PMS activation among the *x*-CMO/Hal series, thus, in this chapter, CMO loaded on Kln at the same loading percentage (40%) were picked out for further investigations. Since both the composite catalysts had the same CMO content, they were briefly referred to as CMO/Hal and CMO/Kln. As stated before in chapter 3, the catalysts were all prepared by co-precipitation with alkali precursor solution, which enabled the spontaneous induction of OVs into manganese-based oxide materials through the fast nucleation/growth under alkaline condition (Jiang et al., 2019). The catalytic activity of obtained composites were evaluated through PMS activation to degrade ofloxacin (OFX). The generation of OVs were determined by electron paramagnetic resonance (EPR), and correlated to the morphology and properties of Kln and Hal.

Ofloxacin (OFX) that is a typical antibiotic pharmaceuticals, has been frequently detected in all the environmental media including water, soil and sediment (Zhang et al., 2015). Larsson et al. reported that in Patancheru, India, the concentration of OFX in a common effluent treatment plant serving the pharmaceutical factories nearby was high up to 150-160 $\mu\text{g L}^{-1}$ (Larsson et al., 2007). OFX was the most common antibiotics

detected in the sediment of Pearl Rivers, China, with the highest concentration of 1560 $\mu\text{g kg}^{-1}$ (Yang et al., 2010). The presence of OFX could pose severe impacts on aquatic organism, e.g., reducing the complexity of prokaryotic community, and chronic and geno-toxicity towards alga (Deng et al., 2022; Miller et al., 2018). The overuse of antibiotics including OFX lead to the accumulation of multi-resistant bacteria and induce the generation of antibiotic resistance genes (Pruden et al., 2006). These genes, along with antibiotics, can accumulate and transfer to human body via food chain (Patel et al., 2019). The increased antibiotic resistance also brings higher risk in the curation of bacteria-caused diseases (Abat et al., 2017; Martínez et al., 2014).

6.2 Results and discussion

6.2.1 Catalytic performances of CMO, CMO/KIn and CMO/Hal

The adsorption of OFX by raw KIn and Hal, bare CMO, and composites of CMO/Hal and CMO/KIn is provided in Fig. 6-1. Based on the BET results provided in Chapter 2, Fig. 4-7b and Table 4-1, the OFX adsorption ability of these materials increased with the increase of SSA and pore volume (Table 6-1), with the removal of less than 5% of OFX. By contrast, CMO/Hal and CMO/KIn showed satisfied catalytic performance in OFX degradation by PMS, achieving removal efficiency of 75% and 90% in 40 min, respectively; this is obviously higher than that by sole PMS (5%) and CMO (50%) and the simple mixture of CMO with KIn or Hal with identical content in the composite (50%) (Fig. 6-2).

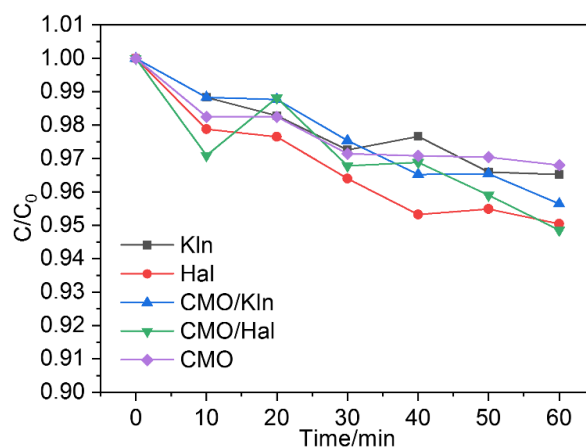


Fig. 6-1 Adsorption of OFX by CMO, Kln, Hal, CMO/Hal and CMO/Kln

General working conditions: [OFX]= 20 μM , [catalyst]= 400mg L^{-1} , pH=6.5

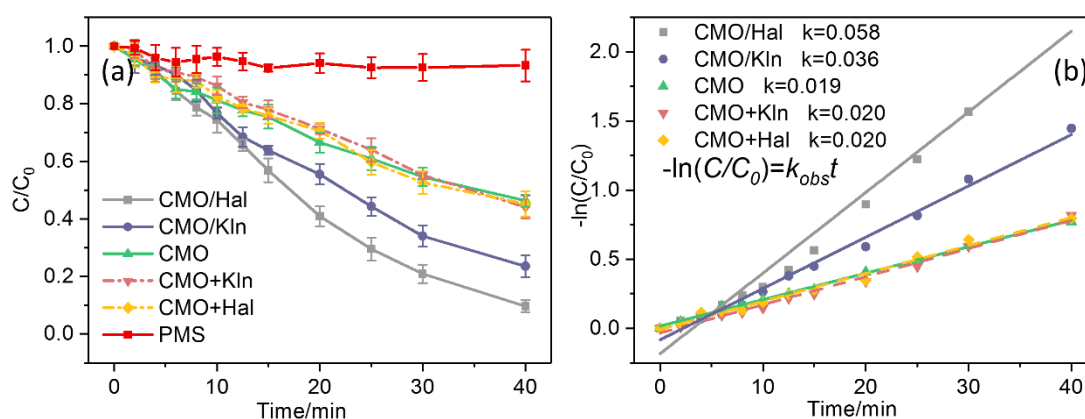
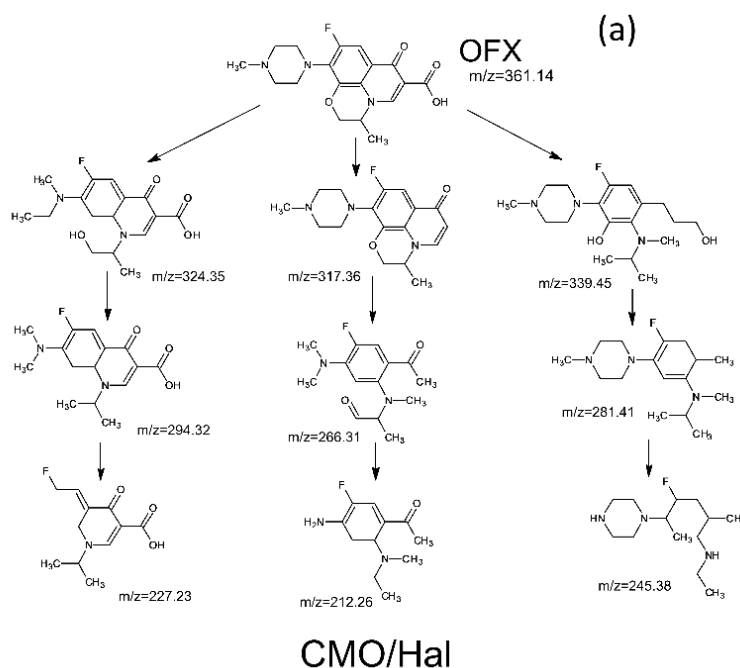


Fig. 6-2 Degradation of OFX in different reaction systems ([CMO + Kln or Hal]: 160 mg L^{-1} CMO + 240 mg L^{-1} Kln or Hal) (a), and corresponding pseudo-first-order kinetic models (b).

General working conditions: [OFX] = 20 $\mu\text{mol L}^{-1}$, [PMS] = 0.1 mmol L^{-1} , [catalyst] = 400 mg L^{-1} , pH = 6.5.

The degradation kinetic is well fitted with the pseudo first-order model (Fig. 6-2b). The obtained rate constants (k_{obs}) of CMO/Hal, CMO/Kln and bare CMO are 0.058, 0.036, and 0.019 min^{-1} , respectively. Compared to bare CMO, CMO/Hal and CMO/Kln with better CMO dispersion and smaller grain size (Fig. 6-2a) provided more reaction sites to activate PMS, and therefore displayed better OFX degradation.

The intermediates and transformation products during OFX degradation was proposed based on the results of LC-MS. Although there were certain similarities in the degradation pathway of CMO/Hal and CMO/KIn due to the same oxidant adopted, the intermediates of them still showed some different. The structures of the intermediates were determined based on the m/z . In Fig. 6-3 using CMO/Hal, 9 intermediates with 3 proposed pathways were detected, while only 7 intermediates divided in 2 ways were found in CMO/KIn. Generally, the main transformation mechanisms in two degradation system included decarboxylation, hydroxylation, piperazinyl dealkylation, oxidation of hydroxyl group and ring cleavage.



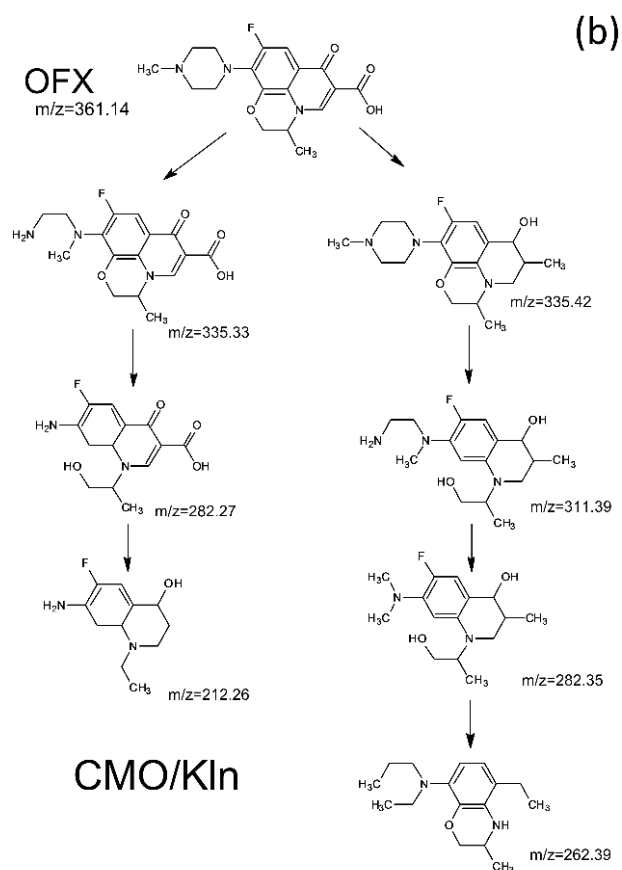


Fig. 6-3 Proposed transformation pathways of OFX using PMS activated by CMO/Hal (a) and CMO/KIn (b).

In CMO/Hal, the formation of $m/z=324.35$ was due to the opening of N-piperazine ring, and $m/z=317.36$ was formed through decarboxylation, which was in agreement with the reported study and frequently occurred in the oxidation of OFX (Changotra et al., 2018; Vasquez et al., 2013). The $m/z=339.45$ was usually formed via attack of OH^\cdot on the heterocyclic ring, followed by the cleavage of C-C bond and loss of the hydroxyl group from another heterocyclic ring near the quinolone moiety. After that, the gradual removal of ammonium group, methyl group and hydroxyl group dominated in path I until the breakdown of benzene ring with F. In line II, after the cleavage of N-piperazine ring, the oxidation of the piperazine side chain occurred continuously until

it was reduced to amino group. In correspondence with the oxidation of the N-piperazine ring, $m/z=266.31$ might be formed from the previous one after losing a carbonyl moiety. In line III, $m/z=339.45$ acted as a promoter of $m/z=281.41$. The $m/z=281.41$ was formed via the loss of the hydroxyl group and carboxyl group. After that, the gradual removal of the methyl group attached to the N of heterocyclic ring dominated the oxidation, followed by the loss of N-piperazine ring.

OFX experienced similar decomposition processes using CMO/KIn with CMO/Hal stated above. However, the intermediates detected in CMO/KIn were relatively large with higher molar weight comparing to CMO/Hal system, revealing that the oxidation of OFX was less complete in CMO/KIn. This was consistent with the TOC results in Fig. 6-4, as CMO/KIn displayed lower mineralization degree than CMO/Hal (about 35% vs 25%). The intermediates stated in Fig.6-3 would still undergo processes like ring cleavage with the attack of ROSSs, generating some short chain organics like propionic and fumaric acid, with most of them turned into inorganics like CO_2 and H_2O .

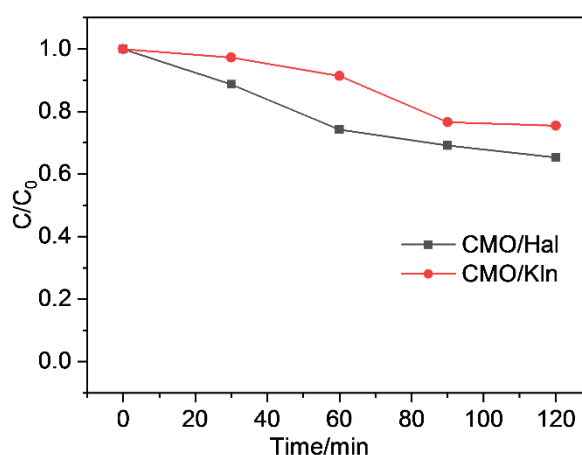


Fig. 6-4 TOC reduction during OFX degradation using PMS activated by CMO/Hal and CMO/KIn.

6.2.2 Effects of working parameters

The effects from OFX and PMS dosages were indicated in Fig. 6-5. Higher the concentration of OFX, lower the degradation efficiency, which could be explained easily by the fact that the limited PMS concentration restricted the further generation of ROSs for OFX oxidation. Similar explanation could also be used on the effect of PMS concentrations' variation on OFX degradation, since higher the PMS concentration, larger amount of ROSs could be generated.

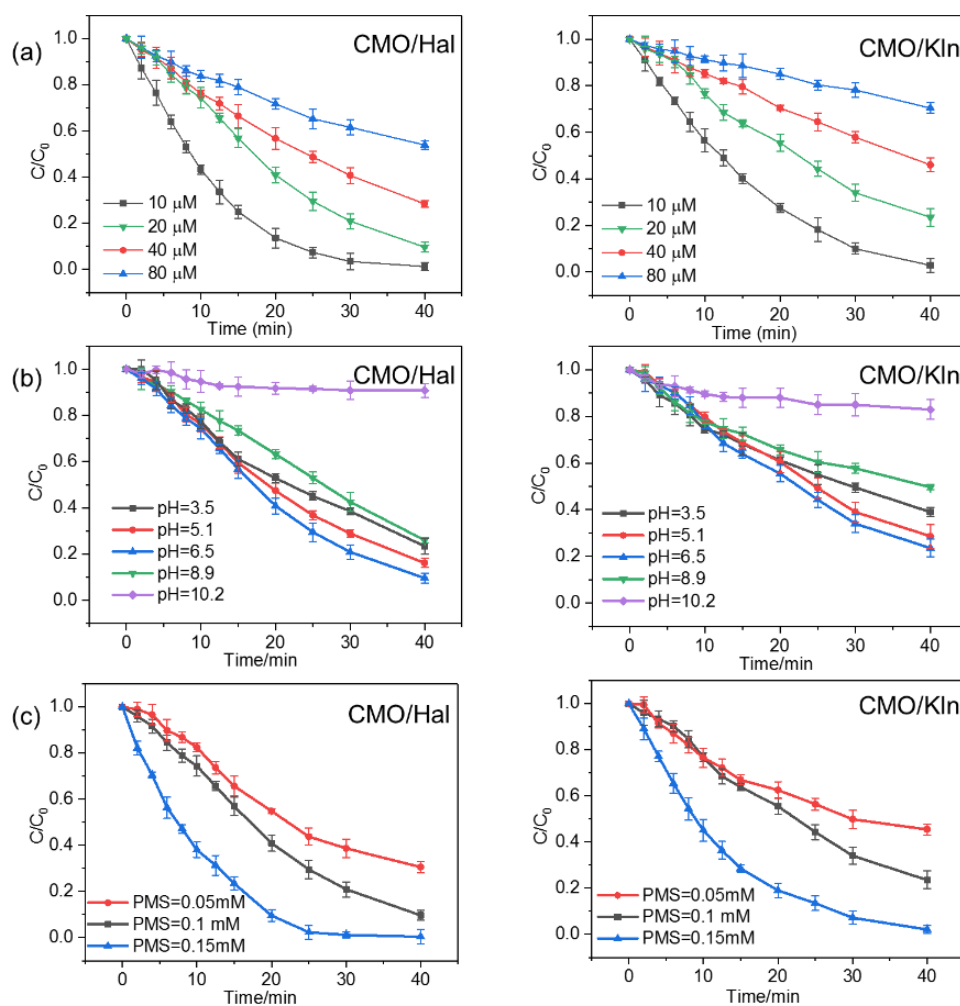


Fig. 6-5 Effects of OFX concentration (a), working pH (b), and PMS concentration (c) on the degradation performances of CMO/Hal and CMO/Kln

General working conditions: [OFX] = 20 μM , [PMS] = 0.1 mM, [catalyst] = 400 mgL^{-1} , pH=6.5.

In order to investigate the impact of working pH, the pH_{pzc} of CMO/Hal and CMO/KIn were tested. The pH_{pzc} of KIn and Hal were reported at around 2.8-2.9, but after anchoring CMO, the pH_{pzc} changed significantly (Almasri et al., 2019). The result in Chapter 4, Fig. 4-9 indicated that the pH_{pzc} of CMO/Hal and CMO/KIn were similar, at around 6.2 and 5.5, separately. Fig. 6-5b revealed that the optimal working pH to remove OFX through PMS activation by both CMO/Hal and CMO/KIn was at around 6.5, while the least OFX residue concentration was detected. However, when working pH varies, the performance of the two catalysts changed somehow. Fig. 6-5b indicated that degradation efficiency of both CMO/Hal and CMO/KIn was retarded obviously under both acidic and alkaline environments like pH=3 and pH=9, and the whole reaction was almost inhibited at pH=10.5. Except this, another reason might be related to the special characterization of OFX itself. It was well known that OFX was amphoteric with two acid dissociation constants ($pK_{a1}= 5.89-6.05$, $pK_{a2} =7.9-8.2$) directed to two ionizable functional groups, N₄ in the piperazinyl group and 3-carboxyl group (Goyne et al., 2005; Van Wieren et al., 2012). Therefore, OFX presented with cationic, zwitterionic, and anionic forms in solution depending on pH. Based on the acid dissociation constants of OFX, it presented zwitterionic while CMO/Hal and CMO/KIn were negatively charged at pH=6.5, therefore, it could be adsorbed by the catalysts through cation exchange and other surface complexation such as hydrogen bonding (Li, Y. et al., 2017). When pH exceeded the range between the two pK_a , the electrostatic repulsion between the catalysts and OFX interfered the adsorption and degradation efficiency. Based on the detailed studies about the effects of key parameters towards the catalytic degradation of OFX, the optimal working parameters were adopted as the general working condition in this work.

6.2.3 Working mechanism

6.2.3.1 Working ROS within OFX degradation

As shown in the EPR results using DMPO and TEMP as spin-trapping reagents (Fig. 6-6), the spin adducts, i.e., DMPO-OH, DMPO-OOH and DMPO-SO₄ were detected after the addition of PMS, indicating the generation of oxygen species of SO₄^{•-}, OH[•] and O₂^{•-}. The intensity of DMPO-SO₄ is much lower than that of DMPO-OH, because the former can quickly transform into DMPO-OH (Cai, T. et al., 2020). The signals of O₂^{•-} showed little intensity variation over time. Interestingly, the formation pattern of ¹O₂ is obviously different from the other oxygen species, as the characteristic triplet peaks of TEMPO-¹O₂ appear simultaneously upon the addition of PMS, and keep increasing. Therefore, the precursor of ¹O₂ might already exist in the solution before PMS addition, which was possibly on the catalyst surface. The intensities of aforementioned ROSs produced from PMS activated by CMO/Hal were obviously higher than that of CMO/KIn, indicating the superior ROS generation ability of the former reaction system. The signals of the four ROSs kept strong during the whole reaction, which guaranteed the sustainable oxidation of OFX.

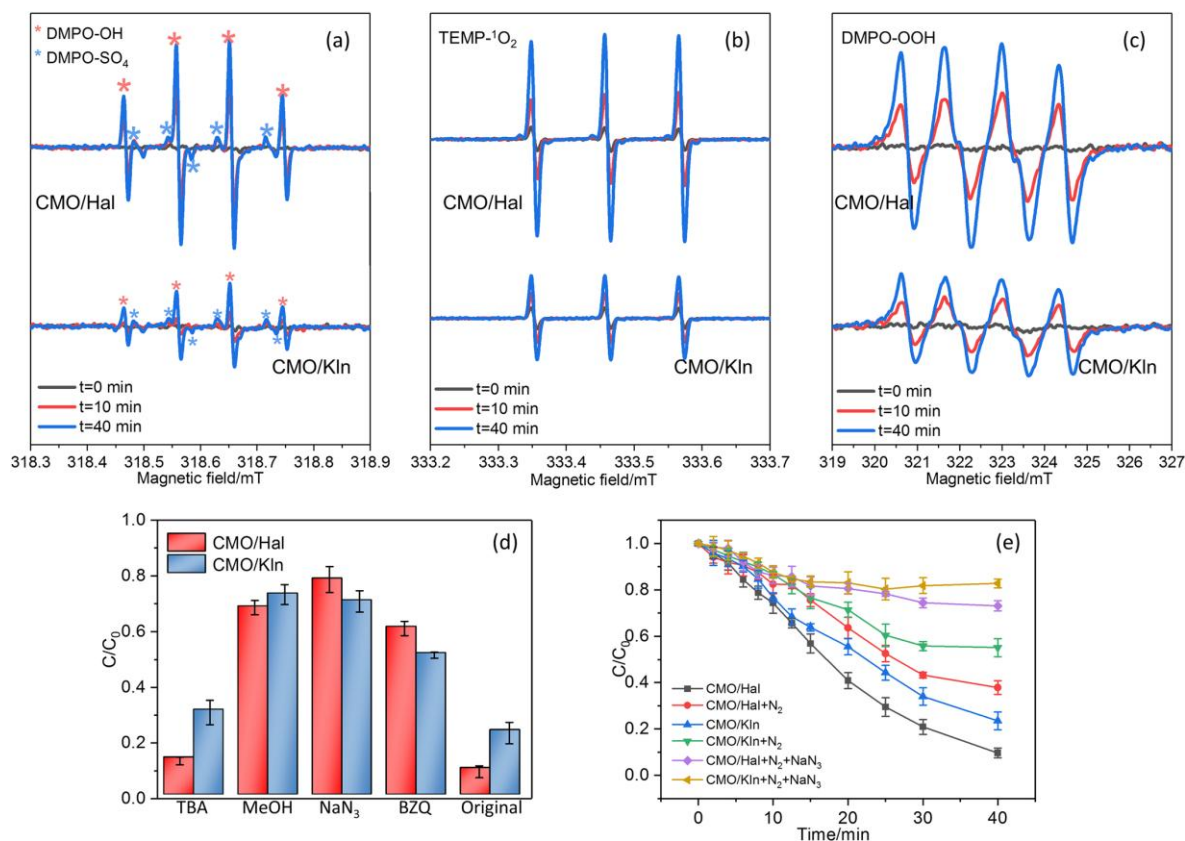


Fig. 6-6 EPR spectra of CMO/Hal and CMO/KIn: (a) OH[•] and SO₄^{•-}, (b) ¹O₂, and (c) O₂^{•-}. Effects of scavengers on OFX degradation (d). Effects of N₂ purging on OFX degradation (e). General working conditions: [OFX] = 20 μM, [PMS] = 0.1 mM, [catalyst]=400mg L⁻¹, [scavengers] = 10 mM, [spin-trapping reagents] = 0.1 M, pH = 6.5.

Traditional trapping experiments were performed separately using radical scavengers including MeOH, TBA, NaN₃ and BZQ to further confirm the contributions of ROS (OH[•] and SO₄^{•-}, OH[•], ¹O₂ and O₂^{•-}) (Fig. 6-6d). The reaction rates of ROSs with the corresponding scavengers were illustrated in Table 6-1. The most obvious inhibitions on CMO/Hal and CMO/KIn were caused by NaN₃ and MeOH, respectively, while the retardations from TBA and BZQ were much alleviated. Thus, SO₄^{•-} and ¹O₂ dominate the reaction (than OH[•] and O₂^{•-}) in OFX degradation with both catalysts, and the contribution of ¹O₂ was higher in CMO/Hal than CMO/KIn.

Table 6-1 A brief summary about the target ROS and their scavengers

Scavenger	Target ROS	Reaction rate K_{obs}	Ref.
<i>tert</i> -butyl alcohol (TBA)	OH^\cdot	$k_{\text{OH}^\cdot} = (3.8\text{--}7.6) \times 10^8 \text{ M}^{-1} \cdot \text{s}^{-1}$	(Dong et al., 2021)
		$k_{\text{SO}_4^{\cdot-}} = (4.0\text{--}9.1) \times 10^5 \text{ M}^{-1} \cdot \text{s}^{-1}$	
Methanol (MeOH)	OH^\cdot ,	$k_{\text{OH}^\cdot} = (1.2\text{--}2.8) \times 10^9 \text{ M}^{-1} \cdot \text{s}^{-1}$	(Dong et al., 2021)
	$\text{SO}_4^{\cdot-}$	$k_{\text{SO}_4^{\cdot-}} = (1.6\text{--}7.7) \times 10^7 \text{ M}^{-1} \cdot \text{s}^{-1}$	
Sodium azide (NaN_3)	$^1\text{O}_2$	$k = 2.2 \times 10^9 \text{ M}^{-1} \cdot \text{s}^{-1}$	(Basu-Modak and Tyrrell, 1993)
1,4-Benzoquinone (BZQ)	O_2^\cdot	$k = 2.9 \times 10^9 \text{ M}^{-1} \cdot \text{s}^{-1}$	(Duan et al., 2020)

6.2.3.2 PMS decomposition mechanism

The recycled CMO/Hal and CMO/KIn were characterized by XPS again to investigate the possible electronic transitions occurred on the metal oxides' surface, and the variations from fresh catalysts were indicated in Fig. 6-7.

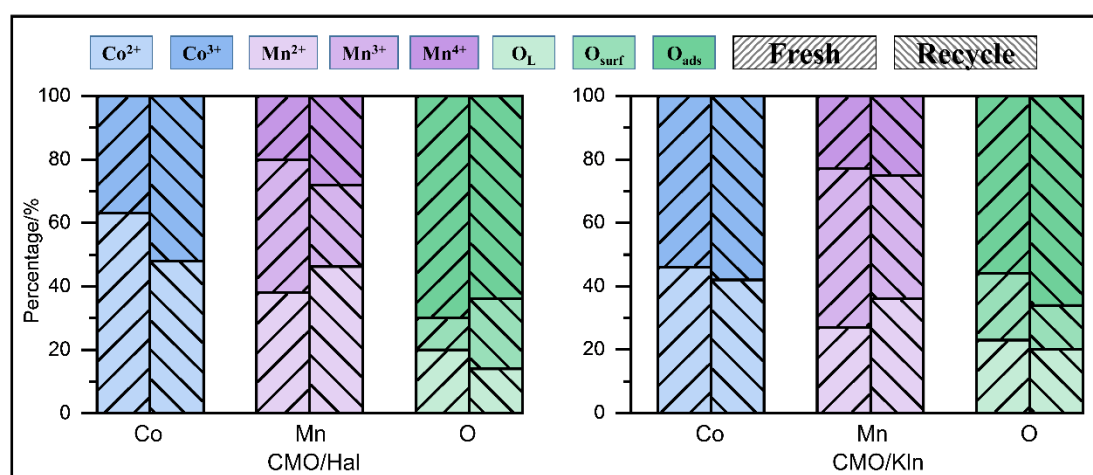
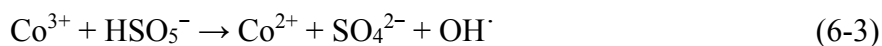
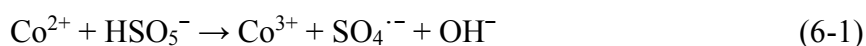
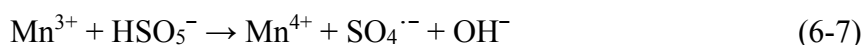
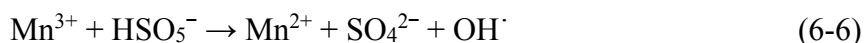
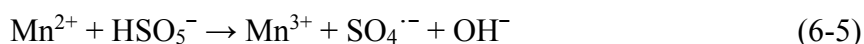
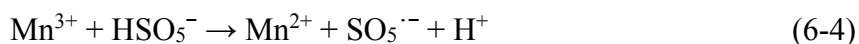


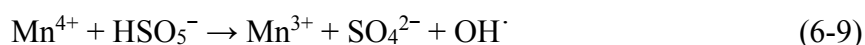
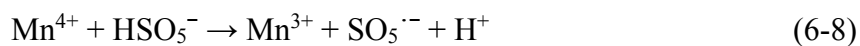
Fig. 6-7 Comparison of Co, Mn, and O between fresh and recycled CMO/Hal and CMO/KIn catalysts.

The characteristic peaks of Co, Mn, Si, and Al in the survey spectra were still monitored clearly in the recycled CMO/Hal and CMO/KIn, revealing the almost unchanged surface chemical compositions of the two catalysts. However, the spectra of Co and Mn showed that each of them experienced certain changes in the valences, which confirmed the existence of electron transfer during the reaction. The decrease of Co^{2+} was observed on both CMO/Hal and CMO/KIn, accompanied with the increase of Co^{3+} . This implies that surface Co^{2+} was oxidized into Co^{3+} by electron transfer to PMS, with the generation of $\text{SO}_4^{\cdot-}$. Afterwards, HSO_5^- and SO_4^{2-} reduced Co^{3+} to Co^{2+} with the formation of $\text{SO}_5^{\cdot-}$ or OH^{\cdot} (Eqs. (6-1)-(6-3)) (Xu et al., 2016).



Similar variation was also found in Mn on CMO/Hal and CMO/KIn, as the proportion of Mn^{2+} increased while that of Mn^{3+} decreased after reactions. This reveals that the electron transfer also happened between Mn^{2+} and Mn^{3+} (Eqs. (6-4)-(6-5)) (Li, C.-X. et al., 2018). The redox reaction between Mn^{4+} and Mn^{3+} was also feasible (Eqs. (6-6)-(6-9)).





Since the standard reduction potential of $\text{Co}^{3+}/\text{Co}^{2+}$ (1.81V) was higher than $\text{Mn}^{3+}/\text{Mn}^{2+}$ (1.51 V) and $\text{Mn}^{4+}/\text{Mn}^{3+}$ (0.15 V), the reduction of Co^{3+} back to Co^{2+} by $\text{Mn}^{3+}/\text{Mn}^{2+}$ and $\text{Mn}^{4+}/\text{Mn}^{3+}$ was thermodynamically feasible (Li, C.-X. et al., 2018). The variation in O 1s spectra clearly showed the consumption of O_{lat} , implying the participation of O species during this degradation.

6.2.3.3 Effect of dissolved oxygen

As stated before, the early appearance of $^1\text{O}_2$ signal at $t=0$ min might be ascribed to the already existed precursors (e.g. dissolved oxygen (DO) in bulk solution and the lattice oxygen on catalyst surface), which quickly reacted with PMS and generated $^1\text{O}_2$. In addition, $^1\text{O}_2$ could also be formed through PMS activated by OV_s and the reaction between $\cdot\text{OH}/\text{H}_2\text{O}$ and O_2^- (Qin et al., 2021; Zhu, C. et al., 2020).

By N_2 purging, the anaerobic OFX degradation using CMO/Hal and CMO/KIn showed a significant reduction by 40% and 65%, respectively (Fig. 6-6e). This confirmed the critical role of DO in the process; while the addition of strong reducing agent NaN_3 salt further retard but not really terminate the process suggesting the existence of other sources for forming $^1\text{O}_2$. The OV_s on the surface of catalysts contained abundant single electrons, which could promote the interfacial electron transfer. Due to the strong Lewis acidity of the oxygen-deficient OV_s, PMS (HSO_5^-) tended to be adsorbed on OV_s with low oxygen coordination, which could be decomposed and released into solution with the formation of active oxygen species (O^*) (Eq. (6-10)) (Zhu, Chengzhang et al., 2020).

Moreover, lattice oxygen near OV_s could also be released and turned into O^{*}. Then, ¹O₂ could be produced from the coupling of O^{*} and HSO₅⁻ (Eq. (6-11)) (Qin et al., 2021). Furthermore, previous studies also reported that DO was able to accept an electron from OV_s to yield O₂⁻ (Eq. (6-13)), which could be converted into ¹O₂ via Eq. (6-12) (Yu, R. et al., 2020; Zeng et al., 2022). The participation of DO was consistent with the retardation of OFX degradation under N₂ purging (Fig. 6-6e).



The production of ¹O₂ by CMO/Hal rose rapidly as the degradation progressed, with more than twice of CMO/KIn's relative intensity at the end of the reaction. A larger amount of ¹O₂ might demonstrate to higher OFX decomposition efficiency, since ¹O₂ contributes specifically to the hydroxylation of phenolate and phenolic groups in addition to SO₄⁻ and OH[·], which would benefit the followed mineralization (Barrios et al., 2021; Kong et al., 2016). This observation correlates well to the better performances of CMO/Hal than CMO/KIn.

6.2.3.4 Recyclability and reusability of the catalysts

CMO/Hal and CMO/KIn maintained satisfied catalytic performance after three reuses with little deterioration (Fig. 6-8a). The metal leakage of CMO/Hal and CMO/KIn measured by ICP-OES indicated that was obviously alleviated comparing to bare CMO, and CMO/KIn showed the lowest metal leaching (Fig. 6-8b). The leaching of Co and Mn were less than 0.1 and 0.2 mg L⁻¹, respectively for both CMO/Hal and CMO/KIn,

which met the limits of Chinese environmental quality standards for surface water (0.1 and 1 mg L⁻¹ for Co and Mn, respectively) (China, 2002). It should be noted that same dosage of CMO, CMO/Hal and CMO/KIn were used in the recycle tests, and the latter two contained only 40% of CMO to the bare one. However, the metal loss of CMO/KIn is still 40% lower than that of bare CMO (about 0.11 for Co and 0.13 mg L⁻¹ for Mn). Thus, mineral matrices could greatly reduce metal leaching and promote the stability of the catalysts, which also suppressed secondary pollution and became more environmental friendly. This is likely due to the limited dissolution of CMO particles attached near the pores of the mineral matrices, and the improved bonding between the metal ions and functional groups on Hal or KIn (Tan et al., 2020).

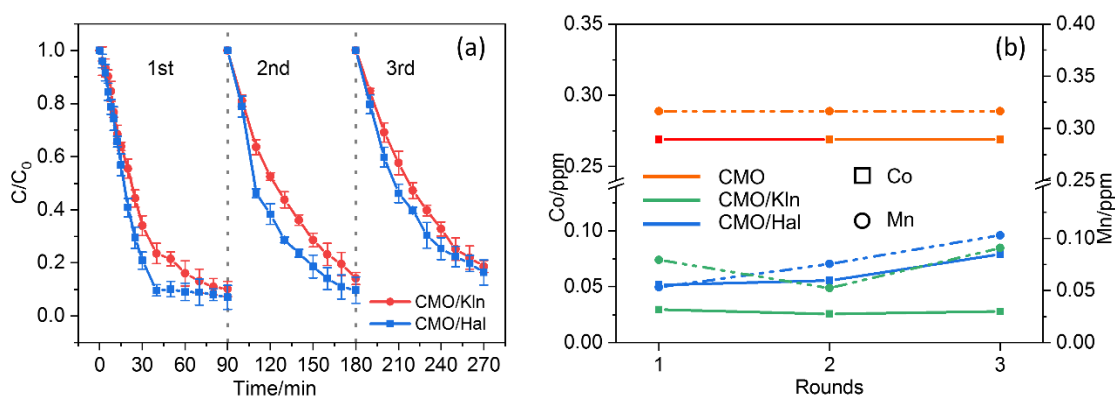


Fig. 6-8 OFX degradation with CMO/Hal and CMO/KIn after three recycle rounds (a), and ICP-OES results of CMO/Hal and CMO/KIn in recycle experiments (b).

Working conditions: [OFX] = 20 μ M, [PMS] = 0.1 mM, [catalyst] = 400 mg L⁻¹, pH = 6.5.

According to the XRD analysis (Fig. 6-9), the pattern of CMO/KIn was almost unchanged, with only slight decrease in relative intensity. This indicates the little change occur on the crystallinity with after 3 recycles. Although the peaks indexed to CMO in fresh CMO/Hal with lower crystallinity was already insignificant, the patterns of recycled ones seemed even worse, as the three strongest peaks of CMO located

between 30 and 40° (2θ) could hardly be distinguished. The almost unchanged XRD pattern of CMO/KIn was also consistent with its low metal leaching. This implies that KIn substrate was advantageous in maintaining structural stability.

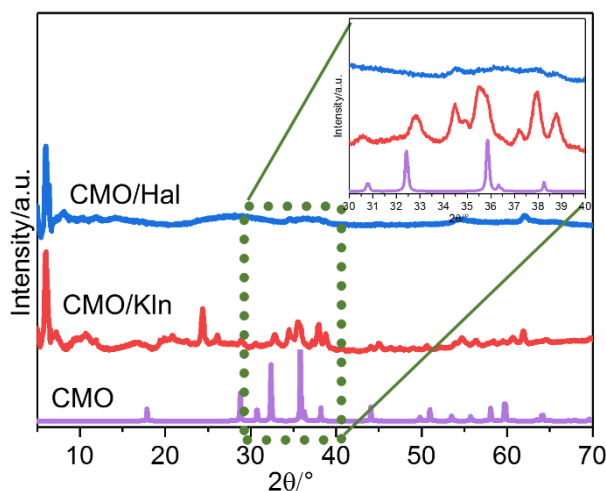


Fig. 6-9 XRD patterns of recycled CMO/Hal and CMO/KIn comparing to fresh CMO

Since metal leakage was still unavoidable in CMO/KIn and CMO/Hal, homogeneous catalytic degradation of OFX was investigated separately using $\text{Co}(\text{NO}_3)_2$ and $\text{Mn}(\text{NO}_3)_2$. Using Mn^{2+} instead of Mn^{3+} is because the latter is unstable and easily reduced to Mn^{2+} (Klewicky and Morgan, 1998). The dosages of $\text{Co}(\text{NO}_3)_2$ and $\text{Mn}(\text{NO}_3)_2$ were both 0.1 mg L^{-1} , corresponding to the highest leaching concentration measured by ICP-OES in Fig. 6-8b. In Fig. 6-10, only about 40% of OFX was removed by Co^{2+} in 40 min while little change was observed with Mn^{2+} , confirming the feasible but deficient PMS activation of Co^{2+} . The k_{obs} of Co^{2+} was 0.013, which only accounted for about 22% and 36% of CMO/Hal and CMO/KIn, separately. Thus, heterogeneous catalysis still played the dominant roles in the process.

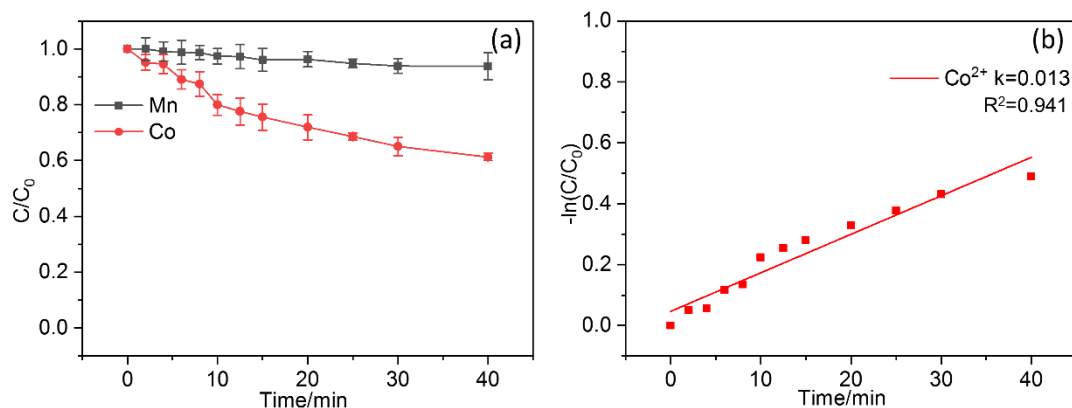


Fig. 6-10 Homogeneous degradation of OFX using Co^{2+} and Mn^{2+} (a), and k_{obs} of Co^{2+} calculated from pseudo-first order model (b).

6.2.3.5 Effects of inorganic anions and NOM on the degradation

The effects of water matrix, including inorganic anions like Cl^- , HCO_3^- and NO_3^- , and natural organic matter (NOM), were tested separately on the degradation of OFX using PMS activated by CMO/Hal and CMO/KIn. Herein, humic acid (HA, Suwannee River Humic Acid, International Humic Substances Society, MN) was used as the model NOM.

As shown in Fig. 6-11, the addition of 0.5 mmol L^{-1} of Cl^- and HCO_3^- inhibited the degradation of OFX in PMS systems activated by both CMO/Hal and CMO/KIn. When the anion concentration increased to 1 mmol L^{-1} , the retardation caused by HCO_3^- grew extremely stronger than that of Cl^- . The dual effect from Cl^- was not unusual in sulfate-based advanced oxidation process (SR-AOPs), as Cl^- could react with OH^\cdot and $SO_4^{\cdot-}$ to generate reactive chloride species like Cl^\cdot , $Cl_2^{\cdot-}$, Cl_2 and $HClO$, or switch the main oxidant from $SO_4^{\cdot-}$ into OH^\cdot (Lee et al., 2020; Peng, G. et al., 2021). However, although some of these chloride reactive species showed higher standard reduction potentials, they tended to be more selective (Zhang and Parker, 2018). The decreased degradation

efficiency here might be caused by this, as OFX was less reactive and thus unsusceptible to be oxidized by these new reactive species (Huang et al., 2021).

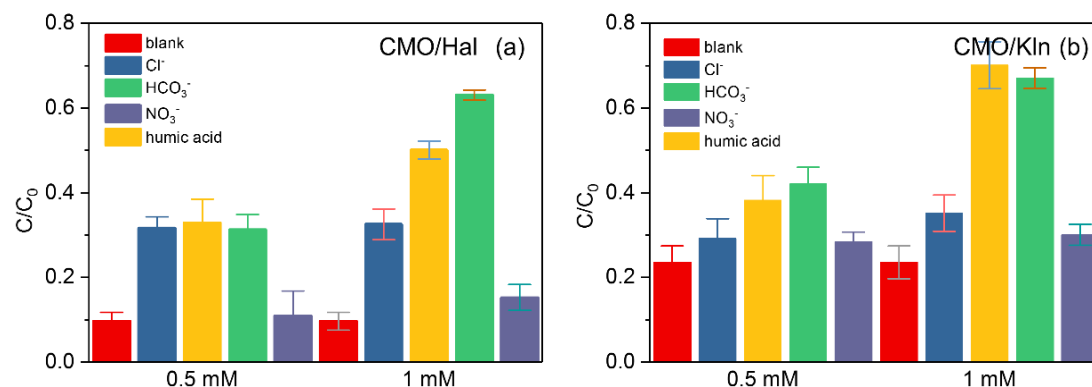


Fig. 6-11 Effect of water matrix on the degradation of OFX using PMS activated by CMO/Hal (a) and CMO/KIn (b).

Working conditions: [OFX]= 20 μM , [PMS]= 0.1 mM, [anions]= 0.5 or 0.1 mM, [humic acid]= 5 or 10mg L⁻¹, [catalyst]= 400mg L⁻¹, pH=6.5.

The insufficient degradation with HCO_3^- added was largely due to its scavenging effect towards $\text{SO}_4^{\cdot-}$, which was commonly found among oxyanions (Lian et al., 2017). Similar phenomenon would also happen on OH^{\cdot} , as HCO_3^- could quench it and generate $\text{CO}_3^{\cdot-}$ which was weaker and more selective. Furthermore, HCO_3^- could attack PMS directly and convert into HCO_4^- , a moderate oxidant, using the oxygen atom transferred from PMS (Lee et al., 2020). The consumption of PMS and $\text{SO}_4^{\cdot-}$ by HCO_3^- also interfered the generation of $^1\text{O}_2$, which further slowed down the degradation of OFX.

The NO_3^- added in the reaction system could hardly interfere the degradation process, since it did not react with $\text{SO}_4^{\cdot-}$ (Ma, J. et al., 2018).

The phenomenon of HA was similar to that of Cl^- , as only slight inhibition was observed at lower concentration and the suppression strengthened dramatically when more HA was added. This might be attributed to the radical scavenging effect caused by the electron-rich moieties within HA. On the other hand, the adsorption of HA on the catalysts led to the reduction of reactive sites (Li, H. et al., 2021). The removal of OFX using CMO/KIn and PMS suffered more suppression under higher HA concentration (Fig. 6-11), which might be due to the larger size of the catalysts with less active sites, and the adsorption of HA worsened the situation.

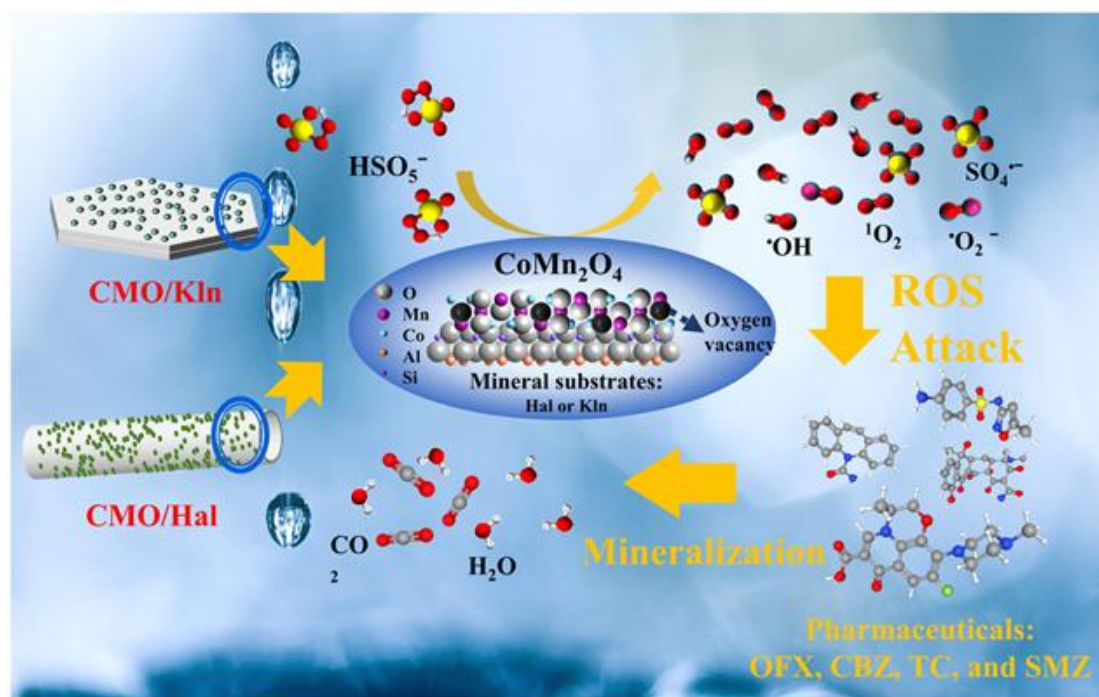
6.3. Conclusion

In this study, two types of OV-abundant catalysts with different mineral matrices, CMO/Hal and CMO/KIn, were fabricated to activate PMS. The efficient degradation of four frequent detected pharmaceuticals revealed the superior catalytic ability and better stability of both CMO/Hal and CMO/KIn than bare CMO with reduced metal usage.

Compared to KIn, Hal not only generated more OVs, but also displayed stronger suppression in CMO's grain size and crystallinity, which promoted the catalytic efficiency significantly. However, CMO/KIn with higher crystallinity and ordered structure maintained structural stability with less metal leakage than CMO/Hal.

Although CMO/Hal and CMO/KIn showed superior PMS activity in degrading pharmaceuticals than bare CMO, they still had some limitations, e.g., the unbalanced improvement of both catalytic activity and structural stability, and the unavoidable metal leaching, which will be investigated in the future by modifying the structure or

inducing more active sites. Besides, combining the current catalyst/PMS reaction system with other technologies including membrane and ultrasonic would be worthy of an attempt, which might alleviate the passivation of the catalysts, and simplify the recycle processes.



Scheme 2. The schematic illustration of radical generation mechanism through PMS activated by CMO/Hal and CMO/Kln.

Chapter 7 Removal of pharmaceuticals using PMS activated by LaCoO_3

7.1 Introduction

In wastewater and natural waters, antibiotics usually coexist with inorganic anions and natural organic matter (NOM), which poses various effects on the removal processes. For instance, Cl^- is identified as a strong scavenger for $\text{SO}_4^{\cdot-}$ in the degradation of methylene blue and levofloxacin (Dung et al., 2020). But it is also reported as a promoter, due to the higher reaction rate of Cl^\cdot generated from Cl^- than $\text{SO}_4^{\cdot-}$ (Luo et al., 2020). As to SO_4^{2-} , the suppressing effect is considered stronger than Cl^- and NO_3^- in the degradation of sulfamethoxazole by PMS, whereas no significant effect was reported in the PMS activation by Fe and S co-doped graphite (Wang, S. et al., 2020a). As a typical natural organic matter (NOM) in water, humic acid (HA) has been found to display synergistic or inhibitory effects. As reported in the decomposition of sulfamethoxazole (SMZ) via PMS activation, the degradation is promoted by HA with low concentration, while an inhibition effect appears with the further increase of HA concentration (Wang, S. et al., 2020b). On the contrary, HA greatly declines the degradation of sulfachloropyridazine by PMS, where the degradation efficiency decreases dramatically from 98.9% to 75.8% with the addition of 0-10 mg L^{-1} of HA (Wang et al., 2017). Considering the widespread distribution of inorganic anions and NOM, as well as their intriguing performance in the reaction, their effects should be considered in the test of the activity of catalysts in activating PMS.

Herein, the degradation of tetracycline (TC) in the activation of PMS by LaCoO_3 was investigated in the following aspects: i) catalytic performance and stability; ii) free

radical species and degradation pathways; and iii) effects of HA and several common inorganic anions (i.e., Cl^- , SO_4^{2-} , NO_3^- and H_2PO_4^-). The obtained results should be benefit for the environmental application of $\text{LaCoO}_3/\text{PMS}$ system in the removal of antibiotics.

7.2 Results and discussion

7.2.1 Influence of experimental parameters

7.2.1.1 Initial TC concentration

First, the catalytic degradation of TC with different initial concentrations in the LCO/PMS system was studied without pH adjustment (Fig. 7-1). It should be noted that due to the acidic chemical properties of PMS, the original pH of the working solution, prior to any adjustment, was 3.3. The LCO/PMS system efficiently removed the selected concentration of TC in approximately 30 min, with a rapid initial decay observed in the first 5 min. Generally, a faster degradation rate constant ($0.07\text{--}0.22\text{ min}^{-1}$) was achieved at lower TC initial concentrations. This is attributed to the limited total amount of the oxidant, i.e., PMS. As the catalyst worked mainly on the activation of PMS, the total amount of free radicals generated was limited by the dosage of PMS. Thus, the degradation efficiency of TC was affected by its initial concentration under identical experimental conditions. If the initial concentration exceeded the potential free radicals generated from PMS by the catalyst, the number of free radicals and other possible active functional groups would be insufficient to meet the degradation requirement, leading to incomplete degradation of TC. Based on the results, the initial concentration of 20 mg/L of TC was selected for the remaining tests, for a more accurate comparison at a reasonable degradation rate.

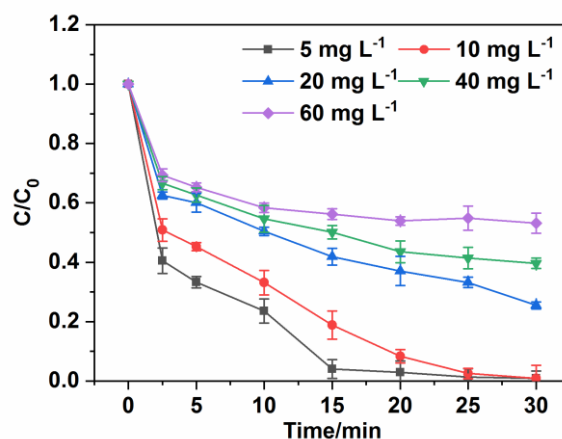


Fig. 7-1 Effect of TC concentration on degradation efficiency.

General working conditions: [PMS] = 50 mg L⁻¹, [LaCoO₃] = 200 mg L⁻¹, pH=3.3 (unadjusted).

7.2.2.2 PMS dosage

Control experiments were first carried out to verify the contribution of individual pathways involved in the LCO/PMS system. The absence of either PMS or catalyst might diminish the degradation performance than that of the combined LCO/PMS system (Fig. 7-2). For the process using solely LCO, less than 10% of TC was removed, likely by adsorption onto the catalyst. In contrast, approximately 50% TC removal was observed in 30 min from the process using solely PMS. However, it should be noted that the measurement of TC removal under solely PMS addition may not necessarily reflect the decomposition of TC molecules into smaller ones, which would finally lead to thorough degradation. Instead, one or more substitutions on the TC molecule might have resulted from the interaction between TC and PMS (Zhou, Y. et al., 2020).

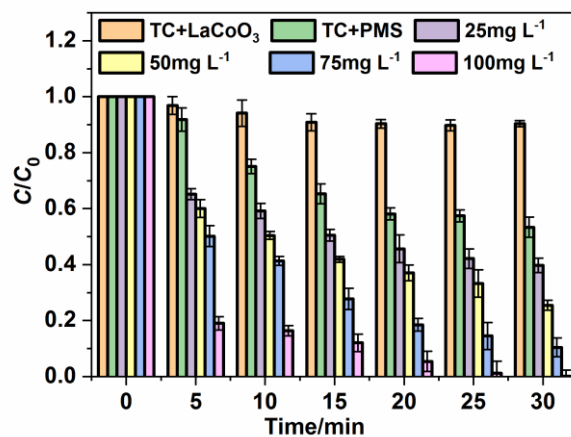


Fig. 7-2 Effect of PMS concentration on degradation efficiency.

General working conditions: [TC] = 20 mg L⁻¹, [LaCoO₃] = 200 mg L⁻¹, pH= 3.3 (unadjusted).

Under these circumstances, most of the PMS remained inactivated. Thus, the extent of free radical oxidation via SO₄⁻ or OH⁻ was minor. With the simultaneous addition of PMS and catalyst, the degradation performance improved significantly. Apparently, free radical generation increased with increasing PMS dosage, likely due to the elevated mass transfer and/or supply of PMS from the bulk of the solution to the catalyst surface. The higher concentration of PMS near the diffusive-double layer of the catalyst accelerated the activation of PMS, leading to a higher concentration of free radicals. It should be noted that from the results of the control groups, especially the one without the addition of PMS, a minor removal of TC was observed, which was attributed to the adsorption of TC onto the catalyst. This minor adsorption effect on LCO indicated that TC was capable of accumulating at (or near) the surface of the catalyst. This provided a good fundamental condition for the reactions that commenced with the addition of PMS; since the distance between the radicals generated and the TC molecules was short, the concentrations of both near the catalyst were slightly increased. Again, for a clearer observation of the decay pattern, a moderate PMS concentration of 50 mg/L was chosen as the exclusive dosage in subsequent experiments. If excessive concentration of PMS

was adopted, the TC degradation process would be shortened obviously, which might pose a negative influence on the observation of the decay pattern.

7.2.2.3 Initial pH

The pH of the catalyst-activated PMS system for organic degradation played an important role in the reaction, probably because it affected the generation of strong oxidising species such as singlet oxygen atoms, and sulphate, hydroxyl, and superoxide radicals. The pH of the solution was measured at given time intervals throughout the reaction (Fig. 7-3a). Although TC could be removed in a wide pH range, its removal was clearly most effective at basic pH (Fig. 7-3b). In the pH range from 3.3 to 11, the removal rate of TC generally increased with increase in initial pH, and the TC remaining at the end of the reaction time decreased from approximately 35% to 10% and 1% of its initial concentration under acidic, neutral, and basic conditions, respectively; indicating the high activity of the LCO catalyst under neutral to basic conditions. This was advantageous in practical use because the natural pH of water usually lies between 7 and 8. Higher pH would accelerate the conversion from $\text{SO}_4^{\cdot-}$ to $\text{OH}^{\cdot-}$, promoting TC removal (Li, N. et al., 2019). It should be noted that there were two pKas for PMS ($\text{pKa}_1 < 0$, $\text{pKa}_2 = 9.4$). Under neutral conditions, PMS is more prone to ionisation, which might enhance active free radical generation. Under these circumstances, the dominant species of PMS in aqueous conditions was $\text{HSO}_5^{\cdot-}$, which might react with $\text{OH}^-/\text{H}_2\text{O}$ to a certain extent to form OH^{\cdot} (Zhang et al., 2019). This offers an additional pathway for TC degradation.



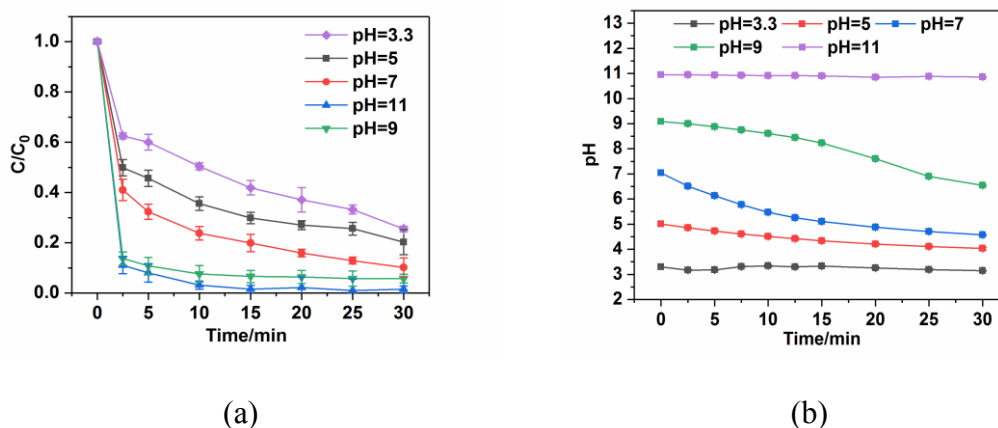


Fig. 7-3 (a) Effect of initial solution pH on degradation efficiency and (b) the variation of pH during the reaction.

General working conditions: $[TC] = 20 \text{ mg L}^{-1}$, $[PMS] = 50 \text{ mg L}^{-1}$, $[LaCoO_3] = 200 \text{ mg L}^{-1}$.

The slower degradation under acidic pH may be attributed to the chemical properties of PMS. PMS is more stable under acidic conditions than it is under neutral or alkaline conditions, which might lead to a relatively slower activation. Thus, fewer active radicals may have been generated for TC degradation (Wu, S. et al., 2019; Xu et al., 2020). Additionally, the increased concentration of H^+ may cause it to capture $SO_4^{\cdot-}$ in the solution under acidic conditions, leading to the waste of activated $SO_4^{\cdot-}$ and hindering mass transfer. It should be noted that at lower pH (*e.g.*, $pH < 5$), it would be easier for H^+ to attach onto the surface of HSO_5^- to generate H-bonds with the O–O bond, which might inhibit the interaction between PMS species and the positively charged surface (Cheng et al., 2020). Therefore, the decomposition of PMS into radicals like $SO_4^{\cdot-}$ and OH^{\cdot} would be retarded, which finally suppressed the TC degradation efficiency.

7.2.2 Effect of co-existing inorganic anions on degradation efficiency

Several kinds of inorganic anions including Cl^- , H_2PO_4^- , NO_3^- and SO_4^{2-} , which were widely detected in real wastewaters or natural waters, were chosen to test their influence on the degradation efficiency of TC at neutral pH. Generally, most of the selected inorganic anions posed positive effects on the degradation of TC at different extent (Fig. 7-4).

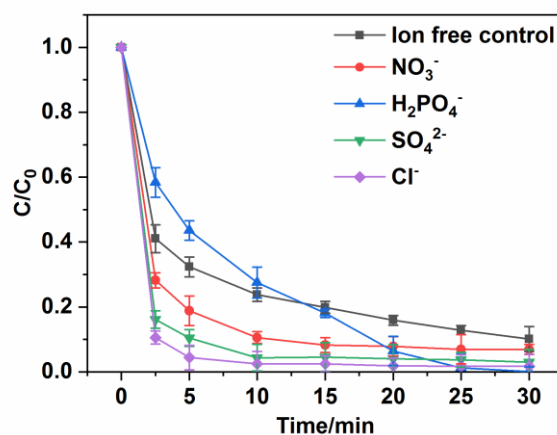


Fig. 7-4 Effect of inorganic anions on the degradation of TC in $\text{LaCoO}_3/\text{PMS}$ system.

General working conditions: $[\text{TC}] = 20 \text{ mg L}^{-1}$, $[\text{PMS}] = 50 \text{ mg L}^{-1}$, $[\text{LaCoO}_3] = 200 \text{ mg L}^{-1}$, initial concentration of Cl^- , NO_3^- , H_2PO_4^- and SO_4^{2-} : 10 mmol L^{-1} , and $\text{pH} = 7.0$.

Among all the tested anions, H_2PO_4^- showed the best outcome. The remaining concentration of TC went down to zero in 30 min after the addition of H_2PO_4^- , far more effective than the control system without inorganic anions. This observation contradicts to the results of some AOPs, where H_2PO_4^- showed inhibitory effect on PMS activation (Li, M. et al., 2020). However, as a nucleophile, H_2PO_4^- was easy to attack PMS, due to its asymmetric structure. This induced a quick decay of PMS (Dong et al., 2020b) and rapid generation of active species such as $\text{SO}_4^{\cdot-}$ and OH^\cdot , leading to the effective

degradation of TC. This was reported feasible in an analogous study carried out by Li *et al.* in 2019 (Li, Chunquan *et al.*, 2019). Because H_2PO_4^- itself seldom consumes or reacts with free radicals, the addition of H_2PO_4^- therefore likely increases the steady-state concentrations of $\text{SO}_4^{\cdot-}$ and OH^\cdot in the solution and then accelerates TC removal. This can be shown in Fig. 7-5, where the increase of $[\text{H}_2\text{PO}_4^-]$ resulted in the less residual of [TC]. Similar effect was also observed on reaction systems, e.g., $\text{CoFe}_2\text{O}_4/\text{Oxone}$ and FeMn bimetallic catalysts with nitrogen-doped graphene /PMS (Chen *et al.*, 2018; Duan *et al.*, 2020).

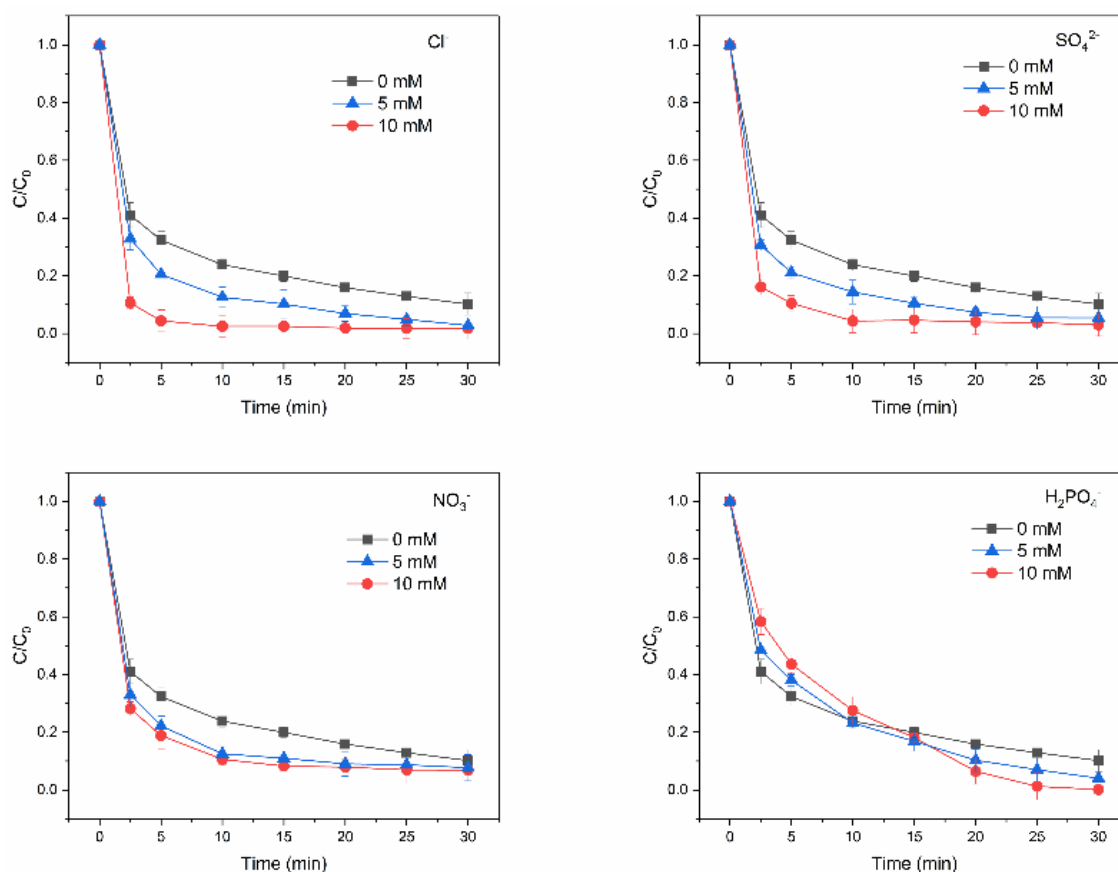
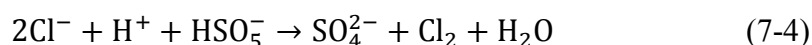


Fig. 7-5 Effect of common anions on the degradation of TC in $\text{LaCoO}_3/\text{PMS}$ system.

General working conditions: $[\text{TC}] = 20 \text{ mg L}^{-1}$, $[\text{PMS}] = 50 \text{ mg L}^{-1}$, $[\text{LaCoO}_3] = 200 \text{ mg L}^{-1}$, $\text{pH} = 7.0$

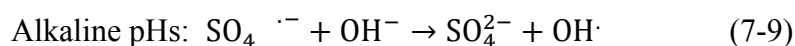
The addition of Cl^- in the $\text{LaCoO}_3/\text{PMS}$ also strongly accelerated the TC degradation,

which diverged from the frequently reported character of Cl^- as a free radical scavenger. The positive effect of Cl^- could be explained by Eqs. (7-4)-(7-6) (Zhang, S. et al., 2020). Cl^- could be oxidized by both PMS and $\text{SO}_4^{\cdot-}$ to active chlorine species. For example, HOCl was the dominant chlorine species in acidic solution, while ClO_3^- with less strong oxidizing ability was the main species at higher pH (Eq. (7-7)). Moreover, $\text{Cl}_2^{\cdot-}$ and Cl^\cdot might also be generated through nonradical pathways (Scialdone et al., 2009). Therefore, active chlorine contributed to the degradation of TC in the $\text{LaCoO}_3/\text{PMS}$ system. Because there is no trace of chlorinated intermediates in the LC/MS analysis, the role of active chlorine species should be simply oxidants, rather than sources of substitution reactions.



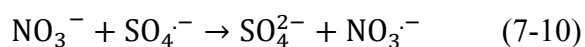
Different from previous studies, the addition of SO_4^{2-} surprisingly promoted the reaction, as the residue TC was further reduced to less than 5% (Fig. 7-4) comparing to that of anion-free reaction. Theoretically, SO_4^{2-} is at a fully oxidized state and generally considered as an inert ion in the solution, owing to its much slower reactivity toward OH^\cdot and $\text{SO}_4^{\cdot-}$, SO_4^{2-} was not a scavenger and did not react with the free radicals in the process (Barzegar et al., 2018; Yuan et al., 2020). The possible reason for the SO_4^{2-} in promoting the reaction is likely through a proper kinetics control of generating radicals in the solution by minimizing the sharp peak of [radical], which is known to induce unwanted/futile side reactions and minimize the waste of the precious radicals,

so that the overall removal TC is increased in the long run. As show by Eqs. (7-8)-(7-9), $\text{SO}_4^{\cdot-}$ can react with H_2O and OH^- to form OH^\cdot , while the presence of high $[\text{SO}_4^{2-}]$ (*i.e.* the end product of $\text{SO}_4^{\cdot-}$ after its usage) at the beginning of the reaction can effectively slow down (but not consume) the formation of both $\text{SO}_4^{\cdot-}$ and OH^\cdot . This mechanism maintains a healthy concentration of [radicals] in the solution and minimize the chance of boosting a peak [radical] in the solution. The risk of futile consumption of free radicals in the solution is therefore reduced and the overall performance in removal of TC in the $\text{LaCoO}_3/\text{PMS}$ process promoted.



For NO_3^- , the influence on degradation was insignificant, as the residue TC was about 7% after 30 min's degradation, close to the control group at 10%. Comparing to the other anions, the interference caused by NO_3^- on the PMS-based AOPs was commonly lower. Most of the relative researches indicated that obvious retardation usually become appreciable when $[\text{NO}_3^-]$ is higher than 50 mM (Li, W. et al., 2020; Wu et al., 2020). In this work, the studied of the effect of $[\text{NO}_3^-]$ on the degradation of TC by LCO/PMS was less than 10 mM, as nitrate concentration within pharmaceutical wastewater commonly ranged between 50-800 ppm (Hoseinzadeh et al., 2018; Rodríguez et al., 2005). The major reason for the weak influence from NO_3^- on TC degradation was the relatively slow reaction rate between $\text{SO}_4^{\cdot-}$ and NO_3^- ($k = 2.1 \times 10^2 \text{ M}^{-1} \text{ S}^{-1}$, pH=7) as indicated in Eq. (7-10) (Cao et al., 2019; Ma, J. et al., 2018; Yang et al., 2020). Comparing to those of other anions, such as H_2PO_4^- ($k = 7 \times 10^6 \text{ M}^{-1} \text{ S}^{-1}$) and Cl^- ($k = 2.5 \times 10^8 \text{ M}^{-1} \text{ S}^{-1}$), the rate of NO_3^- was 10^4 to 10^6 order lower; thus, it showed

neglectable scavenging effect and posed almost no interference on the degradation of TC (Cao et al., 2019; Nie et al., 2014).



Besides, another research indicated that the existence of NO_3^- was beneficial to the generation of active oxygen (Huang et al., 2009). The traditional trapping experiments and EPR tests both confirmed the positive roles of $^1\text{O}_2$ and $\text{O}_2^{\cdot-}$ in the removal of TC, which helped to demonstrate to the promotion of TC oxidation. Similar conclusions were widely reported by other researches using sulfate radical-AOPs (Li, M. et al., 2020; Yang et al., 2020).

The tests with additional lower concentration of inorganic anions, i.e., 5 mmol L^{-1} were carried out. The promotion effect was also observed and generally slower than those at 10 mmol L^{-1} .

7.2.3 Effect of co-existing organic matters on degradation efficiency

Previous research suggests that co-existing organic matter might suppressed the $\text{SO}_4^{\cdot-}$ -based processes (Ma, J. et al., 2018). To evaluate this hypothesis in the degradation of TC under the $\text{LaCoO}_3/\text{PMS}$ system, humic acid (HA) was chosen for investigation. HA is normally detected in the range $5\text{-}20 \text{ mg/L}$, which might greatly affect the water quality (Cai, C. et al., 2020; Wang, Yuxian et al., 2020). Thus, the amount of HA in the reaction system was set to 5 and 20 mg L^{-1} . When the dosage was 5 mg L^{-1} or lower, HA was slightly favourable to the degradation (Fig. 7-6). This might be caused by the

formation of semiquinone radicals, which could be generated from the oxygen-containing functional groups in HA, and subsequently, effectively stimulate PMS to form OH^\bullet and $\text{SO}_4^{\bullet-}$ (Cai, C. et al., 2020). The semiquinone radicals from HA have been reported capable to activate PMS via a self-redox cycle, promoting the formation of OH^\bullet and $\text{SO}_4^{\bullet-}$ and accordingly TC degradation (Fang et al., 2013). Furthermore, the coordination between HA and some metal ions within LaCoO_3 might also have generated some oxidative intermediate products, leading to the formation of OH^\bullet and $\text{O}_2^{\bullet-}$. These radicals may help to promote the degradation, given that $\text{O}_2^{\bullet-}$ was later proved to be one of the working free radicals under the $\text{LaCoO}_3/\text{PMS}$ system (Xu, K. et al., 2017).

However, some inhibition effect was observed at higher concentrations. This was mainly due to the quenching effect of HA on sulphate radicals. With the increasing concentration of HA to even higher than 10 mg L^{-1} , the degradation of TC by LCO/PMS system was gradually retarded. Similar inhibition caused by higher dosage of HA was also observed in some other sulfate based AOPs. This was attributed largely to the competition of $\text{SO}_4^{\bullet-}$ radicals between HA and TC (Wang, S. et al., 2020b). Another possibility was the deeper blockage of active sites on the surface of LCO caused by the functional groups including phenolic, hydroxyl and carboxyl of excessive HA (Ali et al., 2021). This situation would lower the chances for PMS or TC adhering on the surface of LCO. Therefore, the lower HA concentration (i.e., 5 mg L^{-1}) could improve the process, but higher HA concentration ($> 10 \text{ mg L}^{-1}$) would induce a retardation.

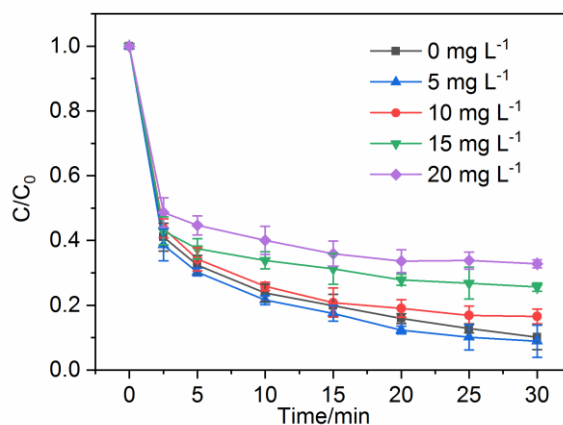


Fig. 7-6 Effect of humic acid on the degradation of TC in LaCoO₃/PMS system.

General working conditions: [TC] = 20 mg L⁻¹, [PMS] = 50 mg L⁻¹, [LaCoO₃] = 200 mg L⁻¹, pH = 7.0

7.2.4 Free radical species and degradation pathways

The generated or existing free radicals in LaCoO₃/PMS suspension was determined through the trapping experiments by the addition of several scavengers. EtOH was an effective quenching agent for both SO₄^{•-} and OH[•] ($k_{\text{OH}\cdot} = (1.2\text{-}2.8) \times 10^9 \text{ M}^{-1} \text{ s}^{-1}$, $k_{\text{SO}_4^{\cdot-}} = (1.6\text{-}7.7) \times 10^7 \text{ M}^{-1} \text{ s}^{-1}$), while TBA was an effective quenching agent mainly for OH[•] ($k_{\text{OH}\cdot} = (3.8\text{-}7.6) \times 10^8 \text{ M}^{-1} \text{ s}^{-1}$), with much lower reaction rate with SO₄^{•-} ($k_{\text{SO}_4^{\cdot-}} = (4\text{-}9.1) \times 10^5 \text{ M}^{-1} \text{ s}^{-1}$) (Chen et al., 2019). Given that superoxide ([•]O₂⁻, 2.2 V) and singlet oxygen (¹O₂, 0.15 V) were also be involved in the PMS activation process, trapping tests for these two radicals were also conducted by using 1,4-benzoquinone (BZQ) and NaN₃ for [•]O₂⁻ ($2.9 \times 10^9 \text{ M}^{-1} \text{ s}^{-1}$) (Duan et al., 2020) and ¹O₂ ($2.2 \times 10^9 \text{ M}^{-1} \text{ s}^{-1}$) (Basu-Modak and Tyrrell, 1993), respectively. They displayed obvious negative effects on TC degradation, whereas the concentration variation posed insignificant influence on the degradation (Figs. 7-7 and 7-8). The inhibitions by BZQ and NaN₃ was even more obvious than those of TBA and EtOH. This is ascribed to their scavenging capability to

OH^\cdot , with the rate constant of BZQ and NaN_3 towards OH^\cdot of 1.2×10^9 and $1.1 \times 10^{10} \text{ M}^{-1} \text{ s}^{-1}$, respectively at neutral pH (Adams and Michael, 1967; Basu-Modak and Tyrrell, 1993). Judging from the small increment for additional retardation resulted from BZQ/ NaN_3 than those of TBA/EtOH, both $^1\text{O}_2$ and $^{\cdot}\text{O}_2^-$ did participate in the degradation of TC. The half-life of $^{\cdot}\text{O}_2^-$ was less than 1 ns, much shorter than $\text{SO}_4^{\cdot-}$ (30-40 μs), $^1\text{O}_2$ (3.5 μs) and OH^\cdot (20 ns) (Guerra-Rodríguez et al., 2018; Taverne et al., 2013). In light of the differences in the half-life times and oxidation ability of radicals, $\text{SO}_4^{\cdot-}$ and OH^\cdot would have the priority to react with TC than $^{\cdot}\text{O}_2^-$ and $^1\text{O}_2$ (Rao and Hayon, 1973; Tian et al., 2020).

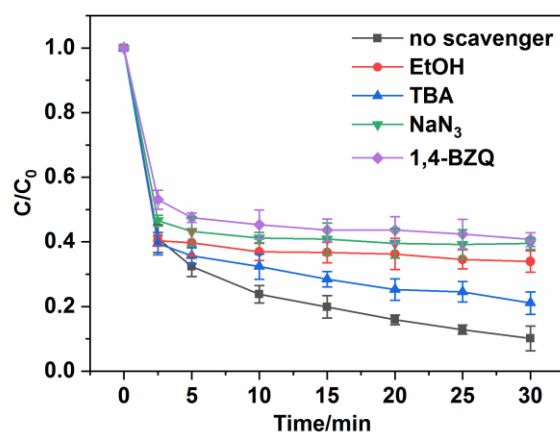


Fig. 7-7 Effect of scavengers on the degradation of TC in $\text{LaCoO}_3/\text{PMS}$ system.

General working conditions: $[\text{TC}] = 20 \text{ mg L}^{-1}$, $[\text{PMS}] = 50 \text{ mg L}^{-1}$, $[\text{LaCoO}_3] = 200 \text{ mg L}^{-1}$, $\text{pH} = 7.0$, $[\text{EtOH}] = [\text{TBA}] = 1 \text{ mol L}^{-1}$, $[\text{NaN}_3] = [\text{BZQ}] = 0.8 \text{ mol L}^{-1}$, and $\text{pH} = 7.0$

To further confirm the existence of the four ROSs mentioned above, electron paramagnetic resonance (EPR) was employed using DMPO and TEMP as typical spin trapping reagents. DMPO and TEMP as the probe compound were used to identify the generation of $\text{SO}_4^{\cdot-}$, $^{\cdot}\text{OH}$, $^{\cdot}\text{O}_2^-$ and $^1\text{O}_2$ through the formation of spin adducts including DMPO- SO_4 , DMPO-OH, DMPO-OOH and TEMPO, respectively. A strong signal of

four consecutive peaks with relative intensities of 1:2:2:1 was detected after the addition of PMS, matching well with the DMPO-OH spectra (Fig. 7-8) (Wang, X. et al., 2020). The signal for DMPO-SO₄ was detected spontaneously, with the relative intensities of 1:2:1:2 (Wang, S. et al., 2020a). This phenomenon confirmed the successful activation of PMS by LCO to produce SO₄^{•-} and [•]OH, which was well consistent with the traditional trapping tests. Besides, the appearance of 1:1:1:1 DMPO-OOH and 1:1:1 TEMPO signals provided solid evidences for the presence of [•]O₂ and ¹O₂ (Zhou et al., 2021).

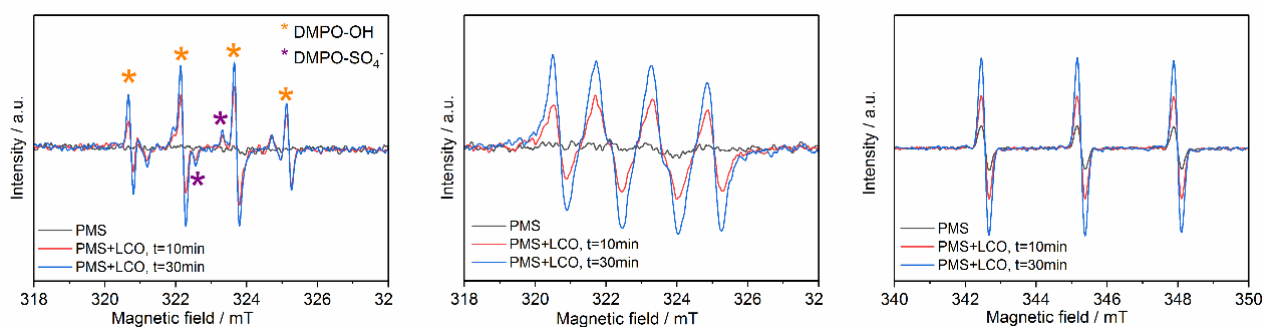


Fig. 7-8 EPR spectra of PMS activation in LaCoO₃/PMS system during the degradation of TC: (a-b) DMPO and (c) TEMP spin trapping.

General working conditions: [TC] = 20 mg L⁻¹, [PMS] = 50 mg L⁻¹, [LaCoO₃] = 200 mg L⁻¹, [DMPO] = 10 mmol L⁻¹, [TEMP] = 10 mmol L⁻¹.

The intermediate products generated in TC degradation over LaCoO₃/PMS system were identified by UPLC-MS (Fig. 7-9). Based on the generation of degradation products with lower molecular weight ($m/z \leq 220$), three degradation pathways could be proposed (Fig. 7-9). Initially, the ring structure of TC was attacked by ROSs (i.e., SO₄^{•-}, OH[•], ¹O₂ and O₂^{•-}) and further transformed into smaller molecules with progressive ring-opening. Then hydroxylation occurred, due to the generation of intermediates with

m/z of 460 and 461. Afterwards, the intermediates with m/z of 414 were obtained by demethylation under the attack of ROSs. Compared to the relevant studies on the degradation of TC by activated PMS, several degradation intermediates, i.e., P3 (m/z=415), P7 (m/z=274) and P8 (m/z=258), were frequently detected, whereas those with much lower m/z (i.e., P9, P10, P11 and P12, m/z=190) varied with the catalysts (Huang, X. et al., 2020; Li, J. et al., 2020; Ye et al., 2020). This can be justified by the intermediates with much lower m/z, resulted from the loss of some functional groups from the higher ones. But in light of the TOC removal (> 70% in 6 h, Fig. 7-10), TC and its associated intermediates could be mineralized into CO₂ and H₂O.

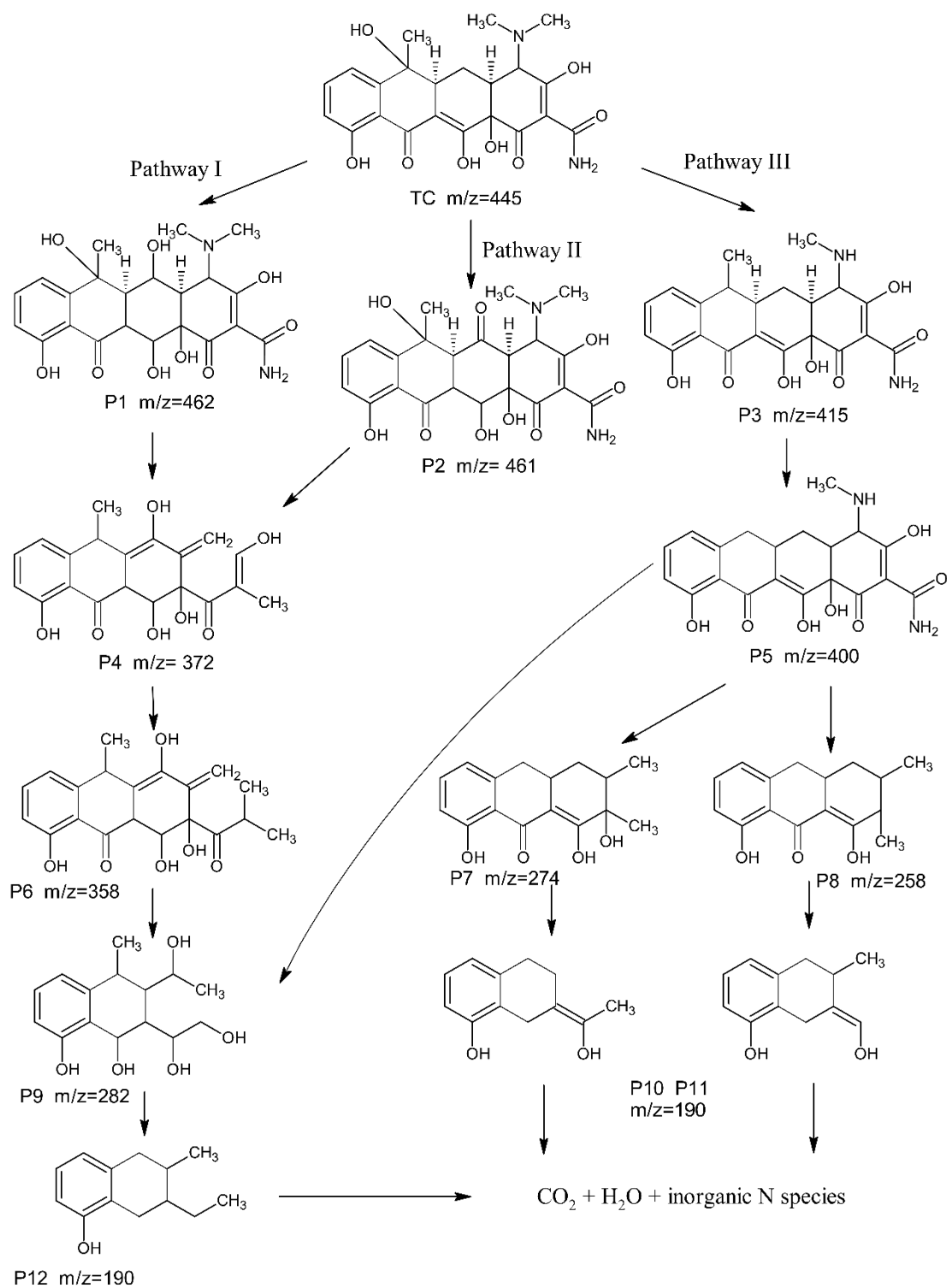


Fig. 7-9 Degradation pathways of TC in LaCoO₃/PMS system.

General working conditions: [TC] = 20 mg L⁻¹, [PMS] = 50 mg L⁻¹, [LaCoO₃] = 200 mg L⁻¹, pH = 7.0

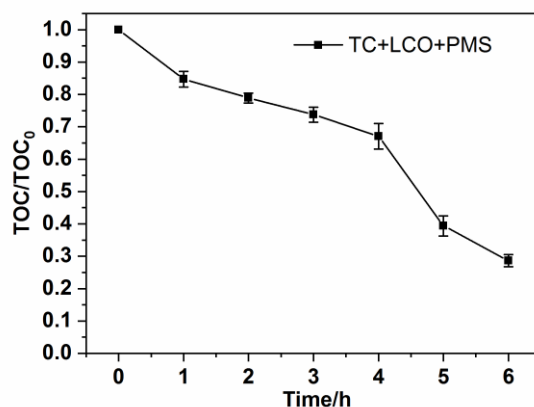
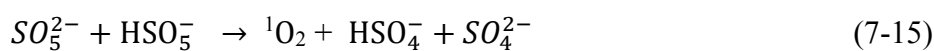
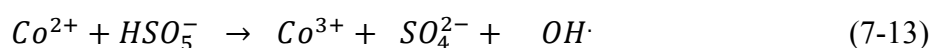
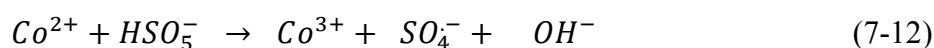
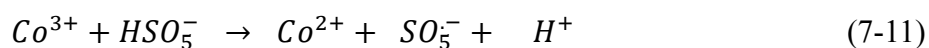


Fig. 7-10 TOC removal rate on the degradation of TC.

General working conditions: [TC] = 20 mg L⁻¹, [PMS] = 50 mg L⁻¹, [LaCoO₃] = 200 mg L⁻¹, pH = 7.0

Based on the above analysis, the preliminary degradation mechanism could be proposed. In control experiments, the sole LaCoO₃ could remove TC to a certain extent (10%), which is attributed to the adsorption on catalyst. Solely PMS addition could degrade partial TC (ca. 50%), as PMS contained HSO₅⁻ anion with strong oxidation ability, which could self-decompose into SO₄⁻ radical (Eq. (7-11)) (Zhang et al., 2019). However, the reaction between TC and inactivated PMS just transformed TC into other 4-ring molecules, rather than smaller molecules with less ring-structure (Cai, T. et al., 2020). With the co-existence of PMS and LaCoO₃, most TC was degraded and then mineralized. Based on the quenching tests, except for the dominant SO₄⁻ and OH[·] oxidation, ¹O₂ and ⁻O₂⁻ also took part in the removal of TC. SO₄⁻ and OH[·] were originated from PMS decomposition by self-decomposition or by LaCoO₃ catalysis (Eqs. (7-11) - (7-14)). Based on some previous researches, the generation of ¹O₂ mainly followed the self-decomposition of PMS at the rate constant of 0.2 M⁻¹ S⁻¹ (Eq. (7-15)) (Gao et al., 2019; Liu et al., 2018). The generated ¹O₂ could adhere to TC directly, to induce oxidative reactions, due to its high redox potential (Gao et al., 2019; Liu et al.,

2018). Additionally, $^1\text{O}_2$ could be also generated through the recombination of $\cdot\text{O}_2^-$ (Eq. (7-16)) (Jiang et al., 2020). But this reaction would consume a great amount of H^+ . Since the TC degradation was mainly carried out under neutral pH, the above reaction could be constrained. Thus, $\cdot\text{O}_2^-$ should exist in the reaction system and act as an effective radical. The formation of $\cdot\text{O}_2^-$ was far more complicated (Zhao, Y. et al., 2019). Based on Eqs. (7-17) - (7-22), $\cdot\text{O}_2^-$ was generated through a series of processes including decomposition and composition of HSO_5^- and $\text{OH}\cdot$.



7.3 Conclusions

In this study, the $\text{LaCoO}_3/\text{PMS}$ system exhibited excellent TC degradation along with

a satisfied mineralization ability and stable reusability. Under the optimal degradation condition at neutral pH, 90% of TC were removed in 30 min. Based on the traditional trapping experiments and EPR spectra, free radicals including $\text{SO}_4^{\bullet-}$, OH^{\bullet} , $^1\text{O}_2$ and $^{\bullet}\text{O}_2^-$ were involved. The main degradation pathways of TC mainly include demethylation, hydroxylation and ring-opening reactions. The degradation performance was accelerated in the presence of common inorganic anions, e.g., Cl^- , H_2PO_4^- and SO_4^{2-} , as well as humic acid at low concentration. This indicates the strong environmental adaptability of the $\text{LaCoO}_3/\text{PMS}$ system. Generally, the $\text{LaCoO}_3/\text{PMS}$ system was proved to be a rapid, economical and stable approach for the degradation of TC, which provided a novel strategy for PMS activation aiming at antibiotic removal in water and wastewater treatment.

Chapter 8 Conclusion and recommendation

8.1 Conclusions

In this study, two series of composite catalysts with CoMn_2O_4 loaded on different natural clay minerals, kaolinite (Kln) and halloysite (Hal), were successfully fabricated through co-precipitation method. After the characterization tests including crystalline structure, micromorphology and surface chemistry, their PMS activation ability were investigated thoroughly and separately towards the degradation of some typical pharmaceuticals which were frequently detected in water environment.

In order to find out the effect from the content of CMO within the composite catalysts towards their PMS activation, 20, 40, and 60-CMO/Hal were investigated and compared with bare CMO spontaneously. After that, the one with the best working performance (40-CMO/Hal) was picked out for further studies under the optimal working conditions, which was determined according to the investigations about the effects of working parameters including working pH, dosage of PMS, and initial concentrations of the target pharmaceuticals (CBZ here). The stability and durability of 40-CMO/Hal and bare CMO were explored through a three-time reuse, while the metal leakage during them were determined by ICP-OES. The potential PMS activation mechanism was proposed according to traditional trapping experiments and results obtained from electron paramagnetic resonance (EPR). The possible degradation pathways and final products of CBZ were determined based on the intermediates detected by LC-MS and the TOC results. Finally, the possible universal application of 40-CMO/Hal in removing some other common antibiotics was verified by targeting TC,

OFX and SMZ. The positive results promise the development of an effective treatment technology for the removal of common pharmaceuticals.

After that, in order to further investigate the impacts from clay mineral substrates with different morphologies towards the composite catalysts in terms of crystal structure, surface chemical properties, and defects, etc., CMO/Hal and CMO/KIn with the same CMO loading percentage (40%), were chosen again for further comparisons and investigations. The results indicated that both Hal and KIn helped to control the crystallinity of CMO spontaneously with induce oxygen vacancies (OVs), which significantly enhanced the working efficiency. The reaction rate constants of Hal/CMO and KIn/CMO towards OFX degradation were nearly triple and twice that of bare CMO, respectively, with a 60% decrease in metal usage. CMO/Hal and CMO/KIn exhibited better stability and durability than CMO, while CMO/KIn showed higher structural stability with lower metal leaching after 3 rounds of reaction than the others. The universal applicability of CMO/Hal and CMO/KIn were also verified by using three other pharmaceuticals as probes.

As for the LCO catalysts, its PMS activation ability was investigated through the degradation efficiency and decomposition mechanism of tetracycline (TC). Moreover, the effects of common inorganic anions and natural organic matter (e.g., humic acid (HA)) on TC degradation performance were also compared thoroughly. Without the presence of coexisting substance, more than 90% of TC was removed completely within 30 min under optimal working conditions with neutral pH, while a 72% mineralization rate was achieved in 6h. The presence of inorganic anions (i.e., H_2PO_4^- , Cl^- and SO_4^{2-}) and low-concentration of HA promoted the degradation. Among them, H_2PO_4^- and

lower concentration of HA showed the most obvious outcome, while SO_4^{2-} promoted the overall performance of the process by regulating the radical formation and minimizing the peak radical level. LCO exhibited stable reusability with minor decrease in TC removal, likely due to the adsorption of intermediate products from previous stages.

8.1.1 Characteristics of the CMO-based catalysts

The characterizations of bare CMO and the x -CMO/Hal series ($x=20, 40$ and 60%) in previous chapters indicated that the CMO nanoparticles were evenly distributed on the outer surface of Hal tubes with little agglomeration and smaller grain size compared to bare CMO. Besides, the presence of Hal carrier was beneficial in: 1) regulating the grain size and crystallinity of CMO particles, and 2) promoting the specific surface area by the evenly distribution of CMO particles. The smaller particle size with reduced crystallinity also helped to provide more reactive sites by forming into several indistinct lattice boundaries.

Furthermore, by comparing CMO/Hal and CMO/KIn with the same CMO loading percentage (40%), it could be found that in addition to the crystallinity control of CMO, both Hal and KIn enabled the induction of oxygen vacancies (OVs) into the composite catalyst, which would help to enhance their working efficiency by providing additional active sites for the reaction and accelerating electron transfer. Hal enabled the generation of more OVs than KIn, spontaneously with stronger suppression in CMO's grain size and crystallinity. However, the characterizations on the recycled catalysts after three times of reuse implied that CMO/KIn with higher crystallinity and ordered

structure maintained structural stability with less metal leakage than CMO/Hal.

8.1.2 Effects of CMO content and mineral substrates in pharmaceutical degradation

The effects of CMO content towards their PMS activation ability was tested through the degradation of CBZ. The reaction using bare CMO and the *x*-CMO/Hal series all followed the pseudo first-order kinetics, and the highest k_{obs} was found in 40-CMO/Hal. Comparing to bare CMO, the presence of Hal carriers helped to enhance the catalytic activity of the *x*-CMO/Hal ones by controlling the grain size, suppressing the unidirectional crystallization, and promoting the evenly dispersion of CMO. However, the overdosed CMO on Hal also brought negative effects towards the degradation, as the aggregates and seriously clustered CMO particles piled on Hal would block the active sites on the catalysts.

The effects of different mineral substrates, Hal and KIn, towards their PMS activation ability was investigated using OFX as target compound. Based on the previous works, 40-CMO/Hal (*Abbrev.* CMO/Hal) with the best working performance was chosen for further studies, and the corresponding 40-CMO/KIn (CMO/KIn), along with bare CMO, were used for comparison. The results showed that the presence of either Hal or KIn alleviated the crystallinity and grain size of CMO, spontaneously with inducing abundant oxygen vacancies into the composite catalyst. Among them, CMO/Hal showed the highest reaction rate constants and the least residue OFX, followed by CMO/KIn and bare CMO. Since the working efficiency of CMO/Hal, CMO/KIn and bare CMO was proportional to their OV content, it was reasonable to infer that the

existence of OVs contributed to promoting PMS decomposition.

8.1.3 Effects of working parameters on the degradation

The determination of optimal working conditions in both Chapter 5 and Chapter 6 were based on the results of controlled variable experiments with comprehensive analysis.

For CBZ degradation, the dosage of catalyst and PMS were 200 mg L^{-1} and 0.1 mM , separately, and the working pH was controlled at 5.8, a near neutral one. Excessive dosage of PMS would retard the degradation due to the scavenging effect from HSO_5^- to the generated $\text{SO}_4^{\cdot-}$. The optimum working pH was close to the pH_{pzc} of the catalyst and could help to keep the stability of HSO_5^- .

The situation for OFX degradation using bare CMO, CMO/Hal and CMO/KIn was similar to CBZ degradation above, and the optimal working pH was set as 6.5 for both CMO/Hal and CMO/KIn according to the pH_{pzc} of the catalysts and the acid dissociation constants for both PMS and OFX.

8.1.4 Reaction mechanisms of the degradation process

The existence and contributions of the reactive oxygen species (ROS) involved in the degradation were determined separately by EPR using DMPO and TEMP as spin-trapping reagents, and traditional trapping experiments with MeOH, TBA, NaN_3 and BZQ as scavengers. The results showed that $\text{SO}_4^{\cdot-}$, OH^\cdot , $\text{O}_2^{\cdot-}$ and $^1\text{O}_2$ were all

generated during PMS activation using the fabricated catalysts, and contributed to the removal of target pharmaceuticals. Besides, the OVs on the surface of catalysts promoted the interfacial electron transfer and boosted the generation of $^1\text{O}_2$, which might demonstrate to higher OFX decomposition efficiency, since $^1\text{O}_2$ contributes specifically to the hydroxylation of phenolate and phenolic groups in addition to $\text{SO}_4^{\cdot-}$ and OH^\cdot , which would benefit the followed mineralization.

Based on the LC-MS and TOC results, it was clear that about 60% of CBZ could be mineralized using PMS activated by 40-CMO/Hal, and the main decomposition of CBZ included oxidation, hydrolysis and the cleavage of rings. As for OFX, its main decomposition route included decarboxylation, hydroxylation, piperazinyl dealkylation, oxidation of hydroxyl group and ring cleavage. Since the mineralization rate of OFX using CMO/Hal and CMO/KIn were 35% and 25%, separately, it could be concluded that CMO/Hal showed better performance in the decomposition of OFX.

8.1.5 Reusability and stability of the catalysts

The continuous batch reuse experiments showed that although both bare CMO and 40-CMO/Hal were still effective after three times working, the metal leakage of Co and Mn from 40-CMO/Hal was still 40% lower than those from bare CMO, even though the CMO content within it was 40% of the bare ones. The results indicated that Hal carrier contributed to the reduction of metal leaching, which minimized the second contamination and maintained the degradation efficiency.

The situation in Chapter 6 was similar, as both CMO/Hal and CMO/KIn maintained

satisfied catalytic performance after three reuses with little deterioration. The metal leakage of CMO/Hal and CMO/Kln was obviously alleviated comparing to bare CMO, and CMO/Kln showed the lowest metal leaching. Besides, based on the XRD analysis, the almost unchanged pattern of CMO/Kln with only slight decrease in its relative intensity implied its hardly affected crystallinity, while the deterioration for CMO/Hal was far more obvious. This implies that Kln substrate was advantageous in maintaining structural stability.

8.1.6 Universal application of the catalysts

The possible universal application of 40-CMO/Hal (i.e., CMO/Hal) and 40-CMO/Kln (i.e., CMO/Kln) were tested in removing some other common pharmaceuticals in addition to the target contaminants which were studied in detail. The results confirmed the effectiveness of these processes, as the degradation rates obtained were at least 65% in 30 min, or at least 80% in 40 min.

8.2 Limitations of this study and recommendations for future work

The experimental results and corresponding analysis of this work revealed the effectiveness and efficiency of the investigated SR-AOPs using PMS activated by CMO loaded on natural clay minerals with the same chemical composition but different morphologies, halloysite (Hal) and kaolinite (Kln). The modified catalysts, either CMO/Hal or CMO/Kln, both overcame the disadvantages of bare CMO (i.e. higher metal leaching and production costs), spontaneously with promoting their PMS

activation efficiency for the degradation of pharmaceuticals. The presence of Hal and KIn contributed to the regulation of CMO particles' grain size and crystallinity, the promotion of specific surface area by the evenly distribution of CMO particles, and the induction of more active OVs. Furthermore, Hal was advantageous in the generation of more OVs with a stronger suppression in CMO's grain size and crystallinity, while CMO/KIn with higher crystallinity and ordered structure maintained better structural stability with less metal leakage. These works shed lights on the application of natural minerals in the modification of transition metal catalysts aimed at heterogeneous PMS activation with enhanced catalytic ability and lower environmental impact in the remediation of pharmaceuticals in wastewater.

However, there still existed some limitations in this work. Firstly, the research experiments in this work were generally performed in laboratory using batch reactors, and focused more on the elimination of single target compound each time in aqueous solution. In order to lay a solid foundation for its future practical applications, it is necessary to conduct continuous pilot tests with the consideration of more relevant elements, *e.g.*, the coexistence of multi chemicals or pharmaceutical contaminants, and the effects of some naturally occurring microorganisms and algae in water. Besides, pilot-scale experiments using real wastewater with abundant pharmaceuticals, *e.g.*, effluents from pharmaceutical industries and hospitals are strongly recommended.

Secondly, although CMO/Hal and CMO/KIn catalysts fabricated in this work both showed superior PMS activity in degrading pharmaceuticals than bare CMO spontaneously with different strengths, they still had some limitations, *e.g.*, the unbalanced improvement of both catalytic activity and structural stability, and the

unavoidable metal leaching. Thus, these catalysts could be further modified or inducing more active sites in the future. Besides, hybrid processes which combined the current catalyst/PMS reaction system with other technologies including membrane and ultrasonic would be worthy of an attempt, which might alleviate the passivation of the catalysts, and simplify the recycle processes. For example, nano-sized catalysts with extremely small grain size are generally considered with hard, time-consuming, and high mass loss during their separation from treated water. Therefore, by entrapping nanocatalysts directly into the pores of porous catalytic membranes can promote the collaborative separation simultaneously with enhanced catalytic efficiency. Among various membrane materials, polyvinylidene difluoride (PVDF), an electroactive semicrystalline thermoplastic material, has received increasing attention with high practicality in water purification due to its high mechanical strength and chemical stability, flexibility, cost-effective, and environmentally friendly (Yao et al., 2022). Previous researches implied that enhanced degradation efficiency can be achieved by inducing nanoparticles into the pores of the porous PVDF membrane through phase inversion (Yao et al., 2022). Therefore, it might be feasible to immobilize the CMO/Hal and/or CMO/KIn catalysts into PVDF membrane through traditional phase conversion method for pharmaceutical degradation via PMS activation. Besides, the working efficiency of heterogenous CMO-based catalysts can also be enhanced through external energy due to synergistic effects, such as photo irradiation, microwave, ultrasound, and electric field (Wei et al., 2022).

Thirdly, although a certain percentage of the contaminants could be mineralized into CO₂ and H₂O after the SR-AOP treatment, and the intermediates generated during the degradation was identified, the toxicology experiments were not performed.

References

- Abat, C., Rolain, J.-M., Dubourg, G., Fournier, P.-E., Chaudet, H., Raoult, D., 2017. Evaluating the Clinical Burden and Mortality Attributable to Antibiotic Resistance: The Disparity of Empirical Data and Simple Model Estimations. *Clin. Infect. Dis.* 65(suppl_1), S58-S63. <https://doi.org/10.1093/cid/cix346>.
- Abu Shmeis, R.M., 2018. Chapter One - Water Chemistry and Microbiology, in: Chormey, D.S., Bakirdere, S., Turan, N.B., Engin, G.Ö. (Eds.), *Comprehensive Analytical Chemistry*. Elsevier, pp. 1-56. <https://doi.org/https://doi.org/10.1016/bs.coac.2018.02.001>.
- Adams, G.E., Michael, B.D., 1967. Pulse radiolysis of benzoquinone and hydroquinone. Semiquinone formation by water elimination from trihydroxy-cyclohexadienyl radicals. *Transactions of the Faraday Society* 63(0), 1171-1180. <https://doi.org/10.1039/TF9676301171>.
- Ahmed, M.B., Zhou, J.L., Ngo, H.H., Guo, W., Thomaidis, N.S., Xu, J., 2017. Progress in the biological and chemical treatment technologies for emerging contaminant removal from wastewater: A critical review. *J. Hazard. Mater.* 323, 274-298. <https://doi.org/https://doi.org/10.1016/j.jhazmat.2016.04.045>.
- Ahmed, S.F., Mofijur, M., Nuzhat, S., Chowdhury, A.T., Rafa, N., Uddin, M.A., Inayat, A., Mahlia, T.M.I., Ong, H.C., Chia, W.Y., Show, P.L., 2021. Recent developments in physical, biological, chemical, and hybrid treatment techniques for removing emerging contaminants from wastewater. *J. Hazard. Mater.* 416, 125912. <https://doi.org/10.1016/j.jhazmat.2021.125912>.
- Alfonso-Muniozguren, P., Serna-Galvis, E.A., Bussemaker, M., Torres-Palma, R.A., Lee, J., 2021. A review on pharmaceuticals removal from waters by single and

- combined biological, membrane filtration and ultrasound systems. *Ultrason. Sonochem.* 76, 105656. <https://doi.org/10.1016/j.ultsonch.2021.105656>.
- Ali, J., Shahzad, A., Wang, J., Ifthikar, J., Lei, W., Aregay, G.G., Chen, Z., Chen, Z., 2021. Modulating the redox cycles of homogenous Fe(III)/PMS system through constructing electron rich thiomolybdate centres in confined layered double hydroxides. *Chem. Eng. J.* 408, 127242. <https://doi.org/10.1016/j.cej.2020.127242>.
- Alkhouraji, T.S., 2019. Advanced oxidation process based on water radiolysis to degrade and mineralize diclofenac in aqueous solutions. *Science of The Total Environment* 688, 708-717. <https://doi.org/https://doi.org/10.1016/j.scitotenv.2019.06.164>.
- Almasri, D.A., Saleh, N.B., Atieh, M.A., McKay, G., Ahzi, S., 2019. Adsorption of phosphate on iron oxide doped halloysite nanotubes. *Scientific Reports* 9(1). <https://doi.org/10.1038/s41598-019-39035-2>.
- An, W., Tian, L., Hu, J., Liu, L., Cui, W., Liang, Y., 2020. Efficient degradation of organic pollutants by catalytic ozonation and photocatalysis synergy system using double-functional MgO/g-C₃N₄ catalyst. *Appl. Surf. Sci.* 534, 147518. <https://doi.org/https://doi.org/10.1016/j.apsusc.2020.147518>.
- Andreozzi, R., Caprio, V., Insola, A., Marotta, R., 1999. Advanced oxidation processes (AOP) for water purification and recovery. *Catal. Today* 53(1), 51-59. [https://doi.org/https://doi.org/10.1016/S0920-5861\(99\)00102-9](https://doi.org/https://doi.org/10.1016/S0920-5861(99)00102-9).
- Anipsitakis, G.P., Dionysiou, D.D., 2003. Degradation of Organic Contaminants in Water with Sulfate Radicals Generated by the Conjunction of Peroxymonosulfate with Cobalt. *Environ. Sci. Technol.* 37(20), 4790-4797. <https://doi.org/10.1021/es0263792>.

- Anipsitakis, G.P., Dionysiou, D.D., 2004. Radical Generation by the Interaction of Transition Metals with Common Oxidants. *Environ. Sci. Technol.* 38(13), 3705-3712. <https://doi.org/10.1021/es035121o>.
- Anis, S.F., Hashaikeh, R., Hilal, N., 2019. Reverse osmosis pretreatment technologies and future trends: A comprehensive review. *Desalination* 452, 159-195. <https://doi.org/https://doi.org/10.1016/j.desal.2018.11.006>.
- Archana, P.S., Jose, R., Vijila, C., Ramakrishna, S., 2009. Improved Electron Diffusion Coefficient in Electrospun TiO₂ Nanowires. *The Journal of Physical Chemistry C* 113(52), 21538-21542. <https://doi.org/10.1021/jp908238q>.
- Baalbaki, A., Ayoub, G.M., Al-Hindi, M., Ghauch, A., 2017. The fate of selected pharmaceuticals in solar stills: Transfer, thermal degradation or photolysis? *Science of The Total Environment* 574, 583-593. <https://doi.org/10.1016/j.scitotenv.2016.09.082>.
- Banza, C.L.N., Nawrot, T.S., Haufroid, V., Decrée, S., De Putter, T., Smolders, E., Kabyla, B.I., Luboya, O.N., Ilunga, A.N., Mutombo, A.M., Nemery, B., 2009. High human exposure to cobalt and other metals in Katanga, a mining area of the Democratic Republic of Congo. *Environ. Res.* 109(6), 745-752. <https://doi.org/10.1016/j.envres.2009.04.012>.
- Bao, T., Dامتie, M.M., Hosseinzadeh, A., Wei, W., Jin, J., Phong Vo, H.N., Ye, J.S., Liu, Y., Wang, X.F., Yu, Z.M., Chen, Z.J., Wu, K., Frost, R.L., Ni, B.-J., 2020. Bentonite-supported nano zero-valent iron composite as a green catalyst for bisphenol A degradation: Preparation, performance, and mechanism of action. *Journal of Environmental Management* 260, 110105. <https://doi.org/10.1016/j.jenvman.2020.110105>.
- Bao, T., Dامتie, M.M., Wu, K., Wei, X.L., Zhang, Y., Chen, J., Deng, C.X., Jin, J., Yu,

- Z.M., Wang, L., Frost, R.L., 2019. Rectorite-supported nano-Fe₃O₄ composite materials as catalyst for P-chlorophenol degradation: Preparation, characterization, and mechanism. *Appl. Clay Sci.* 176, 66-77. <https://doi.org/https://doi.org/10.1016/j.clay.2019.04.020>.
- Barrios, B., Mohrhardt, B., Doskey, P.V., Minakata, D., 2021. Mechanistic Insight into the Reactivities of Aqueous-Phase Singlet Oxygen with Organic Compounds. *Environ. Sci. Technol.* 55(12), 8054-8067. <https://doi.org/10.1021/acs.est.1c01712>.
- Barzegar, G., Jorfi, S., Zarezade, V., Khatebasreh, M., Mehdipour, F., Ghanbari, F., 2018. 4-Chlorophenol degradation using ultrasound/peroxymonosulfate/nanoscale zero valent iron: Reusability, identification of degradation intermediates and potential application for real wastewater. *Chemosphere* 201, 370-379. <https://doi.org/10.1016/j.chemosphere.2018.02.143>.
- Basu-Modak, S., Tyrrell, R.M., 1993. Singlet Oxygen: A Primary Effector in the Ultraviolet A/Near-Visible Light Induction of the Human Heme Oxygenase Gene. *Cancer Res.* 53(19), 4505.
- Bentley, R., 2009. Different roads to discovery; Prontosil (hence sulfa drugs) and penicillin (hence β -lactams). *J. Ind. Microbiol. Biotechnol.* 36(6), 775-786. <https://doi.org/10.1007/s10295-009-0553-8>.
- Björleinius, B., Ripszám, M., Haglund, P., Lindberg, R.H., Tysklind, M., Fick, J., 2018. Pharmaceutical residues are widespread in Baltic Sea coastal and offshore waters – Screening for pharmaceuticals and modelling of environmental concentrations of carbamazepine. *Science of The Total Environment* 633, 1496-1509. <https://doi.org/https://doi.org/10.1016/j.scitotenv.2018.03.276>.

- Brandão, F.P., Rodrigues, S., Castro, B.B., Gonçalves, F., Antunes, S.C., Nunes, B., 2013. Short-term effects of neuroactive pharmaceutical drugs on a fish species: Biochemical and behavioural effects. *Aquat. Toxicol.* 144-145, 218-229. <https://doi.org/https://doi.org/10.1016/j.aquatox.2013.10.005>.
- Brigatti, M.F., Galán, E., Theng, B.K.G., 2013. Chapter 2 - Structure and Mineralogy of Clay Minerals, in: Bergaya, F., Lagaly, G. (Eds.), *Developments in Clay Science*. Elsevier, pp. 21-81. <https://doi.org/https://doi.org/10.1016/B978-0-08-098258-8.00002-X>.
- Brodin, T., Fick, J., Jonsson, M., Klaminder, J., 2013. Dilute Concentrations of a Psychiatric Drug Alter Behavior of Fish from Natural Populations. *Science* 339(6121), 814-815. <https://doi.org/10.1126/science.1226850>.
- Bu, Q., Shi, X., Yu, G., Huang, J., Wang, B., 2016. Assessing the persistence of pharmaceuticals in the aquatic environment: Challenges and needs. *Emerging Contaminants* 2(3), 145-147. <https://doi.org/https://doi.org/10.1016/j.emcon.2016.05.003>.
- Büchele, S., Chen, Z., Fako, E., Krumeich, F., Hauert, R., Safonova, O.V., López, N., Mitchell, S., Pérez - Ramírez, J., 2020. Carrier - Induced Modification of Palladium Nanoparticles on Porous Boron Nitride for Alkyne Semi - Hydrogenation. *Angew. Chem. Int. Ed.* 59(44), 19639-19644. <https://doi.org/10.1002/anie.202005842>.
- Cai, C., Kang, S., Xie, X., Liao, C., Duan, X., Dionysiou, D.D., 2020. Efficient degradation of bisphenol A in water by heterogeneous activation of peroxymonosulfate using highly active cobalt ferrite nanoparticles. *J. Hazard. Mater.* 399, 122979. <https://doi.org/10.1016/j.jhazmat.2020.122979>.
- Cai, C., Zhang, H., Zhong, X., Hou, L., 2015. Ultrasound enhanced heterogeneous

- activation of peroxymonosulfate by a bimetallic Fe–Co/SBA-15 catalyst for the degradation of Orange II in water. *J. Hazard. Mater.* 283, 70-79. <https://doi.org/10.1016/j.jhazmat.2014.08.053>.
- Cai, J., Niu, T., Shi, P., Zhao, G., 2019. Boron - Doped Diamond for Hydroxyl Radical and Sulfate Radical Anion Electrogenation, Transformation, and Voltage - Free Sustainable Oxidation. *Small* 15(48), 1900153. <https://doi.org/10.1002/sml.201900153>.
- Cai, T., Bu, L., Wu, Y., Zhou, S., Shi, Z., 2020. Accelerated degradation of bisphenol A induced by the interaction of EGCG and Cu(II) in Cu(II)/EGCG/peroxymonosulfate process. *Chem. Eng. J.* 395, 125134. <https://doi.org/10.1016/j.cej.2020.125134>.
- Cao, J., Lai, L., Lai, B., Yao, G., Chen, X., Song, L., 2019. Degradation of tetracycline by peroxymonosulfate activated with zero-valent iron: Performance, intermediates, toxicity and mechanism. *Chem. Eng. J.* 364, 45-56. <https://doi.org/10.1016/j.cej.2019.01.113>.
- Capodaglio, A.G., 2017. High-energy oxidation process: an efficient alternative for wastewater organic contaminants removal. *Clean Technologies and Environmental Policy* 19(8), 1995-2006. <https://doi.org/10.1007/s10098-017-1410-5>.
- Carneiro, R.B., Gonzalez-Gil, L., Londoño, Y.A., Zaiat, M., Carballa, M., Lema, J.M., 2020. Acidogenesis is a key step in the anaerobic biotransformation of organic micropollutants. *J. Hazard. Mater.* 389, 121888. <https://doi.org/https://doi.org/10.1016/j.jhazmat.2019.121888>.
- Challis, J.K., Hanson, M.L., Friesen, K.J., Wong, C.S., 2014. A critical assessment of the photodegradation of pharmaceuticals in aquatic environments: defining our

- current understanding and identifying knowledge gaps. *Environmental Science: Processes & Impacts* 16(4), 672. <https://doi.org/10.1039/c3em00615h>.
- Changotra, R., Guin, J.P., Varshney, L., Dhir, A., 2018. Assessment of reaction intermediates of gamma radiation-induced degradation of ofloxacin in aqueous solution. *Chemosphere* 208, 606-613. <https://doi.org/10.1016/j.chemosphere.2018.06.003>.
- Chaturvedi, N.K., Katoch, S.S., 2019. Effect of various parameters during degradation of toxic p-anisidine by Fenton's oxidation. *Applied Water Science* 10(1), 18. <https://doi.org/10.1007/s13201-019-1106-6>.
- Chen, G., Zhang, X., Gao, Y., Zhu, G., Cheng, Q., Cheng, X., 2019. Novel magnetic MnO₂/MnFe₂O₄ nanocomposite as a heterogeneous catalyst for activation of peroxymonosulfate (PMS) toward oxidation of organic pollutants. *Sep. Purif. Technol.* 213, 456-464. <https://doi.org/10.1016/j.seppur.2018.12.049>.
- Chen, L., Ding, D., Liu, C., Cai, H., Qu, Y., Yang, S., Gao, Y., Cai, T., 2018. Degradation of norfloxacin by CoFe₂O₄-GO composite coupled with peroxymonosulfate: A comparative study and mechanistic consideration. *Chem. Eng. J.* 334, 273-284. <https://doi.org/10.1016/j.cej.2017.10.040>.
- Chen, L., Zhang, Y., Ma, C., 2020. Perovskites Sr_xLa_{1-x}Mn_yCo_{1-y}O_{3-δ} coated on Ti as stable non-noble anode for efficient electrocatalytic oxidation of organic wastewater containing ammonia nitrogen. *Chem. Eng. J.* 393, 124514. <https://doi.org/10.1016/j.cej.2020.124514>.
- Chen, N., Fang, G., Zhu, C., Wu, S., Liu, G., Dionysiou, D.D., Wang, X., Gao, J., Zhou, D., 2020. Surface-bound radical control rapid organic contaminant degradation through peroxymonosulfate activation by reduced Fe-bearing smectite clays. *J. Hazard. Mater.* 389, 121819. <https://doi.org/10.1016/j.jhazmat.2019.121819>.

- Chen, Z., Bi, S., Zhao, G., Chen, Y., Hu, Y., 2020. Enhanced degradation of triclosan by cobalt manganese spinel-type oxide activated peroxymonosulfate oxidation process via sulfate radicals and singlet oxygen: Mechanisms and intermediates identification. *Science of The Total Environment* 711, 134715. <https://doi.org/https://doi.org/10.1016/j.scitotenv.2019.134715>.
- Cheng, C., Gao, S., Zhu, J., Wang, G., Wang, L., Xia, X., 2020. Enhanced performance of LaFeO₃ perovskite for peroxymonosulfate activation through strontium doping towards 2,4-D degradation. *Chem. Eng. J.* 384, 123377. <https://doi.org/10.1016/j.cej.2019.123377>.
- Cheng, N., Wang, B., Wu, P., Lee, X., Xing, Y., Chen, M., Gao, B., 2021. Adsorption of emerging contaminants from water and wastewater by modified biochar: A review. *Environ. Pollut.* 273, 116448. <https://doi.org/https://doi.org/10.1016/j.envpol.2021.116448>.
- China, M.o.E.a.E.o.t.P.s.R.o., 2002. Environmental quality standard for surface water (GB 3838-2002). Beijing, China.
- Chokawa, K., Narita, T., Kikuta, D., Shiozaki, K., Kachi, T., Oshiyama, A., Shiraishi, K., 2020. Absence of Oxygen-Vacancy-Related Deep Levels in the Amorphous Mixed Oxide (Al₂O₃)_{1-x}(SiO₂)_x : First-Principles Exploration of Gate Oxides in GaN-Based Power Devices. *Physical Review Applied* 14(1). <https://doi.org/10.1103/PhysRevApplied.14.014034>.
- Chung, H.S., Choi, J.-H., Abd El-Aty, A.M., Lee, Y.-J., Lee, H.S., Kim, S., Jung, H.-J., Kang, T.-W., Shin, H.-C., Shim, J.-H., 2016. Simultaneous determination of seven multiclass veterinary antibiotics in surface water samples in the Republic of Korea using liquid chromatography with tandem mass spectrometry. *J. Sep. Sci.* 39(24), 4688-4699. <https://doi.org/10.1002/jssc.201600968>.

- Dai, J., Zhu, Y., Zhong, Y., Miao, J., Lin, B., Zhou, W., Shao, Z., 2018. Enabling High and Stable Electrocatalytic Activity of Iron - Based Perovskite Oxides for Water Splitting by Combined Bulk Doping and Morphology Designing. *Advanced Materials Interfaces* 6(1), 1801317. <https://doi.org/10.1002/admi.201801317>.
- Dasgupta, A., Klein, K., 2014. Chapter 3 - Oxidative Stress Induced by Air Pollution and Exposure to Sunlight, in: Dasgupta, A., Klein, K. (Eds.), *Antioxidants in Food, Vitamins and Supplements*. Elsevier, San Diego, pp. 41-57. <https://doi.org/https://doi.org/10.1016/B978-0-12-405872-9.00003-3>.
- de Solla, S.R., Gilroy, È.A.M., Klinck, J.S., King, L.E., McInnis, R., Struger, J., Backus, S.M., Gillis, P.L., 2016. Bioaccumulation of pharmaceuticals and personal care products in the unionid mussel *Lasmigona costata* in a river receiving wastewater effluent. *Chemosphere* 146, 486-496. <https://doi.org/https://doi.org/10.1016/j.chemosphere.2015.12.022>.
- Deng, J., Cheng, Y.-q., Lu, Y.-a., Crittenden, J.C., Zhou, S.-q., Gao, N.-y., Li, J., 2017. Mesoporous manganese Cobaltite nanocages as effective and reusable heterogeneous peroxymonosulfate activators for Carbamazepine degradation. *Chem. Eng. J.* 330, 505-517. <https://doi.org/https://doi.org/10.1016/j.cej.2017.07.149>.
- Deng, Y., Debognies, A., Zhang, Q., Zhang, Z., Zhou, Z., Zhang, J., Sun, L., Lu, T., Qian, H., 2022. Effects of ofloxacin on the structure and function of freshwater microbial communities. *Aquat. Toxicol.* 244, 106084. <https://doi.org/10.1016/j.aquatox.2022.106084>.
- Ding, M., Chen, W., Xu, H., Shen, Z., Lin, T., Hu, K., Kong, Q., Yang, G., Xie, Z., 2019. Heterogeneous Fe₂CoTi₃O₁₀-MXene composite catalysts: Synergistic effect of

- the ternary transition metals in the degradation of 2,4-dichlorophenoxyacetic acid based on peroxymonosulfate activation. *Chem. Eng. J.* 378, 122177. <https://doi.org/https://doi.org/10.1016/j.cej.2019.122177>.
- Ding, Y., Wang, X., Fu, L., Peng, X., Pan, C., Mao, Q., Wang, C., Yan, J., 2021. Nonradicals induced degradation of organic pollutants by peroxydisulfate (PDS) and peroxymonosulfate (PMS): Recent advances and perspective. *Science of The Total Environment* 765, 142794. <https://doi.org/https://doi.org/10.1016/j.scitotenv.2020.142794>.
- Dojcinovic, M.P., Vasiljevic, Z.Z., Pavlovic, V.P., Barisic, D., Pajic, D., Tadic, N.B., Nikolic, M.V., 2021. Mixed Mg–Co spinel ferrites: Structure, morphology, magnetic and photocatalytic properties. *J. Alloys Compd.* 855, 157429. <https://doi.org/10.1016/j.jallcom.2020.157429>.
- Dolar, D., Košutić, K., 2013. Chapter 10 - Removal of Pharmaceuticals by Ultrafiltration (UF), Nanofiltration (NF), and Reverse Osmosis (RO), in: Petrovic, M., Barcelo, D., Pérez, S. (Eds.), *Comprehensive Analytical Chemistry*. Elsevier, pp. 319-344. <https://doi.org/https://doi.org/10.1016/B978-0-444-62657-8.00010-0>.
- Dong, C., Bao, Y., Sheng, T., Yi, Q., Zhu, Q., Shen, B., Xing, M., Lo, I.M.C., Zhang, J., 2021. Singlet oxygen triggered by robust bimetallic MoFe/TiO₂ nanospheres of highly efficacy in solar-light-driven peroxymonosulfate activation for organic pollutants removal. *Appl. Catal., B* 286, 119930. <https://doi.org/10.1016/j.apcatb.2021.119930>.
- Dong, X., Duan, X., Sun, Z., Zhang, X., Li, C., Yang, S., Ren, B., Zheng, S., Dionysiou, D.D., 2020a. Natural illite-based ultrafine cobalt oxide with abundant oxygen-vacancies for highly efficient Fenton-like catalysis. *Appl. Catal., B* 261, 118214.

- <https://doi.org/10.1016/j.apcatb.2019.118214>.
- Dong, X., Ren, B., Sun, Z., Li, C., Zhang, X., Kong, M., Zheng, S., Dionysiou, D.D., 2019. Monodispersed CuFe₂O₄ nanoparticles anchored on natural kaolinite as highly efficient peroxymonosulfate catalyst for bisphenol A degradation. *Appl. Catal., B* 253, 206-217. <https://doi.org/10.1016/j.apcatb.2019.04.052>.
- Dong, X., Ren, B., Zhang, X., Liu, X., Sun, Z., Li, C., Tan, Y., Yang, S., Zheng, S., Dionysiou, D.D., 2020b. Diatomite supported hierarchical 2D CoNi₃O₄ nanoribbons as highly efficient peroxymonosulfate catalyst for atrazine degradation. *Appl. Catal., B* 272, 118971. <https://doi.org/10.1016/j.apcatb.2020.118971>.
- Duan, P., Qi, Y., Feng, S., Peng, X., Wang, W., Yue, Y., Shang, Y., Li, Y., Gao, B., Xu, X., 2020. Enhanced degradation of clothianidin in peroxymonosulfate/catalyst system via core-shell FeMn @ N-C and phosphate surrounding. *Appl. Catal., B* 267, 118717. <https://doi.org/10.1016/j.apcatb.2020.118717>.
- Duan, X., Su, C., Miao, J., Zhong, Y., Shao, Z., Wang, S., Sun, H., 2018. Insights into perovskite-catalyzed peroxymonosulfate activation: Maneuverable cobalt sites for promoted evolution of sulfate radicals. *Appl. Catal., B* 220, 626-634. <https://doi.org/10.1016/j.apcatb.2017.08.088>.
- Dung, N.T., Thu, T.V., Van Nguyen, T., Thuy, B.M., Hatsukano, M., Higashimine, K., Maenosono, S., Zhong, Z., 2020. Catalytic activation of peroxymonosulfate with manganese cobaltite nanoparticles for the degradation of organic dyes. *RSC Advances* 10(7), 3775-3788. <https://doi.org/10.1039/c9ra10169a>.
- Durán-Álvarez, J.C., Avella, E., Ramírez-Zamora, R.M., Zanella, R., 2016. Photocatalytic degradation of ciprofloxacin using mono- (Au, Ag and Cu) and bi- (Au–Ag and Au–Cu) metallic nanoparticles supported on TiO₂ under UV-C

- and simulated sunlight. *Catal. Today* 266, 175-187.
<https://doi.org/https://doi.org/10.1016/j.cattod.2015.07.033>.
- Ebele, A.J., Abou-Elwafa Abdallah, M., Harrad, S., 2017. Pharmaceuticals and personal care products (PPCPs) in the freshwater aquatic environment. *Emerging Contaminants* 3(1), 1-16. <https://doi.org/10.1016/j.emcon.2016.12.004>.
- Eckstein, G., 2015. DRUGS ON TAP: MANAGING PHARMACEUTICALS IN OUR NATION'S WATERS. *New York University Environmental Law Journal* 23, 36.
- Eggen, T., Vogelsang, C., 2015. Chapter 7 - Occurrence and Fate of Pharmaceuticals and Personal Care Products in Wastewater, in: Zeng, E.Y. (Ed.) *Comprehensive Analytical Chemistry*. Elsevier, pp. 245-294.
<https://doi.org/https://doi.org/10.1016/B978-0-444-63299-9.00007-7>.
- Espíndola, J.C., Szymański, K., Cristóvão, R.O., Mendes, A., Vilar, V.J.P., Mozia, S., 2019. Performance of hybrid systems coupling advanced oxidation processes and ultrafiltration for oxytetracycline removal. *Catal. Today* 328, 274-280.
<https://doi.org/10.1016/j.cattod.2018.12.040>.
- Fang, G., Gao, J., Dionysiou, D.D., Liu, C., Zhou, D., 2013. Activation of Persulfate by Quinones: Free Radical Reactions and Implication for the Degradation of PCBs. *Environ. Sci. Technol.* 47(9), 4605-4611. <https://doi.org/10.1021/es400262n>.
- Fatimah, I., Fadillah, G., Yanti, I., Doong, R.-a., 2022. Clay-Supported Metal Oxide Nanoparticles in Catalytic Advanced Oxidation Processes: A Review. *Nanomaterials* 12(5), 825. <https://doi.org/10.3390/nano12050825>.
- Fatta-Kassinos, D., Vasquez, M.I., Kümmerer, K., 2011. Transformation products of pharmaceuticals in surface waters and wastewater formed during photolysis and advanced oxidation processes – Degradation, elucidation of byproducts and assessment of their biological potency. *Chemosphere* 85(5), 693-709.

- <https://doi.org/10.1016/j.chemosphere.2011.06.082>.
- Feng, Y., Wu, D., Deng, Y., Zhang, T., Shih, K., 2016. Sulfate Radical-Mediated Degradation of Sulfadiazine by CuFeO₂ Rhombohedral Crystal-Catalyzed Peroxymonosulfate: Synergistic Effects and Mechanisms. *Environ. Sci. Technol.* 50(6), 3119-3127. <https://doi.org/10.1021/acs.est.5b05974>.
- Frascaroli, G., Reid, D., Hunter, C., Roberts, J., Helwig, K., Spencer, J., Escudero, A., 2021. Pharmaceuticals in Wastewater Treatment Plants: A Systematic Review on the Substances of Greatest Concern Responsible for the Development of Antimicrobial Resistance. *Applied Sciences* 11(15). <https://doi.org/10.3390/app11156670>.
- Gadipelly, C., Pérez-González, A., Yadav, G.D., Ortiz, I., Ibáñez, R., Rathod, V.K., Marathe, K.V., 2014. Pharmaceutical Industry Wastewater: Review of the Technologies for Water Treatment and Reuse. *Industrial & Engineering Chemistry Research* 53(29), 11571-11592. <https://doi.org/10.1021/ie501210j>.
- Galán-Mascarós, J.R., 2015. Water Oxidation at Electrodes Modified with Earth-Abundant Transition-Metal Catalysts. *ChemElectroChem* 2(1), 37-50. <https://doi.org/10.1002/celc.201402268>.
- Gao, P., Tian, X., Nie, Y., Yang, C., Zhou, Z., Wang, Y., 2019. Promoted peroxy-monosulfate activation into singlet oxygen over perovskite for ofloxacin degradation by controlling the oxygen defect concentration. *Chem. Eng. J.* 359, 828-839. <https://doi.org/10.1016/j.cej.2018.11.184>.
- García-Espinoza, J.D., Mijaylova-Nacheva, P., Avilés-Flores, M., 2018. Electrochemical carbamazepine degradation: Effect of the generated active chlorine, transformation pathways and toxicity. *Chemosphere* 192, 142-151. <https://doi.org/https://doi.org/10.1016/j.chemosphere.2017.10.147>.

- Germán, S.-M., Gabriela, R.-M., Dora, S.-C., Rubí, R., Reyna, N., 2019. Advanced Oxidation Processes: Ozonation and Fenton Processes Applied to the Removal of Pharmaceuticals, in: Gómez-Oliván, L.M. (Ed.) *Ecopharmacovigilance: Multidisciplinary Approaches to Environmental Safety of Medicines*. Springer International Publishing, Cham, pp. 119-142. https://doi.org/10.1007/978-94-007-698-2_166.
- Ghanbari, F., Hassani, A., Waclawek, S., Wang, Z., Matyszcak, G., Lin, K.-Y.A., Dolatabadi, M., 2021. Insights into paracetamol degradation in aqueous solutions by ultrasound-assisted heterogeneous electro-Fenton process: Key operating parameters, mineralization and toxicity assessment. *Sep. Purif. Technol.* 266, 118533. <https://doi.org/10.1016/j.seppur.2021.118533>.
- Ghanbari, F., Moradi, M., 2017. Application of peroxymonosulfate and its activation methods for degradation of environmental organic pollutants: Review. *Chem. Eng. J.* 310, 41-62. <https://doi.org/10.1016/j.cej.2016.10.064>.
- Ghanbari, M., Emadzadeh, D., Lau, W.J., Lai, S.O., Matsuura, T., Ismail, A.F., 2015. Synthesis and characterization of novel thin film nanocomposite (TFN) membranes embedded with halloysite nanotubes (HNTs) for water desalination. *Desalination* 358, 33-41. <https://doi.org/10.1016/j.desal.2014.11.035>.
- Giannakis, S., Lin, K.-Y.A., Ghanbari, F., 2021. A review of the recent advances on the treatment of industrial wastewaters by Sulfate Radical-based Advanced Oxidation Processes (SR-AOPs). *Chem. Eng. J.* 406, 127083. <https://doi.org/10.1016/j.cej.2020.127083>.
- Glotov, A., Novikov, A., Stavitskaya, A., Nedolivko, V., Kopitsyn, D., Kuchierskaya, A., Ivanov, E., Stytsenko, V., Vinokurov, V., Lvov, Y., 2021a. Nanoreactors based on hydrophobized tubular aluminosilicates decorated with ruthenium:

- Highly active and stable catalysts for aromatics hydrogenation. *Catal. Today* 378, 33-42. <https://doi.org/10.1016/j.cattod.2020.10.001>.
- Glotov, A., Stavitskaya, A., Chudakov, Y., Ivanov, E., Huang, W., Vinokurov, V., Zolotukhina, A., Maximov, A., Karakhanov, E., Lvov, Y., 2019. Mesoporous Metal Catalysts Templated on Clay Nanotubes. *Bull. Chem. Soc. Jpn.* 92(1), 61-69. <https://doi.org/10.1246/bcsj.20180207>.
- Glotov, A., Vutolkina, A., Pimerzin, A., Vinokurov, V., Lvov, Y., 2021b. Clay nanotube-metal core/shell catalysts for hydroprocesses. *Chem. Soc. Rev.* 50(16), 9240-9277. <https://doi.org/10.1039/d1cs00502b>.
- Gómez-Pacheco, C.V., Sánchez-Polo, M., Rivera-Utrilla, J., López-Peñalver, J., 2011. Tetracycline removal from waters by integrated technologies based on ozonation and biodegradation. *Chem. Eng. J.* 178, 115-121. <https://doi.org/https://doi.org/10.1016/j.cej.2011.10.023>.
- Gong, Y., Wu, Y., Shen, J., Zhao, S., Xu, X., Kang, J., Shen, L., Zhou, Y., Zhao, Y., Chen, Z., 2022. Generation of interfacial high-spin manganese intermediates as reactive oxidant during peroxymonosulfate activation mediated by amorphous MnOx supported on polymeric substrate. *Appl. Catal., B* 316, 121671. <https://doi.org/10.1016/j.apcatb.2022.121671>.
- González Peña, O.I., López Zavala, M., Cabral Ruelas, H., 2021. Pharmaceuticals Market, Consumption Trends and Disease Incidence Are Not Driving the Pharmaceutical Research on Water and Wastewater. *Int. J. Environ. Res. Public. Health* 18(5). <https://doi.org/10.3390/ijerph18052532>.
- Goyne, K.W., Chorover, J., Kubicki, J.D., Zimmerman, A.R., Brantley, S.L., 2005. Sorption of the antibiotic ofloxacin to mesoporous and nonporous alumina and silica. *J. Colloid Interface Sci.* 283(1), 160-170.

- <https://doi.org/10.1016/j.jcis.2004.08.150>.
- Grabicová, K., Grabic, R., Fedorova, G., Vojs Staňová, A., Bláha, M., Randák, T., Brooks, B.W., Žlábek, V., 2020. Water reuse and aquaculture: Pharmaceutical bioaccumulation by fish during tertiary treatment in a wastewater stabilization pond. *Environ. Pollut.* 267, 115593. <https://doi.org/https://doi.org/10.1016/j.envpol.2020.115593>.
- Gracia-Lor, E., Sancho, J.V., Serrano, R., Hernández, F., 2012. Occurrence and removal of pharmaceuticals in wastewater treatment plants at the Spanish Mediterranean area of Valencia. *Chemosphere* 87(5), 453-462. <https://doi.org/https://doi.org/10.1016/j.chemosphere.2011.12.025>.
- Greenwood, D., 2010. CHAPTER 1 - Historical introduction, in: Finch, R.G., Greenwood, D., Norrby, S.R., Whitley, R.J. (Eds.), *Antibiotic and Chemotherapy (Ninth Edition)*. W.B. Saunders, London, pp. 2-9. <https://doi.org/https://doi.org/10.1016/B978-0-7020-4064-1.00001-4>.
- Guan, S., Nasu, N., Zhang, Y., Tamamoto, Y., Yamanobe, M., Zhao, X., 2019. Oxygen vacancy and Mn²⁺ induced ferromagnetism in Mn-doped ZnO thin films. *Science China Technological Sciences* 62(10), 1755-1759. <https://doi.org/10.1007/s11431-018-9463-6>.
- Guan, Y.-H., Ma, J., Ren, Y.-M., Liu, Y.-L., Xiao, J.-Y., Lin, L.-q., Zhang, C., 2013. Efficient degradation of atrazine by magnetic porous copper ferrite catalyzed peroxymonosulfate oxidation via the formation of hydroxyl and sulfate radicals. *Water Res.* 47(14), 5431-5438. <https://doi.org/https://doi.org/10.1016/j.watres.2013.06.023>.
- Guerra-Rodríguez, S., Rodríguez, E., Singh, D., Rodríguez-Chueca, J., 2018. Assessment of Sulfate Radical-Based Advanced Oxidation Processes for Water

- and Wastewater Treatment: A Review. *Water* 10(12), 1828.
<https://doi.org/10.3390/w10121828>.
- Guo, G., Ouyang, K., Yu, J., Liu, Y., Feng, S., Wei, M., 2019. Facile Synthesis of LaCoO₃ with a High Oxygen Vacancy Concentration by the Plasma Etching Technique for High-Performance Oxygen Ion Intercalation Pseudocapacitors. *ACS Applied Energy Materials* 3(1), 300-308.
<https://doi.org/10.1021/acsaem.9b01558>.
- Guo, H., Zhou, X., Zhang, Y., Yao, Q., Qian, Y., Chu, H., Chen, J., 2020. Carbamazepine degradation by heterogeneous activation of peroxymonosulfate with lanthanum cobaltite perovskite: Performance, mechanism and toxicity. *J Environ Sci (China)* 91, 10-21. <https://doi.org/10.1016/j.jes.2020.01.003>.
- Gusain, R., Kumar, N., Ray, S.S., 2020. Recent advances in carbon nanomaterial-based adsorbents for water purification. *Coordination Chemistry Reviews* 405, 213111. <https://doi.org/10.1016/j.ccr.2019.213111>.
- Hammouda, S.B., Zhao, F., Safaei, Z., Srivastava, V., Lakshmi Ramasamy, D., Iftekhar, S., Kalliola, S., Sillanpää, M., 2017. Degradation and mineralization of phenol in aqueous medium by heterogeneous monopersulfate activation on nanostructured cobalt based-perovskite catalysts ACoO₃ (A = La, Ba, Sr and Ce): Characterization, kinetics and mechanism study. *Appl. Catal., B* 215, 60-73. <https://doi.org/10.1016/j.apcatb.2017.05.051>.
- Han, C.-H., Park, H.-D., Kim, S.-B., Yargeau, V., Choi, J.-W., Lee, S.-H., Park, J.-A., 2020. Oxidation of tetracycline and oxytetracycline for the photo-Fenton process: Their transformation products and toxicity assessment. *Water Res.* 172, 115514. <https://doi.org/https://doi.org/10.1016/j.watres.2020.115514>.
- Han, F., Ye, X., Chen, Q., Long, H., Rao, Y., 2020. The oxidative degradation of

- diclofenac using the activation of peroxymonosulfate by BiFeO₃ microspheres—Kinetics, role of visible light and decay pathways. *Sep. Purif. Technol.* 232, 115967. <https://doi.org/https://doi.org/10.1016/j.seppur.2019.115967>.
- Harkin, G., Hopkinson, H., 2010. Carbamazepine. *Practical Diabetes International* 27(5), 205-206.
- Hassani, A., Khataee, A., Fathinia, M., Karaca, S., 2018. Photocatalytic ozonation of ciprofloxacin from aqueous solution using TiO₂/MMT nanocomposite: Nonlinear modeling and optimization of the process via artificial neural network integrated genetic algorithm. *Process Safety and Environmental Protection* 116, 365-376. <https://doi.org/10.1016/j.psep.2018.03.013>.
- He, Z., Wang, H., Li, M., Feng, L., Niu, J., Li, Z., Jia, X., Hu, G., 2022. Amorphous cobalt oxide decorated halloysite nanotubes for efficient sulfamethoxazole degradation activated by peroxymonosulfate. *J. Colloid Interface Sci.* 607, 857-868. <https://doi.org/https://doi.org/10.1016/j.jcis.2021.08.168>.
- Hoseinzadeh, E., Rezaee, A., Farzadkia, M., 2018. Nitrate removal from pharmaceutical wastewater using microbial electrochemical system supplied through low frequency-low voltage alternating electric current. *Bioelectrochemistry* 120, 49-56. <https://doi.org/10.1016/j.bioelechem.2017.11.008>.
- Hosny, N.M., Huddersman, K., Atia, N.N., El-Gizawy, S.M., 2019. Novel Heterogeneous Fenton's-Like Catalysis for Degradation of Colchicine Coupled with Extraction of Its Biologically Active Metabolite. *J. Mol. Liq.* 295, 111870. <https://doi.org/https://doi.org/10.1016/j.molliq.2019.111870>.
- Hu, J., Zeng, X., Wang, G., Qian, B., Liu, Y., Hu, X., He, B., Zhang, L., Zhang, X.,

2020. Modulating mesoporous Co₃O₄ hollow nanospheres with oxygen vacancies for highly efficient peroxydisulfate activation. *Chem. Eng. J.* 400, 125869. <https://doi.org/10.1016/j.cej.2020.125869>.
- Hu, Y., Huang, Y., Wang, X., Ding, Y., Huang, J., 2018. Insight into singlet oxygen generation from metastable lattice of Treated-NaBiO₃: A mechanism study. *Materials Chemistry and Physics* 213, 389-399. <https://doi.org/10.1016/j.matchemphys.2018.03.079>.
- Huang, X., Zhu, N., Mao, F., Ding, Y., Zhang, S., Liu, H., Li, F., Wu, P., Dang, Z., Ke, Y., 2020. Enhanced heterogeneous photo-Fenton catalytic degradation of tetracycline over γ -CeO₂/Fh composites: Performance, degradation pathways, Fe²⁺ regeneration and mechanism. *Chem. Eng. J.* 392, 123636. <https://doi.org/10.1016/j.cej.2019.123636>.
- Huang, Y.-H., Huang, Y.-F., Huang, C.-i., Chen, C.-Y., 2009. Efficient decolorization of azo dye Reactive Black B involving aromatic fragment degradation in buffered Co²⁺/PMS oxidative processes with a ppb level dosage of Co²⁺-catalyst. *J. Hazard. Mater.* 170(2-3), 1110-1118. <https://doi.org/10.1016/j.jhazmat.2009.05.091>.
- Huang, Y.-m., Li, G., Li, M., Yin, J., Meng, N., Zhang, D., Cao, X.-q., Zhu, F.-p., Chen, M., Li, L., Lyu, X.-j., 2021. Kelp-derived N-doped biochar activated peroxydisulfate for ofloxacin degradation. *Science of The Total Environment* 754, 141999. <https://doi.org/10.1016/j.scitotenv.2020.141999>.
- Huang, Z., Lin, Q., Luo, H., Guo, P., Weng, Q., Lei, Y., Cheng, S., Liu, S.-S., 2020. Degradation of progesterone by coexisting free radical and nonradical pathways in the CuO/HNTs-PS system. *Chem. Eng. J.* 398, 125458. <https://doi.org/10.1016/j.cej.2020.125458>.

- Iatalese, M., Coluccio, M.L., Onesto, V., Amato, F., Di Fabrizio, E., Gentile, F., 2019. Relating the rate of growth of metal nanoparticles to cluster size distribution in electroless deposition. *Nanoscale Advances* 1(1), 228-240. <https://doi.org/10.1039/c8na00040a>.
- Jaafarzadeh, N., Omidinasab, M., Ghanbari, F., 2016. Combined electrocoagulation and UV-based sulfate radical oxidation processes for treatment of pulp and paper wastewater. *Process Safety and Environmental Protection* 102, 462-472. <https://doi.org/https://doi.org/10.1016/j.psep.2016.04.019>.
- Jiang, H., Zhu, C., Yuan, Y., Yue, C., Ling, C., Liu, F., Li, A., 2020. Enhanced activation of peroxymonosulfate with metal-substituted hollow $M_xCo_{3-x}S_4$ polyhedrons for superfast degradation of sulfamethazine. *Chem. Eng. J.* 384, 123302. <https://doi.org/10.1016/j.cej.2019.123302>.
- Jiang, L., Wu, Z., Wang, Y., Tian, W., Yi, Z., Cai, C., Jiang, Y., Hu, L., 2019. Ultrafast Zinc-Ion Diffusion Ability Observed in 6.0-Nanometer Spinel Nanodots. *ACS Nano* 13(9), 10376-10385. <https://doi.org/10.1021/acsnano.9b04165>.
- Jones, O.A.H., Voulvoulis, N., Lester, J.N., 2015. Human Pharmaceuticals in the Aquatic Environment a Review. *Environ. Technol.* 22(12), 1383-1394. <https://doi.org/10.1080/09593330.2001.11090873>.
- Kaddouri, A., Mazzocchia, C., 2004. A study of the influence of the synthesis conditions upon the catalytic properties of Co/SiO₂ or Co/Al₂O₃ catalysts used for ethanol steam reforming. *Catal. Commun.* 5(6), 339-345. <https://doi.org/10.1016/j.catcom.2004.03.008>.
- Kadir, H.A., Abu Bakar, N.H.H., Sabri, N.A., Abdullah, F.H., Abu Bakar, M., Furuno, H., Saito, N., 2020. Silver nanoparticles incorporated in dicarboxylic/TEPA modified halloysite nanotubes for the degradation of organic contaminants.

- Appl. Surf. Sci. 531, 147417. <https://doi.org/10.1016/j.apsusc.2020.147417>.
- Kanakaraju, D., Glass, B.D., Oelgemöller, M., 2018. Advanced oxidation process-mediated removal of pharmaceuticals from water: A review. *Journal of Environmental Management* 219, 189-207. <https://doi.org/10.1016/j.jenvman.2018.04.103>.
- Kang, Z., Lin, E., Qin, N., Wu, J., Yuan, B., Bao, D., 2021. Effect of oxygen vacancies and crystal symmetry on piezocatalytic properties of Bi₂WO₆ ferroelectric nanosheets for wastewater decontamination. *Environmental Science: Nano* 8(5), 1376-1388. <https://doi.org/10.1039/d1en00022e>.
- Kao, C.-M., Sheu, Y.-T., Ou, J.-H., Lin, W.-H., 2020. Chapter 7 - Application of slow-release materials for in situ and passive remediation of contaminated groundwater, in: Hou, D. (Ed.) *Sustainable Remediation of Contaminated Soil and Groundwater*. Butterworth-Heinemann, pp. 169-199. <https://doi.org/https://doi.org/10.1016/B978-0-12-817982-6.00007-0>.
- Kapteijn, F., Vanlangeveld, A.D., Moulijn, J.A., Andreini, A., Vuurman, M.A., Turek, A.M., Jehng, J.M., Wachs, I.E., 1994. Alumina-Supported Manganese Oxide Catalysts: I. Characterization: Effect of Precursor and Loading. *J. Catal.* 150(1), 94-104. <https://doi.org/https://doi.org/10.1006/jcat.1994.1325>.
- Karim, A.V., Hassani, A., Eghbali, P., Nidheesh, P.V., 2022. Nanostructured modified layered double hydroxides (LDHs)-based catalysts: A review on synthesis, characterization, and applications in water remediation by advanced oxidation processes. *Curr. Opin. Solid State Mater. Sci.* 26(1), 100965. <https://doi.org/10.1016/j.cossms.2021.100965>.
- Kay, P., Hughes, S.R., Ault, J.R., Ashcroft, A.E., Brown, L.E., 2017. Widespread, routine occurrence of pharmaceuticals in sewage effluent, combined sewer

- overflows and receiving waters. *Environ. Pollut.* 220, 1447-1455.
<https://doi.org/https://doi.org/10.1016/j.envpol.2016.10.087>.
- Kendelewicz, T., Kaya, S., Newberg, J.T., Bluhm, H., Mulakaluri, N., Moritz, W., Scheffler, M., Nilsson, A., Pentcheva, R., Brown, G.E., 2013. X-ray Photoemission and Density Functional Theory Study of the Interaction of Water Vapor with the Fe₃O₄(001) Surface at Near-Ambient Conditions. *The Journal of Physical Chemistry C* 117(6), 2719-2733. <https://doi.org/10.1021/jp3078024>.
- Kerber, S.J., Barr, T.L., Mann, G.P., Brantley, W.A., Papazoglou, E., Mitchell, J.C., 1998. The complementary nature of x-ray photoelectron spectroscopy and angle-resolved x-ray diffraction part II: Analysis of oxides on dental alloys. *J. Mater. Eng. Perform.* 7(3), 334-342.
<https://doi.org/10.1361/105994998770347774>.
- Khetan, S.K., Collins, T.J., 2007. Human Pharmaceuticals in the Aquatic Environment: A Challenge to Green Chemistry. *Chem. Rev.* 107(6), 2319-2364.
<https://doi.org/10.1021/cr020441w>.
- Kim, S.C., Shim, W.G., 2010. Catalytic combustion of VOCs over a series of manganese oxide catalysts. *Appl. Catal., B* 98(3-4), 180-185.
<https://doi.org/10.1016/j.apcatb.2010.05.027>.
- Klavarioti, M., Mantzavinos, D., Kassinos, D., 2009. Removal of residual pharmaceuticals from aqueous systems by advanced oxidation processes. *Environ. Int.* 35(2), 402-417. <https://doi.org/10.1016/j.envint.2008.07.009>.
- Klewicki, J.K., Morgan, J.J., 1998. Kinetic Behavior of Mn(III) Complexes of Pyrophosphate, EDTA, and Citrate. *Environ. Sci. Technol.* 32(19), 2916-2922.
<https://doi.org/10.1021/es980308e>.
- Kohantorabi, M., Moussavi, G., Giannakis, S., 2021. A review of the innovations in

- metal- and carbon-based catalysts explored for heterogeneous peroxymonosulfate (PMS) activation, with focus on radical vs. non-radical degradation pathways of organic contaminants. *Chem. Eng. J.* 411, 127957. <https://doi.org/https://doi.org/10.1016/j.cej.2020.127957>.
- Kolpin, D.W., Furlong, E.T., Meyer, M.T., Thurman, E.M., Zaugg, S.D., Barber, L.B., Buxton, H.T., 2002. Pharmaceuticals, Hormones, and Other Organic Wastewater Contaminants in U.S. Streams, 1999–2000: A National Reconnaissance. *Environ. Sci. Technol.* 36(6), 1202-1211. <https://doi.org/10.1021/es011055j>.
- Kong, J., Rui, Z., Ji, H., 2016. Enhanced Photocatalytic Mineralization of Gaseous Toluene over SrTiO₃ by Surface Hydroxylation. *Industrial & Engineering Chemistry Research* 55(46), 11923-11930. <https://doi.org/10.1021/acs.iecr.6b03270>.
- Kot-Wasik, A., Jakimska, A., Śliwka-Kaszyńska, M., 2016. Occurrence and seasonal variations of 25 pharmaceutical residues in wastewater and drinking water treatment plants. *Environ. Monit. Assess.* 188(12). <https://doi.org/10.1007/s10661-016-5637-0>.
- Krumova, K., Cosa, G., 2016. Chapter 1 Overview of Reactive Oxygen Species, Singlet Oxygen: Applications in Biosciences and Nanosciences, Volume 1. The Royal Society of Chemistry, pp. 1-21. <https://doi.org/10.1039/9781782622208-00001>.
- Kubrak, O.I., Husak, V.V., Rovenko, B.M., Storey, J.M., Storey, K.B., Lushchak, V.I., 2011. Cobalt-induced oxidative stress in brain, liver and kidney of goldfish *Carassius auratus*. *Chemosphere* 85(6), 983-989. <https://doi.org/10.1016/j.chemosphere.2011.06.078>.
- Kumar, A., Rana, A., Sharma, G., Naushad, M., Dhiman, P., Kumari, A., Stadler, F.J.,

2019. Recent advances in nano-Fenton catalytic degradation of emerging pharmaceutical contaminants. *J. Mol. Liq.* 290, 111177. <https://doi.org/https://doi.org/10.1016/j.molliq.2019.111177>.
- Kümmerer, K., 2010. Pharmaceuticals in the Environment. *Annu. Rev. Environ. Resour.* 35(1), 57-75. <https://doi.org/10.1146/annurev-environ-052809-161223>.
- Kyzas, G.Z., Fu, J., Lazaridis, N.K., Bikiaris, D.N., Matis, K.A., 2015. New approaches on the removal of pharmaceuticals from wastewaters with adsorbent materials. *J. Mol. Liq.* 209, 87-93. <https://doi.org/https://doi.org/10.1016/j.molliq.2015.05.025>.
- Larsson, D.G.J., 2014. Pollution from drug manufacturing: review and perspectives. *Philosophical Transactions of the Royal Society B: Biological Sciences* 369(1656), 20130571. <https://doi.org/10.1098/rstb.2013.0571>.
- Larsson, D.G.J., de Pedro, C., Paxeus, N., 2007. Effluent from drug manufactures contains extremely high levels of pharmaceuticals. *J. Hazard. Mater.* 148(3), 751-755. <https://doi.org/10.1016/j.jhazmat.2007.07.008>.
- Le-Minh, N., Khan, S.J., Drewes, J.E., Stuetz, R.M., 2010. Fate of antibiotics during municipal water recycling treatment processes. *Water Res.* 44(15), 4295-4323. <https://doi.org/https://doi.org/10.1016/j.watres.2010.06.020>.
- Lee, J., von Gunten, U., Kim, J.-H., 2020. Persulfate-Based Advanced Oxidation: Critical Assessment of Opportunities and Roadblocks. *Environ. Sci. Technol.* 54(6), 3064-3081. <https://doi.org/10.1021/acs.est.9b07082>.
- Lee, V.J., 2007. 7.22 - Anti-Gram Positive Agents of Natural Product Origins, in: Taylor, J.B., Triggle, D.J. (Eds.), *Comprehensive Medicinal Chemistry II*. Elsevier, Oxford, pp. 653-671. <https://doi.org/https://doi.org/10.1016/B0-08-045044-X/00222-4>.

- Li, C.-X., Chen, C.-B., Lu, J.-Y., Cui, S., Li, J., Liu, H.-Q., Li, W.-W., Zhang, F., 2018. Metal organic framework-derived CoMn₂O₄ catalyst for heterogeneous activation of peroxymonosulfate and sulfanilamide degradation. *Chem. Eng. J.* 337, 101-109. <https://doi.org/10.1016/j.cej.2017.12.069>.
- Li, C., Huang, Y., Dong, X., Sun, Z., Duan, X., Ren, B., Zheng, S., Dionysiou, D.D., 2019. Highly efficient activation of peroxymonosulfate by natural negatively-charged kaolinite with abundant hydroxyl groups for the degradation of atrazine. *Appl. Catal., B* 247, 10-23. <https://doi.org/10.1016/j.apcatb.2019.01.079>.
- Li, C., Sun, Z., Song, A., Dong, X., Zheng, S., Dionysiou, D.D., 2018. Flowing nitrogen atmosphere induced rich oxygen vacancies overspread the surface of TiO₂/kaolinite composite for enhanced photocatalytic activity within broad radiation spectrum. *Appl. Catal., B* 236, 76-87. <https://doi.org/10.1016/j.apcatb.2018.04.083>.
- Li, C., Wu, J., Peng, W., Fang, Z., Liu, J., 2019. Peroxymonosulfate activation for efficient sulfamethoxazole degradation by Fe₃O₄/β-FeOOH nanocomposites: Coexistence of radical and non-radical reactions. *Chem. Eng. J.* 356, 904-914. <https://doi.org/10.1016/j.cej.2018.09.064>.
- Li, H., Gao, Q., Wang, G., Han, B., Xia, K., Zhou, C., 2020. Architecturing CoTiO₃ overlayer on nanosheets-assembled hierarchical TiO₂ nanospheres as a highly active and robust catalyst for peroxymonosulfate activation and metronidazole degradation. *Chem. Eng. J.* 392, 123819. <https://doi.org/10.1016/j.cej.2019.123819>.
- Li, H., Qian, J., Pan, B., 2021. N-coordinated Co containing porous carbon as catalyst with improved dispersity and stability to activate peroxymonosulfate for degradation of organic pollutants. *Chem. Eng. J.* 403, 126395.

- <https://doi.org/10.1016/j.cej.2020.126395>.
- Li, H., Shang, J., Yang, Z., Shen, W., Ai, Z., Zhang, L., 2017. Oxygen Vacancy Associated Surface Fenton Chemistry: Surface Structure Dependent Hydroxyl Radicals Generation and Substrate Dependent Reactivity. *Environ. Sci. Technol.* 51(10), 5685-5694. <https://doi.org/10.1021/acs.est.7b00040>.
- Li, J., Hussain, A., Li, D., Yang, M., Xu, S., 2017. Catalytic performance of graphene-bimetallic composite for heterogeneous oxidation of acid orange 7 from aqueous solution. *Environmental Science and Pollution Research* 24(8), 7264-7273. <https://doi.org/10.1007/s11356-017-8379-9>.
- Li, J., Li, X., Wang, X., Zeng, L., Chen, X., Mu, J., Chen, G., 2019. Multiple regulations of Mn-based oxides in boosting peroxymonosulfate activation for norfloxacin removal. *Applied Catalysis A: General* 584, 117170. <https://doi.org/10.1016/j.apcata.2019.117170>.
- Li, J., Xu, M., Yao, G., Lai, B., 2018. Enhancement of the degradation of atrazine through CoFe₂O₄ activated peroxymonosulfate (PMS) process: Kinetic, degradation intermediates, and toxicity evaluation. *Chem. Eng. J.* 348, 1012-1024. <https://doi.org/10.1016/j.cej.2018.05.032>.
- Li, J., Zhu, J., Fang, L., Nie, Y., Tian, N., Tian, X., Lu, L., Zhou, Z., Yang, C., Li, Y., 2020. Enhanced peroxymonosulfate activation by supported microporous carbon for degradation of tetracycline via non-radical mechanism. *Sep. Purif. Technol.* 240, 116617. <https://doi.org/10.1016/j.seppur.2020.116617>.
- Li, M., Huang, F., Hu, L., Sun, W., Li, E., Xiong, D., Zhong, H., He, Z., 2020. Efficient activation of peroxymonosulfate by a novel catalyst prepared directly from electrolytic manganese slag for degradation of recalcitrant organic pollutants. *Chem. Eng. J.* 401, 126085. <https://doi.org/10.1016/j.cej.2020.126085>.

- Li, M., Li, Y.-W., Yu, P.-F., Zhao, H.-M., Xiang, L., Feng, N.-X., Li, Q.-K., He, K.-Y., Luo, X., Cai, Q.-Y., Zhou, S.-Q., Mo, C.-H., Yeung, K.-L., 2022. Exploring degradation mechanism of tetracycline via high-effective peroxymonosulfate catalysts of montmorillonite hybridized CoFe composites and safety assessment. *Chem. Eng. J.* 427, 130930. <https://doi.org/https://doi.org/10.1016/j.cej.2021.130930>.
- Li, N., Tang, S., Rao, Y., Qi, J., Zhang, Q., Yuan, D., 2019. Peroxymonosulfate enhanced antibiotic removal and synchronous electricity generation in a photocatalytic fuel cell. *Electrochimica Acta* 298, 59-69. <https://doi.org/10.1016/j.electacta.2018.12.063>.
- Li, W., Li, S., Tang, Y., Yang, X., Zhang, W., Zhang, X., Chai, H., Huang, Y., 2020. Highly efficient activation of peroxymonosulfate by cobalt sulfide hollow nanospheres for fast ciprofloxacin degradation. *J. Hazard. Mater.* 389, 121856. <https://doi.org/10.1016/j.jhazmat.2019.121856>.
- Li, W., Wu, P.-x., Zhu, Y., Huang, Z.-j., Lu, Y.-h., Li, Y.-w., Dang, Z., Zhu, N.-w., 2015. Catalytic degradation of bisphenol A by CoMnAl mixed metal oxides catalyzed peroxymonosulfate: Performance and mechanism. *Chem. Eng. J.* 279, 93-102. <https://doi.org/https://doi.org/10.1016/j.cej.2015.05.001>.
- Li, X., He, C., Dai, D., Zuo, S., Yan, X., Yao, C., Ni, C., 2020. Nano-mineral induced nonlinear optical LiNbO₃ with abundant oxygen vacancies for photocatalytic nitrogen fixation: boosting effect of polarization. *Applied Nanoscience* 10(9), 3477-3490. <https://doi.org/10.1007/s13204-020-01443-6>.
- Li, X., Shi, H., Yan, X., Zuo, S., Zhang, Y., Wang, T., Luo, S., Yao, C., Ni, C., 2018. Palygorskite Immobilized Direct Z-Scheme Nitrogen-Doped Carbon Quantum dots/PrFeO₃ for Photo-SCR Removal of NO_x. *ACS Sustainable Chemistry &*

- Engineering 6(8), 10616-10627.
<https://doi.org/10.1021/acssuschemeng.8b01956>.
- Li, Y., Bi, E., Chen, H., 2017. Sorption Behavior of Ofloxacin to Kaolinite: Effects of pH, Ionic Strength, and Cu(II). *Water, Air, Soil Pollut.* 228(1).
<https://doi.org/10.1007/s11270-016-3236-x>.
- Li, Y., Chen, Z., Qi, J., Kang, J., Shen, J., Yan, P., Wang, W., Bi, L., Zhang, X., Zhu, X., 2021. Degradation of bisphenol S by peroxymonosulfate activation through monodispersed CoFe₂O₄ nanoparticles anchored on natural palygorskite. *Sep. Purif. Technol.* 277, 119492.
<https://doi.org/https://doi.org/10.1016/j.seppur.2021.119492>.
- Lian, L., Yao, B., Hou, S., Fang, J., Yan, S., Song, W., 2017. Kinetic Study of Hydroxyl and Sulfate Radical-Mediated Oxidation of Pharmaceuticals in Wastewater Effluents. *Environ Sci Technol* 51(5), 2954-2962.
<https://doi.org/10.1021/acs.est.6b05536>.
- Lim, J., Yang, Y., Hoffmann, M.R., 2019. Activation of Peroxymonosulfate by Oxygen Vacancies-Enriched Cobalt-Doped Black TiO₂ Nanotubes for the Removal of Organic Pollutants. *Environ. Sci. Technol.* 53(12), 6972-6980.
<https://doi.org/10.1021/acs.est.9b01449>.
- Lin, H., Li, S., Deng, B., Tan, W., Li, R., Xu, Y., Zhang, H., 2019. Degradation of bisphenol A by activating peroxymonosulfate with Mn_{0.6}Zn_{0.4}Fe₂O₄ fabricated from spent Zn-Mn alkaline batteries. *Chem. Eng. J.* 364, 541-551.
<https://doi.org/10.1016/j.cej.2019.01.189>.
- Lin, K.-Y.A., Chen, Y.-C., Lin, Y.-F., 2017. LaMO₃ perovskites (M=Co, Cu, Fe and Ni) as heterogeneous catalysts for activating peroxymonosulfate in water. *Chem. Eng. Sci.* 160, 96-105. <https://doi.org/10.1016/j.ces.2016.11.017>.

- Liochev, S.I., Fridovich, I., 2013. The Haber-Weiss cycle—70 years later: an alternative view. *Redox Rep.* 7(1), 55-57. <https://doi.org/10.1179/135100002125000190>.
- Liu, D., Wang, C., Song, Y., Wei, Y., He, L., Lan, B., He, X., Wang, J., 2019. Effective mineralization of quinoline and bio-treated coking wastewater by catalytic ozonation using CuFe₂O₄/Sepiolite catalyst: Efficiency and mechanism. *Chemosphere* 227, 647-656. <https://doi.org/10.1016/j.chemosphere.2019.04.040>.
- Liu, L., Li, Y., Pang, Y., Lan, Y., Zhou, L., 2020. Activation of peroxymonosulfate with CuCo₂O₄@kaolin for the efficient degradation of phenacetin. *Chem. Eng. J.* 401, 126014. <https://doi.org/https://doi.org/10.1016/j.cej.2020.126014>.
- Liu, L., Sun, J., Ding, J., Zhang, Y., Sun, T., Jia, J., 2019. Highly Active Mn_{3-x}Fe_xO₄ Spinel with Defects for Toluene Mineralization: Insights into Regulation of the Oxygen Vacancy and Active Metals. *Inorganic Chemistry* 58(19), 13241-13249. <https://doi.org/10.1021/acs.inorgchem.9b02105>.
- Liu, W., Dong, Y., Liu, J., Zhang, L., Lu, Y., Lin, H., 2023. Halloysite nanotube confined interface engineering enhanced catalytic oxidation of photo-Fenton reaction for aniline aerofloat degradation: Defective heterojunction for electron transfer regulation. *Chem. Eng. J.* 451, 138666. <https://doi.org/10.1016/j.cej.2022.138666>.
- Liu, X., Wang, W., Du, C., Su, Y., 2022. Synergistic activation of peroxymonosulfate via oxygen vacancy-rich Co_xMn_{3-x}O₄/montmorillonite catalyst for environmental remediation. *Appl. Clay Sci.* 228, 106625. <https://doi.org/https://doi.org/10.1016/j.clay.2022.106625>.
- Liu, Y., Guo, H., Zhang, Y., Tang, W., Cheng, X., Li, W., 2018. Heterogeneous activation of peroxymonosulfate by sillenite Bi₂₅FeO₄₀: Singlet oxygen

- generation and degradation for aquatic levofloxacin. *Chem. Eng. J.* 343, 128-137. <https://doi.org/10.1016/j.cej.2018.02.125>.
- Loos, G., Scheers, T., Van Eyck, K., Van Schepdael, A., Adams, E., Van der Bruggen, B., Cabooter, D., Dewil, R., 2018. Electrochemical oxidation of key pharmaceuticals using a boron doped diamond electrode. *Sep. Purif. Technol.* 195, 184-191. <https://doi.org/10.1016/j.seppur.2017.12.009>.
- Loos, R., Locoro, G., Comero, S., Contini, S., Schwesig, D., Werres, F., Balsaa, P., Gans, O., Weiss, S., Blaha, L., Bolchi, M., Gawlik, B.M., 2010. Pan-European survey on the occurrence of selected polar organic persistent pollutants in ground water. *Water Res.* 44(14), 4115-4126. <https://doi.org/10.1016/j.watres.2010.05.032>.
- Lu, S., Wang, G., Chen, S., Yu, H., Ye, F., Quan, X., 2018. Heterogeneous activation of peroxymonosulfate by $\text{LaCo}_{1-x}\text{Cu}_x\text{O}_3$ perovskites for degradation of organic pollutants. *J Hazard Mater* 353, 401-409. <https://doi.org/10.1016/j.jhazmat.2018.04.021>.
- Luo, H., Cheng, Y., Zeng, Y., Luo, K., He, D., Pan, X., 2020. Rapid removal of organic micropollutants by heterogeneous peroxymonosulfate catalysis over a wide pH range: Performance, mechanism and economic analysis. *Sep. Purif. Technol.* 248, 117023. <https://doi.org/10.1016/j.seppur.2020.117023>.
- Ma, J., Yang, Y., Jiang, X., Xie, Z., Li, X., Chen, C., Chen, H., 2018. Impacts of inorganic anions and natural organic matter on thermally activated persulfate oxidation of BTEX in water. *Chemosphere* 190, 296-306. <https://doi.org/10.1016/j.chemosphere.2017.09.148>.
- Ma, W., Wu, H., Higaki, Y., Takahara, A., 2018. Halloysite Nanotubes: Green Nanomaterial for Functional Organic-Inorganic Nanohybrids. *The Chemical Record* 18(7-8), 986-999. <https://doi.org/10.1002/tcr.201700093>.

- Manna, S., Roy, U., Biswas, A., Sengupta, S., Basak, P., Das, P., 2021. Review on Trends in the Removal of Pharmaceuticals and Personal Care Products (PPCPs) from Water and Wastewater, in: Kumar, M., Snow, D.D., Honda, R., Mukherjee, S. (Eds.), *Contaminants in Drinking and Wastewater Sources: Challenges and Reigning Technologies*. Springer Singapore, Singapore, pp. 225-250. https://doi.org/10.1007/978-981-15-4599-3_10.
- Martínez, J.L., Coque, T.M., Baquero, F., 2014. What is a resistance gene? Ranking risk in resistomes. *Nat. Rev. Microbiol.* 13(2), 116-123. <https://doi.org/10.1038/nrmicro3399>.
- Massaro, M., Colletti, C.G., Lazzara, G., Milioto, S., Noto, R., Riela, S., 2017. Halloysite nanotubes as support for metal-based catalysts. *Journal of Materials Chemistry A* 5(26), 13276-13293. <https://doi.org/10.1039/c7ta02996a>.
- Mathew, D.S., Juang, R.-S., 2007. An overview of the structure and magnetism of spinel ferrite nanoparticles and their synthesis in microemulsions. *Chem. Eng. J.* 129(1-3), 51-65. <https://doi.org/10.1016/j.cej.2006.11.001>.
- Méndez-Arriaga, F., Torres-Palma, R.A., Pétrier, C., Esplugas, S., Gimenez, J., Pulgarin, C., 2009. Mineralization enhancement of a recalcitrant pharmaceutical pollutant in water by advanced oxidation hybrid processes. *Water Res.* 43(16), 3984-3991. <https://doi.org/10.1016/j.watres.2009.06.059>.
- Merino, N.A., Barbero, B.P., Eloy, P., Cadús, L.E., 2006. $\text{La}_{1-x}\text{Ca}_x\text{CoO}_3$ perovskite-type oxides: Identification of the surface oxygen species by XPS. *Appl. Surf. Sci.* 253(3), 1489-1493. <https://doi.org/10.1016/j.apsusc.2006.02.035>.
- Miller, T.H., Bury, N.R., Owen, S.F., MacRae, J.I., Barron, L.P., 2018. A review of the pharmaceutical exposome in aquatic fauna. *Environ. Pollut.* 239, 129-146. <https://doi.org/10.1016/j.envpol.2018.04.012>.

- Morin-Crini, N., Lichtfouse, E., Fourmentin, M., Ribeiro, A.R.L., Noutsopoulos, C., Mapelli, F., Fenyvesi, É., Vieira, M.G.A., Picos-Corrales, L.A., Moreno-Piraján, J.C., Giraldo, L., Sohajda, T., Huq, M.M., Soltan, J., Torri, G., Magureanu, M., Bradu, C., Crini, G., 2022. Removal of emerging contaminants from wastewater using advanced treatments. A review. *Environ. Chem. Lett.* 20(2), 1333-1375. <https://doi.org/10.1007/s10311-021-01379-5>.
- Mukimin, A., Vistanty, H., Zen, N., 2020. Hybrid advanced oxidation process (HAOP) as highly efficient and powerful treatment for complete demineralization of antibiotics. *Sep. Purif. Technol.* 241, 116728. <https://doi.org/10.1016/j.seppur.2020.116728>.
- Nie, M., Yang, Y., Zhang, Z., Yan, C., Wang, X., Li, H., Dong, W., 2014. Degradation of chloramphenicol by thermally activated persulfate in aqueous solution. *Chem. Eng. J.* 246, 373-382. <https://doi.org/10.1016/j.cej.2014.02.047>.
- Organization, W.H., 2012. Pharmaceuticals in drinking-water, in: Organization, W.H. (Ed.).
- Örn, S., Holbech, H., Madsen, T.H., Norrgren, L., Petersen, G.I., 2003. Gonad development and vitellogenin production in zebrafish (*Danio rerio*) exposed to ethinylestradiol and methyltestosterone. *Aquat. Toxicol.* 65(4), 397-411. [https://doi.org/https://doi.org/10.1016/S0166-445X\(03\)00177-2](https://doi.org/https://doi.org/10.1016/S0166-445X(03)00177-2).
- Othman, I., Hisham Zain, J., Abu Haija, M., Banat, F., 2020. Catalytic activation of peroxymonosulfate using CeVO₄ for phenol degradation: An insight into the reaction pathway. *Appl. Catal., B* 266, 118601. <https://doi.org/https://doi.org/10.1016/j.apcatb.2020.118601>.
- Ouyang, J., Zhao, Z., Suib, S.L., Yang, H., 2019. Degradation of Congo Red dye by a Fe₂O₃@CeO₂-ZrO₂/Palygorskite composite catalyst: Synergetic effects of

- Fe₂O₃. J. Colloid Interface Sci. 539, 135-145.
<https://doi.org/10.1016/j.jcis.2018.12.052>.
- Oyekunle, D.T., Gendy, E.A., Ifthikar, J., Chen, Z., 2022. Heterogeneous activation of persulfate by metal and non-metal catalyst for the degradation of sulfamethoxazole: A review. Chem. Eng. J. 437, 135277.
<https://doi.org/10.1016/j.cej.2022.135277>.
- Pang, X., Guo, Y., Zhang, Y., Xu, B., Qi, F., 2016. LaCoO₃ perovskite oxide activation of peroxymonosulfate for aqueous 2-phenyl-5-sulfobenzimidazole degradation: Effect of synthetic method and the reaction mechanism. Chem. Eng. J. 304, 897-907. <https://doi.org/10.1016/j.cej.2016.07.027>.
- Patel, M., Kumar, R., Kishor, K., Mlsna, T., Pittman, C.U., Mohan, D., 2019. Pharmaceuticals of Emerging Concern in Aquatic Systems: Chemistry, Occurrence, Effects, and Removal Methods. Chem. Rev. 119(6), 3510-3673.
<https://doi.org/10.1021/acs.chemrev.8b00299>.
- Peng, G., Qi, C., Wang, X., Zhou, L., He, Q., Zhou, W., Chen, L., 2021. Activation of peroxymonosulfate by calcined electroplating sludge for ofloxacin degradation. Chemosphere 266, 128944.
<https://doi.org/10.1016/j.chemosphere.2020.128944>.
- Peng, S., Gong, F., Li, L., Yu, D., Ji, D., Zhang, T., Hu, Z., Zhang, Z., Chou, S., Du, Y., Ramakrishna, S., 2018. Necklace-like Multishelled Hollow Spinel Oxides with Oxygen Vacancies for Efficient Water Electrolysis. Journal of the American Chemical Society 140(42), 13644-13653. <https://doi.org/10.1021/jacs.8b05134>.
- Peng, Y., Tang, H., Yao, B., Gao, X., Yang, X., Zhou, Y., 2021. Activation of peroxymonosulfate (PMS) by spinel ferrite and their composites in degradation of organic pollutants: A Review. Chem. Eng. J. 414, 128800.

- <https://doi.org/10.1016/j.cej.2021.128800>.
- Pignatello, J.J., Oliveros, E., MacKay, A., 2006. Advanced Oxidation Processes for Organic Contaminant Destruction Based on the Fenton Reaction and Related Chemistry. *Crit. Rev. Environ. Sci. Technol.* 36(1), 1-84. <https://doi.org/10.1080/10643380500326564>.
- Pruden, A., Pei, R., Storteboom, H., Carlson, K.H., 2006. Antibiotic Resistance Genes as Emerging Contaminants: Studies in Northern Colorado. *Environ. Sci. Technol.* 40(23), 7445-7450. <https://doi.org/10.1021/es060413l>.
- Qiang, L., Cheng, J., Yi, J., Rotchell, J.M., Zhu, X., Zhou, J., 2016. Environmental concentration of carbamazepine accelerates fish embryonic development and disturbs larvae behavior. *Ecotoxicology* 25(7), 1426-1437. <https://doi.org/10.1007/s10646-016-1694-y>.
- Qin, Q., Liu, T., Zhang, J., Wei, R., You, S., Xu, Y., 2021. Facile synthesis of oxygen vacancies enriched α -Fe₂O₃ for peroxymonosulfate activation: A non-radical process for sulfamethoxazole degradation. *J. Hazard. Mater.* 419, 126447. <https://doi.org/10.1016/j.jhazmat.2021.126447>.
- Ramakrishna, S., Jose, R., Archana, P.S., Nair, A.S., Balamurugan, R., Venugopal, J., Teo, W.E., 2010. Science and engineering of electrospun nanofibers for advances in clean energy, water filtration, and regenerative medicine. *J. Mater. Sci.* 45(23), 6283-6312. <https://doi.org/10.1007/s10853-010-4509-1>.
- Rao, P.S., Hayon, E., 1973. Experimental determination of the redox potential of the superoxide radical $\cdot\text{O}_2^-$. *Biochemical and Biophysical Research Communications* 51(2), 468-473. [https://doi.org/https://doi.org/10.1016/0006-291X\(73\)91280-1](https://doi.org/https://doi.org/10.1016/0006-291X(73)91280-1).
- Rayaroth, M.P., Aravind, U.K., Aravindakumar, C.T., 2016. Degradation of

- pharmaceuticals by ultrasound-based advanced oxidation process. *Environ. Chem. Lett.* 14(3), 259-290. <https://doi.org/10.1007/s10311-016-0568-0>.
- Reddy, B.M., Chowdhury, B., Smirniotis, P.G., 2001. An XPS study of the dispersion of MoO₃ on TiO₂-ZrO₂, TiO₂-SiO₂, TiO₂-Al₂O₃, SiO₂-ZrO₂, and SiO₂-TiO₂-ZrO₂ mixed oxides. *Applied Catalysis A: General* 211(1), 19-30. [https://doi.org/https://doi.org/10.1016/S0926-860X\(00\)00834-6](https://doi.org/https://doi.org/10.1016/S0926-860X(00)00834-6).
- Reggiane de Carvalho Costa, L., Guerra Pacheco Nunes, K., Amaral Féris, L., 2021. Ultrasound as an Advanced Oxidative Process: A Review on Treating Pharmaceutical Compounds. *Chem. Eng. Technol.* 44(10), 1744-1758. <https://doi.org/10.1002/ceat.202100090>.
- Ren, F., Wang, T., Liu, H., Liu, D., Zhong, R., You, C., Zhang, W., Lv, S., Liu, S., Zhu, H., Chang, L., Wang, B., 2021. CoMn₂O₄ nanoparticles embed in graphene oxide aerogel with three-dimensional network for practical application prospects of oxytetracycline degradation. *Sep. Purif. Technol.* 259, 118179. <https://doi.org/10.1016/j.seppur.2020.118179>.
- Ren, Y., Lin, L., Ma, J., Yang, J., Feng, J., Fan, Z., 2015. Sulfate radicals induced from peroxymonosulfate by magnetic ferrosipinel MFe₂O₄ (M = Co, Cu, Mn, and Zn) as heterogeneous catalysts in the water. *Appl. Catal., B* 165, 572-578. <https://doi.org/10.1016/j.apcatb.2014.10.051>.
- Rivera-Utrilla, J., Sánchez-Polo, M., Ferro-García, M.Á., Prados-Joya, G., Ocampo-Pérez, R., 2013. Pharmaceuticals as emerging contaminants and their removal from water. A review. *Chemosphere* 93(7), 1268-1287. <https://doi.org/https://doi.org/10.1016/j.chemosphere.2013.07.059>.
- Rodríguez, M.J., Garza, G.Y., Aguilera, C.A., Martínez, A.S.Y., Sosa, S.G.J., 2005. Influence of Nitrate and Sulfate on the Anaerobic Treatment of Pharmaceutical

- Wastewater. Eng. Life Sci. 5(6), 568-573.
<https://doi.org/10.1002/elsc.200520101>.
- Sadighi, Z., Huang, J., Qin, L., Yao, S., Cui, J., Kim, J.-K., 2017. Positive role of oxygen vacancy in electrochemical performance of CoMn₂O₄ cathodes for Li-O₂ batteries. J. Power Sources 365, 134-147.
<https://doi.org/10.1016/j.jpowsour.2017.08.081>.
- Salimi, M., Esrafil, A., Gholami, M., Jonidi Jafari, A., Rezaei Kalantary, R., Farzadkia, M., Kermani, M., Sobhi, H.R., 2017. Contaminants of emerging concern: a review of new approach in AOP technologies. Environ. Monit. Assess. 189(8), 414. <https://doi.org/10.1007/s10661-017-6097-x>.
- Sathya, K., Nagarajan, K., Carlin Geor Malar, G., Rajalakshmi, S., Raja Lakshmi, P., 2022. A comprehensive review on comparison among effluent treatment methods and modern methods of treatment of industrial wastewater effluent from different sources. Applied Water Science 12(4).
<https://doi.org/10.1007/s13201-022-01594-7>.
- Scaria, J., Nidheesh, P.V., 2022. Comparison of hydroxyl-radical-based advanced oxidation processes with sulfate radical-based advanced oxidation processes. Current Opinion in Chemical Engineering 36, 100830.
<https://doi.org/https://doi.org/10.1016/j.coche.2022.100830>.
- Scaria, J., Nidheesh, P.V., Kumar, M.S., 2020. Synthesis and applications of various bimetallic nanomaterials in water and wastewater treatment. Journal of Environmental Management 259, 110011.
<https://doi.org/10.1016/j.jenvman.2019.110011>.
- Scialdone, O., Randazzo, S., Galia, A., Silvestri, G., 2009. Electrochemical oxidation of organics in water: Role of operative parameters in the absence and in the

- presence of NaCl. *Water Res.* 43(8), 2260-2272.
<https://doi.org/10.1016/j.watres.2009.02.014>.
- Sethurajaperumal, A., Ravichandran, V., Banerjee, A., Manohar, A., Varrla, E., 2021. Chapter 18 - Two-dimensional layered nanosheets: structure and unique properties, in: Thomas, S., Kalarikkal, N., Abraham, A.R. (Eds.), *Fundamentals and Properties of Multifunctional Nanomaterials*. Elsevier, pp. 465-497.
<https://doi.org/https://doi.org/10.1016/B978-0-12-822352-9.00022-5>.
- Shan, D., Deng, S., Jiang, C., Chen, Y., Wang, B., Wang, Y., Huang, J., Yu, G., Wiesner, M.R., 2018. Hydrophilic and strengthened 3D reduced graphene oxide/nano-Fe₃O₄ hybrid hydrogel for enhanced adsorption and catalytic oxidation of typical pharmaceuticals. *Environmental Science: Nano* 5(7), 1650-1660.
<https://doi.org/10.1039/c8en00422f>.
- Shenker, M., Harush, D., Ben-Ari, J., Chefetz, B., 2011. Uptake of carbamazepine by cucumber plants – A case study related to irrigation with reclaimed wastewater. *Chemosphere* 82(6), 905-910.
<https://doi.org/https://doi.org/10.1016/j.chemosphere.2010.10.052>.
- Shi, X., Zheng, F., Yan, N., Chen, Q., 2014. CoMn₂O₄ hierarchical microspheres with high catalytic activity towards p-nitrophenol reduction. *Dalton Trans.* 43(37), 13865. <https://doi.org/10.1039/c4dt01686f>.
- Siedlecka, E.M., Ofiarska, A., Borzyszkowska, A.F., Białk-Bielińska, A., Stepnowski, P., Pieczyńska, A., 2018. Cytostatic drug removal using electrochemical oxidation with BDD electrode: Degradation pathway and toxicity. *Water Res.* 144, 235-245. <https://doi.org/https://doi.org/10.1016/j.watres.2018.07.035>.
- Simon, M., Kumar, A., Garg, A., Manisha, 2021. Biological Treatment of Pharmaceuticals and Personal Care Products (PPCPs) Before Discharging to

- Environment, in: Gupta, P.K., Bharagava, R.N. (Eds.), Fate and Transport of Subsurface Pollutants. Springer Singapore, Singapore, pp. 259-282. https://doi.org/10.1007/978-981-15-6564-9_14.
- Solís, R.R., Rivas, F.J., Gimeno, O., Pérez-Bote, J.-L., 2017. Synergism between peroxymonosulfate and LaCoO₃-TiO₂ photocatalysis for oxidation of herbicides. Operational variables and catalyst characterization assessment. J. Chem. Technol. Biotechnol. 92(8), 2159-2170. <https://doi.org/10.1002/jctb.5228>.
- Sopaj, F., Rodrigo, M.A., Oturan, N., Podvorica, F.I., Pinson, J., Oturan, M.A., 2015. Influence of the anode materials on the electrochemical oxidation efficiency. Application to oxidative degradation of the pharmaceutical amoxicillin. Chem. Eng. J. 262, 286-294. <https://doi.org/https://doi.org/10.1016/j.cej.2014.09.100>.
- Su, C., Duan, X., Miao, J., Zhong, Y., Zhou, W., Wang, S., Shao, Z., 2016. Mixed Conducting Perovskite Materials as Superior Catalysts for Fast Aqueous-Phase Advanced Oxidation: A Mechanistic Study. ACS Catalysis 7(1), 388-397. <https://doi.org/10.1021/acscatal.6b02303>.
- Sun, J., Dai, X., Wang, Q., van Loosdrecht, M.C.M., Ni, B.-J., 2019. Microplastics in wastewater treatment plants: Detection, occurrence and removal. Water Res. 152, 21-37. <https://doi.org/https://doi.org/10.1016/j.watres.2018.12.050>.
- Sun, Q., Zhao, Y., Qin, F., Zhang, J., Wang, B., Ye, H., Sheng, J., 2021. Crystallinity and photocatalytic properties of BiVO₄/halloysite nanotubes hybrid catalysts for sunlight-driven decomposition of dyes from aqueous solution. Nanotechnology 32(13), 135602. <https://doi.org/10.1088/1361-6528/abd126>.
- Sun, Z., Liu, X., Dong, X., Zhang, X., Tan, Y., Yuan, F., Zheng, S., Li, C., 2021. Synergistic activation of peroxymonosulfate via in situ growth FeCo₂O₄

- nanoparticles on natural rectorite: Role of transition metal ions and hydroxyl groups. *Chemosphere* 263, 127965. <https://doi.org/https://doi.org/10.1016/j.chemosphere.2020.127965>.
- Tan, Y., Li, C., Sun, Z., Bian, R., Dong, X., Zhang, X., Zheng, S., 2020. Natural diatomite mediated spherically monodispersed CoFe₂O₄ nanoparticles for efficient catalytic oxidation of bisphenol A through activating peroxymonosulfate. *Chem. Eng. J.* 388, 124386. <https://doi.org/10.1016/j.cej.2020.124386>.
- Tang, S., Xu, L., Yu, X., Chen, S., Li, H., Huang, Y., Niu, J., 2021. Degradation of anticancer drug capecitabine in aquatic media by three advanced oxidation processes: Mechanisms, toxicity changes and energy cost evaluation. *Chem. Eng. J.* 413, 127489. <https://doi.org/https://doi.org/10.1016/j.cej.2020.127489>.
- Taoufik, N., Boumya, W., Achak, M., Sillanpää, M., Barka, N., 2021. Comparative overview of advanced oxidation processes and biological approaches for the removal pharmaceuticals. *Journal of Environmental Management* 288, 112404. <https://doi.org/10.1016/j.jenvman.2021.112404>.
- Taran, O.P., Ayusheev, A.B., Ogorodnikova, O.L., Prosvirin, I.P., Isupova, L.A., Parmon, V.N., 2016. Perovskite-like catalysts LaBO₃ (B = Cu, Fe, Mn, Co, Ni) for wet peroxide oxidation of phenol. *Appl. Catal., B* 180, 86-93. <https://doi.org/10.1016/j.apcatb.2015.05.055>.
- Taverne, Y.J.H.J., Bogers, A.J.J.C., Duncker, D.J., Merkus, D., 2013. Reactive Oxygen Species and the Cardiovascular System. *Oxidative Medicine and Cellular Longevity* 2013, 1-15. <https://doi.org/10.1155/2013/862423>.
- Taylor, D., 2016. *The Pharmaceutical Industry and the Future of Drug Development, Pharmaceuticals in the Environment*. The Royal Society of Chemistry, pp. 1-33.

<https://doi.org/10.1039/9781782622345-00001>.

Thanekar, P., Garg, S., Gogate, P.R., 2019. Hybrid Treatment Strategies Based on Hydrodynamic Cavitation, Advanced Oxidation Processes, and Aerobic Oxidation for Efficient Removal of Naproxen. *Industrial & Engineering Chemistry Research* 59(9), 4058-4070.
<https://doi.org/10.1021/acs.iecr.9b01395>.

Tharmavaram, M., Pandey, G., Rawtani, D., 2018. Surface modified halloysite nanotubes: A flexible interface for biological, environmental and catalytic applications. *Advances in Colloid and Interface Science* 261, 82-101.
<https://doi.org/10.1016/j.cis.2018.09.001>.

Tian, C., Li, J., Li, Q., Nie, Y., Tian, X., Dai, C., Yang, C., Zhou, Z., Wang, Y., 2020. Surface weak acid-base pair of FeOOH/Al₂O₃ for enhanced peroxymonosulfate activation in degradation of humic substances from water. *Chem. Eng. J.* 387, 124064.
<https://doi.org/https://doi.org/10.1016/j.cej.2020.124064>.

Tian, Y., Liu, X., Xu, L., Yuan, D., Dou, Y., Qiu, J., Li, H., Ma, J., Wang, Y., Su, D., Zhang, S., 2021. Engineering Crystallinity and Oxygen Vacancies of Co(II) Oxide Nanosheets for High Performance and Robust Rechargeable Zn–Air Batteries. *Adv. Funct. Mater.* 31(20), 2101239.
<https://doi.org/10.1002/adfm.202101239>.

Tixier, C., Singer, H.P., Oellers, S., Müller, S.R., 2003. Occurrence and Fate of Carbamazepine, Clofibric Acid, Diclofenac, Ibuprofen, Ketoprofen, and Naproxen in Surface Waters. *Environ. Sci. Technol.* 37(6), 1061-1068.
<https://doi.org/10.1021/es025834r>.

Tonnesen, H.H., 2004. Photostability of drugs and drug formulations. CRC Press.

- Torres-Luna, J.A., Giraldo-Gómez, G.I., Sanabria-González, N.R., Carriazo, J.G., 2019. Catalytic degradation of real-textile azo-dyes in aqueous solutions by using Cu–Co/halloysite. *Bull. Mater. Sci.* 42(4). <https://doi.org/10.1007/s12034-019-1817-1>.
- Trojanowicz, M., Bobrowski, K., Szreder, T., Bojanowska-Czajka, A., 2018. Chapter 9 - Gamma-ray, X-ray and Electron Beam Based Processes, in: Ameta, S.C., Ameta, R. (Eds.), *Advanced Oxidation Processes for Waste Water Treatment*. Academic Press, pp. 257-331. <https://doi.org/https://doi.org/10.1016/B978-0-12-810499-6.00009-7>.
- Tung, H.-M., Huang, J.-H., Tsai, D.-G., Ai, C.-F., Yu, G.-P., 2009. Hardness and residual stress in nanocrystalline ZrN films: Effect of bias voltage and heat treatment. *Materials Science and Engineering: A* 500(1-2), 104-108. <https://doi.org/10.1016/j.msea.2008.09.006>.
- van den Brandhof, E.-J., Montforts, M., 2010. Fish embryo toxicity of carbamazepine, diclofenac and metoprolol. *Ecotoxicol. Environ. Saf.* 73(8), 1862-1866. <https://doi.org/https://doi.org/10.1016/j.ecoenv.2010.08.031>.
- Van Wieren, E.M., Seymour, M.D., Peterson, J.W., 2012. Interaction of the fluoroquinolone antibiotic, ofloxacin, with titanium oxide nanoparticles in water: Adsorption and breakdown. *Science of The Total Environment* 441, 1-9. <https://doi.org/10.1016/j.scitotenv.2012.09.067>.
- Varsha, M., Senthil Kumar, P., Senthil Rathi, B., 2022. A review on recent trends in the removal of emerging contaminants from aquatic environment using low-cost adsorbents. *Chemosphere* 287, 132270. <https://doi.org/https://doi.org/10.1016/j.chemosphere.2021.132270>.
- Vasquez, M.I., Hapeshi, E., Fatta-Kassinos, D., Kümmerer, K., 2013. Biodegradation

- potential of ofloxacin and its resulting transformation products during photolytic and photocatalytic treatment. *Environmental Science and Pollution Research* 20(3), 1302-1309. <https://doi.org/10.1007/s11356-012-1096-5>.
- Wang, J., Chu, L., 2016. Irradiation treatment of pharmaceutical and personal care products (PPCPs) in water and wastewater: An overview. *Radiat. Phys. Chem.* 125, 56-64. <https://doi.org/https://doi.org/10.1016/j.radphyschem.2016.03.012>.
- Wang, J., Guo, H., Liu, Y., Li, W., Yang, B., 2020. Peroxymonosulfate activation by porous BiFeO₃ for the degradation of bisphenol AF: Non-radical and radical mechanism. *Appl. Surf. Sci.* 507, 145097. <https://doi.org/10.1016/j.apsusc.2019.145097>.
- Wang, J., Wang, S., 2018. Activation of persulfate (PS) and peroxymonosulfate (PMS) and application for the degradation of emerging contaminants. *Chem. Eng. J.* 334, 1502-1517. <https://doi.org/https://doi.org/10.1016/j.cej.2017.11.059>.
- Wang, J., Wang, S., 2019. Preparation, modification and environmental application of biochar: A review. *Journal of Cleaner Production* 227, 1002-1022. <https://doi.org/https://doi.org/10.1016/j.jclepro.2019.04.282>.
- Wang, Q., Shao, Y., Gao, N., Chu, W., Chen, J., Lu, X., Zhu, Y., An, N., 2017. Activation of peroxymonosulfate by Al₂O₃-based CoFe₂O₄ for the degradation of sulfachloropyridazine sodium: Kinetics and mechanism. *Sep. Purif. Technol.* 189, 176-185. <https://doi.org/10.1016/j.seppur.2017.07.046>.
- Wang, S., Liu, Y., Wang, J., 2020a. Iron and sulfur co-doped graphite carbon nitride (FeO_y/S-g-C₃N₄) for activating peroxymonosulfate to enhance sulfamethoxazole degradation. *Chem. Eng. J.* 382, 122836. <https://doi.org/10.1016/j.cej.2019.122836>.
- Wang, S., Liu, Y., Wang, J., 2020b. Peroxymonosulfate Activation by Fe–Co–O-

- Codoped Graphite Carbon Nitride for Degradation of Sulfamethoxazole. *Environ. Sci. Technol.* 54(16), 10361-10369. <https://doi.org/10.1021/acs.est.0c03256>.
- Wang, S., Zhou, N., 2016. Removal of carbamazepine from aqueous solution using sono-activated persulfate process. *Ultrason. Sonochem.* 29, 156-162. <https://doi.org/https://doi.org/10.1016/j.ultsonch.2015.09.008>.
- Wang, X., Jiang, L., Li, K., Wang, J., Fang, D., Zhang, Y., Tian, D., Zhang, Z., Dionysiou, D.D., 2020. Fabrication of novel Z-scheme SrTiO₃/MnFe₂O₄ system with double-response activity for simultaneous microwave-induced and photocatalytic degradation of tetracycline and mechanism insight. *Chem. Eng. J.* 400, 125981. <https://doi.org/10.1016/j.cej.2020.125981>.
- Wang, Y., Chen, L., Cao, H., Chi, Z., Chen, C., Duan, X., Xie, Y., Qi, F., Song, W., Liu, J., Wang, S., 2019. Role of oxygen vacancies and Mn sites in hierarchical Mn₂O₃/LaMnO_{3-δ} perovskite composites for aqueous organic pollutants decontamination. *Appl. Catal., B* 245, 546-554. <https://doi.org/10.1016/j.apcatb.2019.01.025>.
- Wang, Y., Chi, Z., Chen, C., Su, C., Liu, D., Liu, Y., Duan, X., Wang, S., 2020. Facet- and defect-dependent activity of perovskites in catalytic evolution of sulfate radicals. *Appl. Catal., B* 272, 118972. <https://doi.org/10.1016/j.apcatb.2020.118972>.
- Wang, Y., Ji, H., Liu, W., Xue, T., Liu, C., Zhang, Y., Liu, L., Wang, Q., Qi, F., Xu, B., Tsang, D.C.W., Chu, W., 2020. Novel CuCo₂O₄ Composite Spinel with a Meso-Macroporous Nanosheet Structure for Sulfate Radical Formation and Benzophenone-4 Degradation: Interface Reaction, Degradation Pathway, and DFT Calculation. *ACS Applied Materials & Interfaces* 12(18), 20522-20535.

- <https://doi.org/10.1021/acsami.0c03481>.
- Wang, Z., Bush, R.T., Sullivan, L.A., Chen, C., Liu, J., 2014. Selective Oxidation of Arsenite by Peroxymonosulfate with High Utilization Efficiency of Oxidant. *Environ. Sci. Technol.* 48(7), 3978-3985. <https://doi.org/10.1021/es405143u>.
- Wang, Z., Du, C., Lei, S., Ding, D., Chen, R., Yang, S., Cai, T., 2021. Modulation of carbon induced persulfate activation by nitrogen dopants: recent advances and perspectives. *Journal of Materials Chemistry A* 9(46), 25796-25826. <https://doi.org/10.1039/d1ta08335j>.
- Wardman, P., Candeias, L.P., 1996. Fenton chemistry: an introduction. *Radiat. Res.* 145(5), 523-531.
- Wei, J., Li, F., Zhou, L., Han, D., Gong, J., 2022. Strategies for enhancing peroxymonosulfate activation by heterogenous metal-based catalysis: A review. *Chinese Journal of Chemical Engineering*. <https://doi.org/10.1016/j.cjche.2022.07.032>.
- Wojnárovits, L., 2011. Radiation Chemistry, in: Vértes, A., Nagy, S., Klencsár, Z., Lovas, R.G., Rösch, F. (Eds.), *Handbook of Nuclear Chemistry*. Springer US, Boston, MA, pp. 1263-1331. https://doi.org/10.1007/978-1-4419-0720-2_23.
- Wols, B.A., Harmsen, D.J.H., Beerendonk, E.F., Hofman-Caris, C.H.M., 2014. Predicting pharmaceutical degradation by UV (LP)/H₂O₂ processes: A kinetic model. *Chem. Eng. J.* 255, 334-343. <https://doi.org/https://doi.org/10.1016/j.cej.2014.05.088>.
- Wu, C.-H., Yun, W.-C., Wi-Afedzi, T., Lin, K.-Y.A., 2018. ZIF-67 supported on macroscale resin as an efficient and convenient heterogeneous catalyst for Oxone activation. *J. Colloid Interface Sci.* 514, 262-271. <https://doi.org/https://doi.org/10.1016/j.jcis.2017.11.053>.

- Wu, J.-l., Ji, F., Zhang, H., Hu, C., Wong, M.H., Hu, D., Cai, Z., 2019. Formation of dioxins from triclosan with active chlorine: A potential risk assessment. *J. Hazard. Mater.* 367, 128-136. <https://doi.org/https://doi.org/10.1016/j.jhazmat.2018.12.088>.
- Wu, S., Lin, Y., Yang, C., Du, C., Teng, Q., Ma, Y., Zhang, D., Nie, L., Zhong, Y., 2019. Enhanced activation of peroxymonosulfate by LaFeO₃ perovskite supported on Al₂O₃ for degradation of organic pollutants. *Chemosphere* 237, 124478. <https://doi.org/10.1016/j.chemosphere.2019.124478>.
- Wu, S., Xiong, J., Sun, J., Hood, Z.D., Zeng, W., Yang, Z., Gu, L., Zhang, X., Yang, S.-Z., 2017. Hydroxyl-Dependent Evolution of Oxygen Vacancies Enables the Regeneration of BiOCl Photocatalyst. *ACS Applied Materials & Interfaces* 9(19), 16620-16626. <https://doi.org/10.1021/acsami.7b01701>.
- Wu, X., Zhao, W., Huang, Y., Zhang, G., 2020. A mechanistic study of amorphous CoS_x cages as advanced oxidation catalysts for excellent peroxymonosulfate activation towards antibiotics degradation. *Chem. Eng. J.* 381, 122768. <https://doi.org/10.1016/j.cej.2019.122768>.
- Wu, X., Zhao, X., Chen, R., Liu, P., Liang, W., Wang, J., Teng, M., Wang, X., Gao, S., 2022. Wastewater treatment plants act as essential sources of microplastic formation in aquatic environments: A critical review. *Water Res.* 221, 118825. <https://doi.org/https://doi.org/10.1016/j.watres.2022.118825>.
- Wu, Y., Wang, Y., Lin, Z., Wang, Y., Li, Y., Liu, S., Gui, X., Yang, X., 2019. Three-dimensional α -Fe₂O₃/amino-functionalization carbon nanotube sponge for adsorption and oxidative removal of tetrabromobisphenol A. *Sep. Purif. Technol.* 211, 359-367. <https://doi.org/10.1016/j.seppur.2018.10.002>.
- Xia, X., Zhu, F., Li, J., Yang, H., Wei, L., Li, Q., Jiang, J., Zhang, G., Zhao, Q., 2020.

- A Review Study on Sulfate-Radical-Based Advanced Oxidation Processes for Domestic/Industrial Wastewater Treatment: Degradation, Efficiency, and Mechanism. *Frontiers in Chemistry* 8. <https://doi.org/10.3389/fchem.2020.592056>.
- Xiao, R., Wei, Z., Chen, D., Weavers, L.K., 2014. Kinetics and Mechanism of Sonochemical Degradation of Pharmaceuticals in Municipal Wastewater. *Environ. Sci. Technol.* 48(16), 9675-9683. <https://doi.org/10.1021/es5016197>.
- Xie, W., Zhang, P., Liao, W., Tong, M., Yuan, S., 2021. Ligand-Enhanced Electron Utilization for Trichloroethylene Degradation by $\cdot\text{OH}$ during Sediment Oxygenation. *Environ. Sci. Technol.* <https://doi.org/10.1021/acs.est.1c00136>.
- Xiong, T., Zhang, Y., Lee, W.S.V., Xue, J., 2020. Defect Engineering in Manganese - Based Oxides for Aqueous Rechargeable Zinc - Ion Batteries: A Review. *Advanced Energy Materials* 10(34), 2001769. <https://doi.org/10.1002/aenm.202001769>.
- Xu, A., Wei, Y., Zou, Q., Zhang, W., Jin, Y., Wang, Z., Yang, L., Li, X., 2020. The effects of nonredox metal ions on the activation of peroxymonosulfate for organic pollutants degradation in aqueous solution with cobalt based catalysts: A new mechanism investigation. *J Hazard Mater* 382, 121081. <https://doi.org/10.1016/j.jhazmat.2019.121081>.
- Xu, K., Ben, W., Ling, W., Zhang, Y., Qu, J., Qiang, Z., 2017. Impact of humic acid on the degradation of levofloxacin by aqueous permanganate: Kinetics and mechanism. *Water Res.* 123, 67-74. <https://doi.org/10.1016/j.watres.2017.06.037>.
- Xu, Y., Ai, J., Zhang, H., 2016. The mechanism of degradation of bisphenol A using the magnetically separable CuFe_2O_4 /peroxymonosulfate heterogeneous oxidation

- process. *J. Hazard. Mater.* 309, 87-96.
<https://doi.org/10.1016/j.jhazmat.2016.01.023>.
- Xu, Y., Liu, T., Zhang, Y., Ge, F., Steel, R.M., Sun, L., 2017. Advances in technologies for pharmaceuticals and personal care products removal. *Journal of Materials Chemistry A* 5(24), 12001-12014. <https://doi.org/10.1039/c7ta03698a>.
- Yamamoto, H., Nakamura, Y., Moriguchi, S., Nakamura, Y., Honda, Y., Tamura, I., Hirata, Y., Hayashi, A., Sekizawa, J., 2009. Persistence and partitioning of eight selected pharmaceuticals in the aquatic environment: Laboratory photolysis, biodegradation, and sorption experiments. *Water Res.* 43(2), 351-362.
<https://doi.org/https://doi.org/10.1016/j.watres.2008.10.039>.
- Yan, G., Li, G., Tan, H., Gu, Y., Li, Y., 2020. Spinel-type ternary multimetal hybrid oxides with porous hierarchical structure grown on Ni foam as large-current-density water oxidation electrocatalyst. *J. Alloys Compd.* 838, 155662.
<https://doi.org/10.1016/j.jallcom.2020.155662>.
- Yang, J.-F., Ying, G.-G., Zhao, J.-L., Tao, R., Su, H.-C., Chen, F., 2010. Simultaneous determination of four classes of antibiotics in sediments of the Pearl Rivers using RRLC–MS/MS. *Science of The Total Environment* 408(16), 3424-3432.
<https://doi.org/10.1016/j.scitotenv.2010.03.049>.
- Yang, Q., Yang, X., Yan, Y., Sun, C., Wu, H., He, J., Wang, D., 2018. Heterogeneous activation of peroxymonosulfate by different ferromanganese oxides for tetracycline degradation: Structure dependence and catalytic mechanism. *Chem. Eng. J.* 348, 263-270. <https://doi.org/10.1016/j.cej.2018.04.206>.
- Yang, Z., Li, Y., Zhang, X., Cui, X., He, S., Liang, H., Ding, A., 2020. Sludge activated carbon-based CoFe₂O₄-SAC nanocomposites used as heterogeneous catalysts for degrading antibiotic norfloxacin through activating peroxymonosulfate.

- Chem. Eng. J. 384, 123319. <https://doi.org/10.1016/j.cej.2019.123319>.
- Yao, Y., Cai, Y., Wu, G., Wei, F., Li, X., Chen, H., Wang, S., 2015. Sulfate radicals induced from peroxymonosulfate by cobalt manganese oxides ($\text{Co}_x\text{Mn}_{3-x}\text{O}_4$) for Fenton-Like reaction in water. *J. Hazard. Mater.* 296, 128-137. <https://doi.org/10.1016/j.jhazmat.2015.04.014>.
- Yao, Y., Hu, H., Yin, H., Ma, Z., Tao, Z., Qiu, Y., Wang, S., 2022. Pyrite-embedded porous carbon nanocatalysts assembled in polyvinylidene difluoride membrane for organic pollutant oxidation. *J. Colloid Interface Sci.* 608, 2942-2954. <https://doi.org/10.1016/j.jcis.2021.11.021>.
- Ye, S., Zeng, G., Tan, X., Wu, H., Liang, J., Song, B., Tang, N., Zhang, P., Yang, Y., Chen, Q., Li, X., 2020. Nitrogen-doped biochar fiber with graphitization from *Boehmeria nivea* for promoted peroxymonosulfate activation and non-radical degradation pathways with enhancing electron transfer. *Appl. Catal., B* 269, 118850. <https://doi.org/10.1016/j.apcatb.2020.118850>.
- Yin, H., Li, J., Yan, H., Cai, H., Wan, Y., Yao, G., Guo, Y., Lai, B., 2021. Activation of peroxymonosulfate by CuCo_2O_4 nano-particles towards long-lasting removal of atrazine. *Journal of Water Reuse and Desalination* 11(4), 542-559. <https://doi.org/10.2166/wrd.2021.046>.
- Yoon, Y., Westerhoff, P., Snyder, S.A., Wert, E.C., Yoon, J., 2007. Removal of endocrine disrupting compounds and pharmaceuticals by nanofiltration and ultrafiltration membranes. *Desalination* 202(1), 16-23. <https://doi.org/https://doi.org/10.1016/j.desal.2005.12.033>.
- Yu, R., Zhao, J., Zhao, Z., Cui, F., 2020. Copper substituted zinc ferrite with abundant oxygen vacancies for enhanced ciprofloxacin degradation via peroxymonosulfate activation. *J. Hazard. Mater.* 390, 121998.

- <https://doi.org/https://doi.org/10.1016/j.jhazmat.2019.121998>.
- Yu, X., Sui, Q., Lyu, S., Zhao, W., Liu, J., Cai, Z., Yu, G., Barcelo, D., 2020. Municipal Solid Waste Landfills: An Underestimated Source of Pharmaceutical and Personal Care Products in the Water Environment. *Environ. Sci. Technol.* 54(16), 9757-9768. <https://doi.org/10.1021/acs.est.0c00565>.
- Yuan, G.L., Martin, L.W., Ramesh, R., Uedono, A., 2009. The dependence of oxygen vacancy distributions in BiFeO₃ films on oxygen pressure and substrate. *Appl. Phys. Lett.* 95(1), 012904. <https://doi.org/10.1063/1.3171939>.
- Yuan, P., Southon, P.D., Liu, Z., Kepert, C.J., 2012. Organosilane functionalization of halloysite nanotubes for enhanced loading and controlled release. *Nanotechnology* 23(37), 375705. <https://doi.org/10.1088/0957-4484/23/37/375705>.
- Yuan, P., Tan, D., Annabi-Bergaya, F., 2015. Properties and applications of halloysite nanotubes: recent research advances and future prospects. *Appl. Clay Sci.* 112-113, 75-93. <https://doi.org/10.1016/j.clay.2015.05.001>.
- Yuan, R., Jiang, M., Gao, S., Wang, Z., Wang, H., Boczkaj, G., Liu, Z., Ma, J., Li, Z., 2020. 3D mesoporous α -Co(OH)₂ nanosheets electrodeposited on nickel foam: A new generation of macroscopic cobalt-based hybrid for peroxymonosulfate activation. *Chem. Eng. J.* 380, 122447. <https://doi.org/10.1016/j.cej.2019.122447>.
- Zeng, H., Zhu, H., Deng, J., Shi, Z., Zhang, H., Li, X., Deng, L., 2022. New insight into peroxymonosulfate activation by CoAl-LDH derived CoOOH: Oxygen vacancies rather than Co species redox pairs induced process. *Chem. Eng. J.* 442, 136251. <https://doi.org/10.1016/j.cej.2022.136251>.
- Zhan, G., Li, J., Hu, Y., Zhao, S., Cao, S., Jia, F., Zhang, L., 2020. The surface hydroxyl

- and oxygen vacancy dependent Cr(vi) adsorption performance of BiOCl. *Environmental Science: Nano* 7(5), 1454-1463. <https://doi.org/10.1039/d0en00108b>.
- Zhang, F., Sun, Z., Cui, J., 2020. Research on the mechanism and reaction conditions of electrochemical preparation of persulfate in a split-cell reactor using BDD anode. *RSC Advances* 10(56), 33928-33936. <https://doi.org/10.1039/d0ra04669h>.
- Zhang, K., Parker, K.M., 2018. Halogen Radical Oxidants in Natural and Engineered Aquatic Systems. *Environ. Sci. Technol.* 52(17), 9579-9594. <https://doi.org/10.1021/acs.est.8b02219>.
- Zhang, M., Su, X., Ma, L., Khan, A., Wang, L., Wang, J., Maloletnev, A.S., Yang, C., 2021. Promotion effects of halloysite nanotubes on catalytic activity of Co₃O₄ nanoparticles toward reduction of 4-nitrophenol and organic dyes. *J. Hazard. Mater.* 403, 123870. <https://doi.org/10.1016/j.jhazmat.2020.123870>.
- Zhang, Q.-Q., Ying, G.-G., Pan, C.-G., Liu, Y.-S., Zhao, J.-L., 2015. Comprehensive Evaluation of Antibiotics Emission and Fate in the River Basins of China: Source Analysis, Multimedia Modeling, and Linkage to Bacterial Resistance. *Environ. Sci. Technol.* 49(11), 6772-6782. <https://doi.org/10.1021/acs.est.5b00729>.
- Zhang, R., Wan, Y., Peng, J., Yao, G., Zhang, Y., Lai, B., 2019. Efficient degradation of atrazine by LaCoO₃/Al₂O₃ catalyzed peroxymonosulfate: Performance, degradation intermediates and mechanism. *Chem. Eng. J.* 372, 796-808. <https://doi.org/10.1016/j.cej.2019.04.188>.
- Zhang, S., Gao, H., Xu, X., Cao, R., Yang, H., Xu, X., Li, J., 2020. MOF-derived CoN/N-C@SiO₂ yolk-shell nanoreactor with dual active sites for highly

- efficient catalytic advanced oxidation processes. *Chem. Eng. J.* 381, 122670. <https://doi.org/10.1016/j.cej.2019.122670>.
- Zhang, X., Zhao, R., Zhang, N., Su, Y., Liu, Z., Gao, R., Du, C., 2020. Insight to unprecedented catalytic activity of double-nitrogen defective metal-free catalyst: Key role of coal gangue. *Appl. Catal., B* 263, 118316. <https://doi.org/10.1016/j.apcatb.2019.118316>.
- Zhang, Y., Xie, Y., Tang, A., Zhou, Y., Ouyang, J., Yang, H., 2014. Precious-Metal Nanoparticles Anchored onto Functionalized Halloysite Nanotubes. *Industrial & Engineering Chemistry Research* 53(13), 5507-5514. <https://doi.org/10.1021/ie404326j>.
- Zhao, H., Qu, Z., Sun, H., 2020. Rational design of spinel CoMn_2O_4 with Co-enriched surface as high-activity catalysts for NH_3 -SCO reaction. *Appl. Surf. Sci.* 529, 147044. <https://doi.org/10.1016/j.apsusc.2020.147044>.
- Zhao, Q., Fu, L., Jiang, D., Ouyang, J., Hu, Y., Yang, H., Xi, Y., 2019. Nanoclay-modulated oxygen vacancies of metal oxide. *Communications Chemistry* 2(1). <https://doi.org/10.1038/s42004-019-0112-9>.
- Zhao, Y., An, H., Feng, J., Ren, Y., Ma, J., 2019. Impact of Crystal Types of AgFeO_2 Nanoparticles on the Peroxymonosulfate Activation in the Water. *Environ. Sci. Technol.* 53(8), 4500-4510. <https://doi.org/10.1021/acs.est.9b00658>.
- Zheng, Y., Wang, L., Zhong, F., Cai, G., Xiao, Y., Jiang, L., 2020. Site-Oriented Design of High-Performance Halloysite-Supported Palladium Catalysts for Methane Combustion. *Industrial & Engineering Chemistry Research* 59(13), 5636-5647. <https://doi.org/10.1021/acs.iecr.9b06679>.
- Zhou, X., Luo, C., Luo, M., Wang, Q., Wang, J., Liao, Z., Chen, Z., Chen, Z., 2020. Understanding the synergetic effect from foreign metals in bimetallic oxides for

- PMS activation: A common strategy to increase the stoichiometric efficiency of oxidants. *Chem. Eng. J.* 381, 122587. <https://doi.org/10.1016/j.cej.2019.122587>.
- Zhou, X., Luo, H., Sheng, B., Chen, X., Wang, Y., Chen, Q., Zhou, J., 2021. Cu²⁺/Cu⁺ cycle promoted PMS decomposition with the assistance of Mo for the degradation of organic pollutant. *J. Hazard. Mater.* 411, 125050. <https://doi.org/10.1016/j.jhazmat.2021.125050>.
- Zhou, X.F., Dai, C.M., Zhang, Y.L., Surampalli, R.Y., Zhang, T.C., 2010. A preliminary study on the occurrence and behavior of carbamazepine (CBZ) in aquatic environment of Yangtze River Delta, China. *Environ. Monit. Assess.* 173(1-4), 45-53. <https://doi.org/10.1007/s10661-010-1369-8>.
- Zhou, Y., Gao, Y., Jiang, J., Shen, Y.-M., Pang, S.-Y., Wang, Z., Duan, J., Guo, Q., Guan, C., Ma, J., 2020. Transformation of tetracycline antibiotics during water treatment with unactivated peroxymonosulfate. *Chem. Eng. J.* 379, 122378. <https://doi.org/10.1016/j.cej.2019.122378>.
- Zhu, C., Wei, X., Li, W., Pu, Y., Sun, J., Tang, K., Wan, H., Ge, C., Zou, W., Dong, L., 2020. Crystal-Plane Effects of CeO₂{110} and CeO₂{100} on Photocatalytic CO₂ Reduction: Synergistic Interactions of Oxygen Defects and Hydroxyl Groups. *ACS Sustainable Chemistry & Engineering* 8(38), 14397-14406. <https://doi.org/10.1021/acssuschemeng.0c04205>.
- Zhu, C., Zhang, Y., Fan, Z., Liu, F., Li, A., 2020. Carbonate-enhanced catalytic activity and stability of Co₃O₄ nanowires for (1)O₂-driven bisphenol A degradation via peroxymonosulfate activation: Critical roles of electron and proton acceptors. *J Hazard Mater* 393, 122395. <https://doi.org/10.1016/j.jhazmat.2020.122395>.
- Zhu, M.-P., Yang, J.-C.E., Duan, X., Zhang, D.-D., Wang, S., Yuan, B., Fu, M.-L., 2020. Interfacial CoAl₂O₄ from ZIF-67@ γ -Al₂O₃ pellets toward catalytic activation

of peroxymonosulfate for metronidazole removal. Chem. Eng. J. 397, 125339.

<https://doi.org/10.1016/j.cej.2020.125339>.

Zhu, S., Xu, Y., Zhu, Z., Liu, Z., Wang, W., 2020. Activation of peroxymonosulfate by magnetic Co-Fe/SiO₂ layered catalyst derived from iron sludge for ciprofloxacin degradation. Chem. Eng. J. 384, 123298.

<https://doi.org/10.1016/j.cej.2019.123298>.